



National Library  
of Canada

Acquisitions and  
Bibliographic Services Branch

395 Wellington Street  
Ottawa, Ontario  
K1A 0N4

Bibliothèque nationale  
du Canada

Direction des acquisitions et  
des services bibliographiques

395, rue Wellington  
Ottawa (Ontario)  
K1A 0N4

For the / Pour l'adresse

Order / Commande

## NOTICE

The quality of this microform is heavily dependent upon the quality of the original thesis submitted for microfilming. Every effort has been made to ensure the highest quality of reproduction possible.

If pages are missing, contact the university which granted the degree.

Some pages may have indistinct print especially if the original pages were typed with a poor typewriter ribbon or if the university sent us an inferior photocopy.

Reproduction in full or in part of this microform is governed by the Canadian Copyright Act, R.S.C. 1970, c. C-30, and subsequent amendments.

## AVIS

La qualité de cette microforme dépend grandement de la qualité de la thèse soumise au microfilmage. Nous avons tout fait pour assurer une qualité supérieure de reproduction.

S'il manque des pages, veuillez communiquer avec l'université qui a conféré le grade.

La qualité d'impression de certaines pages peut laisser à désirer, surtout si les pages originales ont été dactylographiées à l'aide d'un ruban usé ou si l'université nous a fait parvenir une photocopie de qualité inférieure.

La reproduction, même partielle, de cette microforme est soumise à la Loi canadienne sur le droit d'auteur, SRC 1970, c. C-30, et ses amendements subséquents.

**Geotechnical Behavior of Shell Foundations**

**Mohamed Abdel-Rahman**

**A Thesis  
in  
The Department  
of  
Civil Engineering**

**Presented in Partial Fulfillment of the Requirements  
for the Degree of Doctor of Philosophy at  
Concordia University**

**March 1996**

**© Mohamed Abdel-Rahman, 1996**



National Library  
of Canada

Acquisitions and  
Bibliographic Services Branch

395 Wellington Street  
Ottawa, Ontario  
K1A 0N4

Bibliothèque nationale  
du Canada

Direction des acquisitions et  
des services bibliographiques

395, rue Wellington  
Ottawa (Ontario)  
K1A 0N4

*Vous le* *Notre référence*

*Vous le* *Notre référence*

**The author has granted an irrevocable non-exclusive licence allowing the National Library of Canada to reproduce, loan, distribute or sell copies of his/her thesis by any means and in any form or format, making this thesis available to interested persons.**

**L'auteur a accordé une licence irrévocable et non exclusive permettant à la Bibliothèque nationale du Canada de reproduire, prêter, distribuer ou vendre des copies de sa thèse de quelque manière et sous quelque forme que ce soit pour mettre des exemplaires de cette thèse à la disposition des personnes intéressées.**

**The author retains ownership of the copyright in his/her thesis. Neither the thesis nor substantial extracts from it may be printed or otherwise reproduced without his/her permission.**

**L'auteur conserve la propriété du droit d'auteur qui protège sa thèse. Ni la thèse ni des extraits substantiels de celle-ci ne doivent être imprimés ou autrement reproduits sans son autorisation.**

ISBN 0-612-10814-7

**Canada**

## ABSTRACT

### Geotechnical Behavior of Shell Foundations

Mohamed Abdel-Rahman, Ph.D.  
Concordia University, 1996

The geotechnical behavior of shell foundations was investigated experimentally, numerically, and theoretically. Experimental investigation was carried out on nine prototype foundation models in loose, medium, and dense sands. Experimental set-up was organized and instrumented to perform the testing program. Loading tests were conducted on surface as well as embedded footings. Triangular, conical, and pyramidal shell models were tested against conventional strip, circular, and square flat counterparts, respectively. The influences of shell configuration on the ultimate bearing capacity, settlement, contact pressure distribution, and stresses within the soil mass, were investigated. Special loading tests using colored sand layers in a Plexiglas tank were performed to determine the failure mechanism of shell foundations. Numerical modelling, using the finite element code "CRISP", was conducted to simulate the experimental tests conditions of the plane strain models. Elastic perfectly plastic soil model, employing Mohr-Coulomb's yield criteria, was adopted to simulate the behavior of the tested sand. Deformed meshes, displacement vectors, stresses, strains, and displacements of the plane strain models are analyzed and presented. A theoretical model to predict the ultimate bearing capacity of shell foundations was developed. The theory provides kinematically and statically admissible solution. The effects of shell configuration on the shape of rupture surface and accordingly on the ultimate bearing capacity were incorporated. A computer program "*BC-Shell*" was developed to perform the mathematical calculations of the theoretical analysis. The program "*BC-Shell*" was then designed in an interactive mode for an easy application to predict the ultimate bearing capacity. Parametric study was conducted to examine the sensitivity of the governing parameters on the ultimate bearing capacity. Design charts and design tables are also presented to determine the bearing capacity coefficients and depth factors. In addition, the theory was extended to predict the ultimate bearing capacity of shell foundations in axisymmetrical and three dimensional conditions by introducing shape factors for shell foundations. The results of this study support that shell foundations should come into wider use in the geotechnical field as a serious alternative to shallow and deep foundations.

*To My Family:  
my wife Youmna,  
my sons Alaa & Karim,  
and my Parents.*

## ACKNOWLEDGMENTS

The author gratefully acknowledges the valuable guidance, understanding, and cooperation of Professor Adel M. Hanna, under his supervision this research work was carried out. Dr. Hanna also provided me with his support and precious advice through the years, which helped me to manage and cope with many problems in my life.

The author also wishes to thank Dr. Arul Britto, Professor in the Department of Engineering, Cambridge University, U.K., for his useful suggestions and consultation through e-mail on the use of the finite element program "CRISP".

Many thanks are due to Mr. Paul Scheiwiler and the team of the machine shop at Concordia University for their patience and effort during the fabrication process of the experimental setup and the foundation models. Special thanks are also due to Messrs. Andrew Chociwski, Technical Officer; Daniel Roy, Lab Technician; and Norman Landry, CGEB student, for their valuable help during the experimental investigation phase.

The cooperation of Mss. Manon, Angie and Carol, the secretaries of the department of Civil Engineering, is highly appreciated.

The financial supports from the Natural Sciences and Engineering Research Council of Canada (NSERC), the department of Civil Engineering at Concordia University, and Quebec Ministry of Education are gratefully acknowledged.

The stimulating discussions with my former colleague Dr. Ashraf Ghaly, Professor in the Department of Civil Engineering, Union Collage, N.Y., are highly acknowledged.

I wish to thank my wife for bearing with me the tough student life and for her continuous encouragement; I couldn't have done it without her love.

Last but not least, I wish to express my sincere gratitude to my parents for their kindness, love, and support throughout the course of my graduate studies in Canada.

## TABLE OF CONTENTS

	<i>Page</i>
TABLE OF CONTENTS	vi
LIST OF FIGURES	viii
LIST OF PLATES	xvii
LIST OF TABLES	xviii
LIST OF SYMBOLS	xx
CHAPTER 1	
INTRODUCTION	1
1.1 Historical Background	1
1.2 Classification of Shells	3
1.3 Shells in Foundation Engineering	3
CHAPTER 2	
LITERATURE REVIEW & SCOPE OF THE THESIS	9
2.1 General	9
2.2 Field Applications	9
2.3 Research on Shell Foundations	17
2.3.1 Structural Performance	18
2.3.2 Geotechnical Behavior	19
2.4 Scope of The Thesis	24
2.4.1 Experimental Phase	24
2.4.2 Numerical Phase	25
2.4.3 Theoretical Phase	25
CHAPTER 3	
EXPERIMENTAL INVESTIGATION	27
3.1 General	27
3.2 Foundation Models	27
3.3 Experimental Set-Up	41
3.3.1 Testing Tanks	41
3.3.2 Loading System	41
3.3.3 Pressure Transducers	44
3.3.4 Data Acquisition System	50
3.4 Experimental Testing Program	51
3.5 Sand Characteristics	52

	<i>Page</i>
3.6 Embedment Depth	57
3.7 Experimental Test Procedure	57
3.8 Experimental Test Results	62
3.8.1 In-Situ Stresses in Sand	62
3.8.2 Load-Settlement Curves	68
3.8.3 Contact Pressure Distribution	88
3.8.4 Lateral & Vertical Stresses	138
3.9 Special Loading Tests	157
<b>CHAPTER 4</b>	
<b>NUMERICAL MODELLING</b>	160
4.1 General	160
4.2 Mesh Design	160
4.3 Soil & Foundation Modelling	161
4.4 Loading Scheme	165
4.5 Finite Element's Output	165
<b>CHAPTER 5</b>	
<b>THEORETICAL MODELLING</b>	182
5.1 General	182
5.2 Theoretical Model for Shell Foundation	183
5.3 Program " <i>BC-Shell</i> "	208
5.4 Comparison between Theoretical & Experimental Results	209
5.5 Parametric Study	212
5.6 Design Charts & Tables	218
5.7 Depth & Shape Factors	219
<b>CHAPTER 6</b>	
<b>CONCLUSIONS &amp; RECOMMENDATIONS</b>	238
6.1 General	238
6.2 Conclusions	238
6.3 Recommendations for Future Research	243
<b>LIST OF REFERENCES</b>	245
<b>APPENDIX I : Computer Program "<i>BC-Shell</i>"</b>	253
<b>APPENDIX II: Design Tables for <math>N_c</math>, <math>N_q</math>, &amp; <math>N_\gamma</math></b>	261



## LIST OF FIGURES

	<i>Page</i>
<b>CHAPTER 1</b>	
Figure 1.1 : Inverted Brick Arch Foundation	2
Figure 1.2 : Hyperbolic Paraboloid Shell Foundation	4
Figure 1.3 : Conical Shell Foundations	4
Figure 1.4 : Pyramidal Shell Foundation	5
Figure 1.5 : Spherical Shell Foundation	6
Figure 1.6 : Inverted Dome Shell Foundation	6
Figure 1.7 : Elliptic Paraboloid Shell Foundation	7
Figure 1.8 : Paraboloid & Hyperboloid Shell Foundations	8
<b>CHAPTER 2</b>	
Figure 2.1 : Barrel Shell Foundation, Mexico	10
Figure 2.2 : Hypar Footing for St-Vincent Chapel, Mexico	11
Figure 2.3 : Hypar Shell for Shed in Lamex S.A., Mexico	11
Figure 2.4 : Inverted Cylindrical Shell Foundation, India	12
Figure 2.5 : Hypar Footing on Timber Piles, India	13
Figure 2.6 : Egg Underground Amphitheater in Paris, France	14
Figure 2.7 : Conical Shell Substructure for Stuttgart TV Tower , Germany	15
Figure 2.8 : Hollow Conic Shell Foundation, China	16
<b>CHAPTER 3</b>	
Figure 3.1 : Strip Flat Foundation Model	28
Figure 3.2 : Triangular (1) Strip Shell Foundation Model ( $a/b=1/2$ )	29
Figure 3.3 : Triangular (2) Strip Shell Foundation Model ( $a/b=1$ )	30
Figure 3.4 : Circular Flat Foundation Model	31
Figure 3.5 : Conical (1) Shell Foundation Model ( $a/b=1/2$ )	32
Figure 3.6 : Conical (2) Shell Foundation Model ( $a/b=1$ )	33
Figure 3.7 : Square Flat Foundation Model	34
Figure 3.8 : Pyramidal (1) Shell Foundation Model ( $a/b=1/2$ )	35
Figure 3.9 : Pyramidal (2) Shell Foundation Model ( $a/b=1$ )	36
Figure 3.10 : Sketch of Experimental Set-Up	42
Figure 3.11 : Pressure Transducer Model (1)	45
Figure 3.12 : Pressure Transducer Model (2)	46

	<i>Page</i>
Figure 3.13 : Transducers Box Unit	46
Figure 3.14 : Typical Arrangement of Pressure Transducers Units	47
Figure 3.15 : Mechanical Sieve Analysis Graph	53
Figure 3.16 : Compaction Time versus Sand Unit Weight inside Plexiglas Tank	54
Figure 3.17 : Compaction Time versus Sand Unit Weight inside Steel Tank	54
Figure 3.18 : Shear Stress versus Horizontal Displacement from Direct Shear Box Tests	55
Figure 3.19 : Shear Stress versus Normal Stress from Direct Shear Box Tests	56
Figure 3.20 : Unit Weight versus Angle of Shearing Resistance ( $\phi^\circ$ )	56
Figure 3.21 : Lateral & Vertical Stresses after Sand Placing inside Steel Tank	66
Figure 3.22 : Distribution of $K_{om}$ & OCR after Sand Placing inside Steel Tank	67
Figure 3.23 : Load-Settlement Curves for Strip Flat Footing	70
Figure 3.24 : Load-Settlement Curves for Triangular (1) Shell Footing	71
Figure 3.25 : Load-Settlement Curves for Triangular (2) Shell Footing	72
Figure 3.26 : Load-Settlement Curves for Circular Flat Footing	73
Figure 3.27 : Load-Settlement Curves for Conical (1) Shell Footing	74
Figure 3.28 : Load-Settlement Curves for Conical (2) Shell Footing	75
Figure 3.29 : Load-Settlement Curves for Square Flat Footing	76
Figure 3.30 : Load-Settlement Curves for Pyramidal (1) Shell Footing	77
Figure 3.31 : Load-Settlement Curves for Pyramidal (2) Shell Footing	78
Figure 3.32 : Ultimate Loads ( $Q_u$ ) for Plane Strain Condition	80
Figure 3.33 : Ultimate Loads ( $Q_u$ ) for Axisymmetrical Condition	81
Figure 3.34 : Ultimate Loads ( $Q_u$ ) for Three Dimensional Condition	82
Figure 3.35 : Settlement Factor ( $F_\delta$ ) for Plane Strain Condition	85
Figure 3.36 : Settlement Factor ( $F_\delta$ ) for Axisymmetrical Condition	86
Figure 3.37 : Settlement Factor ( $F_\delta$ ) for Three Dimensional Condition	87
Figure 3.38 : Contact Pressure Envelopes for Strip Flat Footing on Loose Sand	90
Figure 3.39 : Contact Pressure Envelopes for Strip Flat Footing on	

	<i>Page</i>
Medium Sand	91
Figure 3.40: Contact Pressure Envelopes for Strip Flat Footing on Dense Sand	92
Figure 3.41: Contact Pressure Envelopes for Triangular (1) Shell Footing on Loose Sand	93
Figure 3.42: Contact Pressure Envelopes for Triangular (1) Shell Footing on Medium Sand	94
Figure 3.43: Contact Pressure Envelopes for Triangular (1) Shell Footing on Dense Sand	95
Figure 3.44: Contact Pressure Envelopes for Triangular (2) Shell Footing on Loose Sand	96
Figure 3.45: Contact Pressure Envelopes for Triangular (2) Shell Footing on Medium Sand	97
Figure 3.46: Contact Pressure Envelopes for Triangular (2) Shell Footing on Dense Sand	98
Figure 3.47: Contact Pressure Envelopes for Circular Flat Footing on Loose Sand	99
Figure 3.48: Contact Pressure Envelopes for Circular Flat Footing on Medium Sand	100
Figure 3.49: Contact Pressure Envelopes for Circular Flat Footing on Dense Sand	101
Figure 3.50: Contact Pressure Envelopes for Conical (1) Shell Footing on Loose Sand	102
Figure 3.51: Contact Pressure Envelopes for Conical (1) Shell Footing on Medium Sand	103
Figure 3.52: Contact Pressure Envelopes for Conical (1) Shell Footing on Dense Sand	104
Figure 3.53: Contact Pressure Envelopes for Conical (2) Shell Footing on Loose Sand	105
Figure 3.54: Contact Pressure Envelopes for Conical (2) Shell Footing on Medium Sand	106
Figure 3.55: Contact Pressure Envelopes for Conical (2) Shell Footing on Dense Sand	107
Figure 3.56: Contact Pressure Envelopes for Square Flat Footing on	

	<i>Page</i>
Loose Sand	108
Figure 3.57 : Contact Pressure Envelopes for Square Flat Footing on Medium Sand	109
Figure 3.58 : Contact Pressure Envelopes for Square Flat Footing on Dense Sand	110
Figure 3.59 : Contact Pressure Envelopes for Pyramidal (1) Shell Footing on Loose Sand	111
Figure 3.60 : Contact Pressure Envelopes for Pyramidal (1) Shell Footing on Medium Sand	112
Figure 3.61 : Contact Pressure Envelopes for Pyramidal (1) Shell Footing on Dense Sand	113
Figure 3.62 : Contact Pressure Envelopes for Pyramidal (2) Shell Footing on Loose Sand	114
Figure 3.63 : Contact Pressure Envelopes for Pyramidal (2) Shell Footing on Medium Sand	115
Figure 3.64 : Contact Pressure Envelopes for Pyramidal (2) Shell Footing on Dense Sand	116
Figure 3.65 : Contact Pressure Distribution for Strip Flat Footing	129
Figure 3.66 : Contact Pressure Distribution for Triangular (1) Shell Footing	130
Figure 3.67 : Contact Pressure Distribution for Triangular (2) Shell Footing	131
Figure 3.68 : Contact Pressure Distribution for Circular Flat Footing	132
Figure 3.69 : Contact Pressure Distribution for Conical (1) Shell Footing	133
Figure 3.70 : Contact Pressure Distribution for Conical (2) Shell Footing	134
Figure 3.71 : Contact Pressure Distribution for Square Flat Footing	135
Figure 3.72 : Contact Pressure Distribution for Pyramidal (1) Shell Footing	136
Figure 3.73 : Contact Pressure Distribution for Pyramidal (2) Shell Footing	137
Figure 3.74 : Vertical & Lateral Stresses for Circular Flat Footing on Loose Sand	139
Figure 3.75 : Vertical & Lateral Stresses for Circular Flat Footing on Medium Sand	140

	<i>Page</i>
Figure 3.76 : Vertical & Lateral Stresses for Circular Flat Footing on Dense Sand	141
Figure 3.77 : Vertical & Lateral Stresses for Conical (1) Shell Footing on Loose Sand	142
Figure 3.78 : Vertical & Lateral Stresses for Conical (1) Shell Footing on Medium Sand	143
Figure 3.79 : Vertical & Lateral Stresses for Conical (1) Shell Footing on Dense Sand	144
Figure 3.80 : Vertical & Lateral Stresses for Conical (2) Shell Footing on Loose Sand	145
Figure 3.81 : Vertical & Lateral Stresses for Conical (2) Shell Footing on Medium Sand	146
Figure 3.82 : Vertical & Lateral Stresses for Conical (2) Shell Footing on Dense Sand	147
Figure 3.83 : Vertical & Lateral Stresses for Square Flat Footing on Loose Sand	148
Figure 3.84 : Vertical & Lateral Stresses for Square Flat Footing for Medium Sand	149
Figure 3.85 : Vertical & Lateral Stresses for Square Flat Model on Dense Sand	150
Figure 3.86 : Vertical & Lateral Stresses for Pyramidal (1) Shell Footing on Loose Sand	151
Figure 3.87 : Vertical & Lateral Stresses for Pyramidal (1) Shell Footing on Medium Sand	152
Figure 3.88 : Vertical & Lateral Stresses for Pyramidal (1) Shell Footing on Dense Sand	153
Figure 3.89 : Vertical & Lateral Stresses for Pyramidal (2) Shell Footing on Loose Sand	154
Figure 3.90 : Vertical & Lateral Stresses for Pyramidal (2) Shell Footing on Medium Sand	155
Figure 3.91 : Vertical & Lateral Stresses for Pyramidal (2) Shell Footing on Dense Sand	156

#### CHAPTER 4

Figure 4.1 : Finite Element Meshes for Strip Flat Footing	162
-----------------------------------------------------------	-----

	<i>Page</i>
Figure 4.2 : Finite Element Meshes for Triangular (1) Shell Footing	163
Figure 4.3 : Finite Element Meshes for Triangular (2) Shell Footing	164
Figure 4.4 : Typical Undeformed/Deformed Mesh & Displacement Vectors for Triangular (1) Shell Surface Footing	168
Figure 4.5 : Typical Distributions for Horizontal & Vertical Strain for Triangular (1) Surface Shell Footing	169
Figure 4.6 : Typical Distributions for Horizontal & Vertical Stress for Triangular (1) Shell Surface Footing	170
Figure 4.7 : Typical Distributions for Horizontal & Vertical Displacement for Triangular (1) Shell Surface Footing	171
Figure 4.8 : Typical Undeformed/Deformed Mesh & Displacement Vectors for Triangular (1) Shell Embedded Footing	172
Figure 4.9 : Typical Distributions for Horizontal & Vertical Strain for Triangular (1) Embedded Shell Footing	173
Figure 4.10 : Typical Distributions for Horizontal & Vertical Stress for Triangular (1) Shell Embedded Footing	174
Figure 4.11 : Typical Distributions for Horizontal & Vertical Displacement for Triangular (1) Shell Embedded Footing	175

## CHAPTER 5

Figure 5.1 : Rupture Surface for Strip Shell Foundation	185
Figure 5.2 : Mohr-Coulomb's Failure Criteria	186
Figure 5.3 : Equilibrium According to Kötter's Equation	188
Figure 5.4 : Equilibrium of Forces under Shell Foundation	200
Figure 5.5 : Theoretical & Experimental Results for Surface Strip Footings	210
Figure 5.6 : Theoretical & Experimental Results for Embedded Strip Footings	211
Figure 5.7 : Effect of The Cohesion of Soil ( $c$ ) on Factor ( $\rho$ )	213
Figure 5.8 : Effect of Foundation Width ( $B$ ) on Factor ( $\rho$ )	214
Figure 5.9 : Effect of Unit Weight of Soil ( $\gamma$ ) on Factor ( $\rho$ )	215
Figure 5.10 : Effect of Embedment Ratio (ER) on Factor ( $\rho$ )	216
Figure 5.11 : Effect of Shell Ratio (SR) on Factor ( $\rho$ )	217
Figure 5.12 : Design Chart for Bearing Capacity Coefficient ( $N_c$ ) for ER = 0.0	220

	<i>Page</i>
Figure 5.13 : Design Chart for Bearing Capacity Coefficient ( $N_q$ ) for ER = 0.0	221
Figure 5.14 : Design Chart for Bearing Capacity Coefficient ( $N_\gamma$ ) for ER = 0.0	222
Figure 5.15 : Design Chart for Bearing Capacity Coefficient ( $N_c$ ) for ER = 0.25	223
Figure 5.16 : Design Chart for Bearing Capacity Coefficient ( $N_q$ ) for ER = 0.25	224
Figure 5.17 : Design Chart for Bearing Capacity Coefficient ( $N_\gamma$ ) for ER = 0.25	225
Figure 5.18 : Design Chart for Bearing Capacity Coefficient ( $N_c$ ) for ER = 0.50	226
Figure 5.19 : Design Chart for Bearing Capacity Coefficient ( $N_q$ ) for ER = 0.50	227
Figure 5.20 : Design Chart for Bearing Capacity Coefficient ( $N_\gamma$ ) for ER = 0.50	228
Figure 5.21 : Design Chart for Bearing Capacity Coefficient ( $N_c$ ) for ER = 0.75	229
Figure 5.22 : Design Chart for Bearing Capacity Coefficient ( $N_q$ ) for ER = 0.75	230
Figure 5.23 : Design Chart for Bearing Capacity Coefficient ( $N_\gamma$ ) for ER = 0.75	231
Figure 5.24 : Depth Factors $f_{dq}$ & $f_{d\gamma}$ from The Experimental Results	232
Figure 5.25 : Shape Factors $f_{sq}$ & $f_{s\gamma}$ for Axisymmetrical Condition	233
Figure 5.26 : Shape Factors $f_{sq}$ & $f_{s\gamma}$ for Three Dimensional Condition	234
Figure 5.27 : Design Chart for Depth Factors $f_{dq}$ & $f_{d\gamma}$ for Flat Footing ( $\theta= 0^\circ$ )	235
Figure 5.28 : Design Chart for Depth Factors $f_{dq}$ & $f_{d\gamma}$ for Shell Angle ( $\theta= 30^\circ$ )	236
Figure 5.29 : Design Chart for Depth Factors $f_{dq}$ & $f_{d\gamma}$ for Shell Angle ( $\theta= 60^\circ$ )	237

## LIST OF PLATES

*Page*

### CHAPTER 3

Plate 3.1	: "CNC" Vertical Milling Machine (Mazak VQC-15/40)	37
Plate 3.2	: Pyramidal Shell Model During Fabrication Process	38
Plate 3.3	: Pyramidal Shell Model after Fabrication Completed	38
Plate 3.4	: Overall View of All Foundation Models	39
Plate 3.5	: Close-Up View of Strip Flat & Triangular shell Models	39
Plate 3.6	: Close-Up View of Circular Flat & Conical Shell Models	40
Plate 3.7	: Close-Up View of Square Flat & Pyramidal Shell Models	40
Plate 3.8	: Plexiglas Testing Tank	43
Plate 3.9	: Steel Testing Tank	43
Plate 3.10	: Close-Up View of The Loading System	44
Plate 3.11	: Calibration Process of Pressure Transducer	49
Plate 3.12	: Data Acquisition System	50
Plate 3.13	: Sand Reservoir	59
Plate 3.14	: Funnel Assembly Used for Sand Spreading Technique	59
Plate 3.15	: Air Pressure Compactor	60
Plate 3.16	: Process of Sand Filling under Shell Model	60
Plate 3.17	: Shell Model in Place after Sand Filling Process	61
Plate 3.18	: Circular Foundation Model before Testing	61
Plate 3.19	: Circular Foundation Model during Loading Process	62
Plate 3.20	: Strip Flat Footing before Testing	157
Plate 3.21	: Strip Flat Footing during Testing	158
Plate 3.22	: Strip Flat Footing at Ultimate Stage	158
Plate 3.23	: Triangular (1) Shell Footing at Ultimate Stage	159
Plate 3.24	: Triangular (2) Shell Footing at Ultimate Stage	159



## LIST OF TABLES

	<i>Page</i>
<b>CHAPTER 3</b>	
Table 3.1 : Coordinates of Pressure Transducers Units	48
Table 3.2 : Experiment:u Testing Program	51
Table 3.3 : Physical and Mechanical Characteristics of Sand in Plexiglass Tank	57
Table 3.4 : Physical and Mechanical Characteristics of Sand in Steel Tank	57
Table 3.5 : Compaction Results for Loose Sand ( $\phi = 33.86^\circ$ ) in Steel Tank	65
Table 3.6 : Compaction Results for Medium Sand ( $\phi = 37.73^\circ$ ) in Steel Tank	65
Table 3.7 : Compaction Results for Dense Sand ( $\phi = 40.61^\circ$ ) in Steel Tank	65
Table 3.8 : Ultimate Load ( $Q_u$ ) & Settlement ( $\delta_u$ ) for Plane Strain Models	68
Table 3.9 : Ultimate Load ( $Q_u$ ) & Settlement ( $\delta_u$ ) for Axisymmetrical Models	69
Table 3.10 : Ultimate Load ( $Q_u$ ) & Settlement ( $\delta_u$ ) for Three Dimensional Models	69
Table 3.11 : Shell Efficiency Factor ( $\eta$ )%	84
Table 3.12 : Settlement Factor ( $F_\delta$ ) at Ultimate Load ( $\times 10^3$ )	84
Table 3.13 : Ratios of ( $Q_t/Q_u$ ) & ( $Q_b/Q_u$ ) for Plane Strain Condition	117
Table 3.14 : Ratios of ( $Q_t/Q_u$ ) & ( $Q_b/Q_u$ ) for Axisymmetrical Condition	118
Table 3.15 : Ratios of ( $Q_t/Q_u$ ) & ( $Q_b/Q_u$ ) for Three Dimensional Condition	118
Table 3.16 : Locations of Reference Points From The Center of Footing (mm)	119
Table 3.17 : Contact Pressures for Plane Strain Condition for Surface Footings	120
Table 3.18 : Contact Pressures for Plane Strain Condition for Embedded Footings	121

	<i>Page</i>
Table 3.19 : Contact Pressures for Axisymmetrical Condition for Surface Footings	122
Table 3.20 : Contact Pressures for Axisymmetrical Condition for Embedded Footings	123
Table 3.21 : Contact Pressures for Three Dimensional Condition for Surface Footings	124
Table 3.22 : Contact Pressures for Three Dimensional Condition for Embedded Footings	125
 <b>CHAPTER 4</b>	
Table 4.1 : Number of Nodes & Elements in F.E. Meshes	161
Table 4.2 : Summary of Numerical Results for The Distribution of Horizontal Strain ( $\epsilon_{xx}$ )	176
Table 4.3 : Summary of Numerical Results for The Distribution of Vertical Strain ( $\epsilon_{yy}$ )	177
Table 4.4 : Summary of Numerical Results for The Distribution of Horizontal Stress ( $\sigma_{xx}$ ) (in kPa)	178
Table 4.5 : Summary of Numerical Results for The Distribution of Vertical Stress ( $\sigma_{yy}$ ) (in kPa)	179
Table 4.6 : Summary of Numerical Results for The Distribution of Horizontal Displacement ( $\delta_x$ ) (in meters)	180
Table 4.7 : Summary of Numerical Results for The Distribution of Vertical Displacement ( $\delta_y$ ) (in meters)	181
 <b>CHAPTER 5</b>	
Table 5.1 : Data Input Used for Program " <i>BC-Shell</i> "	209
Table 5.2 : Parameters Used in The Parametric Study for Factor ( $\rho$ )	212
Table 5.3 : Data Input Used for The Design	218

## LIST OF SYMBOLS

*The following symbols are used in the thesis:*

- a = shell rise
- $a_c$  = width of foundation column
- b = half of foundation width
- B = foundation width (= 2b)
- c = soil cohesion
- $c_v$  = vertical component of soil cohesion force
- $C_c$  = coefficient of curvature of soil
- $C_u$  = coefficient of uniformity of soil
- $d_c$  = depth of foundation column
- D,  $D_f$  = depth of embedment from ground surface to foundation level
- $D_{fb}$  = distance from ground surface to bottom of rupture surface
- $D_r$  = relative density
- e = base of natural logarithms (~2.7183)
- $E_c$  = horizontal earth pressure force due to soil cohesion
- $E_h$  = total horizontal earth pressure force
- $E_\gamma$  = horizontal earth pressure force due to soil unit weight
- ER = embedment ratio
- $f_{dq}, f_{d\gamma}$  = depth factors
- $f_{sq}, f_{s\gamma}$  = shape factors
- F.E. = finite elements
- $G_s$  = specific gravity of soil
- H = distance from ground surface to point of intersection between circular and plane parts of rupture surface
- I = substitution for integration
- $I_i$  = substitution for integration (i = 1 to 3)
- $k_{o(nc)}$  = coefficient of earth pressure at rest for normally consolidated soil
- $k_{o(oc)}$  = coefficient of earth pressure at rest for overconsolidated soil
- $lw_{bi}$  = lever arm to center of rupture circle for weight of backfill ( $w_{bi}$ )
- $lw_{fi}$  = lever arm to center of rupture circle for weight of foundation ( $w_{fi}$ )
- $lw_i$  = lever arm to center of rupture circle for weight of soil prism ( $w_i$ )

$lE_c$	=	lever arm to center of rupture circle for earth pressure force ( $E_c$ )
$lE_\gamma$	=	lever arm to center of rupture circle for earth pressure force ( $E_\gamma$ )
LVTD	=	linear variable displacement transducer
$M$	=	substitution used for integration
$Mw_b$	=	moment of total weight of soil backfill
$Mw_f$	=	moment of total weight of foundation
$Mw_t$	=	total moment of the total weight of soil prism
$ME_h$	=	moment of total horizontal earth pressure
$MP$	=	moment of forces acting on rupture surface under foundation
$MT$	=	moment of total shear stress acting on rupture surface
$N$	=	substitution used for integration
$N_c, N_q, N_\gamma$	=	bearing capacity coefficients
OCR	=	overconsolidation ratio
$P$	=	resultant force acting on rupture surface
$P_h$	=	horizontal component of forces acting on rupture surface
$P_v$	=	vertical component of forces acting on rupture surface
$q_u$	=	ultimate bearing capacity
$Q_b$	=	bearing capacity load
$Q_l$	=	local shear failure load
$Q_u$	=	ultimate load
$r_{center}$	=	radial distance between transducer unit and center of foundation
$r_{max}$	=	maximum radial distance between transducer unit and foundation
$r_{min}$	=	minimum radial distance between transducer unit and foundation
$R$	=	radius of circular part of rupture surface
$s$	=	infinite inclined distance on rupture surface
SR	=	shell ratio
$T$	=	resultant force
$T_i$	=	transducer at the base of foundation model ( $i = 1$ to $6$ )
$T_h$	=	horizontal component of resultant force
$T_v$	=	vertical component of resultant force
$T_{vc}$	=	vertical component of force acting on circular part of rupture surface
$T_{vp}$	=	vertical component of force acting on plane part of rupture surface
$w_b$	=	total weight of soil backfill

- $w_b$  = total weight of soil backfill  
 $w_{bi}$  = parts of total weight of soil backfill  
 $w_f$  = total weight of foundation  
 $w_{fi}$  = parts of total weight of foundation ( $i = 1$  to  $3$ )  
 $w_i$  = weight for soil prism ( $i = 1$  to  $6$ )  
 $w_s$  = weight of soil prism under shell surface  
 $w_t$  = total weight of soil prism in the rupture surface  
 $w_w$  = weight of soil prism between shell surface and rupture surface  
 $x, y$  = coordinates of transducer units in the steel tank  
 $x_c, z_c$  = coordinates of center of rupture circle  
 $z$  = soil depth
- $\alpha$  = failure angle  
 $\gamma$  = soil unit weight  
 $\gamma_f$  = unit weight of foundation  
 $\partial$  = partial derivative  
 $\delta_u$  = settlement at ultimate load  
 $\delta_x$  = horizontal displacement calculated from F.E. analysis  
 $\delta_y$  = vertical displacement calculated from F.E. analysis  
 $\epsilon_{xx}$  = horizontal strain calculated from F.E. analysis  
 $\epsilon_{yy}$  = vertical strain calculated from F.E. analysis  
 $\eta$  = shell efficiency factor  
 $\theta$  = shell angle  
 $\lambda_1, \lambda_2$  = integration constants  
 $\mu$  = function of ( $\psi, \tau_{cir}$ ) used for integration  
 $\nu$  = Poisson's Ratio  
 $\pi$  = pi ( $\cong 3.1416$ )  
 $\rho$  = ratio between radius and half foundation width ( $R/b$ )  
 $\sigma_{lm}$  = measured lateral pressure  
 $\sigma_0$  = theoretical lateral pressure at rest  
 $\sigma_{vm}$  = measured vertical pressure  
 $\sigma_{xx}$  = vertical pressure calculated from F.E. analysis  
 $\sigma_{yy}$  = lateral pressure calculated from F.E. analysis

- $\sigma_z$  = theoretical vertical pressure
- $\tau$  = shear stress at tangent point for Mohr-Coulomb's envelope
- $\tau_{cir}$  = shear stress for circular part of rupture surface
- $\tau_{pl}$  = shear stress for plane part of rupture surface
- $\tau_{xy}$  = shear stress at point (x, y)
- $\phi$  = angle of shearing resistance of soil
- $\psi_1$  = slope of tangent at point of intersection with ground surface
- $\psi_2$  = slope of tangent at point of intersection with circular curve
- $\omega_n$  = constants (n = 1 to 3)
- $\xi_i$  = constants (i = 1 to 24)
- $\int$  = integral

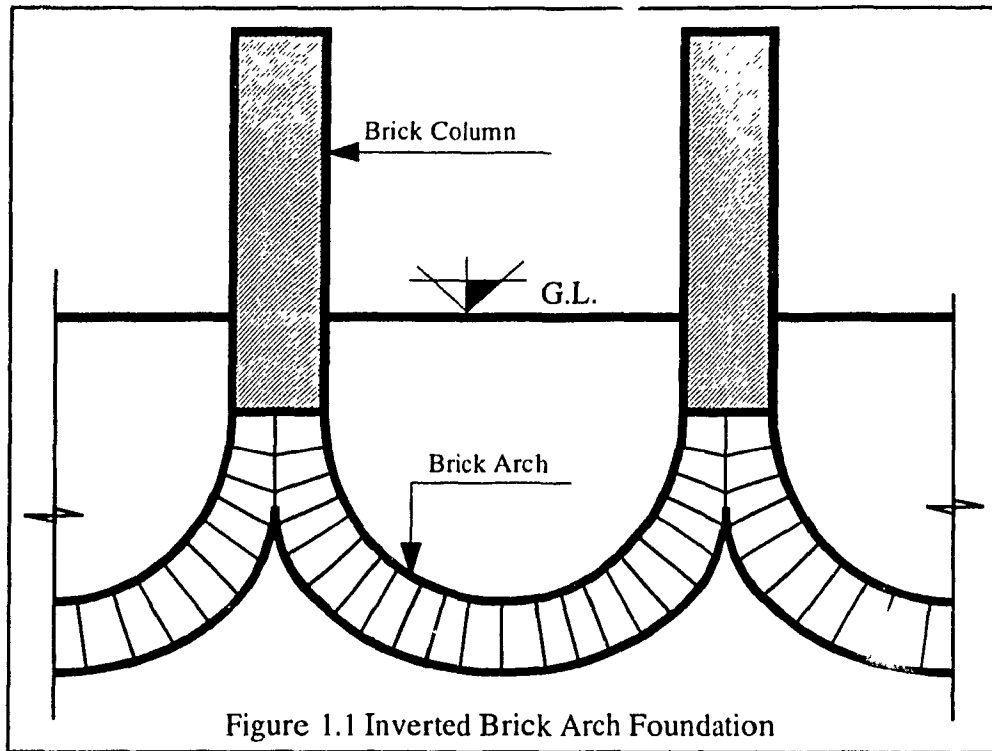
# CHAPTER 1

## INTRODUCTION

### 1.1 Historical Background

Shells are structures which derive their strength from geometry rather than mass. This quality enables them to obtain maximum structural integrity with minimum consumption of construction materials. In structural engineering, shells are widely used to replace flat slabs in covering large areas. In Germany, roofs made of shell structures showed remarkable resistance against bombing during World War II. The damaged roof parts of several industrial plants were cut-away and rebuilt repeatedly after successive bombing incidents, where a total collapse was almost inconceivable. About one decade later, the performance of shells in roof structures initiated the idea of using shells as foundations. The concept is to transmit the loads from the superstructure to the soil through a spatial system which can resist the loads through membrane forces. Although shell foundations are considered newcomers to the field of foundation engineering, some buildings constructed during ancient civilizations showed that inverted brick arch structures were used as foundation elements (see Figure 1.1).

It has been less than five decades since the Mexican architect, Felix Candela, designed the first reinforced concrete shell footing and poured it on Mexican soil. Since then, the use of shells in the field of foundation engineering has drawn considerable interest in different parts of the world. They were proven to provide higher bearing capacity, less settlement, and higher resistance to lateral loads as compared to their conventional flat counterparts. Shell foundations were employed effectively in situations involving heavy loads transmitted to weak soil, or for towers subjected to high lateral forces due to wind or earthquake loads such as telecommunications towers, silos, and chimneys.



On the other hand, shells can hold prospect for adoption in foundation engineering only if they can provide a global economical alternative to conventional flat foundations. Therefore, the initial enthusiasm for shell foundations, generated by the scope for large scale savings in construction materials, should be tempered by the extra cost of construction due to the complexity in their geometry.

However, shell foundations hold considerable economical promise specifically for developing countries, as high material-to-labour cost ratio is one of the typical characteristics of their economy. This is why shell foundations enjoyed the widest use in Latin America, in particular Mexico, as well as in China, India, Eastern Europe (such as Poland and Hungary), Russia, and some African countries. Nevertheless, shell foundations have also been employed effectively in some developed countries such as: Germany, France, Japan, and U.S.A., where they have high labour costs. However, their use was proven to provide more effective and economical foundations when compared to the flat ones.



## 1.2 Classification of Shells

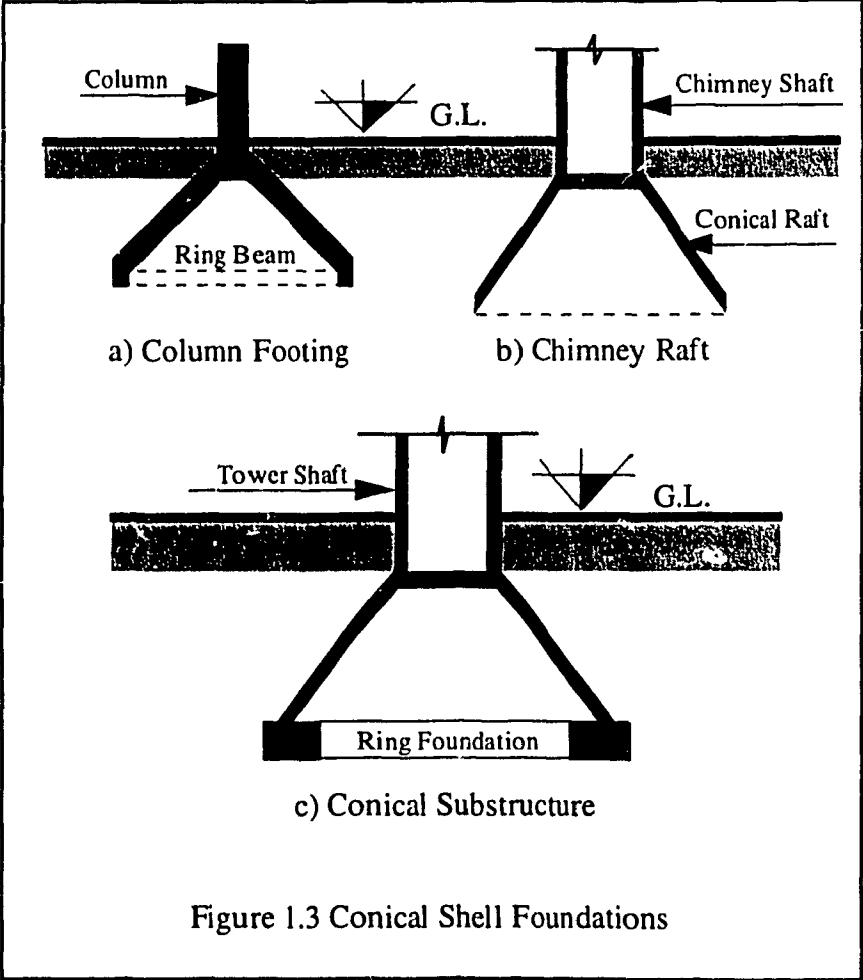
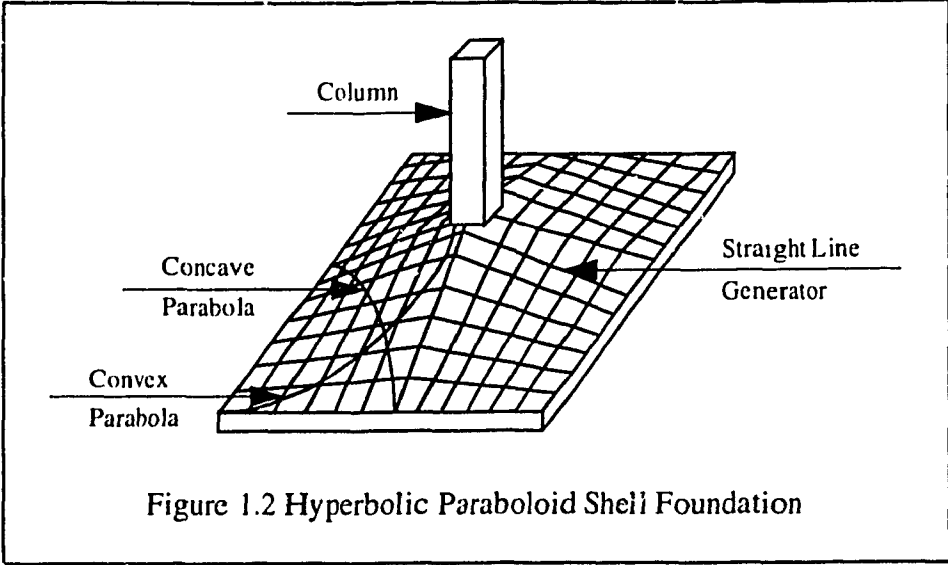
Shells are broadly classified as singly and doubly curved. Singly curved shells are defined as developable shells, i.e., the shell can be developed into plane surface, whereas doubly curved shells are non-developable. Therefore, doubly curved shells are more rigid than singly curved shells. Doubly curved shells are subdivided into synclastic and anticlastic, based on whether the curvatures of the shell are in the same or the opposite directions, respectively. Further subdivisions depend upon whether the shell surface is either revolution, translation, or ruled. All shells which have ruled surfaces, whether singly or doubly curved anticlastic, are described to possess the straight-line property.

## 1.3 Shells in Foundation Engineering

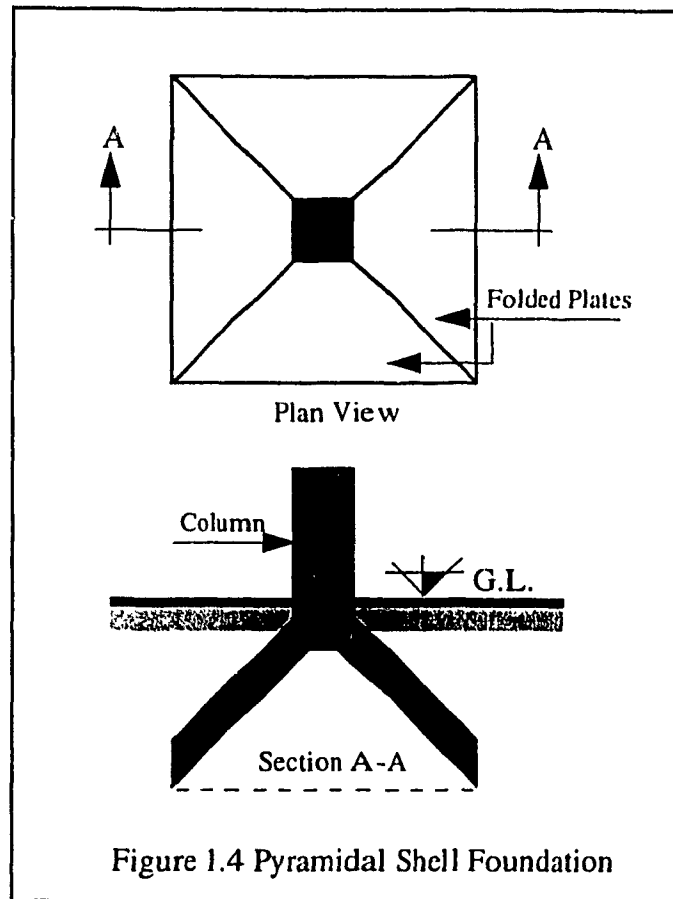
Although a variety of shells have been widely used in roof structures, those that can be judiciously adopted for the use as foundations are far too few. The followings are the most common types of shells which can be employed effectively in the field of foundation engineering:

The hyperbolic paraboloid (*hypar*) is a shell which is known to combine great elegance and versatility. It is a doubly curved anticlastic shell, which has translation as well as ruled surfaces. Hypar shells, as compared to the other shells employed in foundation engineering, have the widest applications in the construction field. Hypar shells as shown in Figure 1.2, can be used in different forms such as: isolated, combined footings, or raft foundation.

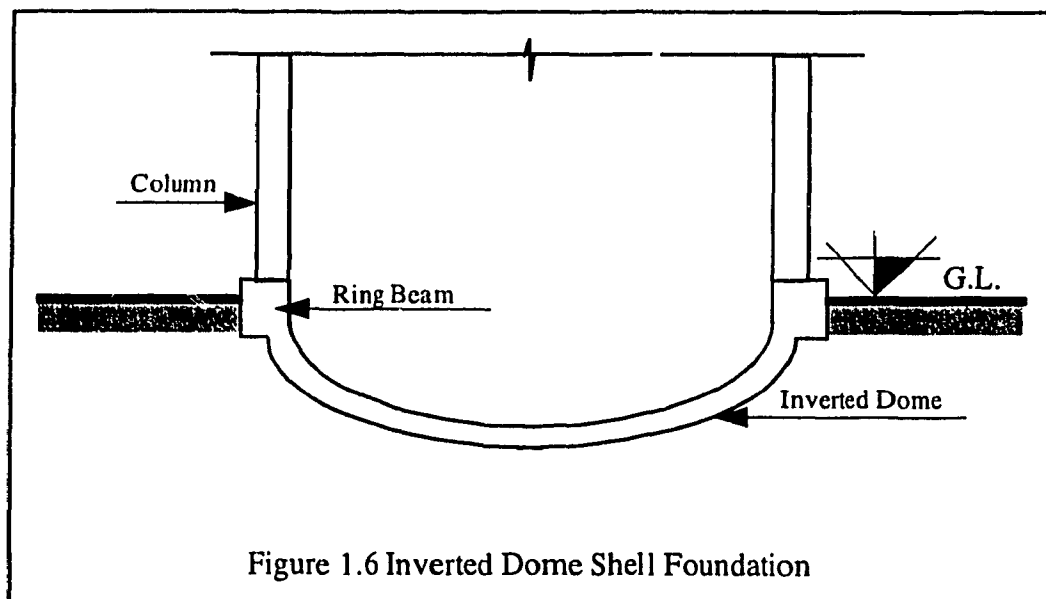
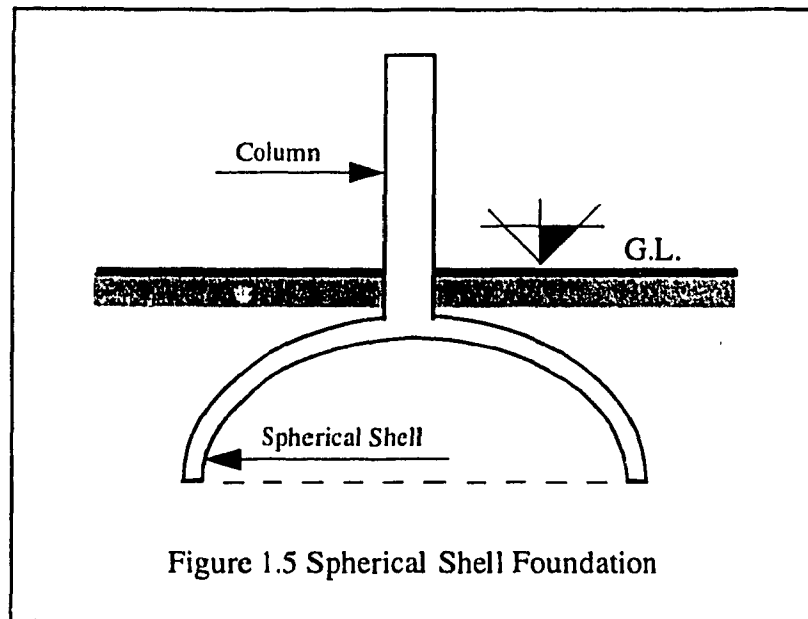
The conical shell is the most simple form of shell which can be employed in foundation engineering due to its singly curved surface. However, due to its circular plan, the use of conical shell foundation is limited to isolated footings. A conical shell can also serve as the substructure for towers to link the tower shaft to its ring foundation. Figures 1.3 (a), (b), and (c) illustrate different applications of conical shell foundations.



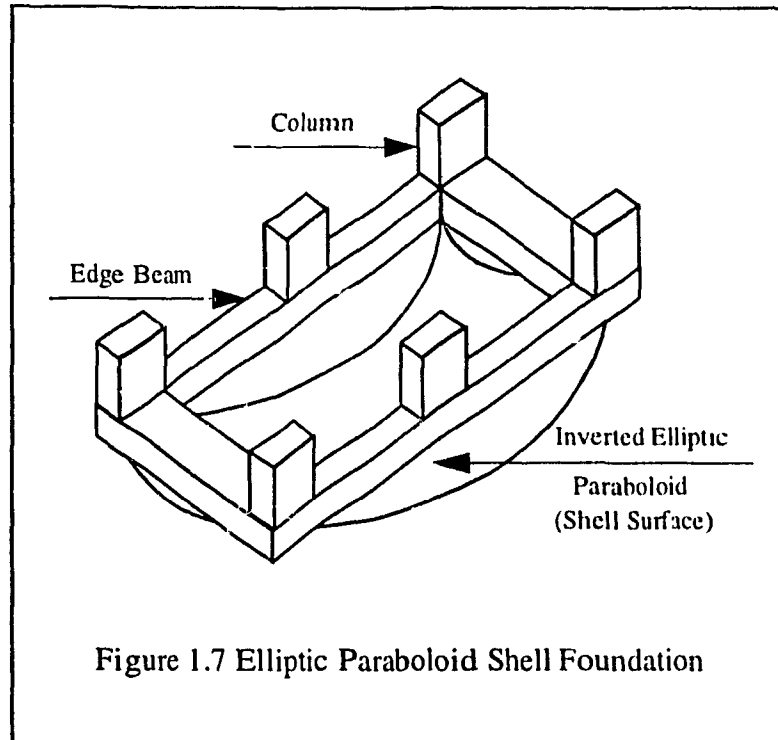
A pyramidal combination of four inclined trapezoidal plate elements, (see Figure 1.4), is a typical folded plates structure which can be used as a foundation element. Since the pyramid can be portrayed as square or rectangular in plan, multiple units of pyramidal shell foundation can be jointly integrated to act as combined footings or raft foundation.



Spherical shell, (see Figure 1.5), is another type of shell foundations which can only be used as an isolated footing. It does not possess the straight-line property as compared to the above mentioned shells which makes its construction process more costly and complex. However, for circular or overhead structures, such as water tanks, supported on a circular row of columns located on the perimeter of a ring beam, the thin inverted spherical dome was proven to provide an overall economical alternative to a thick circular raft foundation, (see Figure 1.6).



The elliptic paraboloid shell is a doubly curved synclastic shell. Its translational surface is obtained by moving one parabola over another, where both parabolas are curved in the same direction. An inverted elliptic paraboloidal shell bounded by parabolas and edge beams can be used as a single unit foundation to support several columns built on the perimeter of the edge beams as shown in Figure 1.7.



A funicular shell is a type of shell foundations for which the design objective is to determine the best geometrical configuration in order to achieve good performance. In the case of a regular shell foundation, the shell geometry is predetermined, and for specific loading and boundary conditions, the state of stress is to be determined. Whereas in the case of funicular shells, the analysis process is reversed. The shell configuration that would give a specific state of stress for the given loading and boundary conditions is to be developed. However, a funicular shell is considered to be funicular only under an assigned set of loading and boundary conditions which were prescribed in the analysis. A funicular shell is not limited in shape; it can serve the same purpose as an inverted dome and elliptic paraboloid shell foundation. It can be used to act as either single or multiple shell footings.

The paraboloid and hyperboloid of revolution shells are two other examples of shell foundations which can be utilized in foundation engineering especially for tower-shaped structures as shown in Figures 1.8 (a), and (b), respectively.

It should be mentioned here that the above description is limited to those shells, which can be employed effectively in foundation engineering.

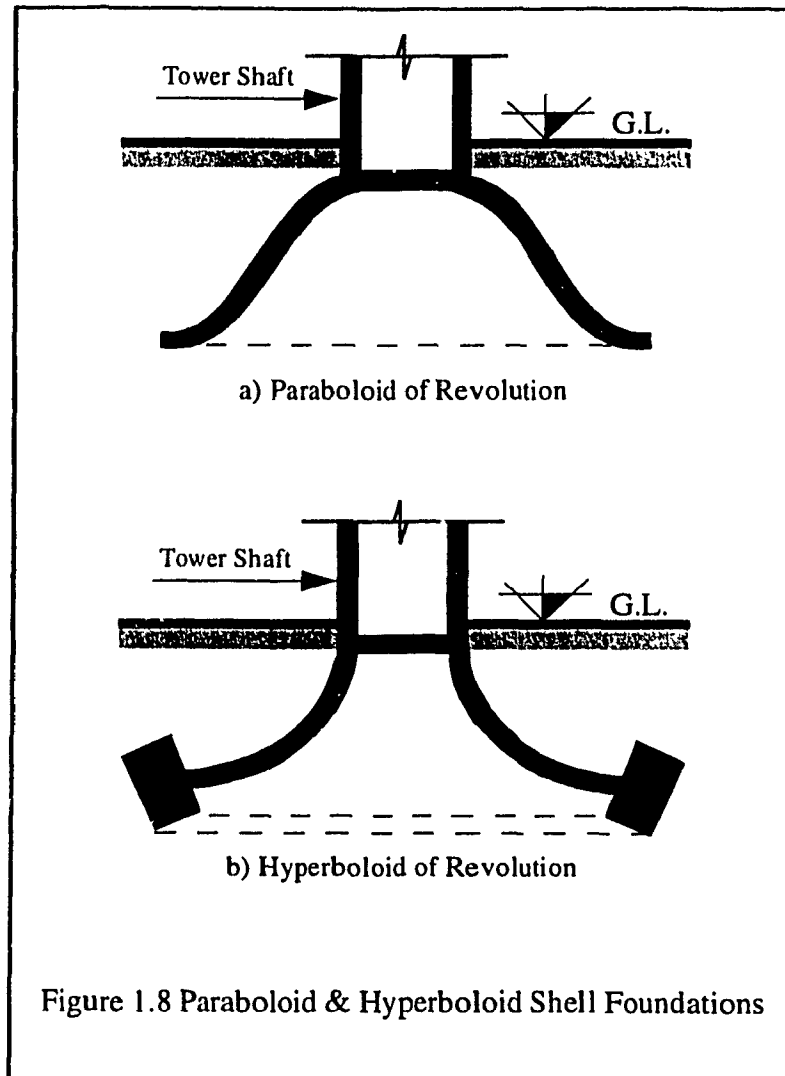


Figure 1.8 Paraboloid & Hyperboloid Shell Foundations

## CHAPTER 2

### LITERATURE REVIEW & SCOPE OF THE THESIS

#### 2.1 General

Shells were introduced to modern foundation engineering during the mid fifties in Mexico. Like many other new developments in civil engineering, their application in the field preceded the research. In the early days, the construction of shell foundations was made of reinforced concrete using the traditional cast-in-place technique. During the last two decades, there was a rapid advances in the efficiency and reliability of precast concrete technology, which already has been effectively employed in the construction of conventional flat foundations. Therefore, utilizing precast units for shell foundations could lead to reduce the gap between the construction cost of shell and flat foundations. Furthermore, the employment of robotics on construction sites is expanding. It can be programmed to perform soil excavation with great accuracy to the required shapes, elevations, and tolerances. This development can turn the excavation process for shell foundations into a routine operation and consequently a more economical one.

#### 2.2 Field Applications

Mexico is the original home of shell foundations, particularly the hypar type, where the largest number of shell foundations were constructed. The first hypar footing in the history of modern foundations was built by Candela in 1953 for the Customs Warehouse in Mexico City. The original design was a conventional strip footing of width 1.20 m. However, due to the poor soil bearing capacity encountered at the site, increasing the width to 3.30 m was necessary. By introducing the shell concept to the flat footing, it was possible to adopt the original width and substantial economy was achieved as the final construction cost was considerably lower than that of the original design (Candela 1955).

The Nonoalco-Tlaltelolco project was an interesting example of employing shells as foundation elements in Mexico. Several buildings in the project were founded on hyperbolic isolated footings. A barrel shell raft was used for the Nonoalco Tower, an office building 128 m high resting on the top of 27.43 m of a soft clay layer. Part of the tower's weight was supported by cast-in-place friction piles, while the rest of the weight was compensated for by the excavation. The net load was transmitted to the soil by means of the transverse barrel shells as illustrated in Figure 2.1. The circular barrel shell with a thickness equal to 1/50 of the span has provided overall savings of 50% as compared to conventional flat foundations (Enriquez and Fierro 1963).

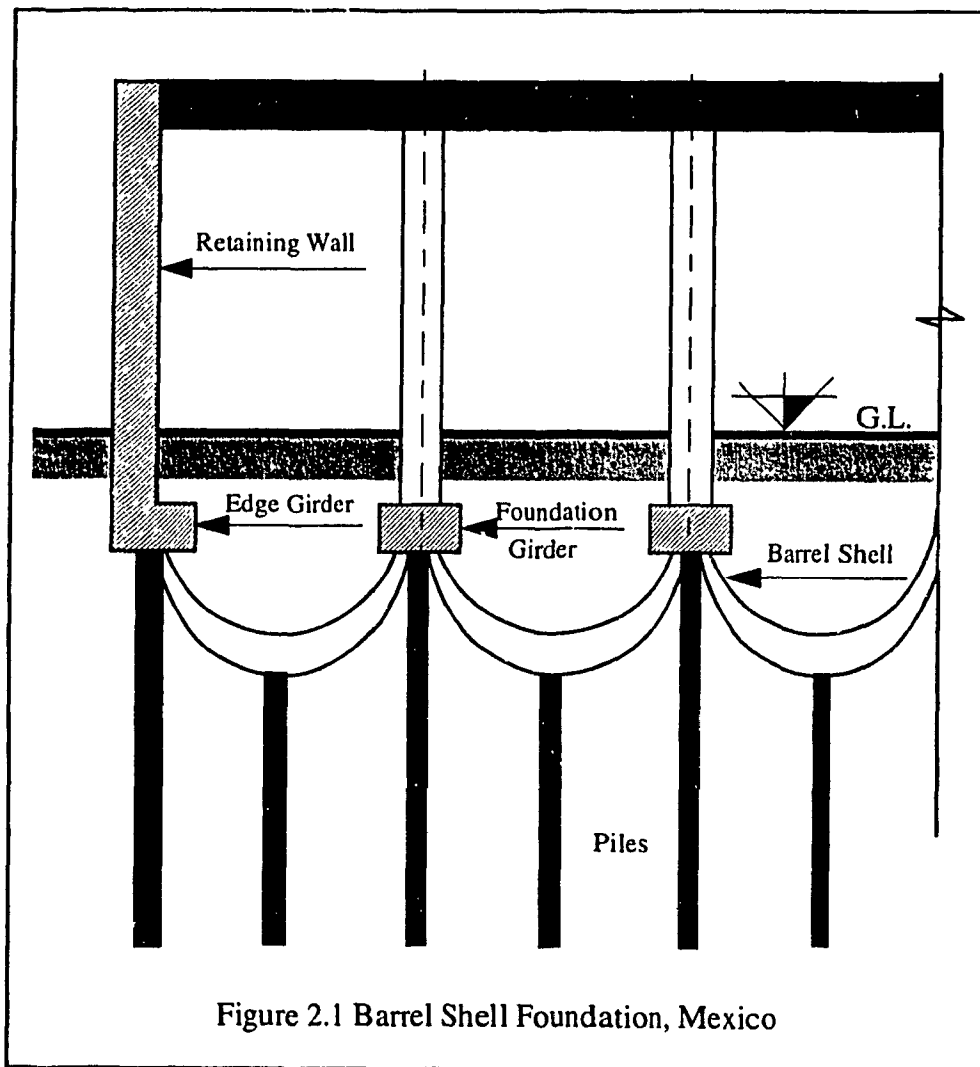
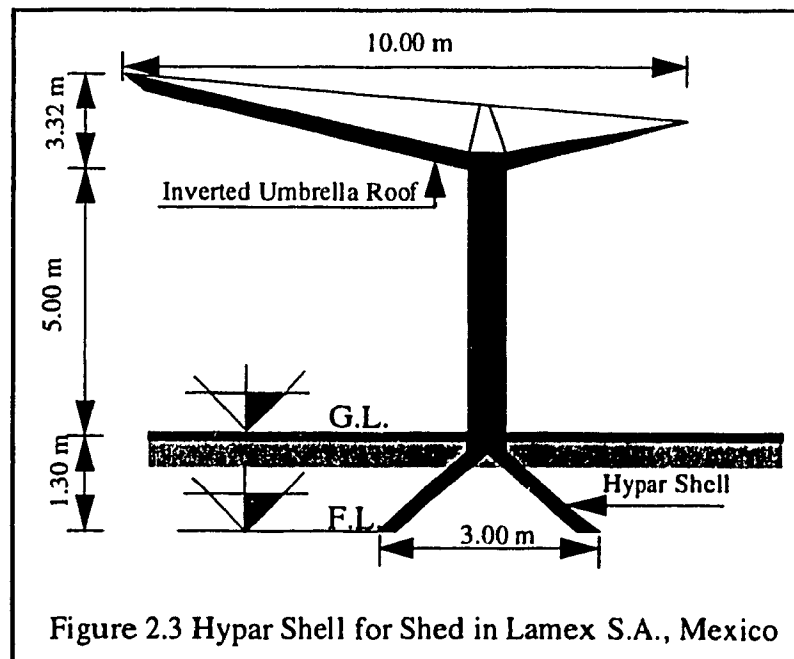
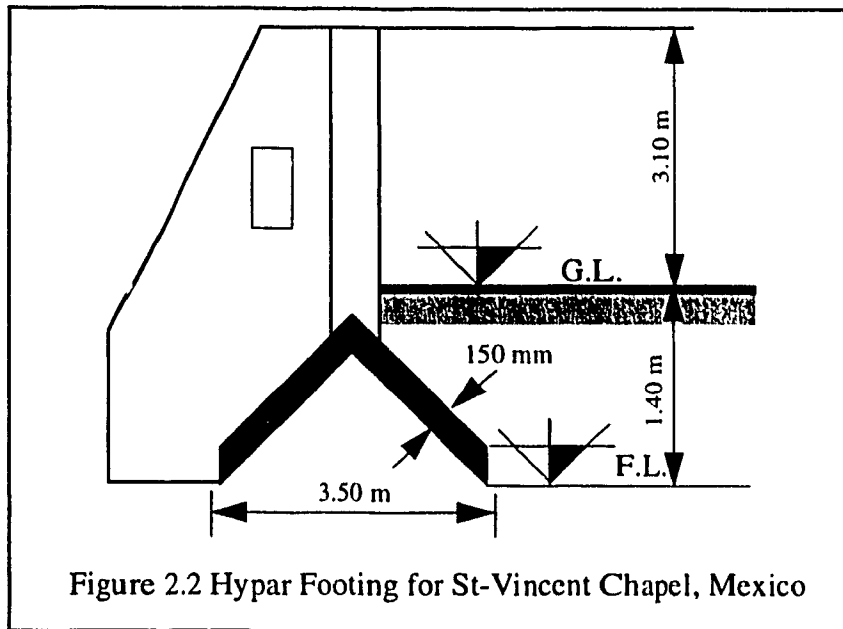


Figure 2.1 Barrel Shell Foundation, Mexico



Several other hyper shell foundations were constructed in Mexico, and two examples of these foundations are shown in Figures 2.2 and 2.3. In spite of the soft clay dominating the Mexican soil, shell footings had to be an economical and potential alternative to conventional flat foundations (Kurian 1982).



In India, there are also several applications of shell foundations. The first example is the Shalimar tar products factory project near Calcutta, where hypar shells were used as isolated footings. The thickness of the shell footings was 229 mm which were founded on a weak soil deposit with a low bearing capacity of 55 kPa (Kurian 1982).

An inverted continuous cylindrical shell foundation was constructed for a yeast factory at Konnagar near Calcutta, India. The reinforced concrete shells were poured on stabilized soil, which was prepared to the exact shape required for the foundation. Then, the brick stiffeners were provided as shown in Figure 2.4. This shell foundation was proven to provide savings of 72% in comparison with the conventional raft foundation and 55% in comparison with pile foundation (Kurian 1982).

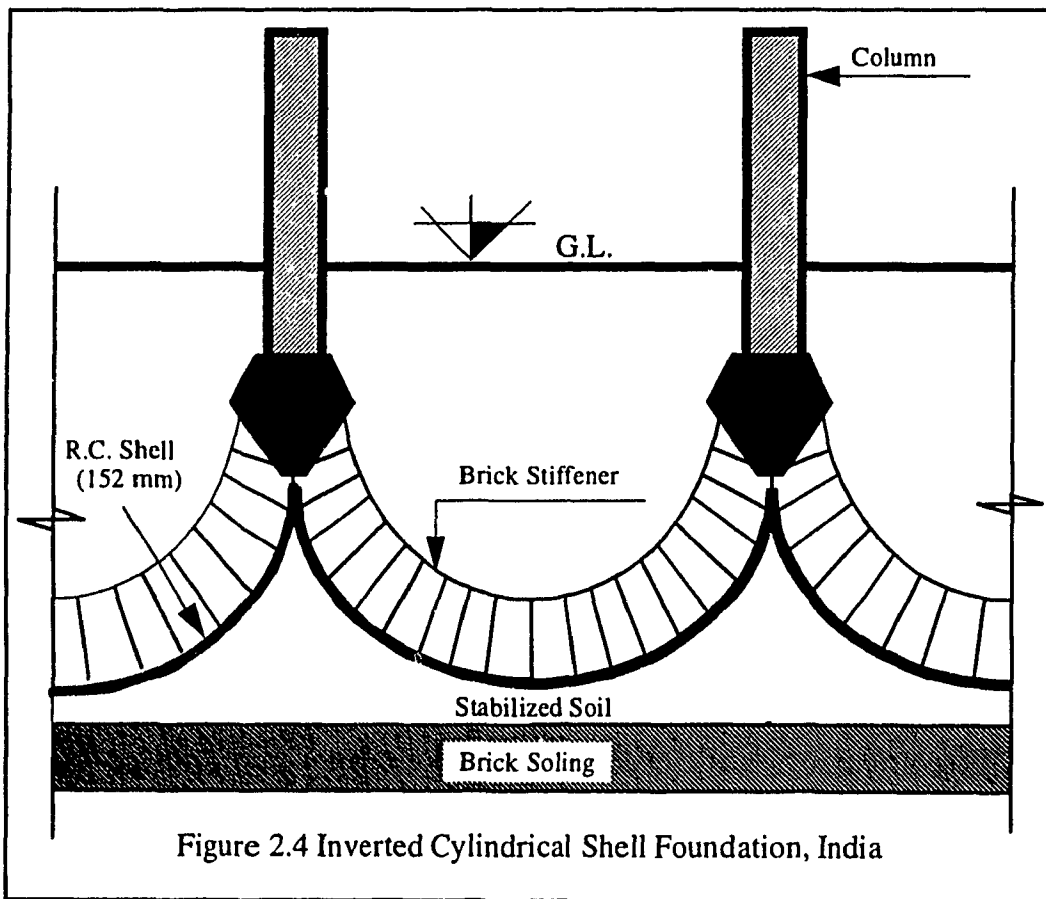
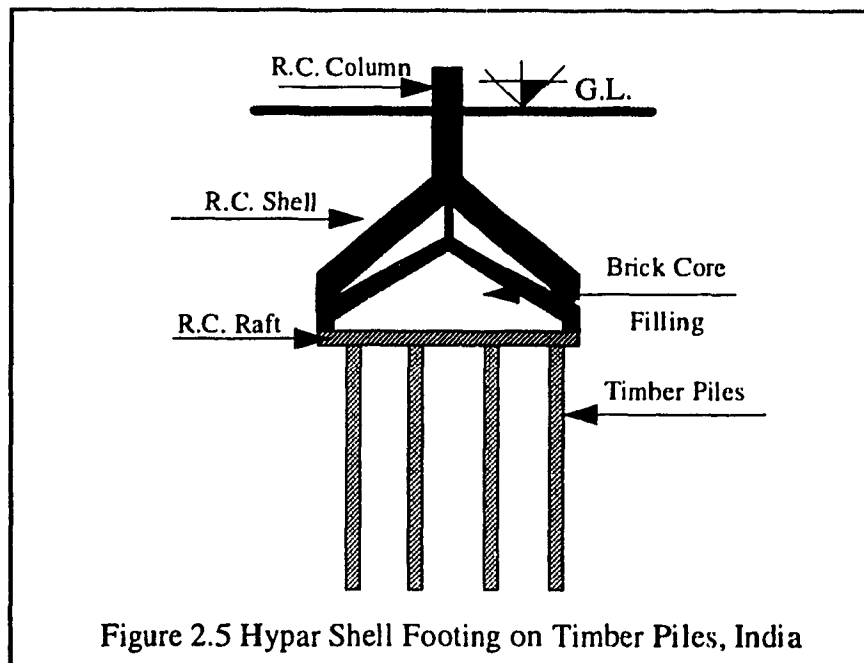


Figure 2.4 Inverted Cylindrical Shell Foundation, India

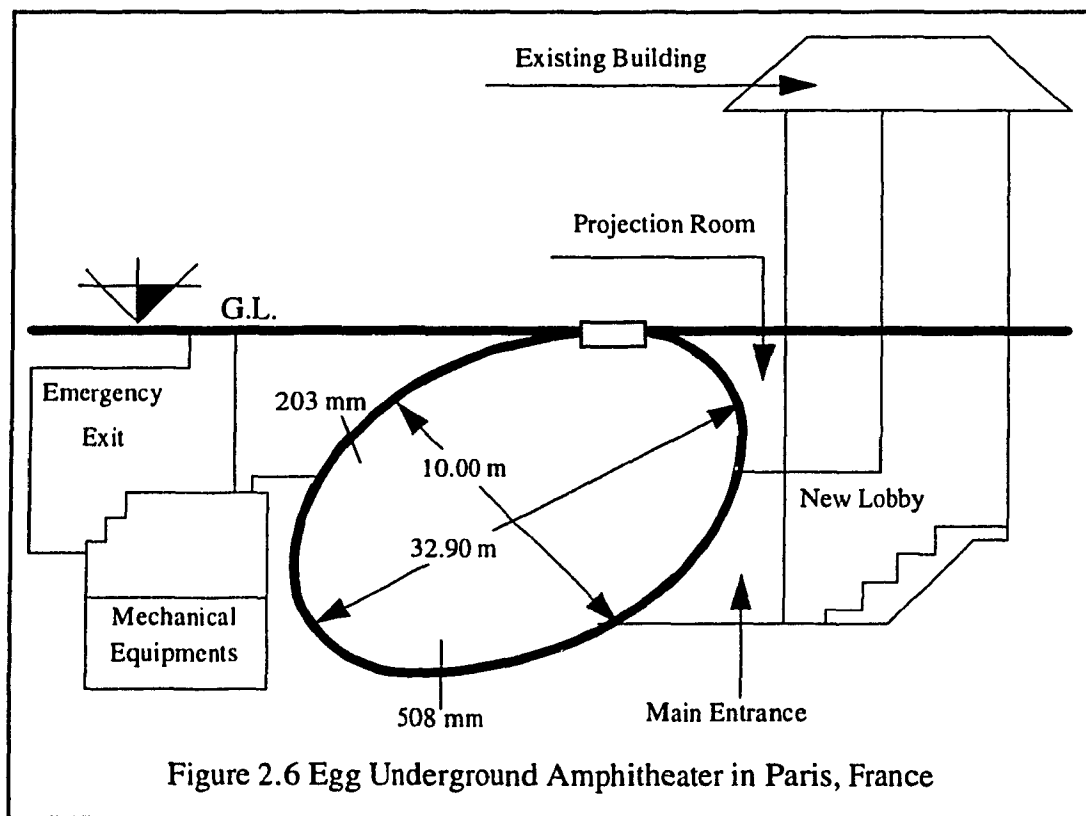
Another application from India was the foundation of the water tower at Adityapour in Blhar. The tower was supported on a single column founded on a 305 mm thick hypar shell foundation resting on a sandy clay soil. The hypar shell foundation was provided with heavily reinforced ribs to account for the high bending moment transmitted from the column to the foundation (Kurian 1982).

Hypar shell footings were used for an apartment building in a housing project in Madras, India. The soil was a medium beach sand with an allowable bearing capacity of 56 kPa. The hypar footings were proven to provide an economical alternative to the conventional trapezoidal and combined footings which were used for other buildings in the same project (Kaimal 1967).

Another interesting example was the hypar shell footings used for the Caustic Soda factory at Khardah, India. The soil was soft clay. Timber piles were first driven in groups below each column to control the settlement (see Figure 2.5). Then, a concrete mat was placed at the top level of these piles, over which a cement brickwork was laid down to form the core below the 381 mm thick reinforced concrete shell (Anon1965).



In France, a 1000-seat underground amphitheater for Ecole Nationale d'Ingenieur des Arts et Metiers, an engineering college in Paris, was built beneath the campus courtyard. Because of the existence of abandoned mine tunnels under the site, a 25 m deep pier foundation would have been necessary for a flat base raft. The designers shaped the underground chamber like an egg, as shown in Figure 2.6, to distribute the weight over a larger area. The curved base slab transmitted less than 2.4 kPa to the soil underneath (*Engineering News Record* 1964).



In U.S.A., Sumner High School in Washington had a 2000-seat stadium assembled from precast prestressed concrete units. The site was a fill underlain by a deep deposit of soft mud. Thin reinforced concrete hyper shell footings were adopted for this project to satisfy the engineering requirements in addition to the savings in construction materials (Anderson 1960).

Literature from Russia abounds with examples of various types of shell foundations. The most famous one is the conical shell used as a substructure for the Moscow telecommunications tower at Ostankino. The tower has a height of 533 m and weight of 550 MN. The conical shell was used in order to connect the tower's shaft to the prestressed ring foundation (Kurian 1982).

A worldwide celebrated hollow conical foundation is the one designed by Prof. F. Leonhardt for the Stuttgart TV tower in Germany which was built in 1956 (see Figure 2.7). The conical reinforced concrete shaft is 161 m high. The truncated hollow conical foundation of the tower was constructed over a prestressed circular slab. It was reported that this foundation was able to take up to 2.5 times the design wind loads, keeping the contact surface of the foundation base under compression stresses. The factor of safety against overturning was varied from 8 to 14 under different loading conditions. The vertical pressure on the soil at a depth of 8.0 m from the tower does not exceed the pressure from the soil own-weight prior to excavation. The average contact pressure on soil was 353 kPa and the maximum one was 392.3 kPa (Jumikis 1987).

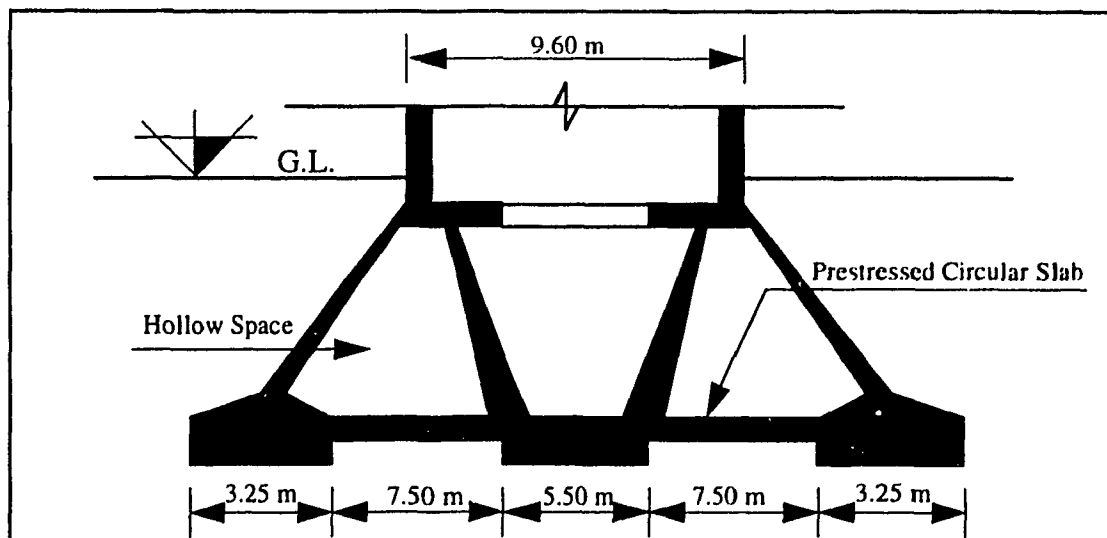
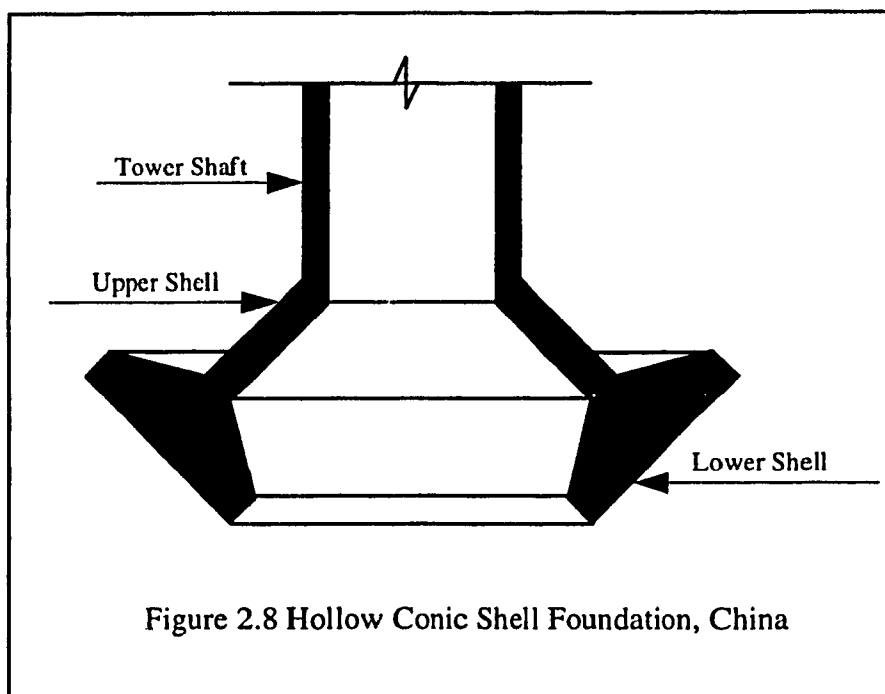


Figure 2.7 Hollow Conical Shell Substructure for Stuttgart TV Tower, Germany

In Mombasa, Kenya, several isolated and combined hyper shell footings were used for a two-stories building. The soil at the site was soft clay which is highly susceptible to moisture variation. The hyper footings were utilized as they were proven to perform better than the conventional flat counterparts (Kurian 1982).

From Poland, it was reported that a reinforced concrete raft foundation needed to support a 200 m high chimney would be 35.0 m in diameter and 4.0 m in thickness. A conical shell foundation was used instead of the proposed raft foundation where a savings of about 50% in the construction materials was achieved (Ciesielski 1966).

In China, the hollow conic shell foundation "hcs" was primary introduced to the engineering practice by He Chongzhang in 1969. This shell foundation consists of a normal conical shell and an inverted one as shown in Figure 2.8. It is especially applicable to chimneys and telecommunications towers. The use of "hcs" in China has resulted a savings of 50% in concrete and steel reinforcement as compared to the conventional flat foundations (He Chongzhang 1984; 1985).



In Japan, the term *Shell Foundation* was named by Prof. J. K. Minami to represent a combination of thin hollow cylindrical shell installed underneath an ordinary shallow spread footing. This concept was developed in order to minimize the settlement and increase the bearing capacity of the footing (Minami 1949). However, in recent years, the same design concept is being utilized more frequently under the name of "*Skirted Foundation or Tubular Foundation*". This system was effectively used in countries which often suffered from devastating earthquakes such as Japan and India. The effectiveness of this type of foundations in resisting the liquefaction of loose sandy ground due to earthquakes is particularly appreciated in Japan (Kotoda and Numakami 1987). Moreover, top-shaped, T-shaped, and conical concrete blocks were used recently in Japan as foundation for small structures. They were proven to increase the bearing capacity and reduce the settlement of the structures (Yasuda et al 1994).

### **2.3 Research on Shell Foundations**

The research on shell foundations can be divided into two main categories: structural performance and geotechnical behavior.

The first category is concentrated to study the structural performance of shell foundations with respect to membrane stresses, bending moment, shear, deflection, and ultimate strength of the shell itself as a reinforced concrete structural element. The results of the research in this category can be further translated into a savings in concrete and steel reinforcement as compared to conventional flat foundations.

The second category involves the geotechnical behavior of shell foundations to determine the soil response with respect to settlement, ultimate bearing capacity, contact pressure distribution, lateral and vertical stresses, and displacements induced within the soil mass. It should be mentioned here that while the first category has received lots of attention from researchers in the literature, the second category has received little attention.

### 2.3.1 Structural Performance

Although the structural performance of shell foundations is out of the scope of this study, it is essential to highlight some research results and their impact on the geotechnical behavior of shell foundations. Several research reports are available in the literature on this subject, where different types of shell foundations such as: hyperbolic, conical, spherical, funicular, and cylindrical shells were investigated.

Experimental and theoretical investigations were reported to evaluate the stresses and straining actions on the shell structure such as membrane stresses, bending moment, shear, and deflection. In the theoretical studies, mathematical formulations, finite difference technique, and finite elements analyses were utilized. In some reports, linear Winkler and Pasternak soil models were used to simulate the soil behavior under different types of shell foundations. In a few reports, the distribution of the soil contact pressure on shell foundations was also examined. The results indicated a non-uniform contact pressure distribution along the soil-shell interface. However, the structural design of shell foundations is currently based on membrane theory, in which the soil contact pressure distribution is assumed to be uniform (Pandian and Ranganatham 1970; Kurian and Varghese 1971; Bhattachary and Ramaswamy 1977; Jain et al. 1977; Das and Kedia 1977; Fareed and Dawoud 1979; Dierks and Kurian 1981; He Chongzhang 1984; Huang-Yih 1984; Nath and Jain 1985; Paliwal et al. 1986; Paliwal and Sinha 1986; Paliwal and Rai 1987; Melerski 1987; and Dierks and Kurian 1988).

The ultimate strength of shell foundations was also investigated both experimentally and theoretically; and comparisons were performed with conventional flat foundations. All studies reached the same conclusion confirming the savings achieved in the construction materials and the admirable structural performance of shell foundations. The findings of these investigations have direct impact on the construction cost of shell foundations as compared to the conventional flat counterparts (Kurian 1971; Kurian and Varghese



1972; 1973; Kurian 1973; Kurian and Mohan 1980; Dierks and Kurian 1981; Kurian 1983; and Dierks and Kurian 1988).

Sharma (1973) conducted a field investigation on a spherical shell (3.0 m in diameter) used for the foundation of a water tower. The results revealed that a reduction of 32% in the maximum deflection was achieved due to the replacement of a flat raft foundation with a shell one. Also, a savings of 30% in concrete and steel reinforcement was reported.

Sharma (1984) reported that conical and hyper shell foundations were investigated theoretically versus circular and square counterparts, respectively. The results indicated a savings of 38% and 45% in construction materials when conical and hyper shell foundations were used to replace circular and square flat ones, respectively.

Kurian and Shah (1984) performed cost analyses on conical and inverted dome shell foundations. The results of this study demonstrated the advantages of shell foundations especially in situations involving higher loads to be transmitted to a weak soil.

Wang Chunxiao (1985) reported that "M" shaped shell foundation was used instead of pile foundation for a water tank constructed in China. This resulted in a savings of 24.30% in concrete and 22.80% in steel reinforcement.

### **2.3.2 Geotechnical Behavior**

The research conducted on the geotechnical behavior of shell foundations has been considerably lagging behind the one conducted on their structural performance. Few research reports were directed to investigate the influence of shell configuration on the geotechnical behavior. However, there are no theories or empirical design formulas available in the literature to predict ultimate bearing capacity of shell foundations with the exception of the theoretical model reported by Abdel-Rahman (1987); and Hanna and Abdel-Rahman (1990). They are currently assumed to behave identically to the conventional flat ones.

Nicholls and Izadi (1968) performed an experimental investigation on conical and hypar shell footings to determine the contact pressure distribution as a function of the ultimate load. The conical and hypar shell models were compared with circular and square flat models, respectively. The diameter of the conical and circular models was 304.8 mm and the width of the hypar and square models was 355.6 mm. The results indicated that the contact pressure increased near the perimeter of the shell models about 1.5 times the contact pressure measured at the center. This increase was contributed due to the arching action. The ultimate bearing capacity as well as the settlement of the shell models were significantly improved as compared to the conventional flat counterparts. In addition, Kurian and Varghese (1969), in a discussion on this study, confirmed that the use of shell elements in rafts in place of the conventional flat elements was proven to be more economical.

Iyer and Rao (1970) reported a detailed experimental study conducted on the feasibility of using a funicular shell footing resting on sand as a replacement to a flat raft foundation. Precast funicular shell models were developed in two different sizes: 150 mm and 400 mm. The results showed that the bearing capacity of the shell footing was considerably greater than that of the flat footing of the same plan dimensions. Furthermore, under the same applied load, the shell footing provided lower settlement than the flat one. This significant differences were attributed to the shape effect and the stiffness of shell elements.

Kurian and Jeyachandran (1972) conducted an experimental investigation directed to study the influence of shell geometry on bearing capacity, settlement, and contact pressure distribution. Four types of shell foundations models were examined in normal and inverted positions. These shell models were: circular cylindrical, folded plates, cone, and hypar. The models were made of perfectly rigid cast iron plates providing a constant width or diameter of 360 mm. The contact surfaces of the models were machine-ground and hand-polished to a high degree of smoothness. The results of this study indicated a marginal increase in the bearing capacity. The settlement of shells were relatively higher than the flat

models, however the variation of the initial tangent moduli was not consistent with this behavior. The distribution of contact pressures generally showed a tendency for edge concentration for the upright shells and the square flat model. However, an opposite behavior was reported for the case of inverted shells and the circular flat model. Contrary to the conclusions of other reports, the authors stated that the advantages of shells in foundation engineering are more structural than can be derived in terms of soil response. These controversial results may be attributed to the smooth interface of the shell models.

Jain et al. (1977) studied the general behavior of conical shell footings under vertical load using linear solid axisymmetrical finite elements analysis. The effects of several parameters such as the modulus of elasticity of the soil, half vertex angle of the conical shell, and the provision of a toe at the footing edge were examined. A mathematical idealization for the contact pressure distribution was introduced. The results indicated that the presence of an edge toe reduced the soil pressures and increased the bearing capacity. For the same value of elastic modulus of soil, the pressures within the soil mass were higher for footings with wider spread.

Kurian and Mohan (1981) conducted an experimental study in order to measure the contact pressure distribution under different hyperbolic paraboloidal models at the elastic and ultimate loading stages. The plan dimensions of the models ranged from 300 x 300 mm to 600 x 600 mm. The results indicated substantial deviation from the linear distribution assumed in the current design method. The contact pressure distribution showed a definite tendency for edge concentration in the elastic stage and exhibited a definite tendency for progressive shift of concentration towards the central region at the ultimate stage.

Agarwal and Gupta (1983) conducted an experimental investigation on the soil-structure interaction of conical and hyper shell models on different sand states. The behavior of the shell models was compared to that of circular and square flat models having the same plan dimensions. The width or diameter of the models ranged from 150 to 250 mm.

The ultimate bearing capacity of the shell models was reported to vary from 11% to 22% higher than that of the flat ones. The increase in the ultimate bearing capacity was attributed to the increase in the angle of friction between the core soil under the shell models and the soil below.

Hanna and Hadid (1987) conducted a theoretical study to determine the optimum geometrical configuration which gives a uniform contact pressure distribution below foundation base for plane strain condition. The harmonic sine curve function was found to satisfy this requirement under a prescribed loading and boundary conditions. However, it should be mentioned that, if these conditions were changed the contact pressure distribution would become a non-uniform one.

Arai et al. (1987) investigated the settlement of top-base foundations by conducting plate loading and long term consolidation tests on soft clay soil in Japan. The in-situ plate loading tests indicated that the one layer top-base foundation has 1/3 to 1/2 of the immediate settlement of the primary non-treated ground and 1/3 of the consolidation settlement. Another study conducted by Arai et al. (1988) confirmed that this type of foundation tends to disperse stress concentration and the bearing capacity of the foundation increased up to 50% to 100% in comparison to the primary non-treated ground. Moreover, it was pointed out that the combination of top-shaped concrete blocks and filling gravel has the trend to prevent the lateral deformation and to control the surface settlement of the foundations.

Abdel-Rahman (1987); Hanna (1988); Hanna and Abdel-Rahman (1990) performed experimental investigation to study the ultimate bearing capacity of triangular shell strip models on sand. The results indicated that the triangular shell models provide higher bearing capacity and produce less settlement under the same loading condition as compared to the strip flat model. Empirical expression was introduced to account for the change in the triangular shell angle ( $\theta$ ). Design charts for the modified bearing capacity coefficients were presented as a function of the shell angle ( $\theta$ ) and the angle of shearing resistance ( $\phi$ ).

Yasuda et al. (1994) performed experimental and numerical studies to examine the effectiveness of three types of foundations in preventing the settlement of small structures built on loose sandy ground subjected to seismic conditions. The foundations were top-shaped, T-shaped blocks, and conical concrete blocks. The results indicated that the final settlements of the structure were considerably lower when these foundations were used. According to the distribution of the mean effective principle stress obtained from a finite elements elastic analysis, the confined stress increased within a larger ground area under the top-shaped foundation than that without any countermeasure. The stresses were reported to be relatively widely dispersed when using the top-shaped foundation and the liquefaction resistance was increased.

Abdel-Rahman and Hanna (1994) conducted parametric study using finite elements analysis to examine the vertical displacement induced in soil by conical shell foundations. The effect of shell configuration, depth of embedment, Poisson's ratio, and the modulus of elasticity on the vertical displacement were investigated. The numerical results showed that shell configuration caused a reduction of 10% in the vertical displacement. This reduction trend was similar for both surface and embedded foundations. When Poisson's ratio increased, the vertical displacement decreased for about 10% for surface foundations. However, this effect was not significant for the embedded foundations. Also, it was reported that the modulus of elasticity has a significant effect on the vertical displacement and an empirical relationship for this effect was developed.

Kurian (1994) examined the behavior of different types of shell foundations under subsidence of core soil using finite elements analysis and compared them with identical flat plates under partial contacts. It was reported that in respect of all shell models, the difference between full and 75% contact was very marginal. The shell system was proven to be more stable than the flat plates. The author emphasized the use of shell foundations wherever conditions are favorable for their economic adoption.

Based on the above, it can be concluded that shells were employed effectively as foundation elements in different parts of the world. This is mainly due to their cost effectiveness and admirable structural performance. However, it is clear that the research conducted on the geotechnical behavior of shell foundations is still lagging behind the research conducted on the structural performance, and the subject of soil response for shell foundations is still not well defined and further research is warranted. While Kurian and Jeyachandran (1972) concluded that the advantages of shell foundations with respect to soil response are marginal, the other reports indicated considerable increase in the bearing capacity and reduction in settlement of shell foundations as compared to their flat counterparts.

## **2.4 Scope of The Thesis**

The objective of this research program is to conduct a comprehensive investigation on the geotechnical behavior of shell foundations and to examine their performance against the conventional flat ones. To achieve this objective, the ultimate bearing capacity, settlement, and contact pressure distribution of different shell and flat foundations are investigated experimentally, numerically, and theoretically. In addition, it is intended to develop a theory to predict the ultimate bearing capacity of shell foundations. This study will lead to position shell foundations in the field of geotechnical engineering as a serious alternative to conventional shallow flat and deep foundations.

### **2.4.1 Experimental Phase**

An experimental testing program was developed to investigate the geotechnical behavior of shell foundations. Three types of shell foundations namely, triangular strip, conical, and pyramidal shell models were examined against strip, circular, and square flat models, respectively. These models represent the plane strain, axisymmetrical, and three dimensional field conditions. In order to investigate the effect of shell configuration on the geotechnical behavior, two shell configurations were examined for each shell model. Furthermore, in order to study the effect of embedment, the models were tested on the surface

and at embedment ratio of  $D/B = 0.75$ . The soil used in the present investigation was a dry sand tested in loose, medium, and dense states.

Load-settlement data and contact pressures on the soil-foundation interface were recorded up-to failure for all loading tests. In addition, the lateral and vertical stresses within the soil mass were recorded for the loading tests conducted on the axisymmetrical and three dimensional models. All experimental results were measured using calibrated electrical measuring devices such as load cell, LVTD's, and pressure transducers. All devices were connected to Data Acquisition System for data registration.

Special tests were conducted in a Plexiglas tank using colored layered sand to investigate the failure mechanism in the soil underneath the foundation models. Photographs were taken during different loading stages until failure occurred. This technique allowed the capture of the movement of the colored sand layers and accordingly the prediction of the shape of the rupture surface.

#### **2.4.2 Numerical Phase**

Finite elements analyses using the program "CRISP", developed by the geotechnical group at Cambridge University, were conducted for the plane strain models. Elastic perfectly plastic soil model using Mohr-Coulomb's yield criteria was employed to represent the behavior of the tested sand at its three states. The deformed meshes, displacement vectors, stresses, strains, and displacements for the strip flat model as well as the two shell strip models were investigated. The deformed meshes and displacement vectors were used to predict and check the shape of the rupture surface obtained from the experimental phase.

#### **2.4.3 Theoretical Phase**

A theoretical model using the limit equilibrium method of analysis to represent the failure mechanism of strip shell foundations was proposed. The rupture surface suggested from the results of the experimental and numerical investigations in the present study was

employed in the theoretical analysis. The proposed rupture surface composed of circular and plane surfaces, which provides a kinematically and statically admissible solution. Kötter's differential equation was considered to simulate the shear stress distribution along the circular and plane parts of the rupture surface for the passive stress state.

Shell Ratio (SR) was proposed to take into account the effect of shell configuration on the failure mechanism, the shape of rupture surface, and the ultimate bearing capacity ( $q_u$ ). A computer program "*BC-Shell*" was developed to perform the theoretical analysis to identify the rupture surface, which satisfies the equilibrium equations. A parametric study was conducted to examine the influence of the parameters involved in the analysis on the ultimate bearing capacity of shell foundations. The bearing capacity coefficients ( $N_c$ ,  $N_q$ ,  $N_\gamma$ ) for shell foundations were determined using the program "*BC-Shell*". Design tables and design charts for the bearing capacity coefficients were also presented.

To validate the proposed theoretical model, a comparison between the experimental results for the plane strain cases and the respective theoretical results was conducted. The theoretical values for the bearing capacity coefficients, obtained from the program "*BC-Shell*" for the plane strain models were employed to establish relationships for depth factors  $f_{dq}$  and  $f_{d\gamma}$  as a function of the angle of shearing resistance ( $\phi$ ), shell angle ( $\theta$ ), and embedment ratio (ER). By employing these depth factors and the experimental results measured for the plane strain models, the bearing capacity coefficients  $N_q$  and  $N_\gamma$  were determined. The experimental results for the axisymmetrical and three dimensional models were employed to originate empirical shape factors:  $f_{sq}$ , and  $f_{s\gamma}$ .



## CHAPTER 3

### EXPERIMENTAL INVESTIGATION

#### 3.1 General

The objective of the present experimental investigation is to examine the behavior of different types of shell foundations as compared to the conventional flat ones; and to produce valuable experimental data which will be employed in the next stages of the present investigation. An experimental testing program was developed to investigate the influence of shell configuration on the ultimate bearing capacity, settlement, contact pressure, lateral and vertical stresses. An experimental set-up was organized to perform the testing program. Load-settlement data was recorded up-to failure by means of load cell and LVTD in order to establish the ultimate load. Contact pressures were measured at soil-foundation interface by pressure transducers to determine the nature of the distribution at any loading stages. Furthermore, lateral and vertical stresses were measured within the soil mass to investigate the effect of the foundation models on their distribution.

#### 3.2 Foundation Models

Three types of shell foundations were used in the present investigation namely, triangular strip, conical, and pyramidal shell models, which simulate the plane strain, axisymmetrical, and three dimensional field conditions, respectively. Two different shell rises were chosen for each shell type to examine the effect of rise-to-half width ratio ( $a/b$ ) on the behavior. The ratios of  $1/2$  and  $1$  were used in this investigation as they provide practical range for construction purpose. Strip, circular, and square flat models with the same plan dimensions, were compared with triangular strip, conical, and pyramidal shell models, respectively. Sketches of these foundation models are illustrated in Figures 3.1 through 3.9.

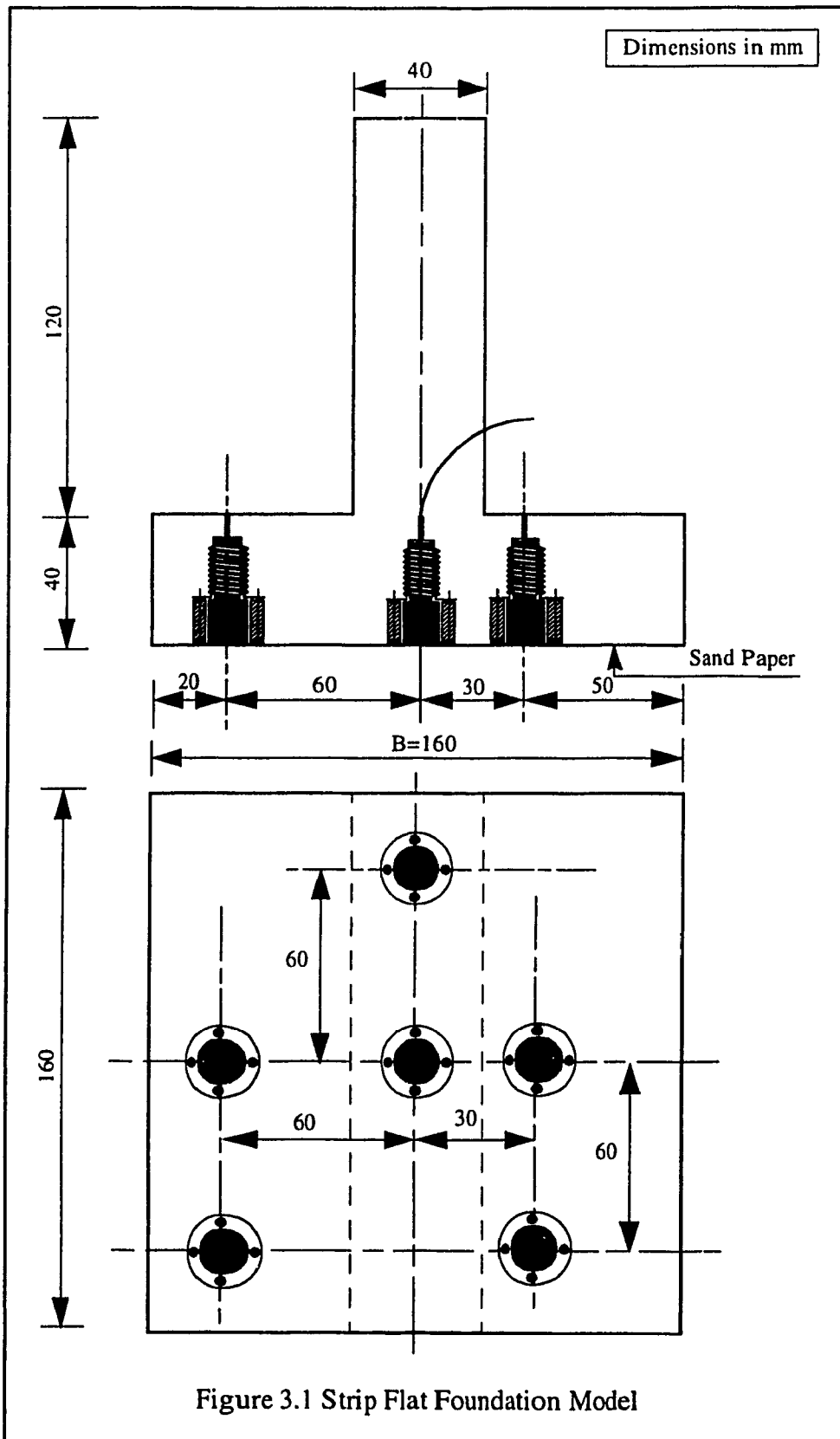
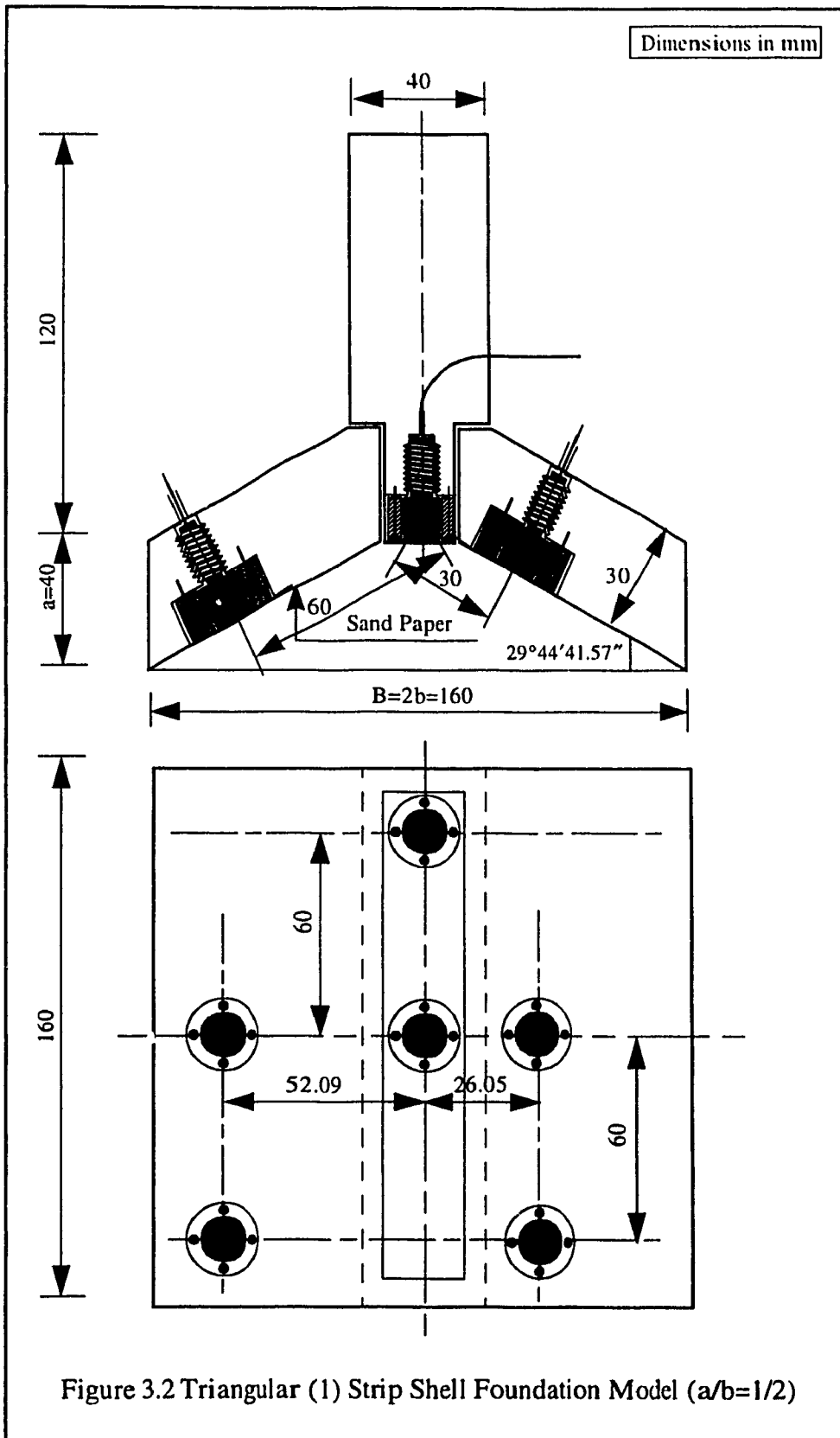
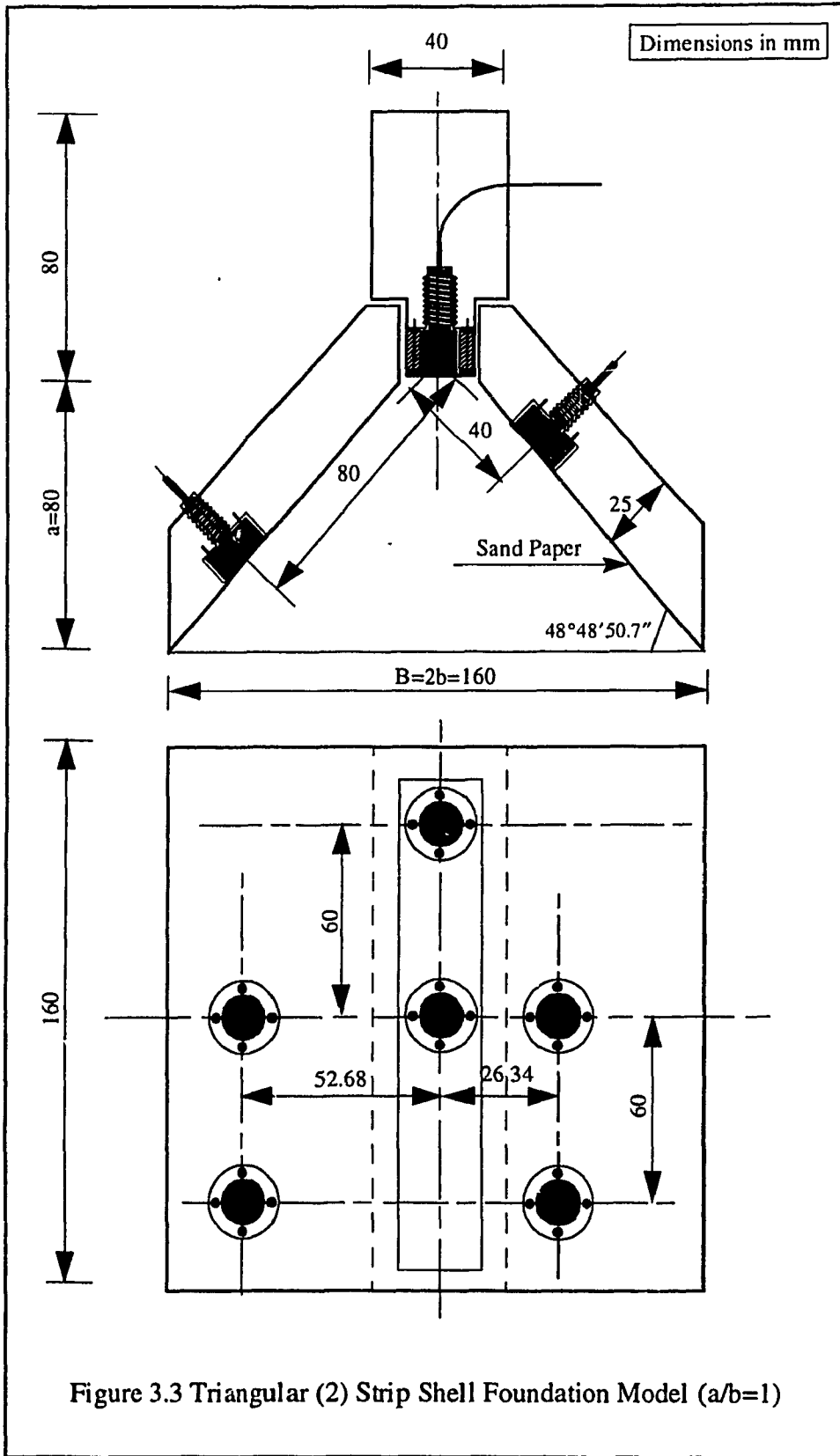
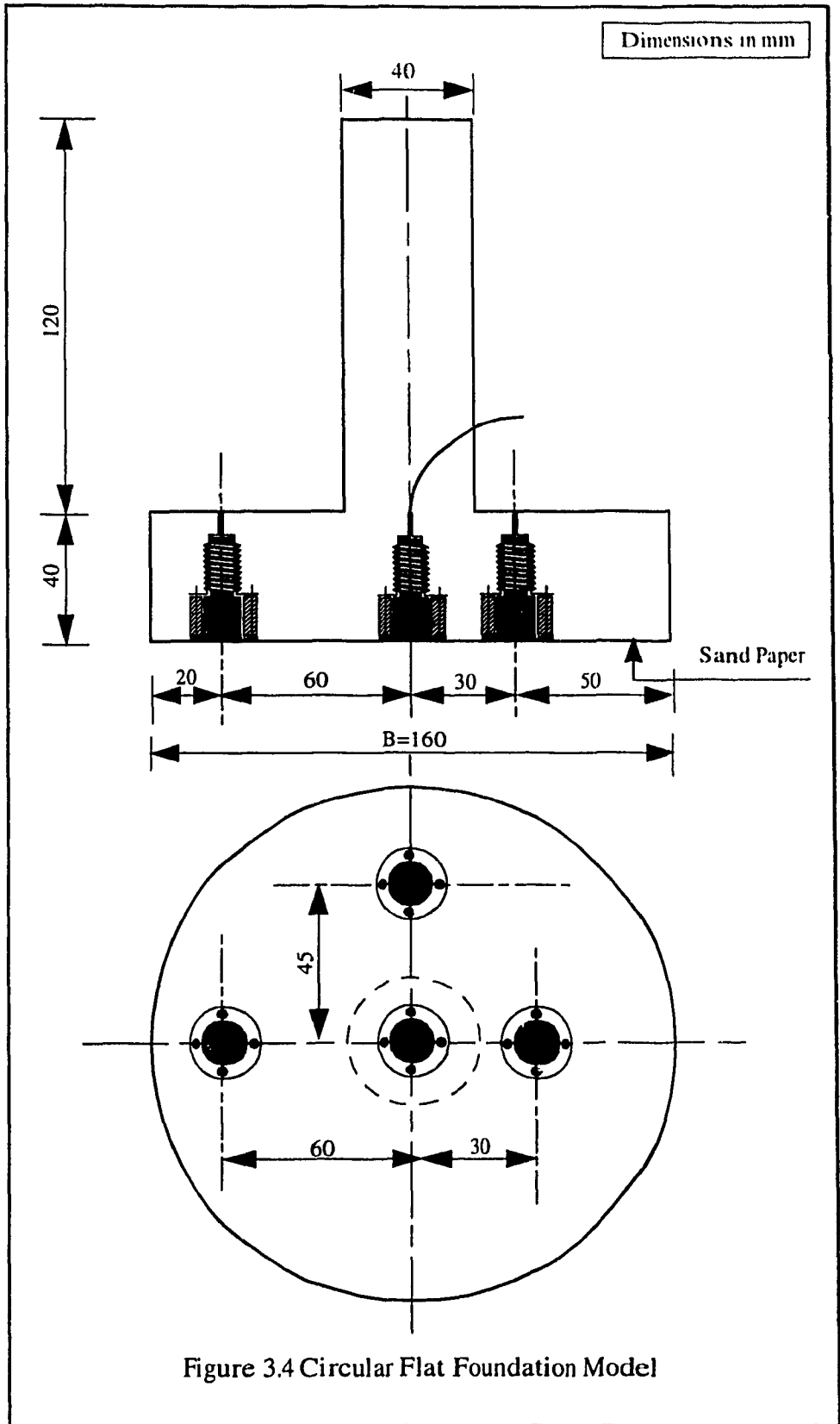
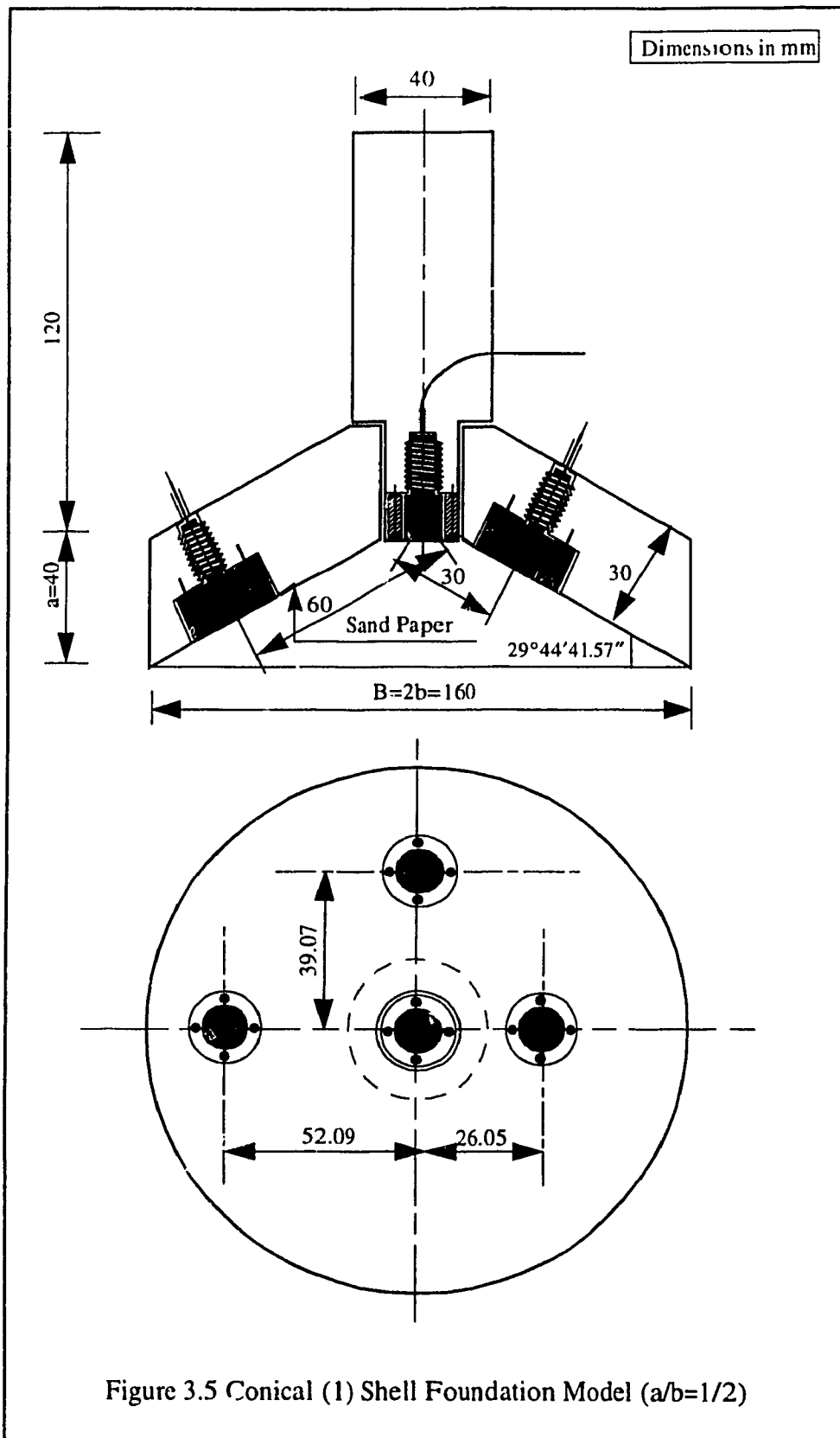


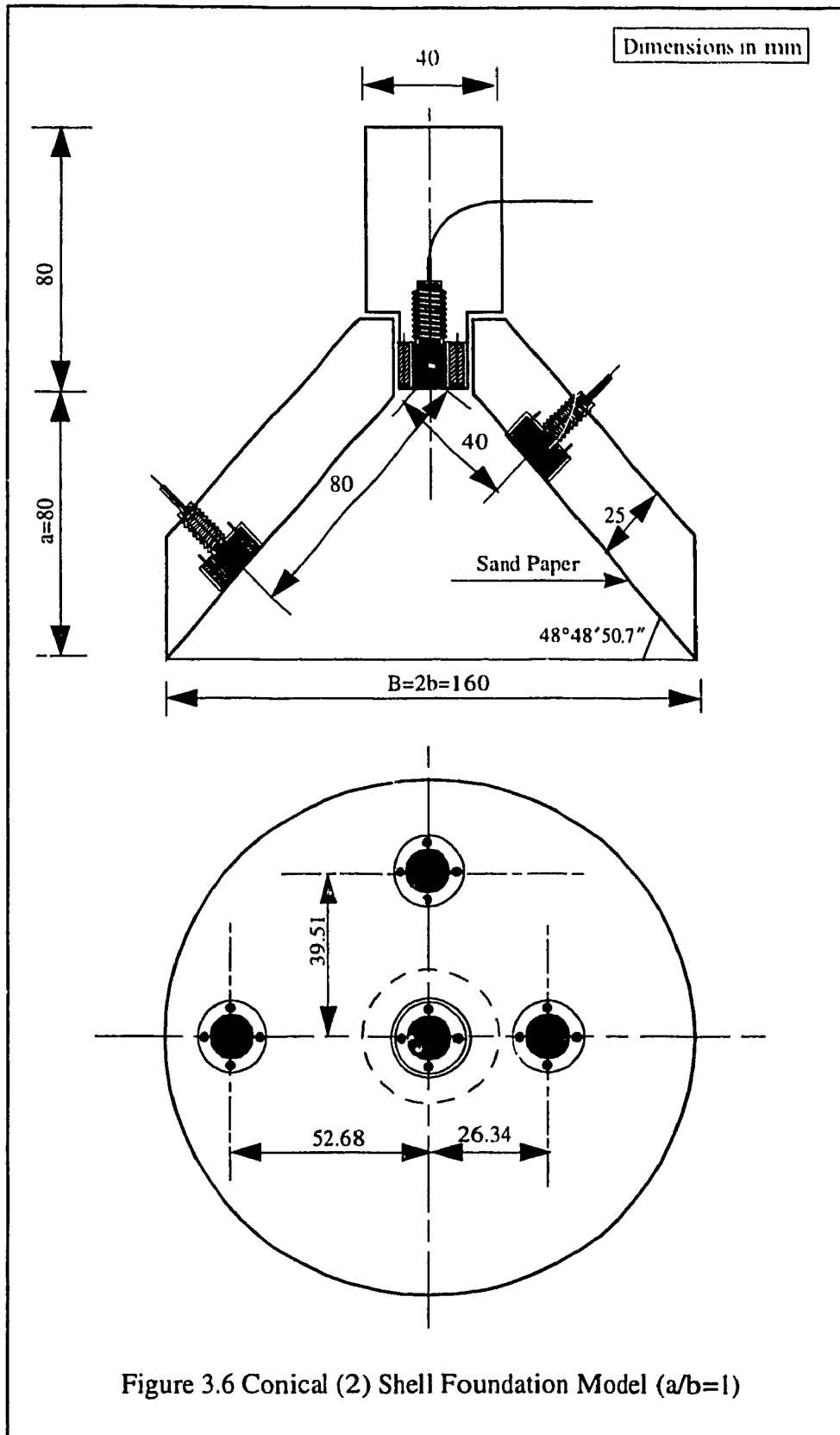
Figure 3.1 Strip Flat Foundation Model

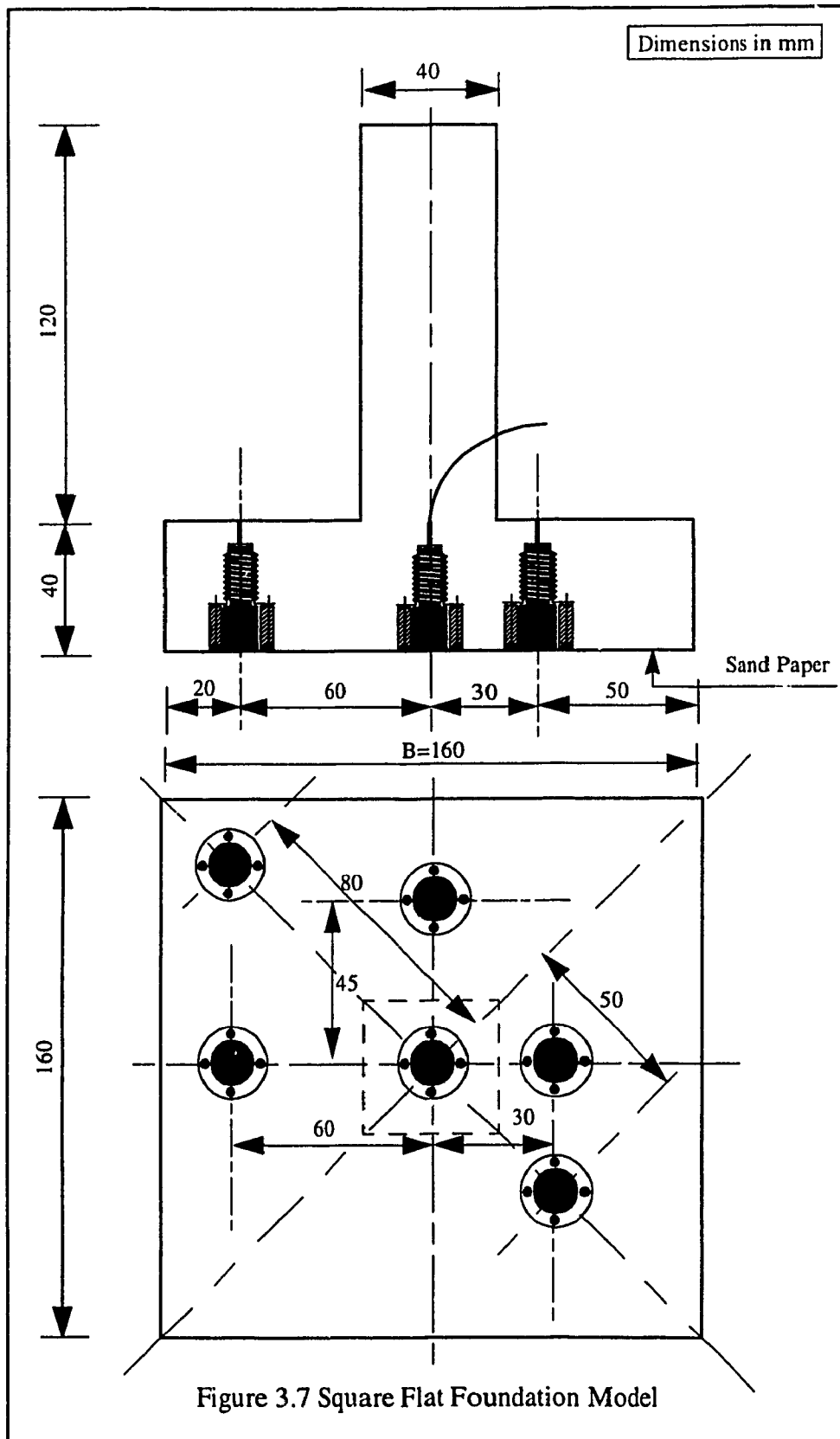




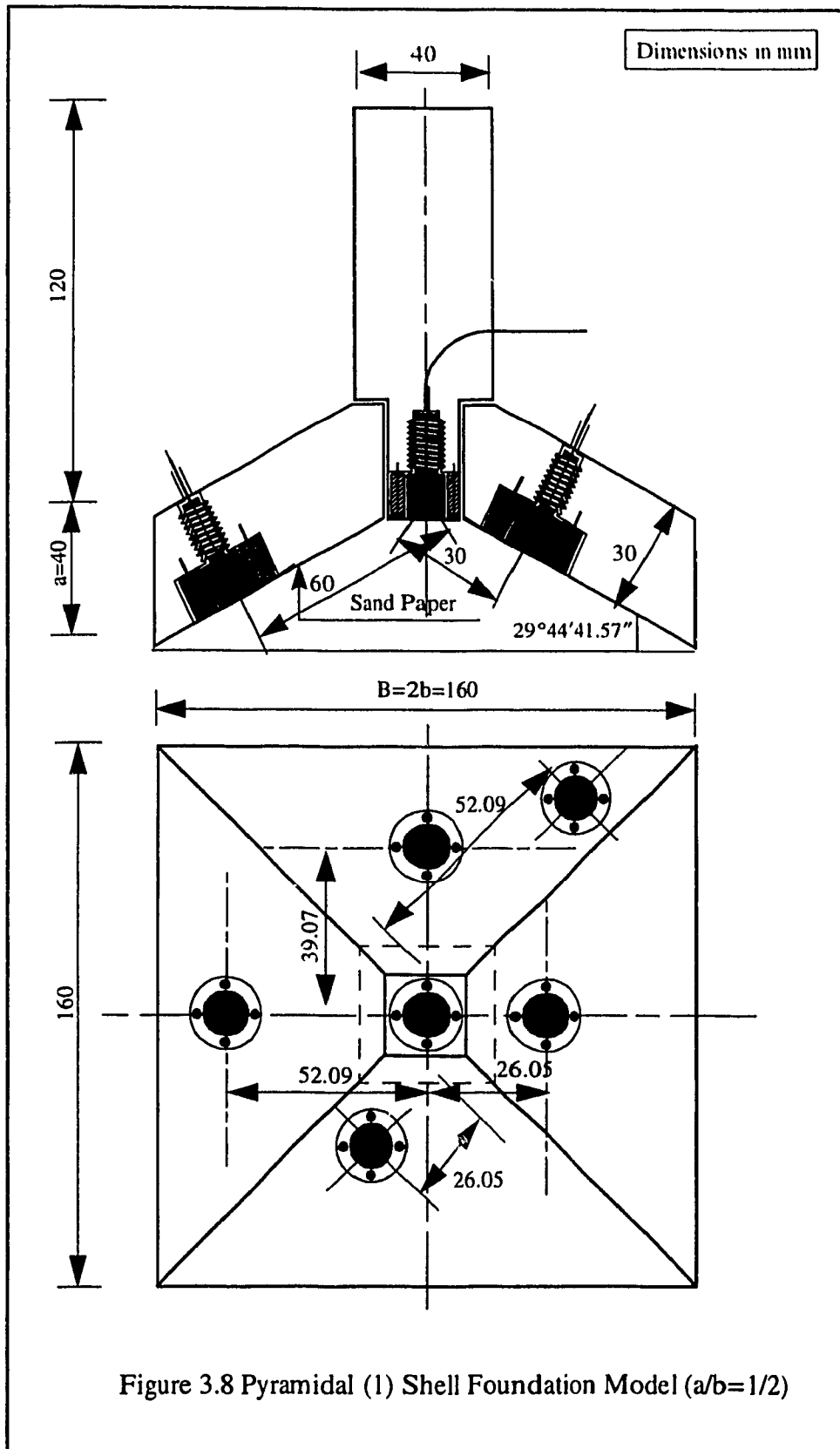












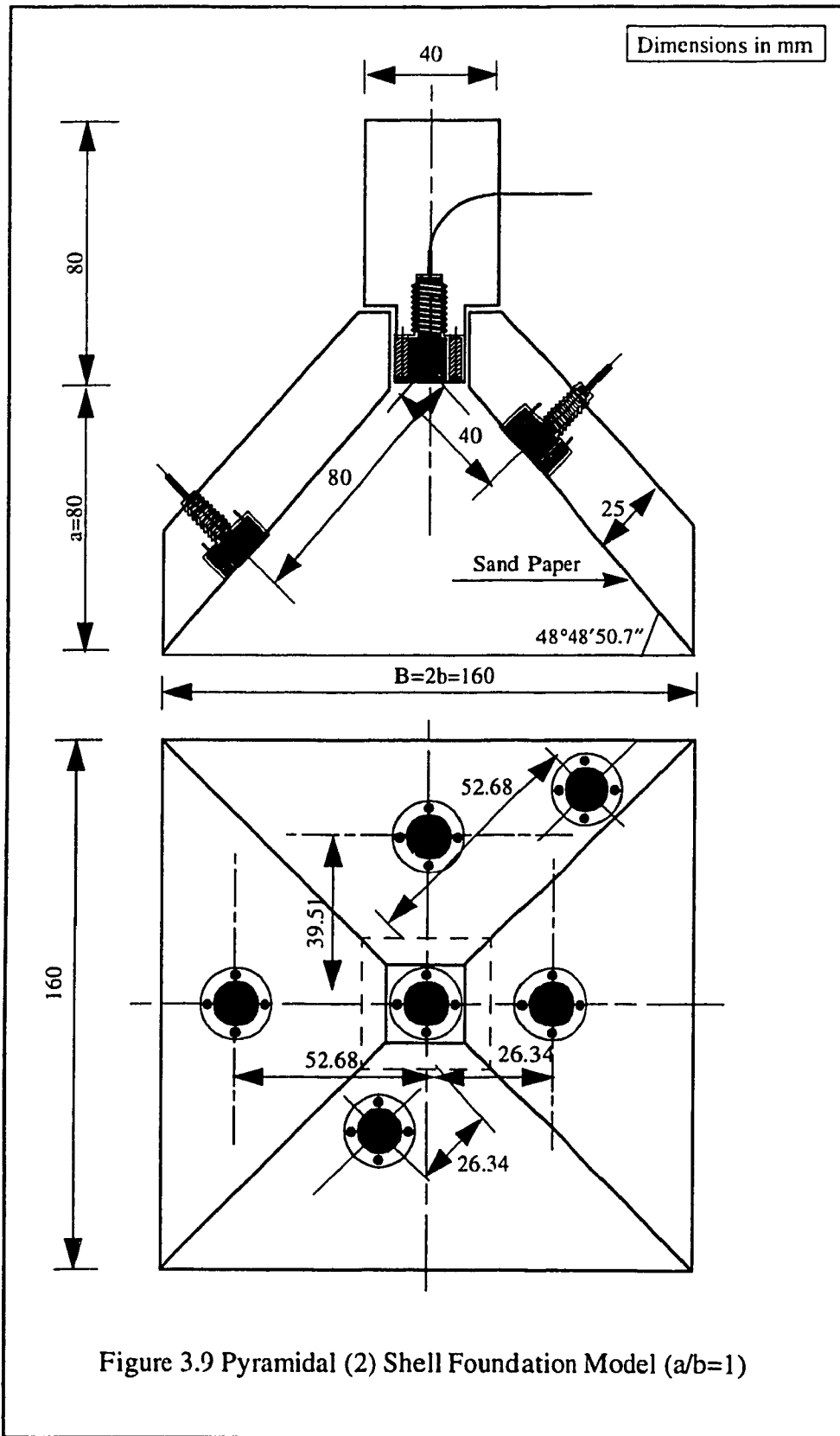
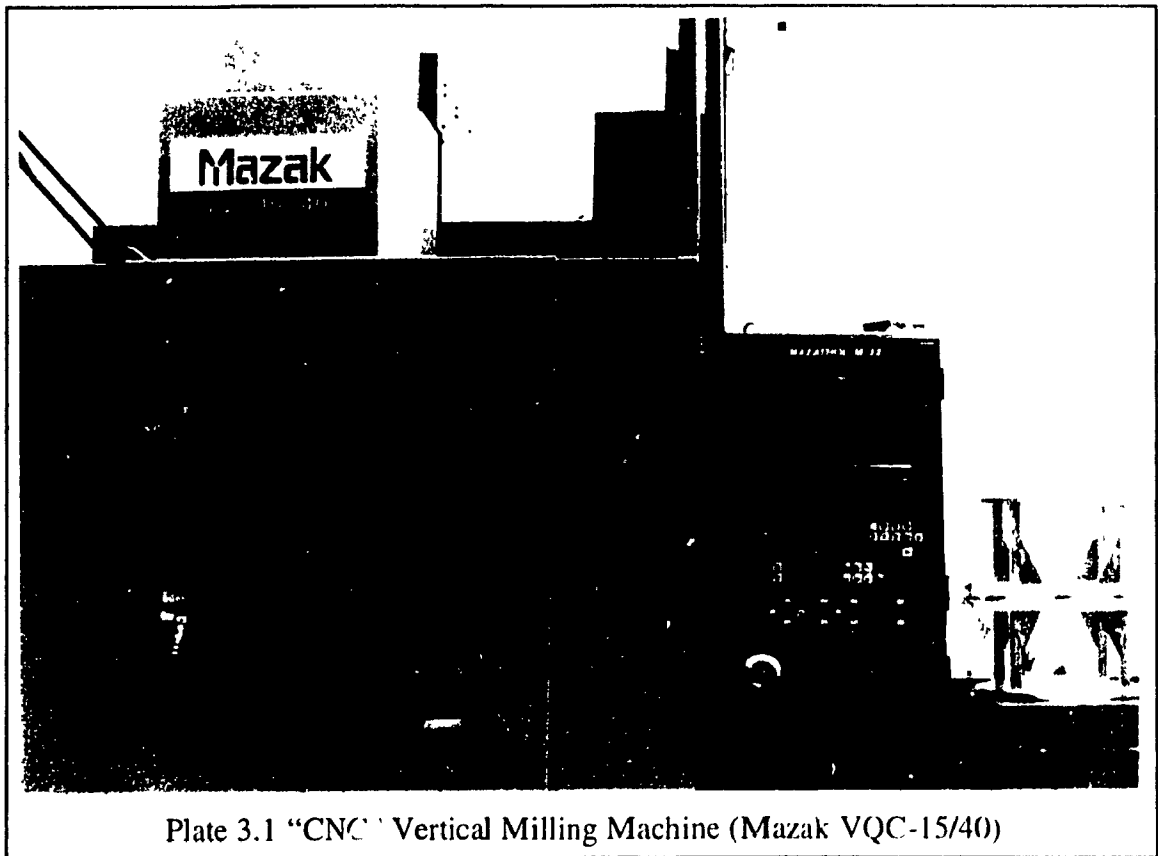


Figure 3.9 Pyramidal (2) Shell Foundation Model ( $a/b=1$ )

The models were fabricated from high quality stainless Atlas Alloys (Type 6061 T651) using the Computer Numerical Control "CNC" Vertical Milling Machine (Mazak VQC-15/40), which is shown in Plate 3.1 To avoid using any bolts or welds in the structure of the models, each model was fabricated from a single piece of alloy. Detailed shop drawing including dimensions and locations of holes required for pressure transducers was prepared for each model. These data was provided as an input file to the computer connected to the machine, which precisely shaped each model from the given piece of alloy. Sand papers were glued to the base of the models to provide rough surface condition



Plates 3.2 and 3.3 show one of the pyramidal shell models during fabrication process and after completion, respectively. An overall view of the nine foundation models after fabrication is shown in Plate 3.4. Close-up views of the strip flat and triangular shell models, the circular flat and conical shell models, and the square flat and pyramidal shell models are shown in Plates 3.5, 3.6, and 3.7, respectively.

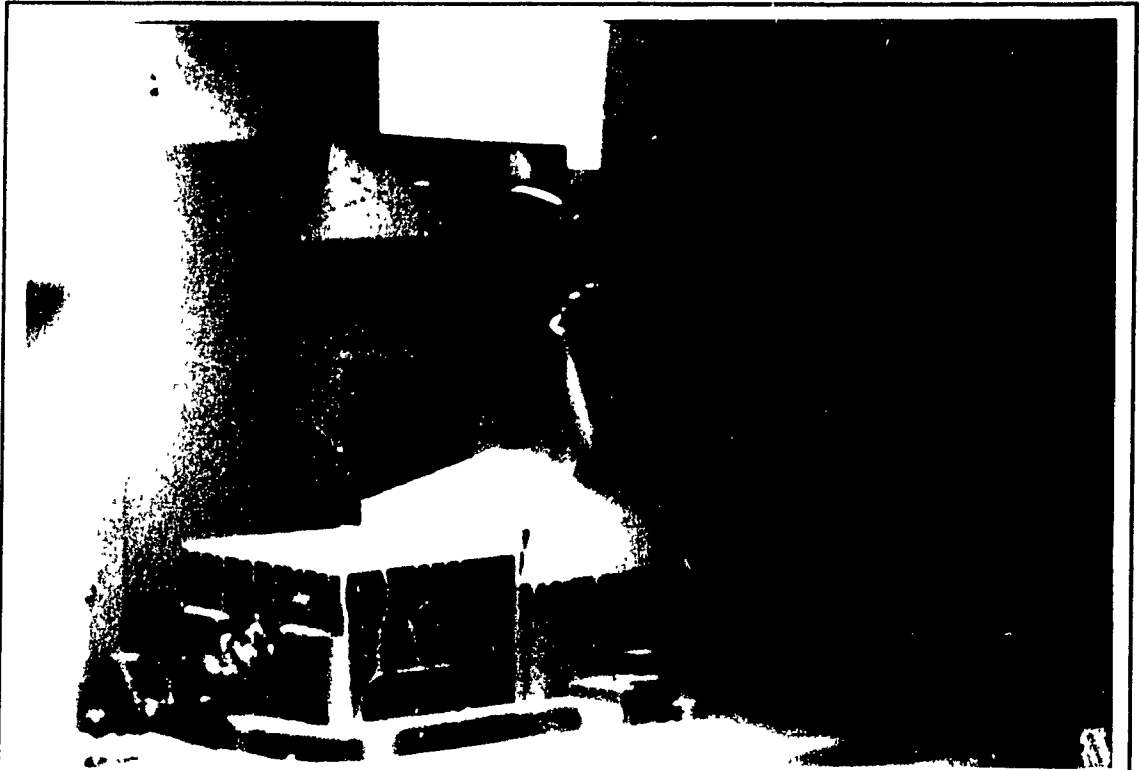


Plate 3.2 Pyramidal Shell Model During Fabrication Process

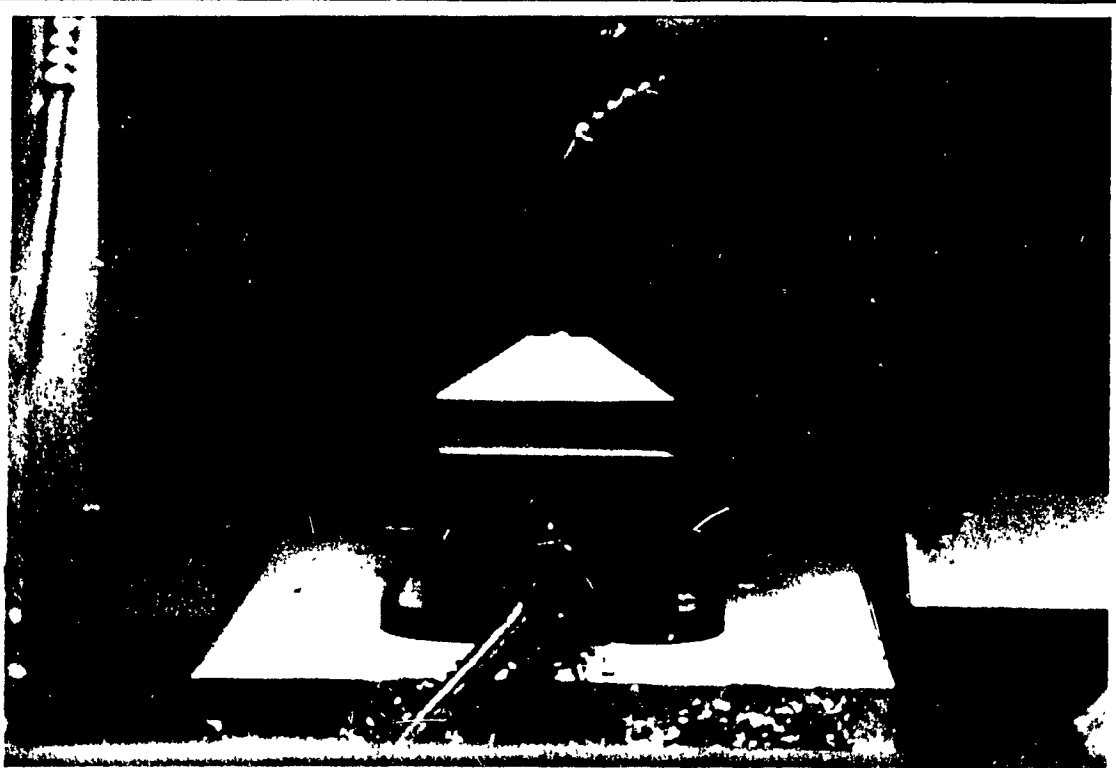


Plate 3.3 Pyramidal Shell Model after Fabrication Completed

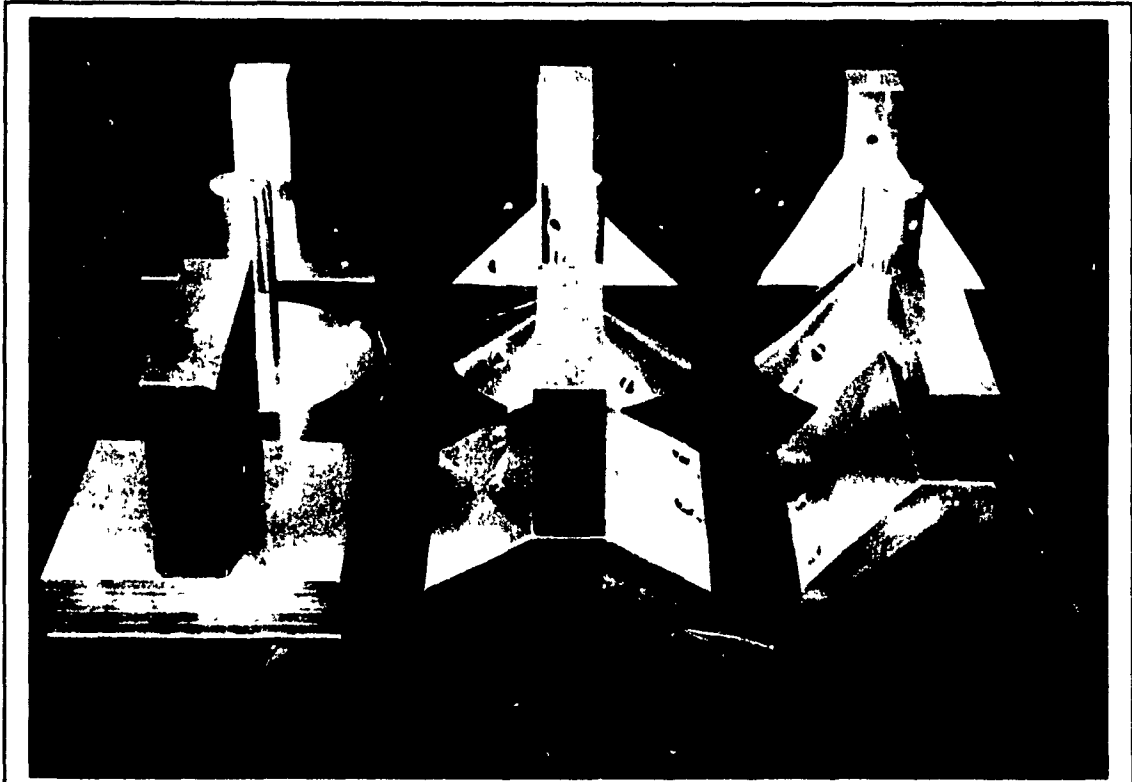


Plate 3.4 Overall View of All Foundation Models

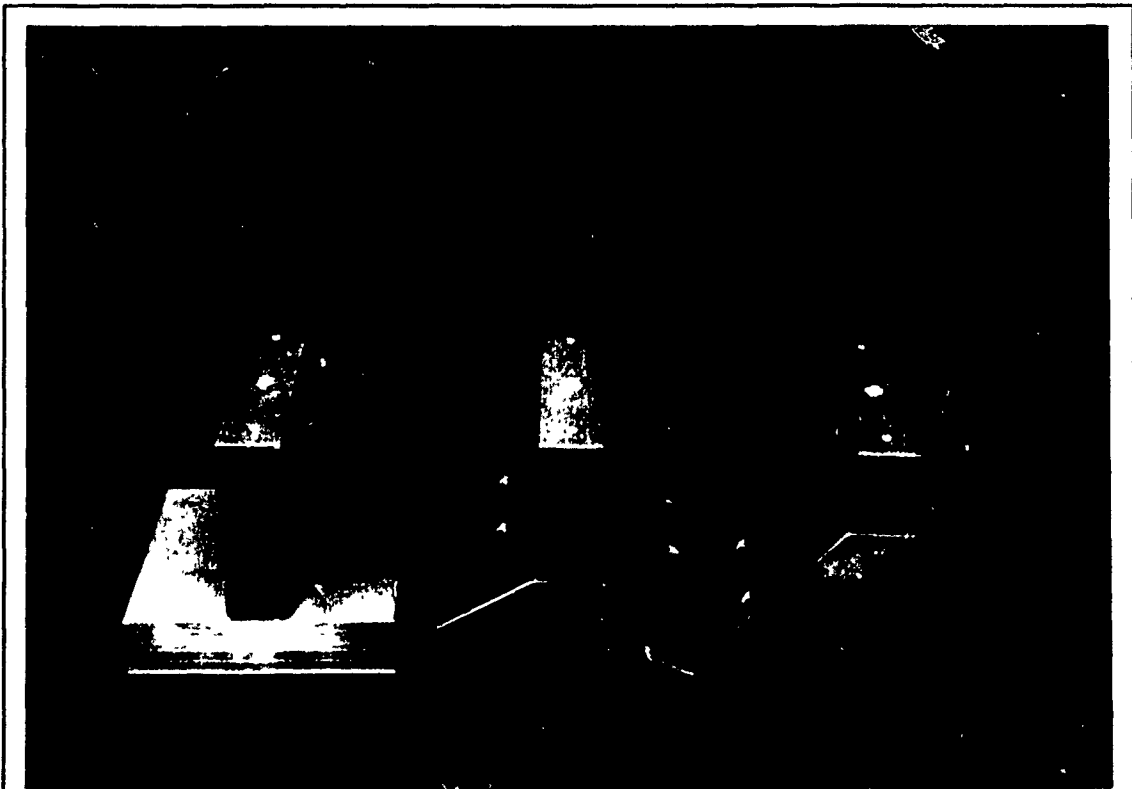


Plate 3.5 Close-Up View of Strip Flat & Triangular Shell Models

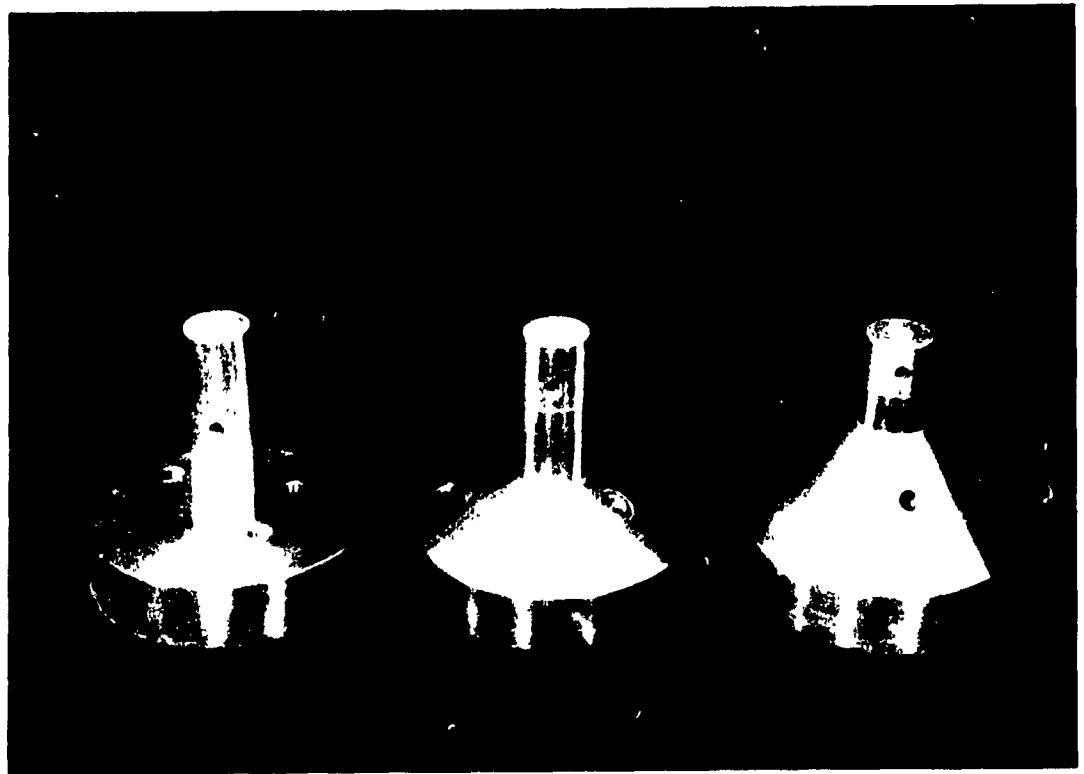


Plate 3.6 Close-Up View of Circular Flat & Conical Shell Models

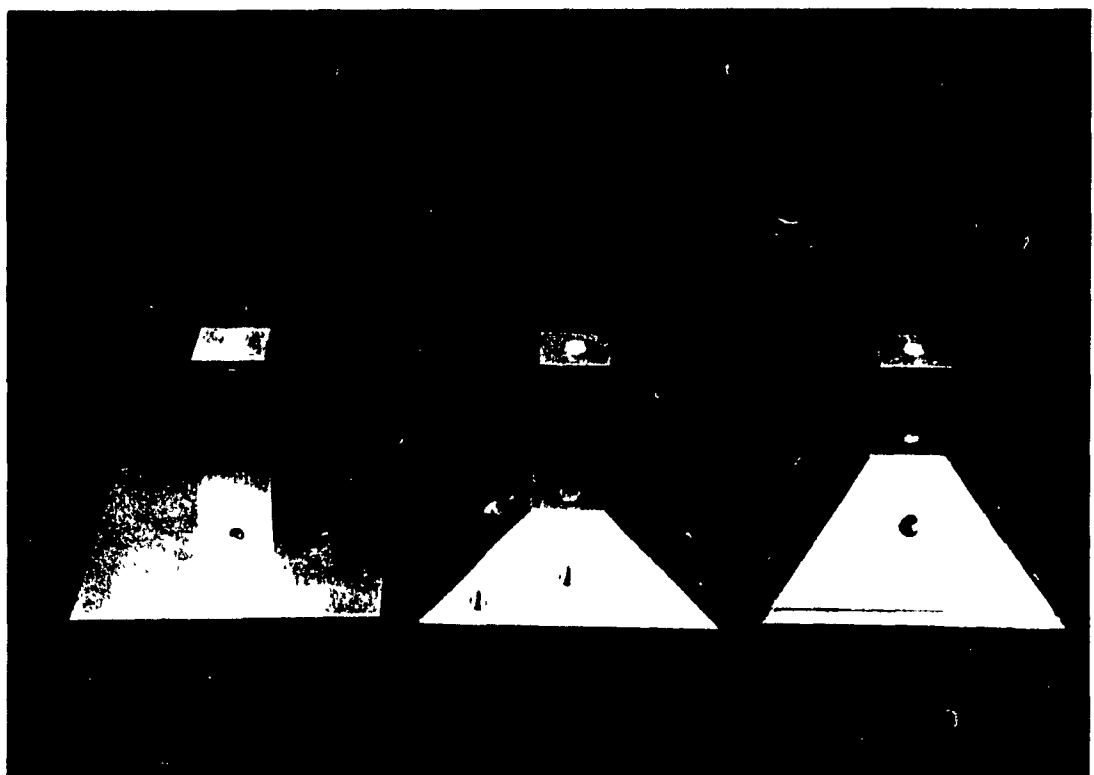


Plate 3.7 Close-Up View of Square Flat & Pyramidal Shell Models

### **3.3 Experimental Set-Up**

An overall sketch of the experimental set-up is illustrated in Figure 3.10, and the followings are the description of the elements used in the testing set-up:

#### **3.3.1 Testing Tanks**

Two testing tanks were used in this investigation. A plexiglas tank was used for testing plane strain models and also for special tests on colored layered sand. A steel tank was used for testing axisymmetrical and three dimensional models. The first tank was made of two plexiglas walls of one inch thickness (25.40 mm), see Plate 3.8. The base and sides were made of wooden sheets of two inches thickness (50.80 mm). The tank has internal dimensions of 800 x 165 x 640 mm for length, width, and depth, respectively. The thickness of the plexiglas walls was chosen to provide lateral support in order to prevent or to minimize the lateral buckling of walls during testing. The tank width was chosen to be almost equal to the width of strip models (a difference of 5 mm) to assure plane strain condition.

The second tank was made of steel plates of 6.50 mm thickness for the base and walls, (see Plate 3.9). The tank has internal dimensions of 1000 x 1000 x 1250 mm for length, width, and depth, respectively. The tank walls were braced with four steel angles (L 50 x 50 x 5), located at mid height, to prevent lateral buckling of the walls during testing.

#### **3.3.2 Loading System**

The loading system composed of a gear box device which generates a downward displacement with a constant rate of 2 mm/minute. This displacement was transformed into a force through a steel arm positioned at the centre of the foundation model. A load cell of 5000 lbs capacity (22.24 kN) was connected to the gear box to measure the applied load. Linear Variable Displacement Transducer "LVDT" was mounted on the gear box device to record the movement of the model during testing. Plate 3.10 shows a close-up view of the gear box device together with the load cell and the LVDT.

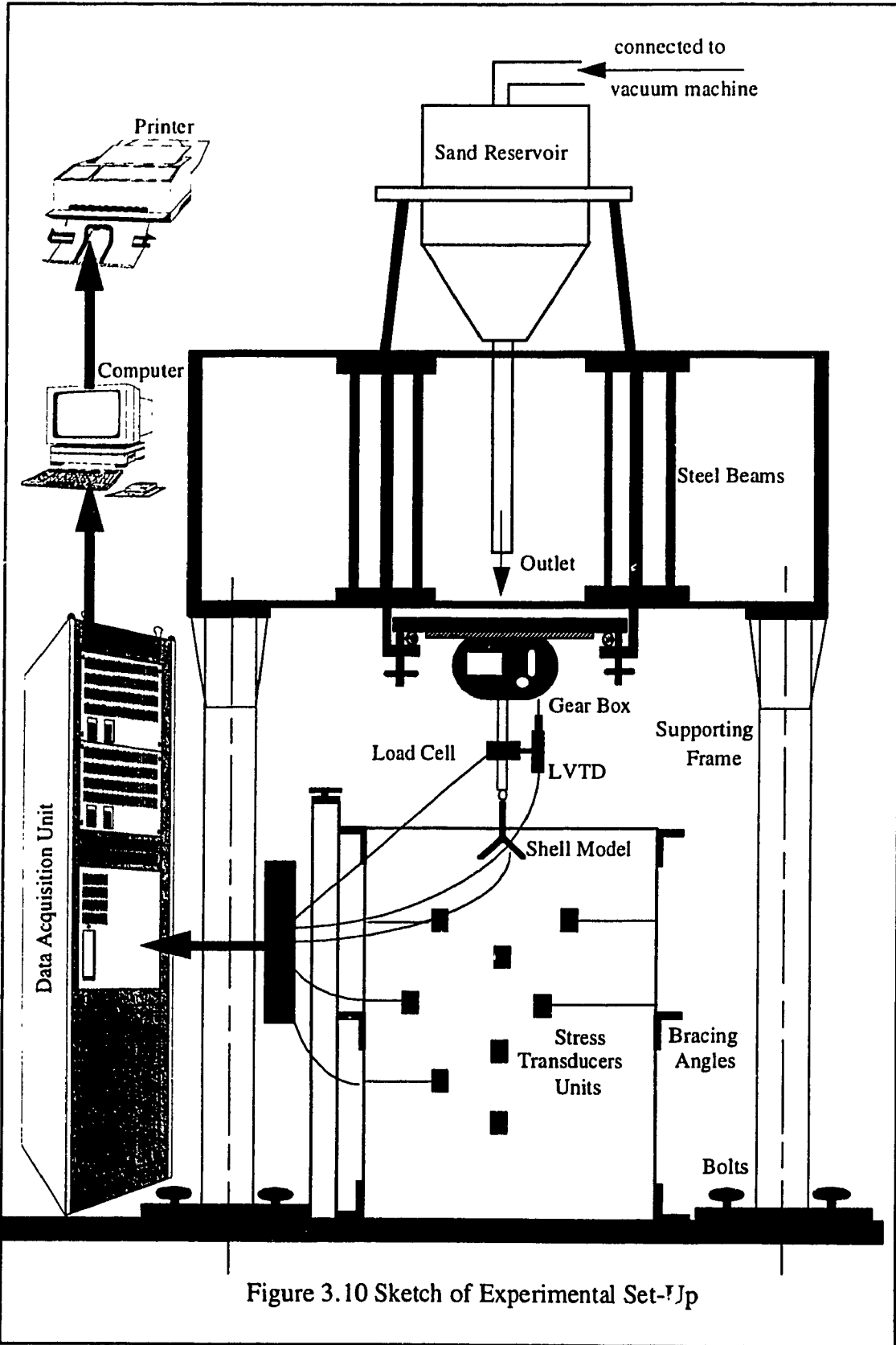


Figure 3.10 Sketch of Experimental Set-up



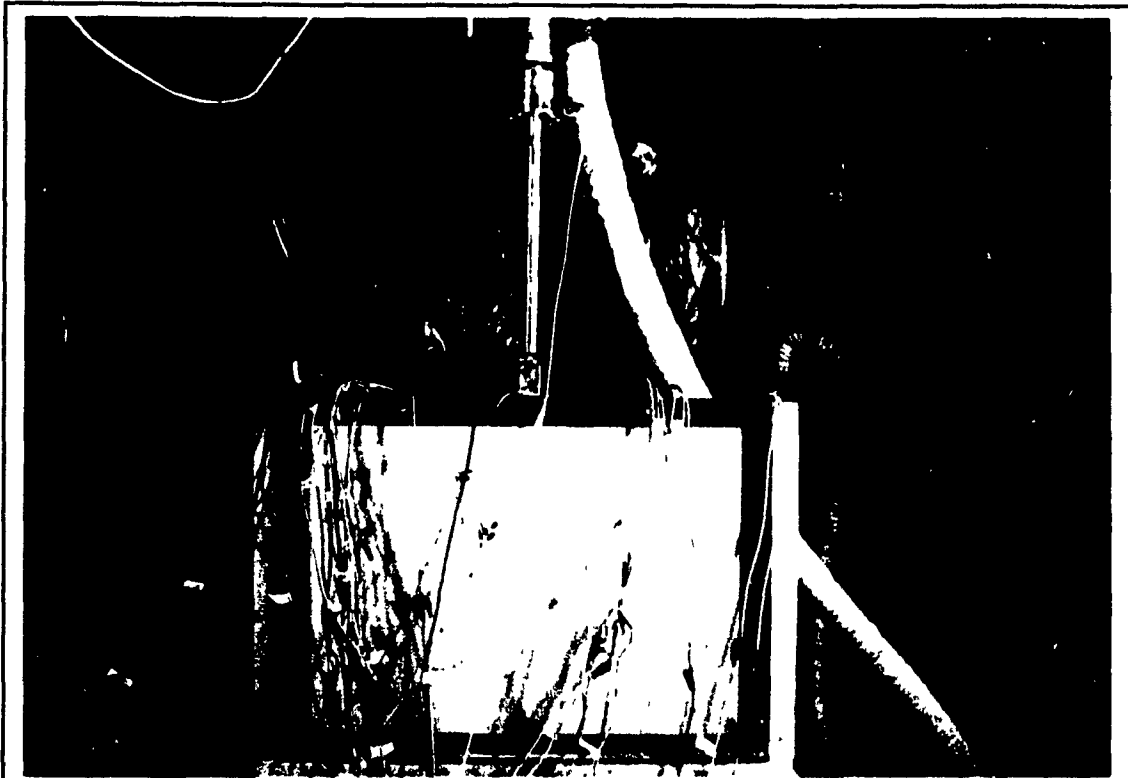


Plate 3.8 Plexiglas Testing Tank

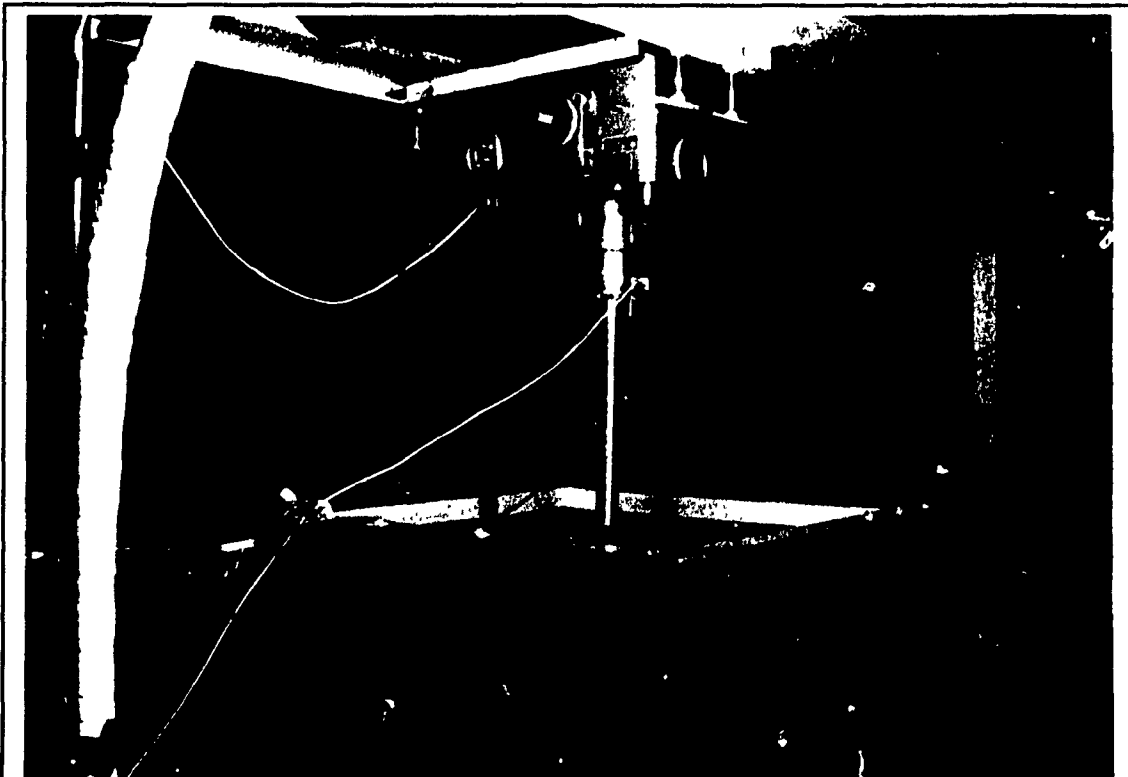


Plate 3.9 Steel Testing Tank

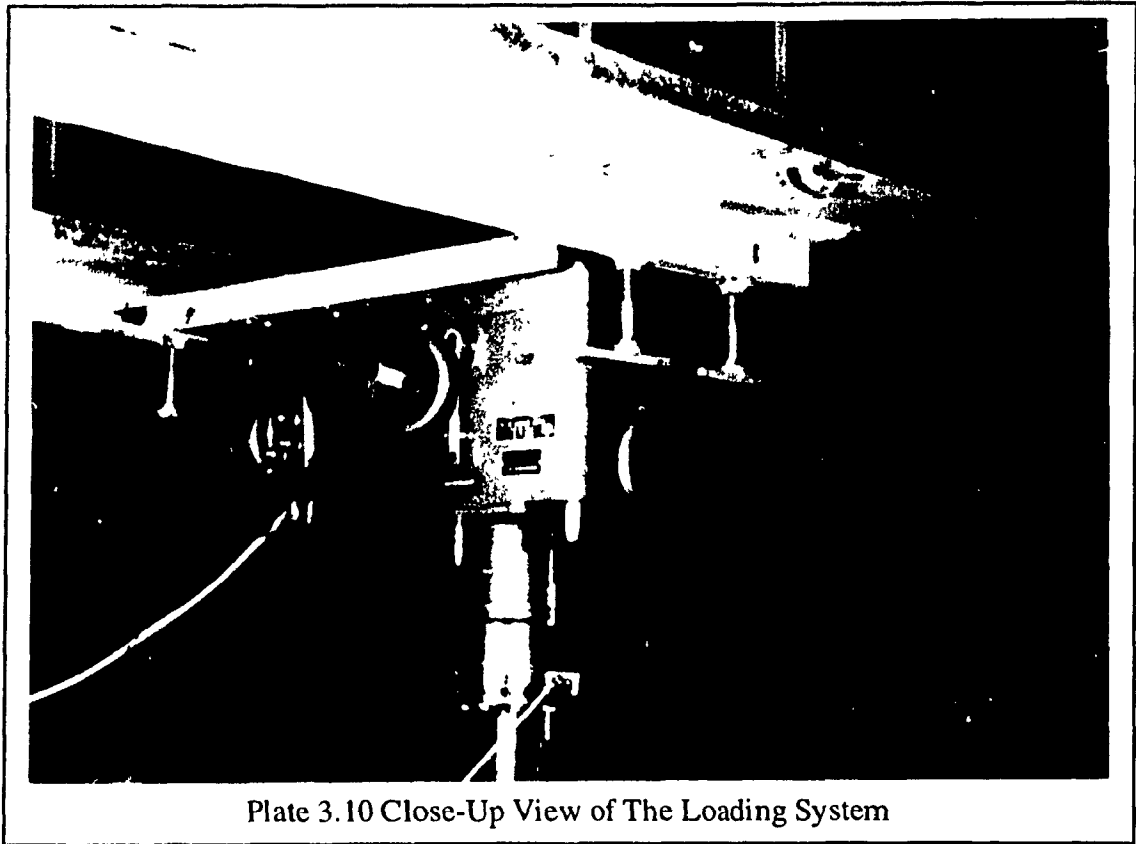
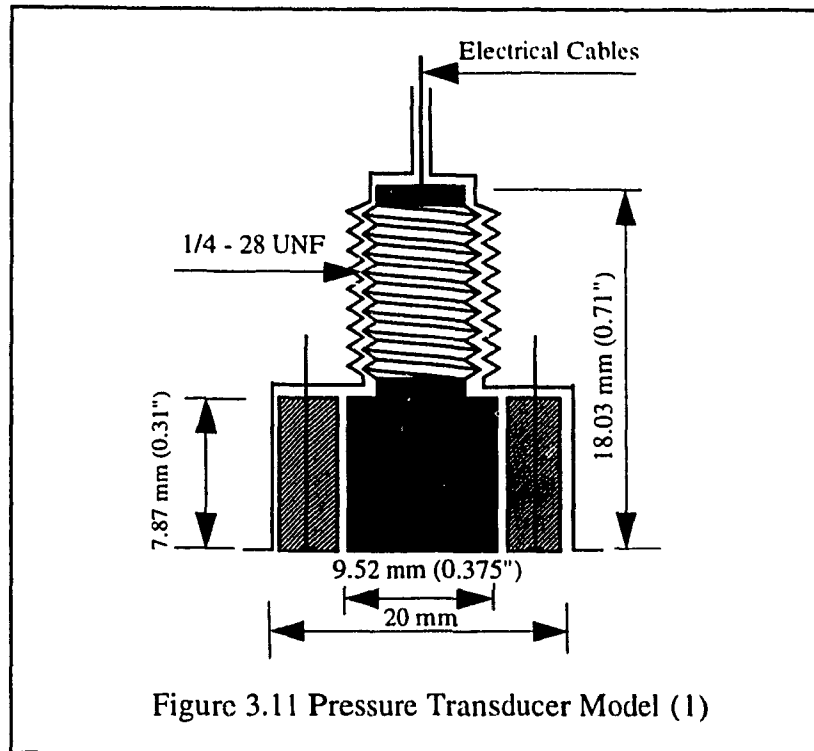


Plate 3.10 Close-Up View of The Loading System

### 3.3.3 Pressure Transducers

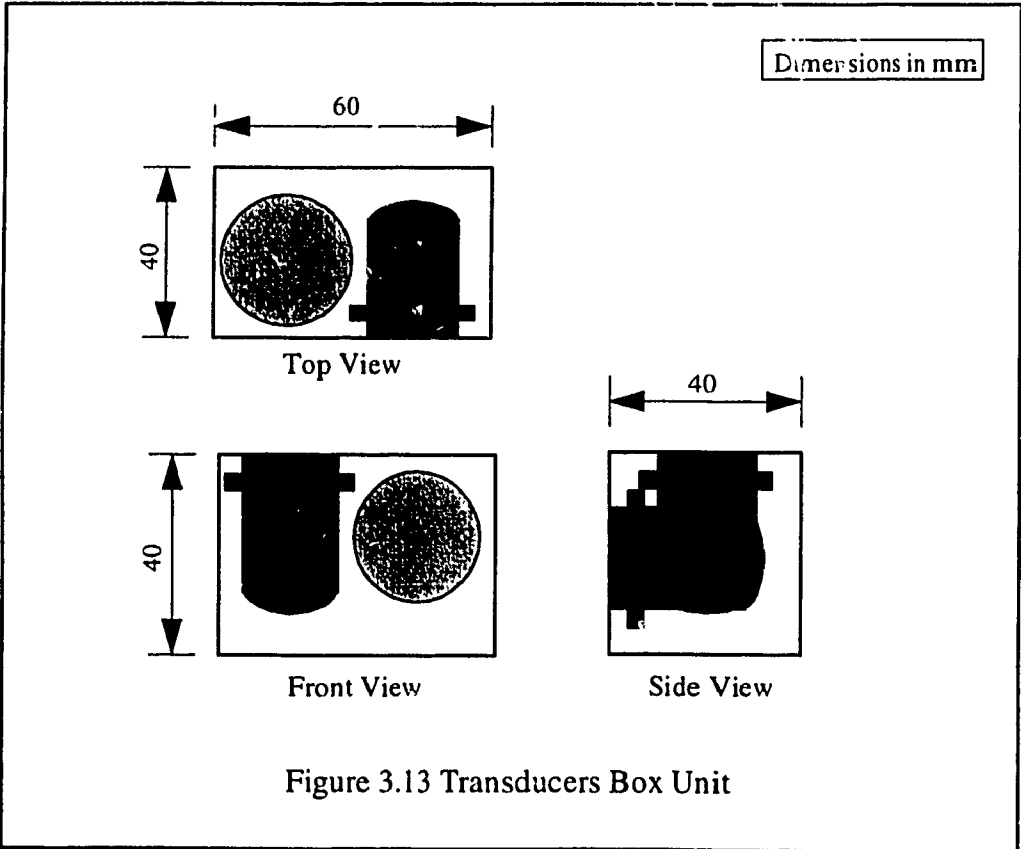
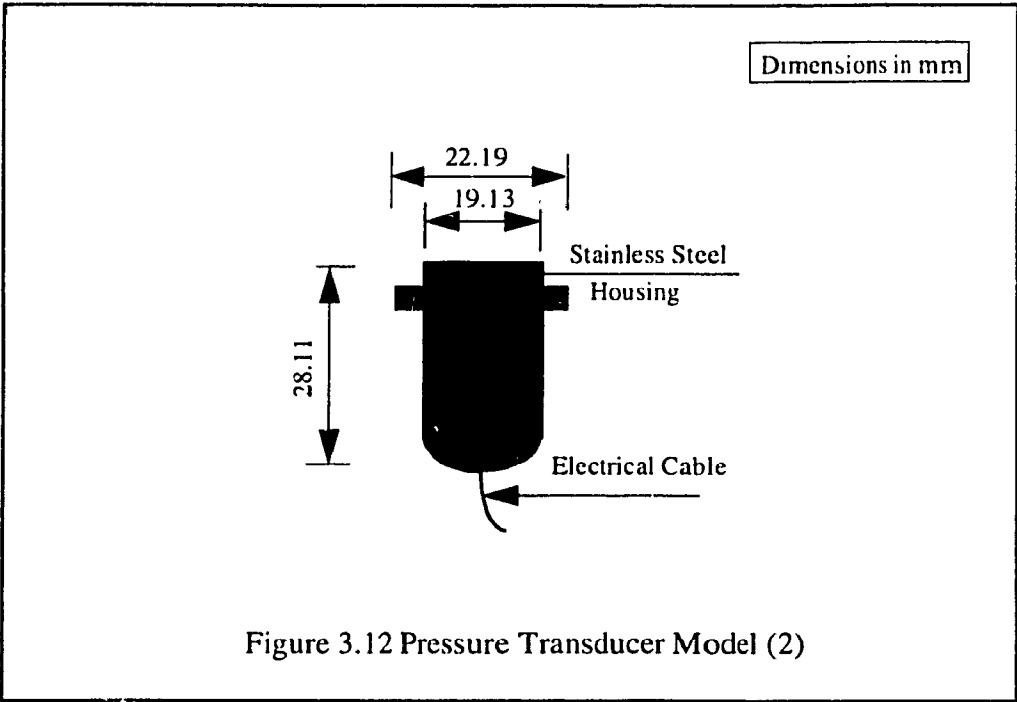
Two different models of pressure transducers were used in the present investigation. Both models of the pressure transducers were of high stiffness and insensitive to temperature variations.

The first transducer (Model 1) is shown in Figure 3.11, which was screwed at the base of the foundation models to measure the contact pressures on the soil-foundation interface during testing. The surface of the transducer was flush with the foundation base to avoid the existence of any pockets of higher or lower soil densities which could lead to either stress concentration or stress reduction, respectively. The electrical cables of these pressure transducers were connected directly to Data Acquisition System for contact pressure registration.



The vertical and lateral stresses developed within the soil mass were measured for the axisymmetrical and three dimensional models by another pressure transducer (Model 2). Figure 3.12 illustrates a detailed sketch of this transducer. An alloy box unit of 40 x 40 x 60 mm for the height, width, and length, respectively, was designed to accommodate two pressure transducers (see Figure 3.13). The transducers were located in the vertical and horizontal directions in order to measure the pressures acting normal to its surface.

Each transducer was protected against stress concentration by a surrounding inactive area and was sealed into the metallic box to prevent any fine sand particles from entering the box unit. Flexible O-rings were used to ensure firm contact between the pressure transducers and the unit. Inside the steel tank, each unit was attached to a thin hollow bar, through which the electrical cables of the two transducers were connected to Data Acquisition System for lateral and vertical stresses registration. A typical arrangement of these units inside the steel tank is shown in Figure 3.14.



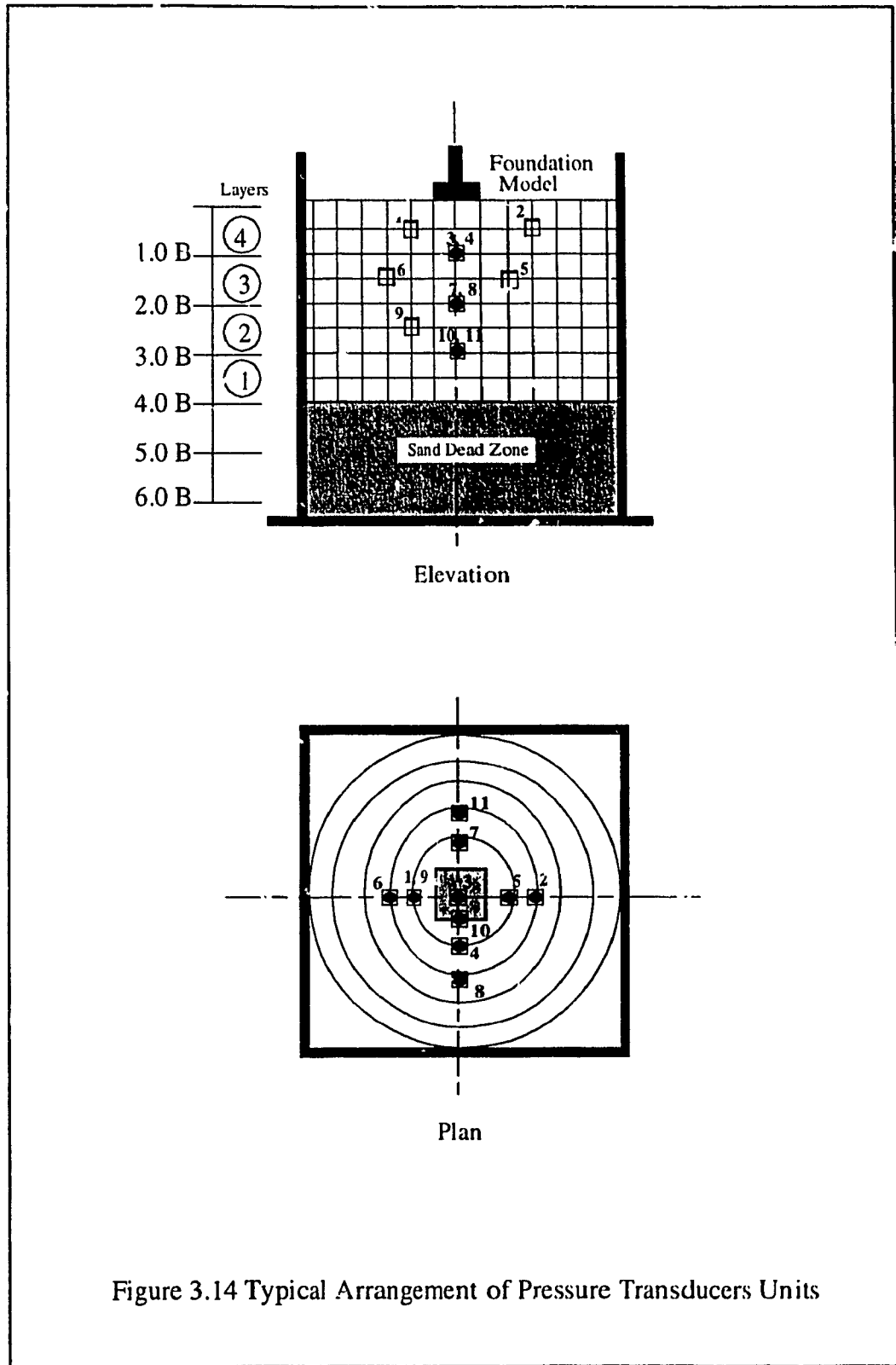
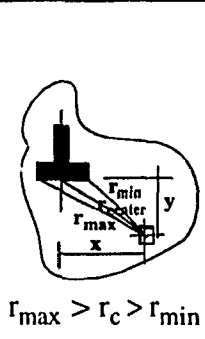


Figure 3.14 Typical Arrangement of Pressure Transducers Units

Table 3.1 presents the cartesian coordinates ( $x$  and  $y$ ) as well as the radial distances of each transducer:  $r_{max}$ ,  $r_c$ , and  $r_{min}$ , with respect to the foundation model. The units were placed in staggered positions. In plan, they were located at the center of tank and on the perimeter of two circles of 160 and 320 mm in diameter from the center. In elevation, the vertical spacing between any two consecutive rows of units was 80 mm center to center.

Table 3.1 Coordinates of Pressure Transducers Units

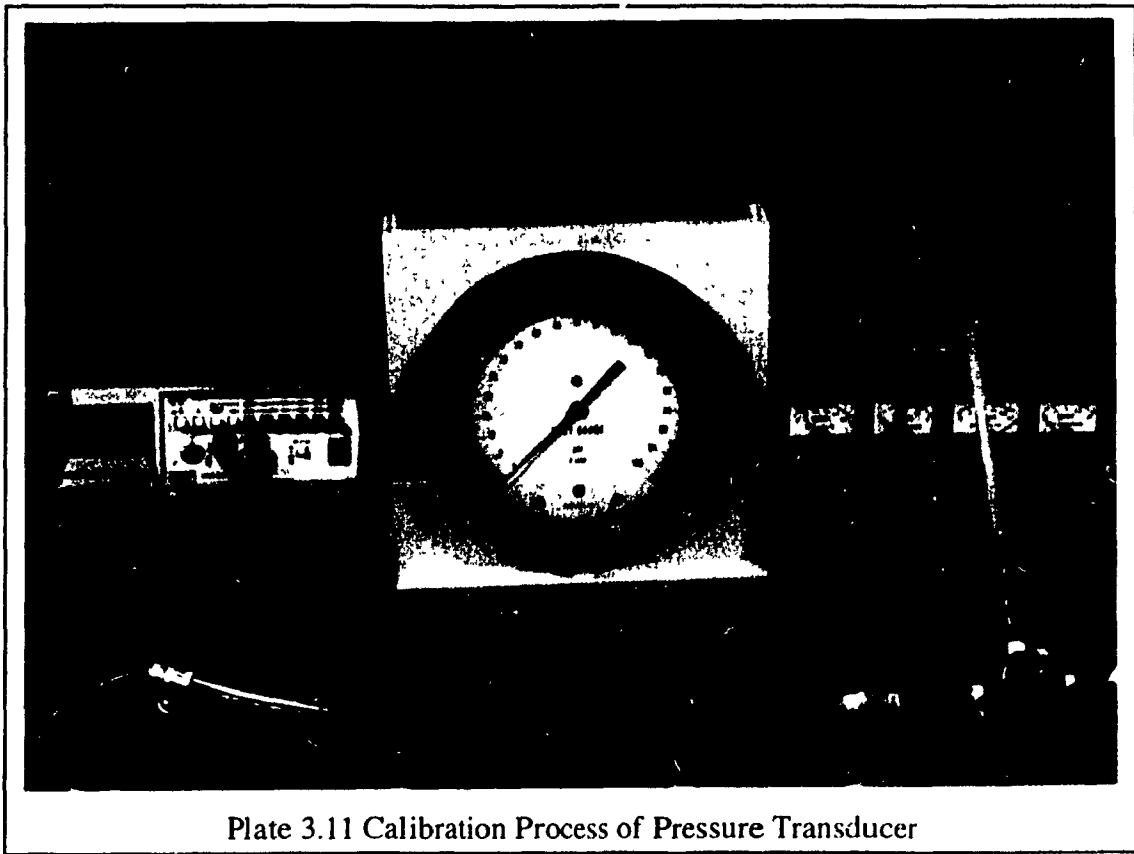
Depth	Unit	Coordinates		Radial distances			Key Sketch
		$x$	$y$	$r_{max}$	$r_{center}$	$r_{min}$	
0.5 B	1	1.00 B	0.50 B	1.58 B	1.21 B	0.71 B	 <p><math>r_{max} &gt; r_c &gt; r_{min}</math></p>
	2	1.50 B	0.50 B	2.06 B	1.58 B	1.12 B	
1.0 B	3	0	1.00 B	1.12 B	1.00 B	1.12 B	
	4	1.00 B	1.00 B	1.80 B	1.41 B	1.12 B	
1.5 B	5	1.00 B	1.50 B	2.12 B	1.80 B	1.58 B	
	6	1.50 B	1.50 B	2.50 B	2.12 B	1.80 B	
2.0 B	7	1.00 B	2.00 B	2.50 B	2.24 B	2.06 B	
	8	1.50 B	2.00 B	2.82 B	2.50 B	2.24 B	
2.5 B	9	1.00 B	2.50 B	2.92 B	2.69 B	2.55 B	
3.0 B	10	0.50 B	3.00 B	3.35 B	3.04 B	3.04 B	
	11	1.50 B	3.00 B	3.61 B	3.35 B	3.16 B	

Before the installation procedure began, each pressure transducer was calibrated individually by using incremental application of air pressure passing through a closed circuit. By measuring the applied air pressure on the transducer and recording the voltage output from the transducer by a voltmeter, a calibration factor was determined for each transducer. Plate 3.11 shows a calibration process for a pressure transducer in progress.

Throughout the testing process, a routine checkup was performed to calibrate the transducers all in one shot to check if any damage occurred during testing. Having all units

fixed in place inside the tank, the upper surface of the tank was closed firmly by a heavy steel plate, which was surrounded by a rubber coat at its circumference to prevent any air leakage. Air pressure was then applied inside the tank through an assembly with adjustable valve connected to a sensitive pressure gauge. The O-rings which were installed between the contact area of the pressure transducers and the box units act to prevent any air pressure dissipation through the unit.

All transducers were connected to Data Acquisition System, which registered the voltage for each transducer separately and gave the pressure according to its calibration factor. By reading the air pressure applied inside the tank from the pressure gauge and comparing it with the output from the Data Acquisition System for each transducer, any damaged transducer was easily identified and replaced.



### 3.3.4 Data Acquisition System

The data recorded for each loading test were measured by a variety of electrical devices namely: load cell, LVDT, and pressure transducers. All devices were connected to an HP Data Acquisition System, which register voltage changes. A computer program was developed to convert these voltage readings into load, displacement, and pressure using a specific calibration factor for each individual device. The program allows the data registration process to be set either to manual or automatic modes. While the manual mode gives the freedom to register all readings at any desired point of time, the automatic mode records the data at a predetermined time interval. Manual mode was used for data registration during compaction process and the transducers routine checkup; the automatic mode was used during all loading tests for systematic data output. Plate 3.12 shows a general view of the Data Acquisition System connected to a computer during a loading test.

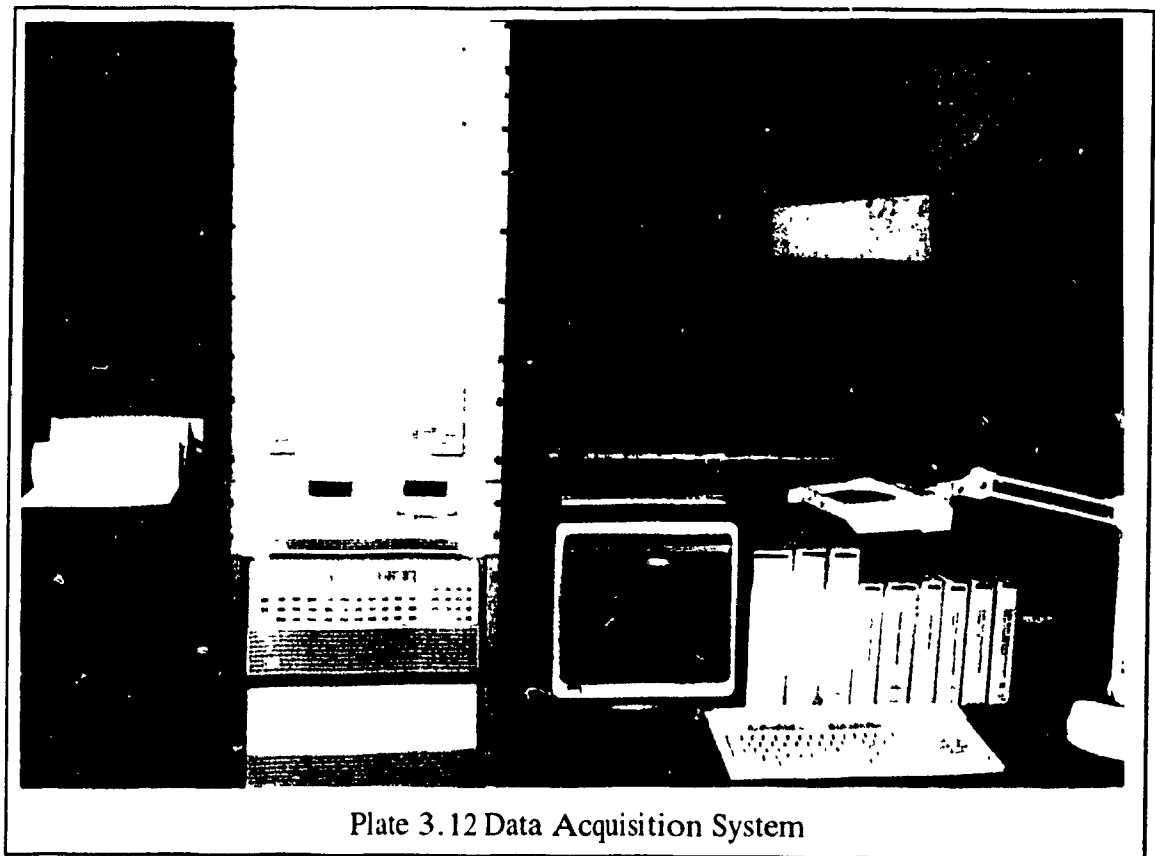


Plate 3.12 Data Acquisition System



### 3.4 Experimental Testing Program

A total number of 54 tests were conducted on the prescribed foundation models using three different sand states. Surface and embedded models at embedment ratio of ( $D/B=0.75$ ) were tested. Table 3.2 summarizes the testing program.

Table 3.2 Experimental Testing Program

	Foundation Model	Test No.	Surface Tests ( $D/B = 0$ )	Test No.	Embedded Tests ( $D/B = 0.75$ )
Plane Strain Models	Strip Flat Model	1	Loose Sand	4	Loose Sand
		2	Medium Sand	5	Medium Sand
		3	Dense Sand	6	Dense Sand
	Triangular (1) Shell Model	7	Loose Sand	10	Loose Sand
		8	Medium Sand	11	Medium Sand
		9	Dense Sand	12	Dense Sand
	Triangular (2) Shell Model	13	Loose Sand	16	Loose Sand
		14	Medium Sand	17	Medium Sand
		15	Dense Sand	18	Dense Sand
Axisymmetrical Models	Circular Flat Model	19	Loose Sand	22	Loose Sand
		20	Medium Sand	23	Medium Sand
		21	Dense Sand	24	Dense Sand
	Conical (1) Shell Model	25	Loose Sand	28	Loose Sand
		26	Medium Sand	29	Medium Sand
		27	Dense Sand	30	Dense Sand
	Conical (2) Shell Model	31	Loose Sand	34	Loose Sand
		32	Medium Sand	35	Medium Sand
		33	Dense Sand	36	Dense Sand
Three Dimensional Models	Square Flat Model	37	Loose Sand	40	Loose Sand
		38	Medium Sand	41	Medium Sand
		39	Dense Sand	42	Dense Sand
	Pyramidal (1) Shell Model	43	Loose Sand	46	Loose Sand
		44	Medium Sand	47	Medium Sand
		45	Dense Sand	48	Dense Sand
	Pyramidal (2) Shell Model	49	Loose Sand	52	Loose Sand
		50	Medium Sand	53	Medium Sand
		51	Dense Sand	54	Dense Sand

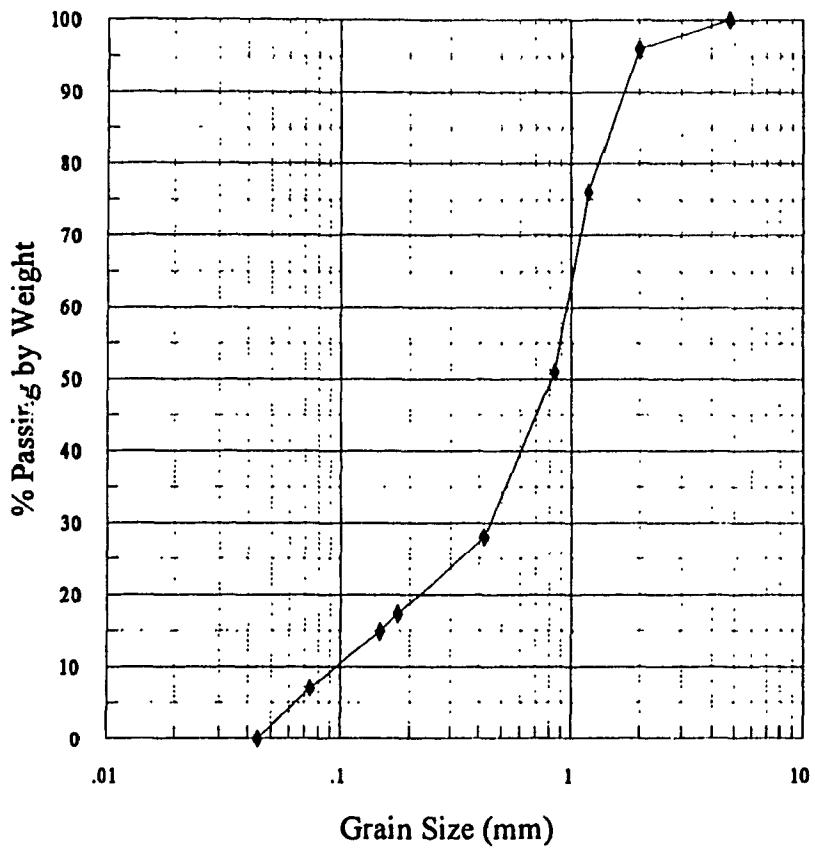
### 3.5 Sand Characteristics

Three different sand states were used in the present investigation namely, loose, medium, and dense states. A mixture of well graded sand was obtained from five different gradation of 99.9% high silica sand imported from the United States. The sand mixture consisted of percentage passing by weight from mesh #10: #16: #24: #40: #140 = 2: 1: 3: 2: 2. Based on the Unified Soil Classification System, the tested sand was classified as well graded and has a uniformity coefficient  $C_u = 9.50$ , coefficient of curvature  $C_c = 2.13$ , and an average specific gravity ( $G_s$ ) of 2.68. Figure 3.15 shows the mechanical sieve analysis graph of a sample of the mixture sand used in this investigation.

A sand placing technique was developed and calibrated several times before starting the testing program to ensure the reproducibility of a predetermined unit weight inside both testing tanks. This technique was achieved by placing the sand in layers and applying mechanical compaction by means of an air pressure hammer using constant air pressure. By changing the duration of compaction, as an external controlled factor in the compaction process, different unit weights of the sand were produced.

In the plexiglas tank, three layers of 160 mm thickness each were poured and the air pressure was set constant to 40 psi (275.79 kPa), and four layers of 160 mm thickness each were poured in the steel tank and the air pressure was set constant to 37 psi (255.10 kPa). Figures 3.16 and 3.17 show compaction time versus sand unit weight at different layers inside the plexiglas tank and the steel tank, respectively.

Direct shear box tests were performed on different sand samples of the unit weights: 16.0, 17.0, 18.0, and 19.0 kN/m<sup>3</sup>. The shear box test results are presented in Figures 3.18 through 3.20. Tables 3.2 and 3.3 summarize the physical and mechanical characteristics of the sand used in the testing program inside the plexiglas and the steel tanks, respectively.



<b>SAND</b>		
<b>Fine</b>	<b>Medium</b>	<b>Coarse</b>

Figure 3.15 Mechanical Sieve Analysis Graph

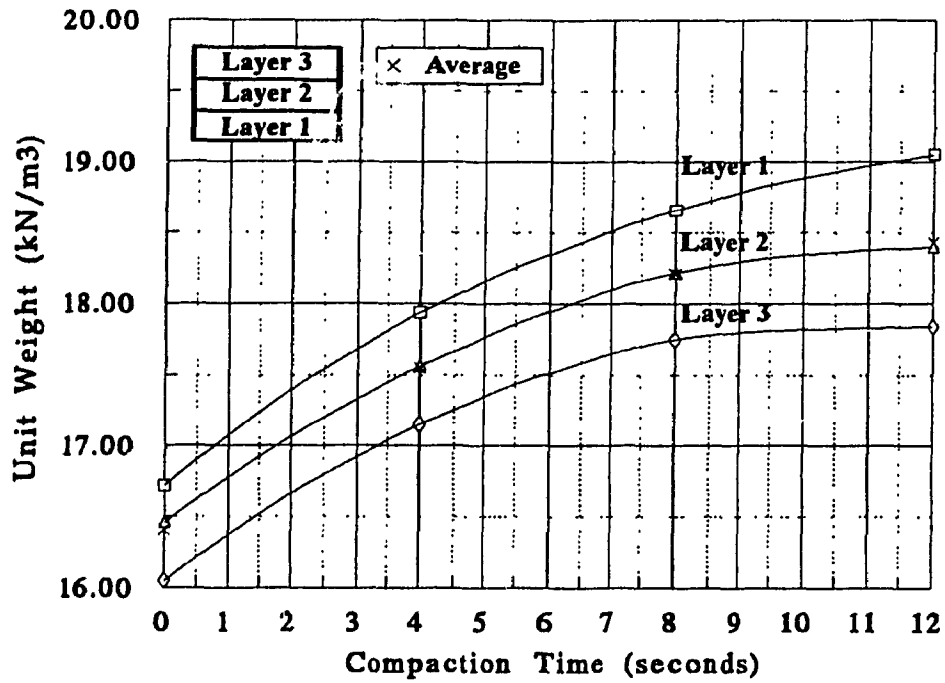


Figure 3.16 Compaction Time versus Sand Unit Weight inside Plexiglass Tank

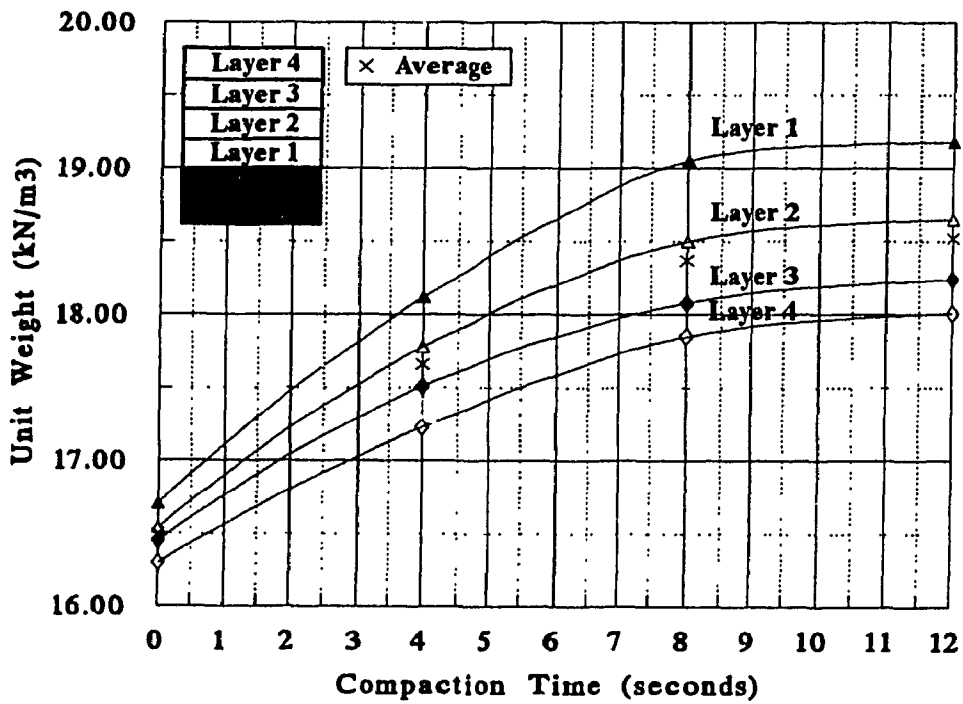


Figure 3.17 Compaction Time versus Sand Unit Weight inside Steel Tank

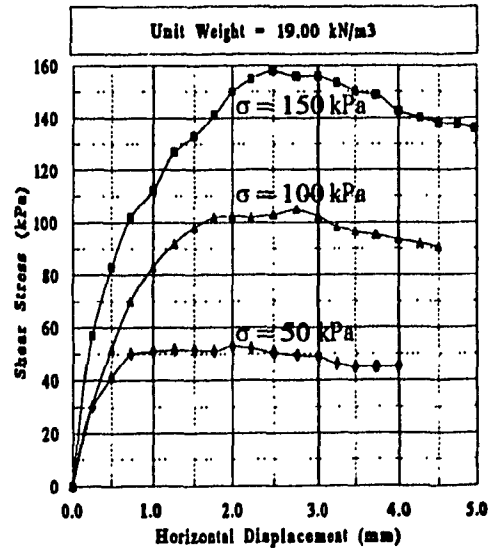
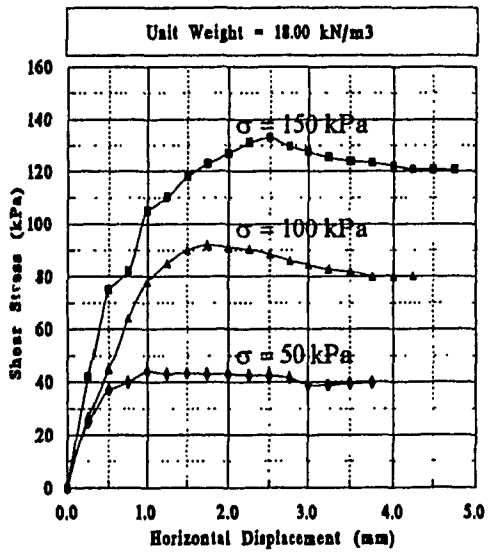
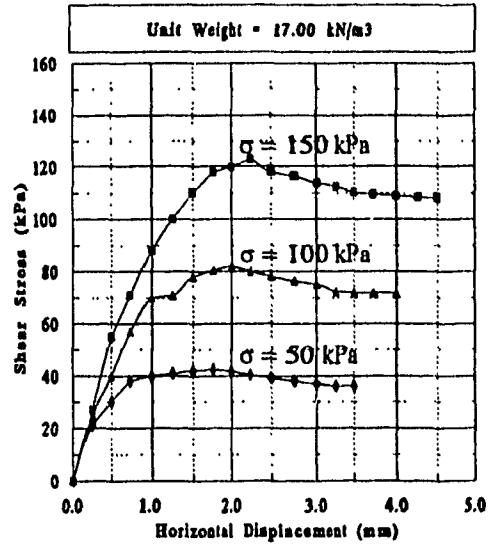
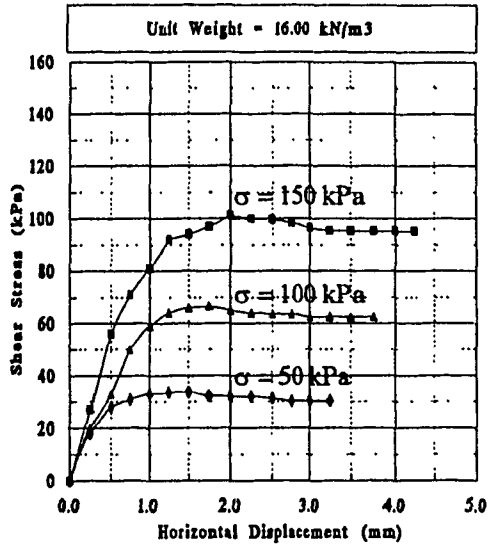


Figure 3.18 Shear Stress versus Horizontal Displacement from Direct Shear Box Tests

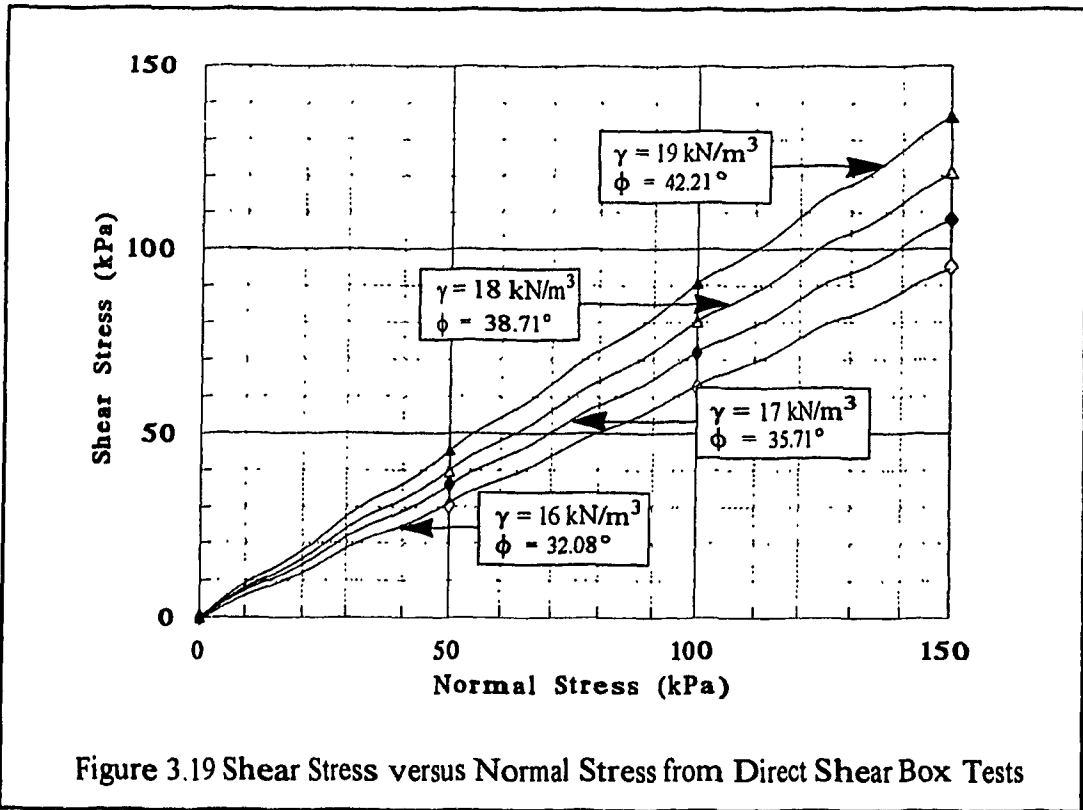


Figure 3.19 Shear Stress versus Normal Stress from Direct Shear Box Tests

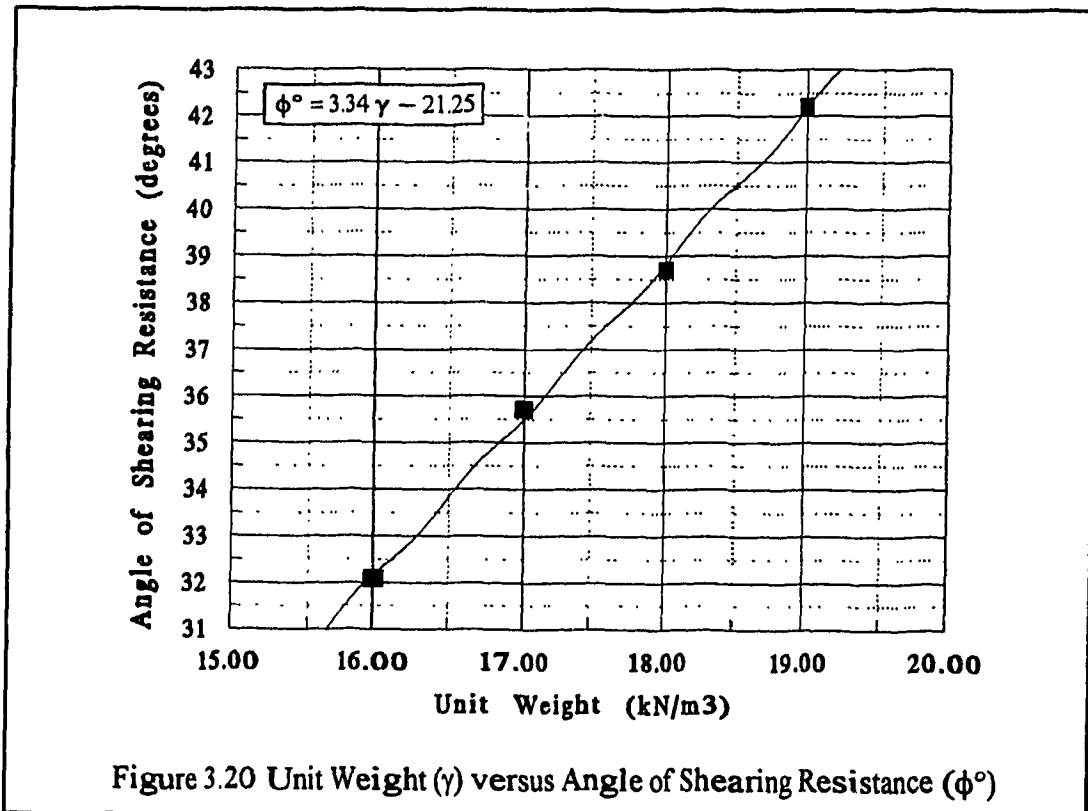


Figure 3.20 Unit Weight ( $\gamma$ ) versus Angle of Shearing Resistance ( $\phi^\circ$ )

Table 3.3 Physical and Mechanical Characteristics of Sand in Plexiglas Tank

Sand State	Unit Weight $\gamma$ kN/m <sup>3</sup>	Angle of Shearing Resistance $\phi^\circ$	Relative Density $D_r\%$
Loose	16.41	33.56	19.57
Medium	17.55	37.37	53.66
Dense	18.43	40.31	77.09

Table 3.4 Physical and Mechanical Characteristics of Sand in Steel Tank

Sand State	Unit Weight $\gamma$ kN/m <sup>3</sup>	Angle of Shearing Resistance $\phi^\circ$	Relative Density $D_r\%$
Loose	16.50	33.86	22.44
Medium	17.66	37.73	56.72
Dense	18.52	40.61	79.36

### 3.6 Embedment Depth

In order to study the effect of embedment on the geotechnical behavior of the foundation models, two embedment ratios (depth/width) were used in the present investigation namely, surface models, i.e., at  $D/B = 0$ , and embedded models at  $D/B = 0.75$ .

### 3.7 Experimental Test Procedure

The sand mixture was prepared to the prescribed gradation and pumped up by a vacuum machine to the sand reservoir, located above the testing tank, see Plate 3.13. The sand was poured into the tank through a funnel assembly, see Plate 3.14, which was moved by hand in a consistent way over the testing tank to achieve a uniform sand distribution. When the sand surface reached the top of first layer (160 mm), the compaction was then applied using the air pressure hammer, see Plate 3.15. The air pressure was set constant and the compaction duration was applied according to the required sand state. Spreading and compaction process were repeated for other sand layers until the foundation level was reached.

For the surface loading tests, i.e., at  $D/B=0$ , the flat model was placed at the center of the testing tank then the load application started. In order to prepare the soil core under the shell surface for axisymmetrical and three dimensional models, the shell model was filled with a specified calculated volume of sand according to the desired sand state in order to achieve the requisite unit weight.

Plate 3.16 shows the sand filling process of a shell model. A thin steel plate was then placed on the top of the shell model and transferred to its location at the center of the tank, see Plate 3.18. Finally, the steel plate was removed from underneath the shell and good care was taken to insure full contact between the sand and the shell surface. In addition, the top part of the shell model was removed and some extra sand was added to compensate for what might be lost during the removal process of the steel plate.

For the triangular shell strip models, the sand was poured through three holes located at the top portion of the model and by looking through the sides of the plexiglas tank, the full contact between the sand and shell surface was easily verified.

For embedded loading tests, i.e., at  $D/B = 0.75$ , the sand spreading continued until the upper surface of sand was reached and then the compaction was applied carefully at the top surface outside the area of the foundation model.

After the testing tank was prepared, the Data Acquisition System was initialized and a checking stage for all electrical devices was performed to check the existence of any wire disconnection. When the checking stage was completed, then the load application stage started. Vertical load, settlement, contact pressures, and lateral and vertical stresses within the soil mass were automatically recorded during testing. The loading tests were continued beyond failure point, i.e., when the settlement was increasing rapidly and the load either decreased or remained almost constant. Plates 3.18 and 3.19 show the circular foundation model at the beginning of a loading test and during the loading process.





Plate 3.13 Sand Reservoir

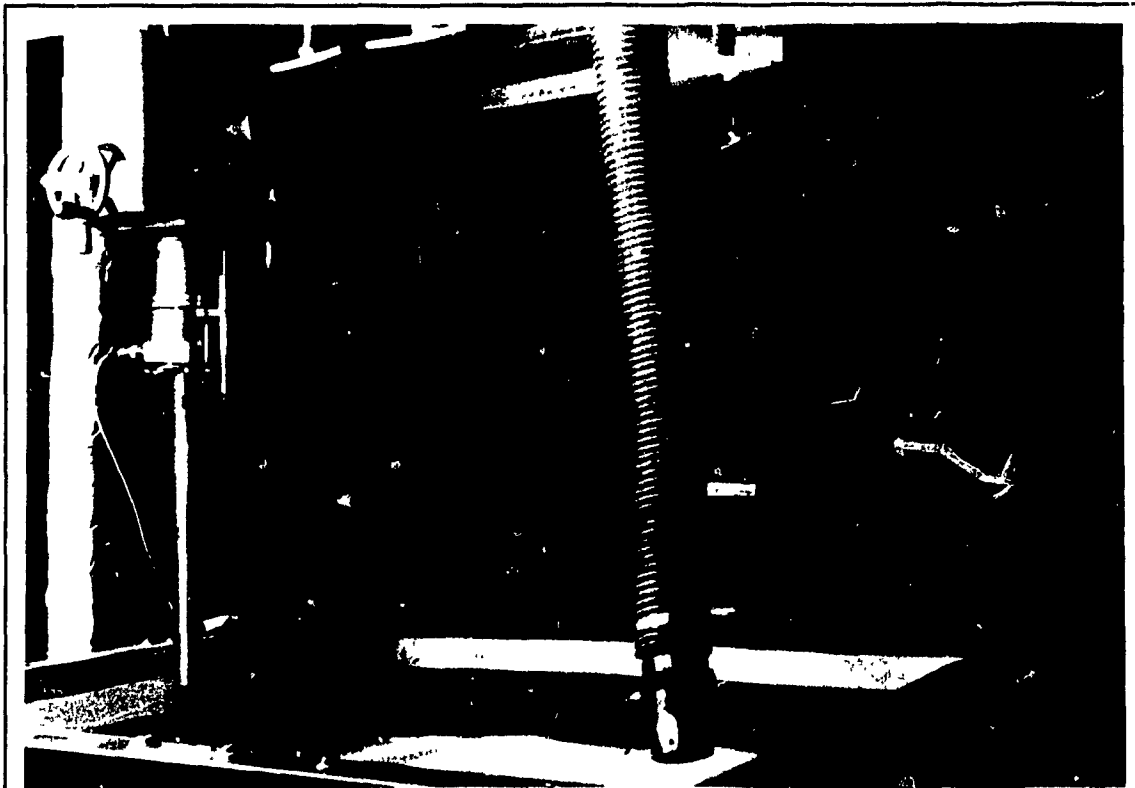


Plate 3.14 Funnel Assembly Used for Sand Spreading Technique

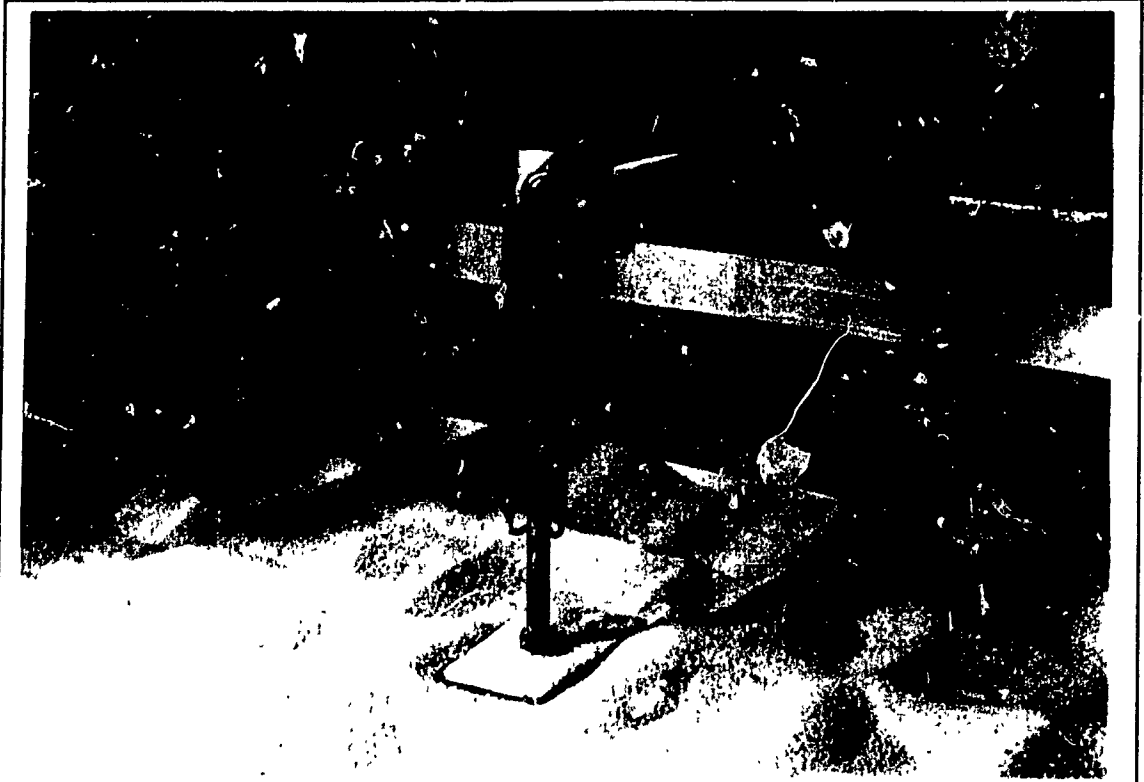


Plate 3.15 Air Pressure Compactor

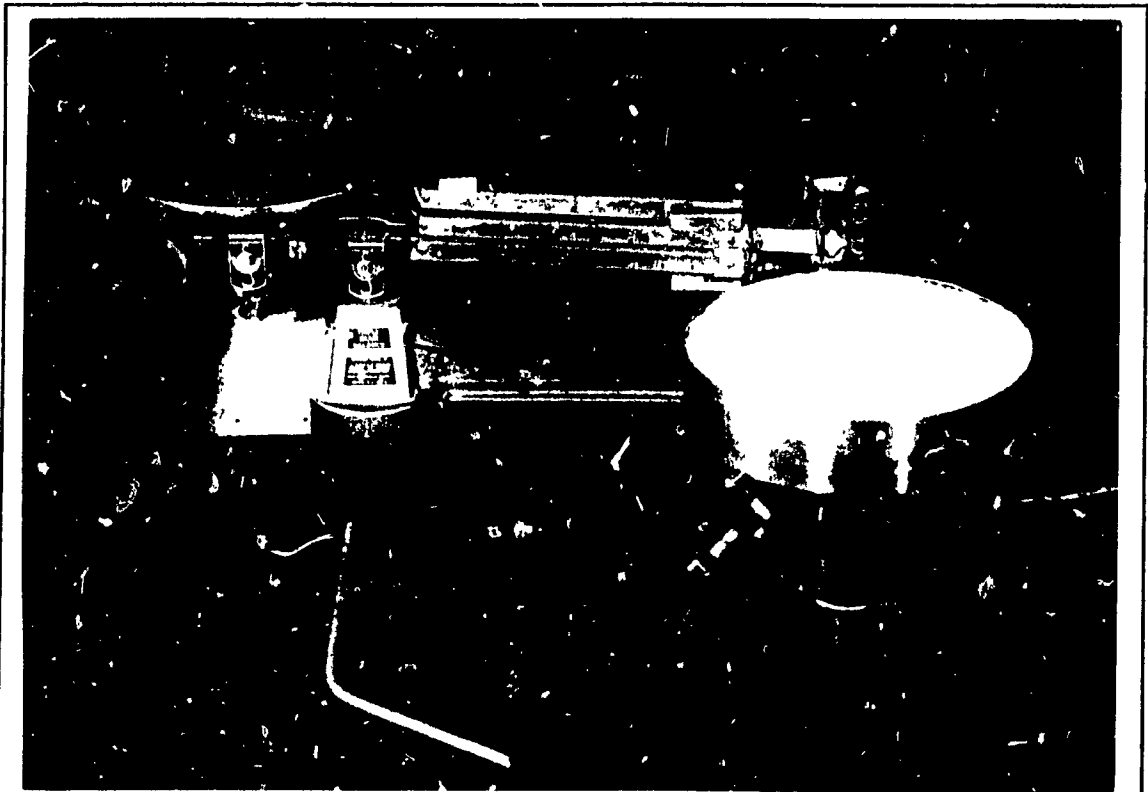


Plate 3.16 Process of Sand Filling under Shell Model

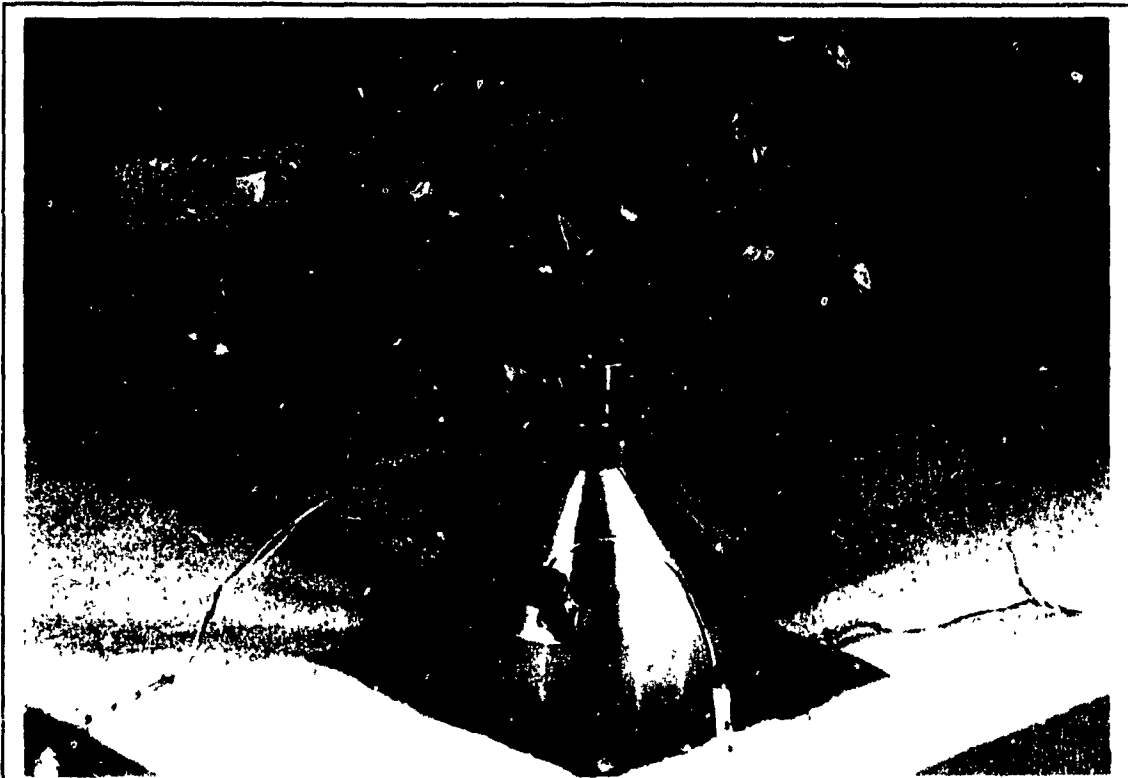


Plate 3.17 Shell Model in Place after Sand Filling Process



Plate 3.18 Circular Foundation Model before Testing

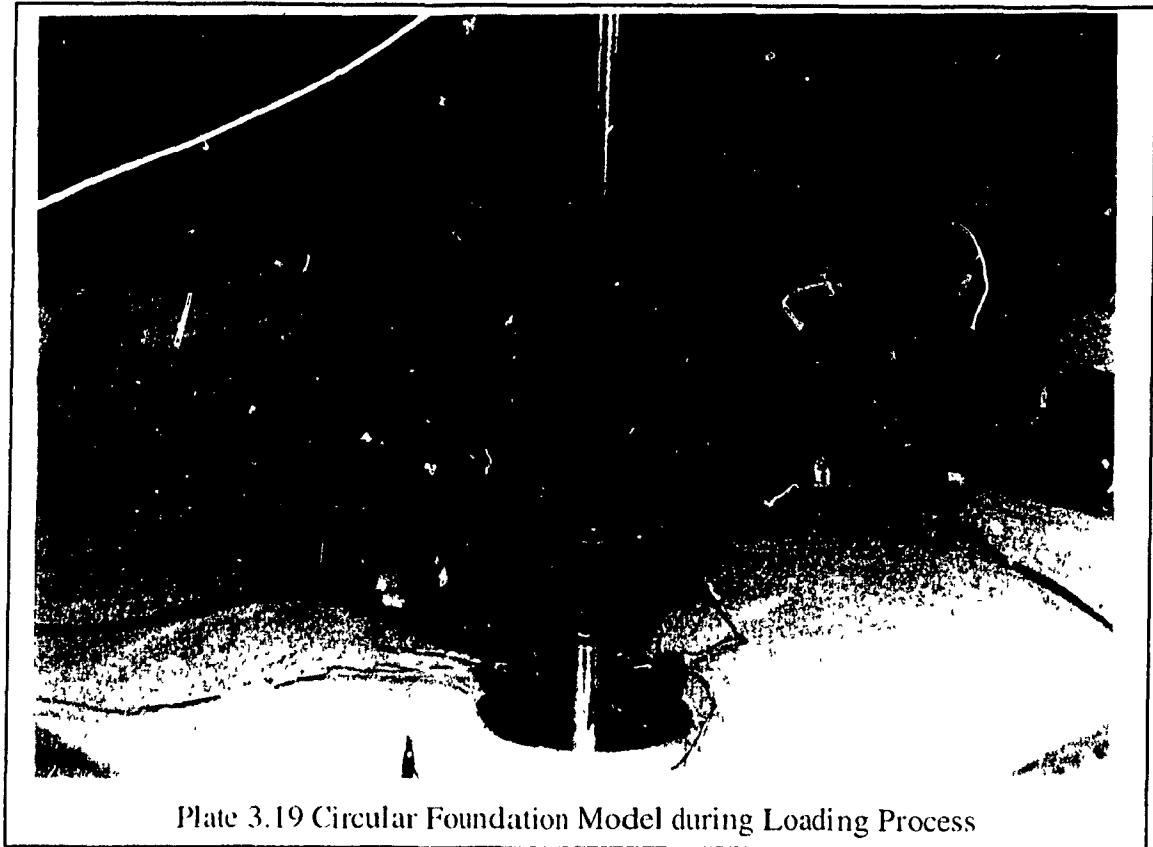


Plate 3.19 Circular Foundation Model during Loading Process

### 3.8 Experimental Tests Results

#### 3.8.1 In-Situ Stresses in Sand

The lateral earth pressure at rest ( $\sigma_o$ ) for normally consolidated soil can be calculated theoretically using the well known coefficient of lateral earth pressure at rest ( $k_o$ ) given by Jaky in 1944 as follows:

$$\sigma_o = \sigma_z k_{o(nc)} \quad (3.1)$$

where:

$$\sigma_z = \gamma z \quad (3.2)$$

$$k_{o(nc)} = 1 - \sin(\phi) \quad (3.3)$$

In the present investigation, the vertical and lateral stresses within the sand mass were measured during and after the completion of sand placing in the steel testing tank by

means of the pressure transducers. During the compaction process of sand layers, the additional pressure resulted from the vibration of the air pressure hammer caused a remarkable increase in both the vertical and lateral stresses within the sand mass as compared to the theoretical values calculated for the sand before compaction, i.e., for normally consolidated soil. However, when compaction process terminated, the vertical stresses gradually decreased until they reached values slightly above the overburden pressure ( $\sigma_z$ ) and lateral stresses also decreased but they remained relatively higher than ( $\sigma_o$ ). Based on this, it can be deduced that compaction process leads to produce overconsolidated sand.

The measured coefficient of lateral earth pressure at rest of an overconsolidated sand layer ( $k_{om}$ ) was calculated as the ratio between the lateral stress ( $\sigma_{lm}$ ) and the vertical stress ( $\sigma_{vm}$ ) measured at a given depth of embedment immediately after placing and compacting the sand layer. The overconsolidated ratio (OCR) of the sand depends on the applied compaction effort and on the depth of embedment. The values of (OCR) at different sand layers were calculated using the relationship given by Wroth in 1974, which is as follows:

$$k_{o(oc)} = k_{o(nc)} OCR - \left( \frac{v}{1-v} \right) (OCR - 1) \quad (3.4)$$

where:  $k_{o(oc)}$  is coefficient of lateral earth pressure for overconsolidated soil;

$k_{o(nc)}$  is coefficient of lateral earth pressure for normally consolidated soil;

OCR is overconsolidation ratio; and  $v$  is Poisson's ratio.

This expression was employed in a reverse way in order to determine the value of the overconsolidation ratio (OCR). Since ( $k_{o(nc)}$ ) can be calculated from the theoretical relationship given by Jaky and ( $k_{o(oc)}$ ) in equation 3.4 is the one measured from the experiment, Wroth's expression can be applied as follows:

$$OCR = \frac{\left(k_{o(oc)} - \left(\frac{v}{1-v}\right)\right)}{\left(k_{o(nc)} - \left(\frac{v}{1-v}\right)\right)} \quad (3.5)$$

The value of ( $v$ ) usually has a relatively small effect on the calculated (OCR). Nevertheless, proper values for Poisson's ratio for different sand states were adopted from the literature (Harr 1966) as 0.25, 0.20, and 0.15 for loose, medium, and dense states, respectively. The experimental results and the calculated values of (OCR) for loose, medium, and dense sand in the steel tank are reported in Tables 3.5 through 3.7.

From the data shown in these tables, it can be observed that for a given sand state the (OCR) increases as the soil depth increases. Moreover, for a given depth of embedment, the (OCR) increases with the increase of compaction effort. The comparison between the theoretical values of ( $k_{o(nc)}$ ) and the measured values of ( $k_{o(oc)}$ ) indicates that there was a relative increase in the magnitude of lateral stresses due to the compaction process. This increase becomes greater as the depth of embedment increases due to the increase in the (OCR), i.e., the sand was slightly overconsolidated.

This can be explained in terms of the applied compaction effort induced in each layer of sand. A lower layer was subjected to a higher compaction effort than a higher one. Furthermore, greater residual stresses were locked-in at the lower sand layers due to the reflection of vibration from the side walls of the steel testing tank. This can also explain the increase of (OCR) as the depth of embedment of sand increases, contrary to what is usually observed in natural soils.

Figure 3.21 shows the measured vertical and lateral stresses with respect to the theoretical values for normally consolidated sand. Figure 3.22 shows the distribution of ( $k_{om}$ ) and (OCR) for the three sand states inside the steel testing tank.

Table 3.5 Compaction Results for Loose Sand ( $\phi = 33.86^\circ$ ) in Steel Tank

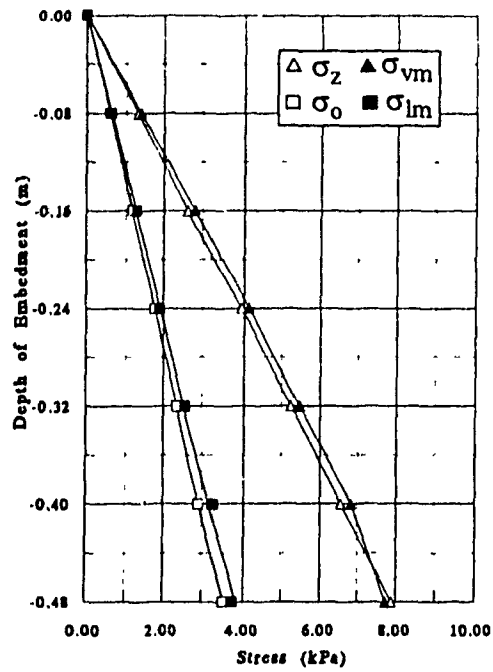
Depth (m)	$\sigma_{vm}$ (kPa)	$\sigma_{lm}$ (kPa)	$k_{o(oc)}$	OCR
0.08	1.39	0.62	0.446	1.03
0.16	2.82	1.28	0.454	1.10
0.24	4.12	1.90	0.461	1.17
0.32	5.46	2.58	0.473	1.28
0.40	6.82	3.27	0.479	1.33
0.48	7.72	3.72	0.482	1.36

Table 3.6 Compaction Results for Medium Sand ( $\phi = 37.73^\circ$ ) in Steel Tank

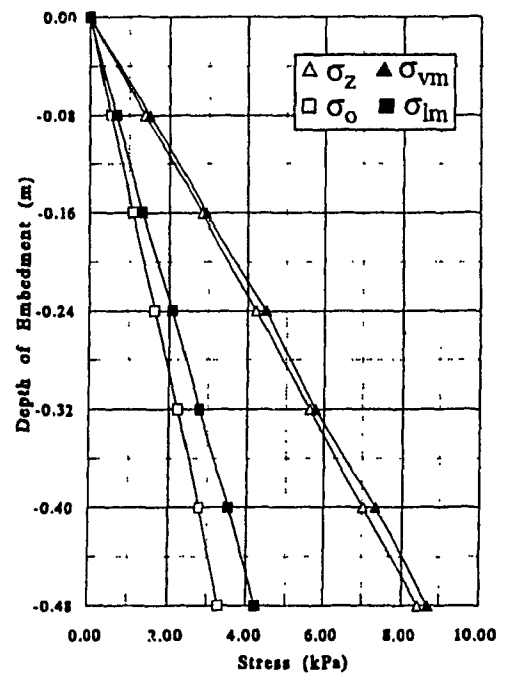
Depth (m)	$\sigma_{vm}$ (kPa)	$\sigma_{lm}$ (kPa)	$k_{o(oc)}$	OCR
0.08	1.52	0.68	0.447	1.38
0.16	2.93	1.34	0.457	1.45
0.24	4.46	2.08	0.466	1.51
0.32	5.78	2.76	0.478	1.59
0.40	7.34	3.55	0.484	1.63
0.48	8.69	4.22	0.486	1.65

Table 3.7 Compaction Results for Dense Sand ( $\phi = 40.61^\circ$ ) in Steel Tank

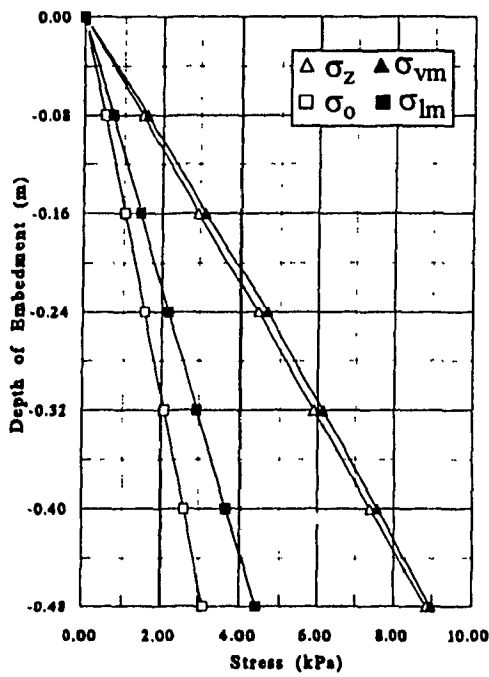
Depth (m)	$\sigma_{vm}$ (kPa)	$\sigma_{lm}$ (kPa)	$k_{o(oc)}$	OCR
0.08	1.60	0.72	0.450	1.58
0.16	3.15	1.45	0.460	1.64
0.24	4.66	2.18	0.468	1.69
0.32	6.13	2.95	0.481	1.76
0.40	7.56	3.68	0.487	1.80
0.48	8.96	4.39	0.490	1.82



a) Loose Sand ( $\phi = 33.86^\circ$ )



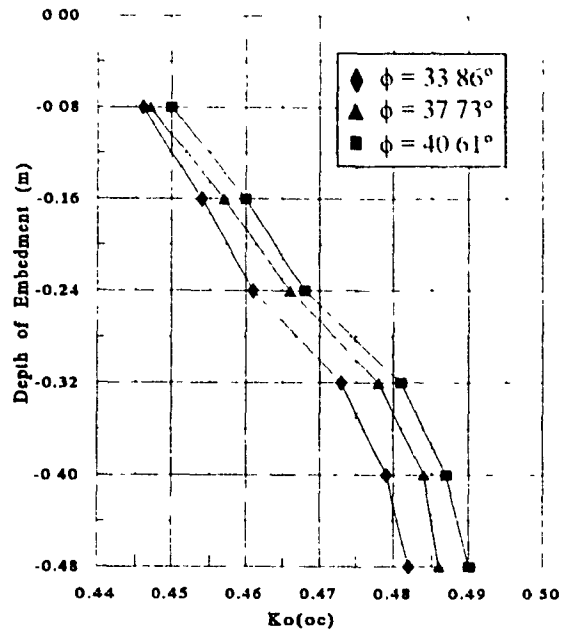
b) Medium Sand ( $\phi = 37.73^\circ$ )



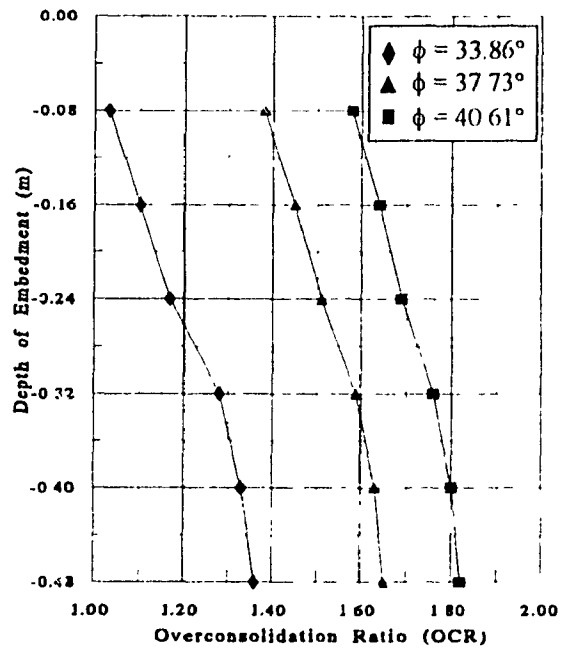
c) Dense Sand ( $\phi = 40.61^\circ$ )

Figure 3.21 Lateral and Vertical Stresses after Sand Placing in The Steel Tank





a) Distribution of  $K_{o(oc)}$



a) Distribution of OCR

Figure 3.22 Distribution of  $K_{o(oc)}$  & OCR after Sand Placing inside Steel Tank

### 3.8.2 Load-Settlement Curves

In the present experimental investigation, the settlement of the foundation models ( $\delta$ ) and the corresponding applied load ( $Q$ ) were recorded and plotted for all loading tests. The ultimate load ( $Q_u$ ) was defined at the point of maximum load obtained from the load-settlement ( $Q$ - $\delta$ ) curve, at which the load starts to decrease while the settlement continues to increase.

The values of the ultimate load ( $Q_u$ ) and the corresponding settlement ( $\delta_u$ ) were determined from the experimental tests results and presented in Tables 3.8, 3.9, and 3.10 for the plane strain, axisymmetrical, and the three dimensional conditions, respectively. The load-settlement curves for the tests are presented in Figures 3.23 through 3.31.

Table 3.8 Ultimate Load ( $Q_u$ ) & Settlement ( $\delta_u$ ) for Plane Strain Condition

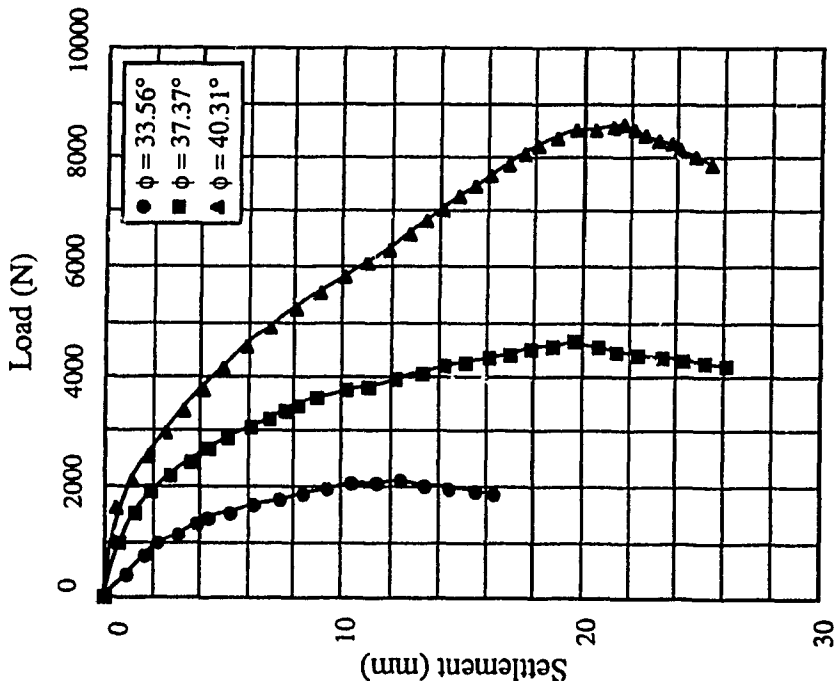
Footing	$\phi^\circ$	Surface Footings (D/B= 0)		Embedded Footings (D/B= 0.75)	
		$Q_u$ (N)	$\delta_u$ (mm)	$Q_u$ (N)	$\delta_u$ (mm)
Strip	33.56	2081	12.42	4813	17.83
	37.37	4613	19.71	9278	24.64
	40.31	8572	21.76	15875	31.44
Triang. (1)	33.56	2477	13.05	5321	16.48
	37.37	5241	17.13	10036	22.29
	40.31	9567	19.26	16880	29.86
Triang. (2)	33.56	2811	14.13	5699	16.24
	37.37	5816	18.06	10666	22.18
	40.31	10336	20.02	17837	29.48

Table 3.9 Ultimate Load ( $Q_u$ ) & Settlement ( $\delta_u$ ) for Axisymmetrical Condition

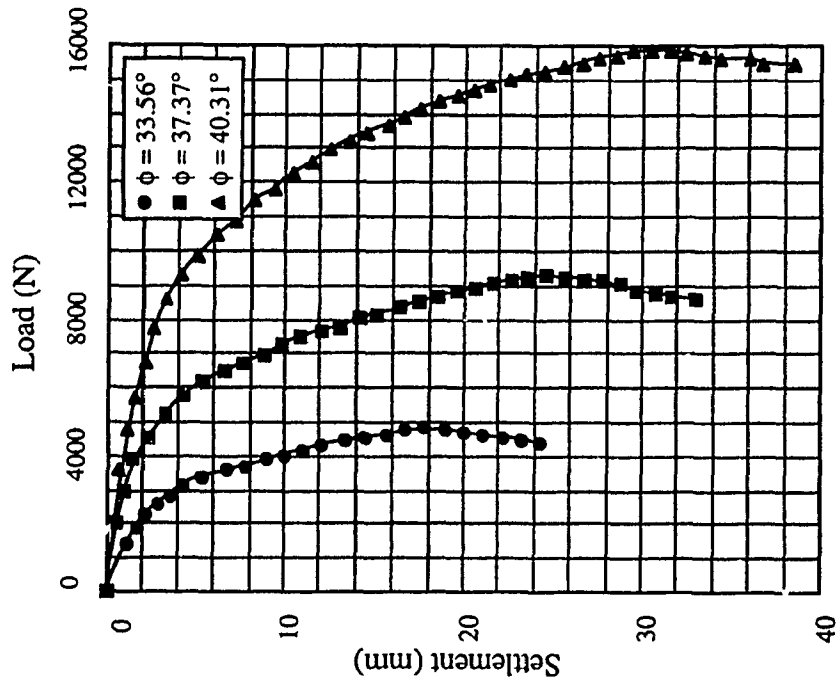
Footings	$\phi^\circ$	Surface Footings (D/B= 0)		Embedded Footings (D/B= 0.75)	
		$Q_u$ (N)	$\delta_u$ (mm)	$Q_u$ (N)	$\delta_u$ (mm)
Circular	33.86	1794	11.57	4673	17.23
	37.73	3727	17.12	8638	25.72
	40.61	6730	21.05	14557	32.61
Conical (1)	33.86	2153	11.13	5215	17.66
	37.73	4287	16.62	9444	26.16
	40.61	7730	20.45	15665	33.14
Conical (2)	33.86	2457	12.09	5619	17.41
	37.73	4816	16.74	10122	25.39
	40.61	8414	20.78	16731	33.54

Table 3.10 Ultimate Load ( $Q_u$ ) & Settlement ( $\delta_u$ ) for Three Dimensional Condition

Footings	$\phi^\circ$	Surface Footings (D/B= 0)		Embedded Footings (D/B= 0.75)	
		$Q_u$ (N)	$\delta_u$ (mm)	$Q_u$ (N)	$\delta_u$ (mm)
Square	33.86	2370	12.07	6103	17.43
	37.73	4959	16.62	11273	26.68
	40.61	9035	22.45	19018	32.08
Pyram. (1)	33.86	2854	11.25	6790	17.19
	37.73	5686	16.04	12304	25.92
	40.61	10179	22.97	20391	30.37
Pyram. (2)	33.86	3272	11.03	7318	16.79
	37.73	6351	16.72	13173	26.15
	40.61	11111	23.86	21708	32.06

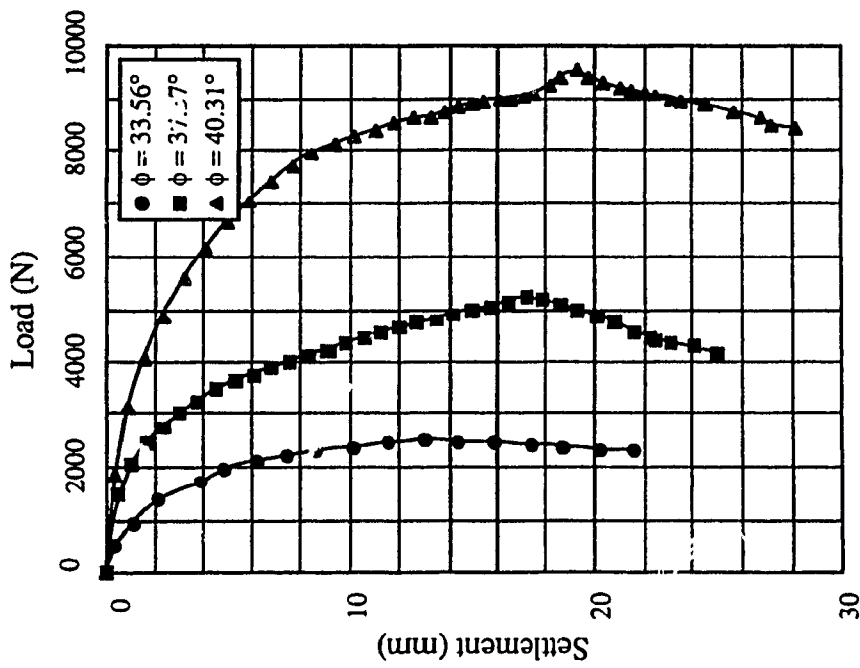


a) Surface Footing

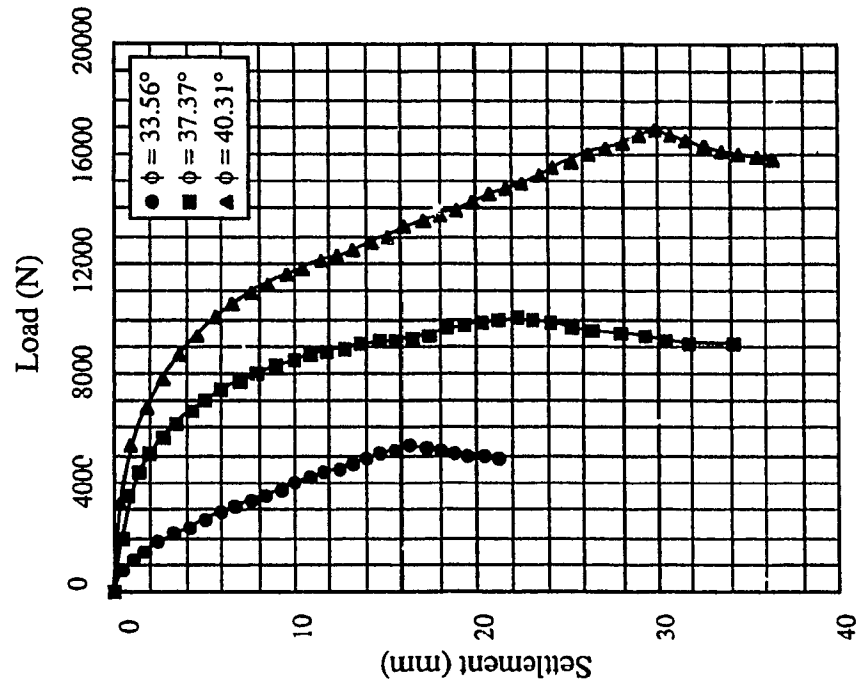


b) Embedded Footing

Figure 3.23 Load-Settlement Curves for Strip Flat Footing

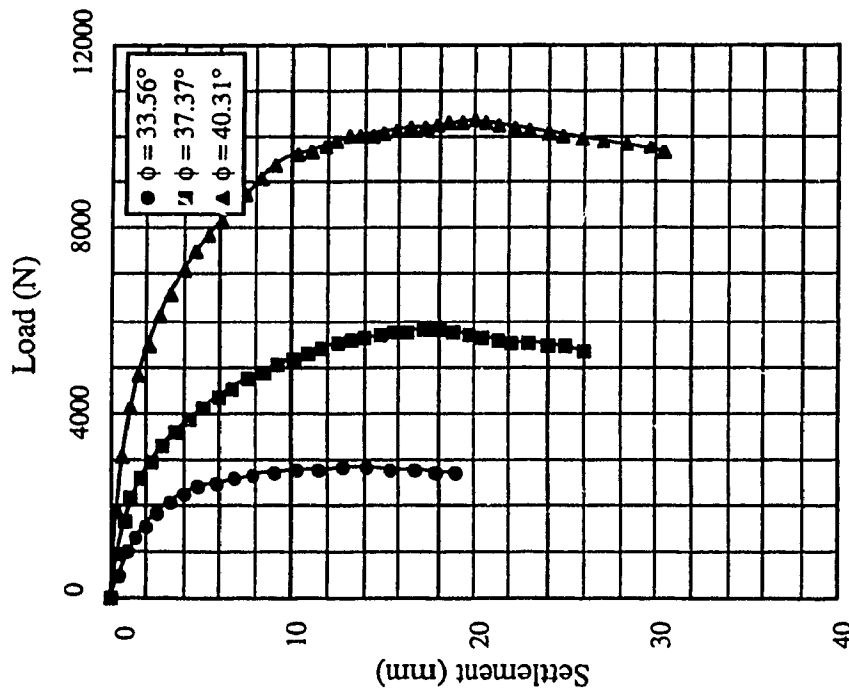


a) Surface Footing

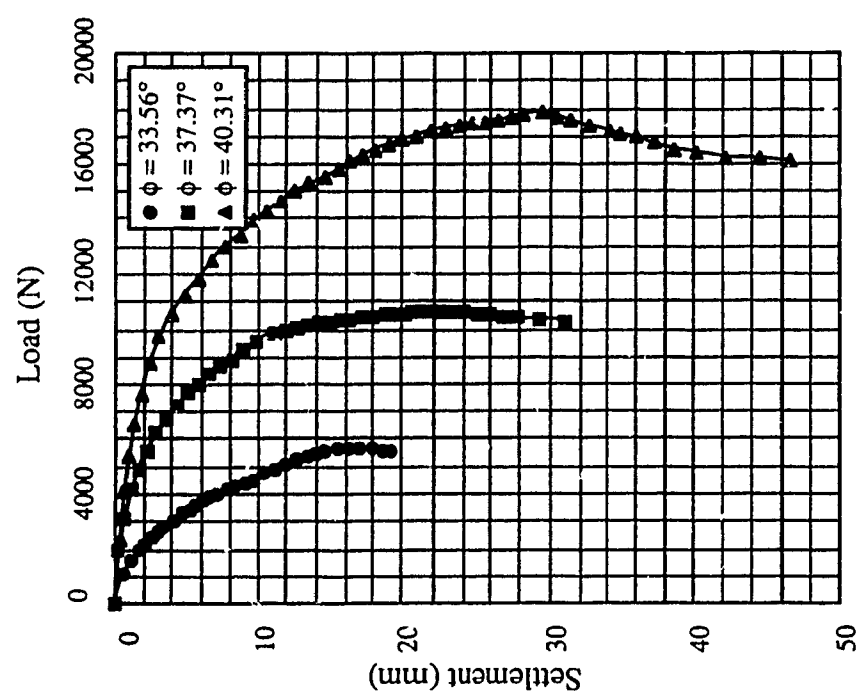


b) Embedded Footing

Figure 3.24 Load-Settlement Curves for Triangular (1) Shell Footing

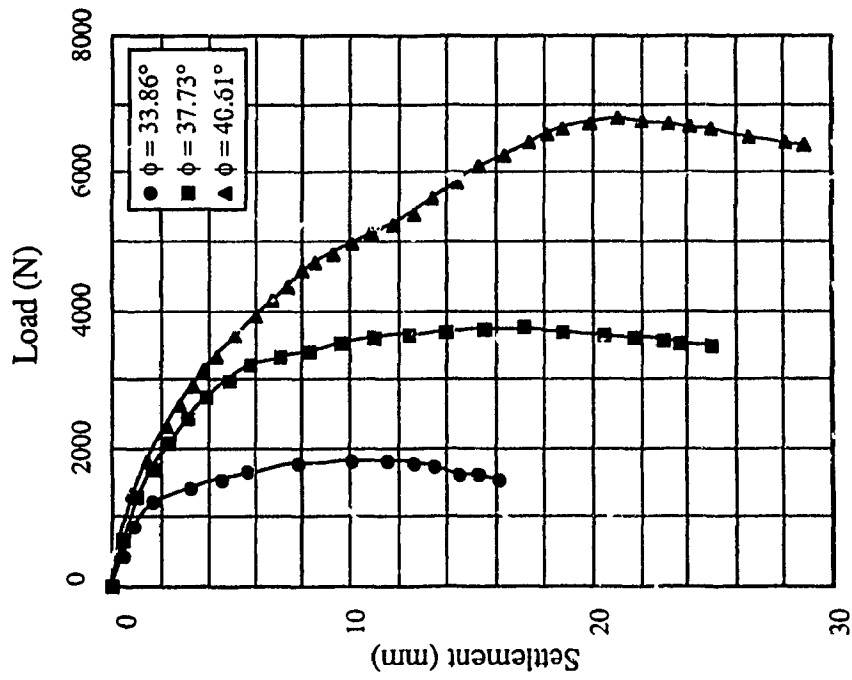


a) Surface Footing

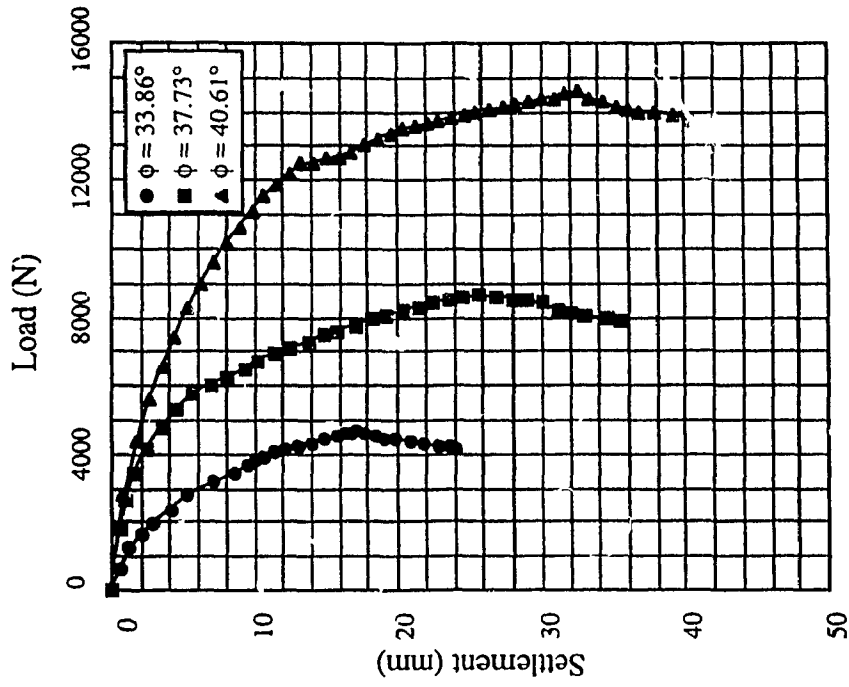


b) Embedded Footing

Figure 3.25 Load-Settlement Curves for Triangular (2) Shell Footing

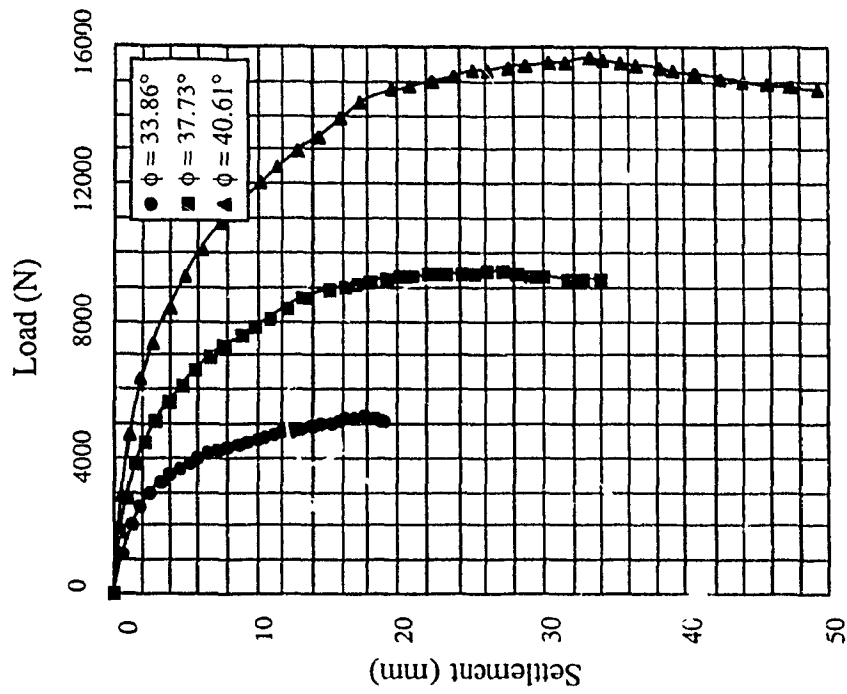


a) Surface Footing

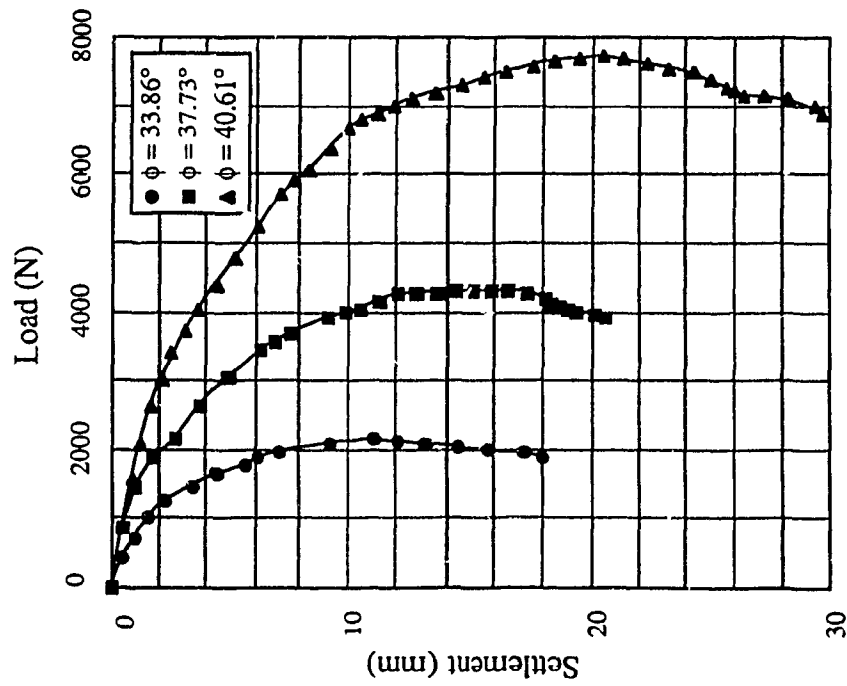


b) Embedded Footing

Figure 3.26 Load-Settlement Curves for Circular Flat Footing



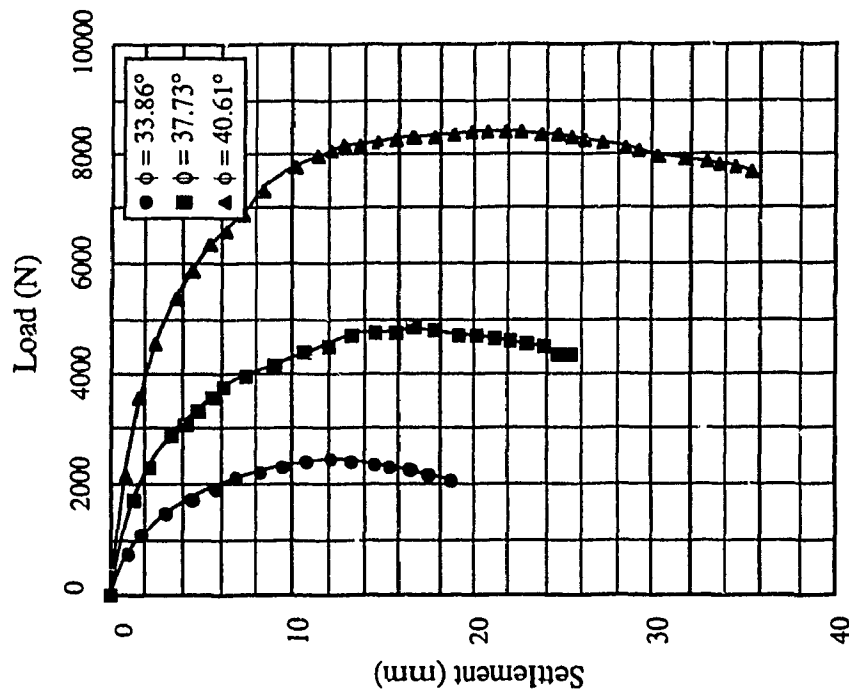
b) Embedded Footing



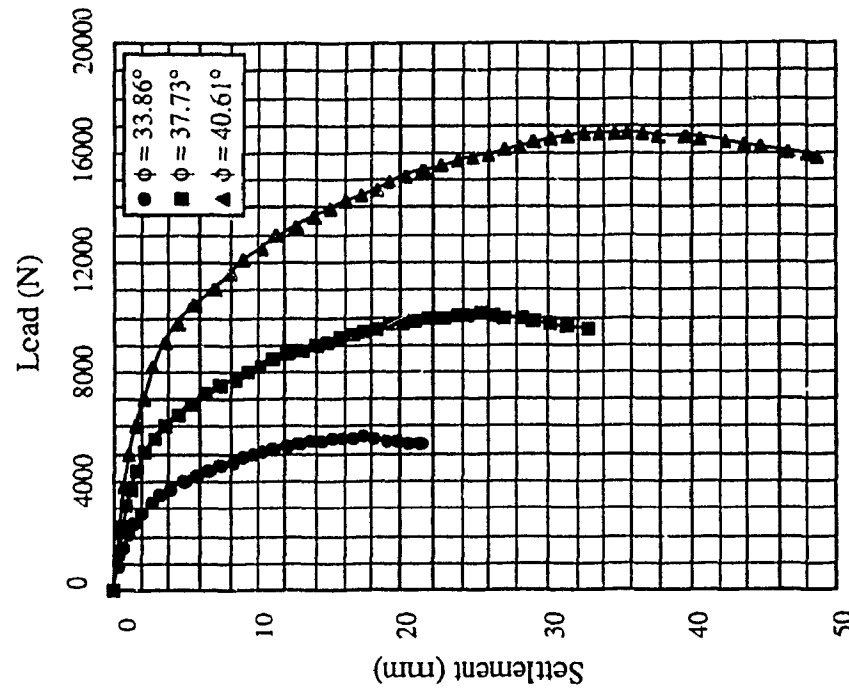
a) Surface Footing

Figure 3.27 Load-Settlement Curves for Conical (1) Shell Footing



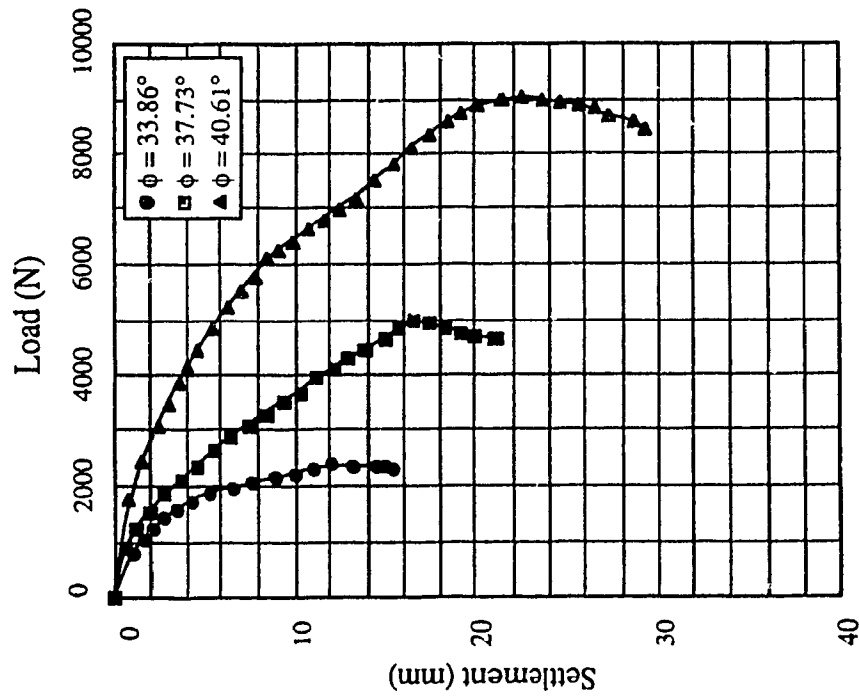


a) Surface Footing

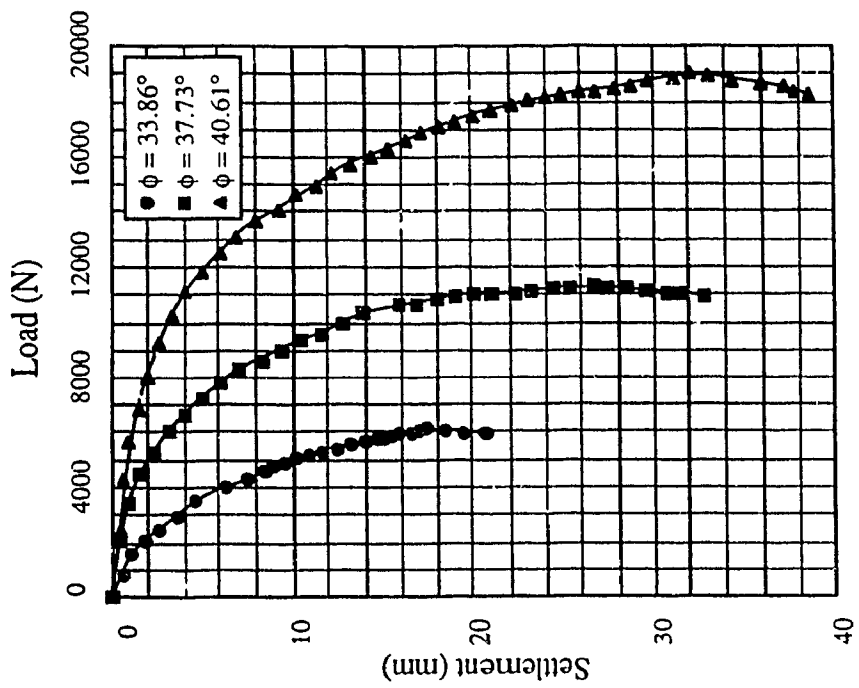


b) Embedded Footing

Figure 3.28 Load-Settlement Curves for Conical (2) Shell Footing

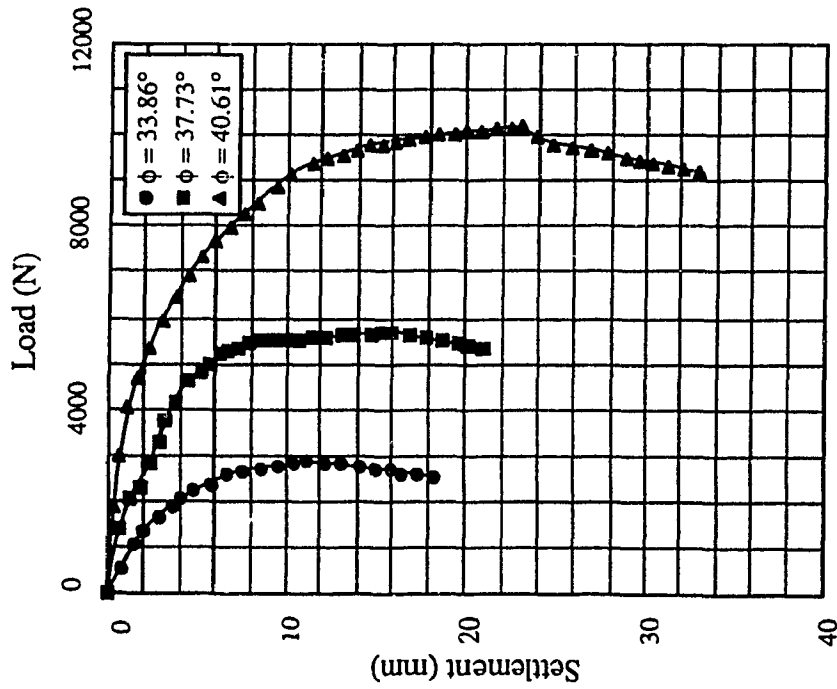


a) Surface Footing

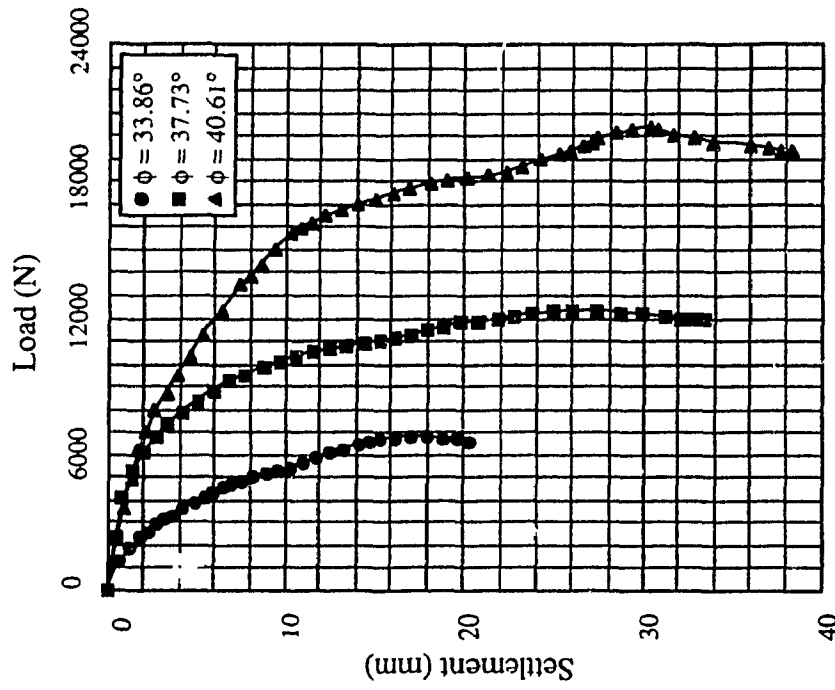


b) Embedded Footing

Figure 3.29 Load-Settlement Curves for Square Flat Footing

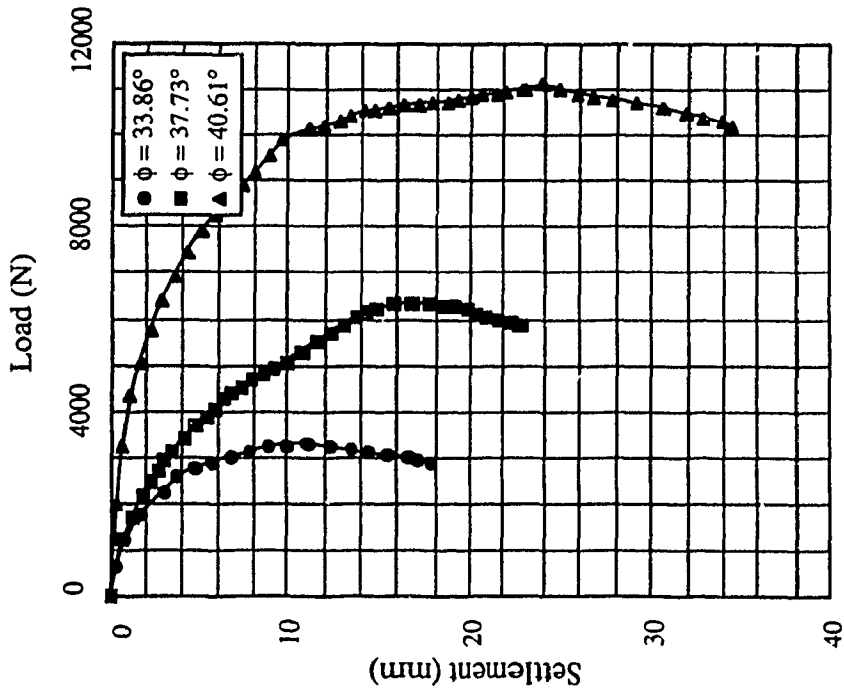


a) Surface Footing

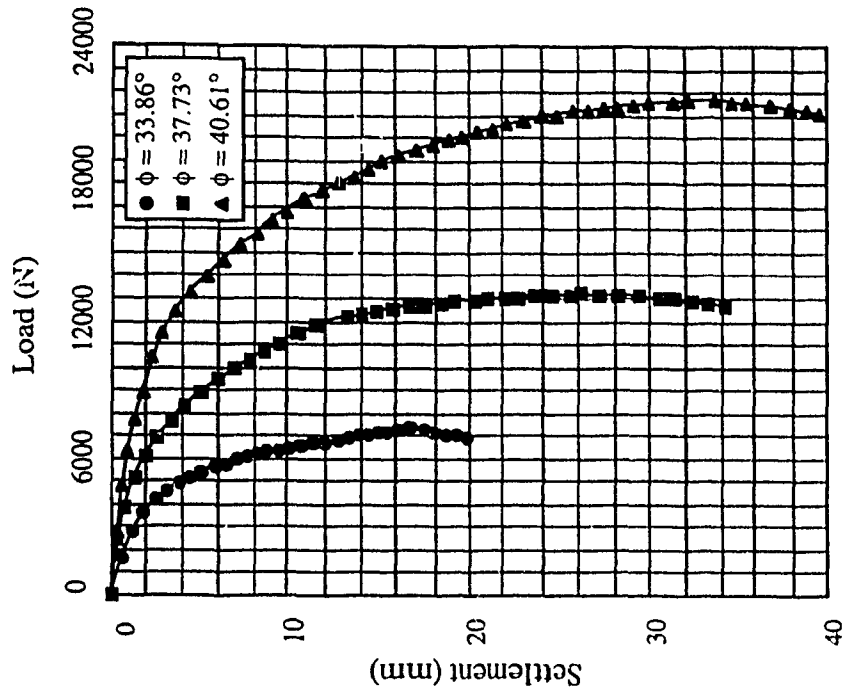


b) Embedded Footing

Figure 3.30 Load-Settlement Curves for Pyramidal (1) Shell Footing



a) Surface Footing



b) Embedded Footing

Figure 3.31 Load-Settlement Curves for Pyramidal (2) Shell Footing

The load-settlement data are summarized and presented in figures 3.32, 3.33, and 3.34 as curves of the ultimate load ( $Q_u$ ) versus the angle of shearing resistance ( $\phi$ ) for the plane strain, axisymmetrical, and three dimensional conditions, respectively. It can be observed from these curves that the ultimate load ( $Q_u$ ) increases with the increase in the angle of shearing resistance ( $\phi$ ). Also, it can be seen that shell footings have higher ultimate loads than conventional flat ones. The ultimate load ( $Q_u$ ) increases as the depth of embedment increases for flat as well as shell footings. The relationship between the ultimate load ( $Q_u$ ) and the angle of shearing resistance ( $\phi$ ) has similar trend for the three prescribed conditions.

The increase in the ultimate load of a shell footing as compared to its flat counterpart is recognized in the present study as the shell efficiency factor ( $\eta$ ). It is defined as given in equation (3.6) as the ratio between the difference in ultimate loads of shell and flat footings over the ultimate load of the flat footing.

$$\eta = \frac{Q_{us} - Q_{uf}}{Q_{uf}} \quad (3.6)$$

Where:  $\eta$  : shell efficiency factor;  
 $Q_{us}$  : ultimate load of shell footing;  
 $Q_{uf}$  : ultimate load of flat footing.

Table 3.11 presents the calculated shell efficiency factors ( $\eta$ ) deduced in the present experimental investigation. In general, it can be concluded from Table 3.11 that shell efficiency factor ( $\eta$ ) decreases with the increase in the angle of shearing resistance ( $\phi$ ), i.e., the effect of shell configuration diminishes when the soil becomes denser. Moreover, the shell efficiency factor ( $\eta$ ) reduces remarkably for the tests conducted on the embedded footings as compared with the surface ones. This trend holds true for all the shell footings at any sand state. Also, it can be noticed that the shell efficiency factor ( $\eta$ ) for the conical and pyramidal footings are higher than that of the triangular ones. The comparison between

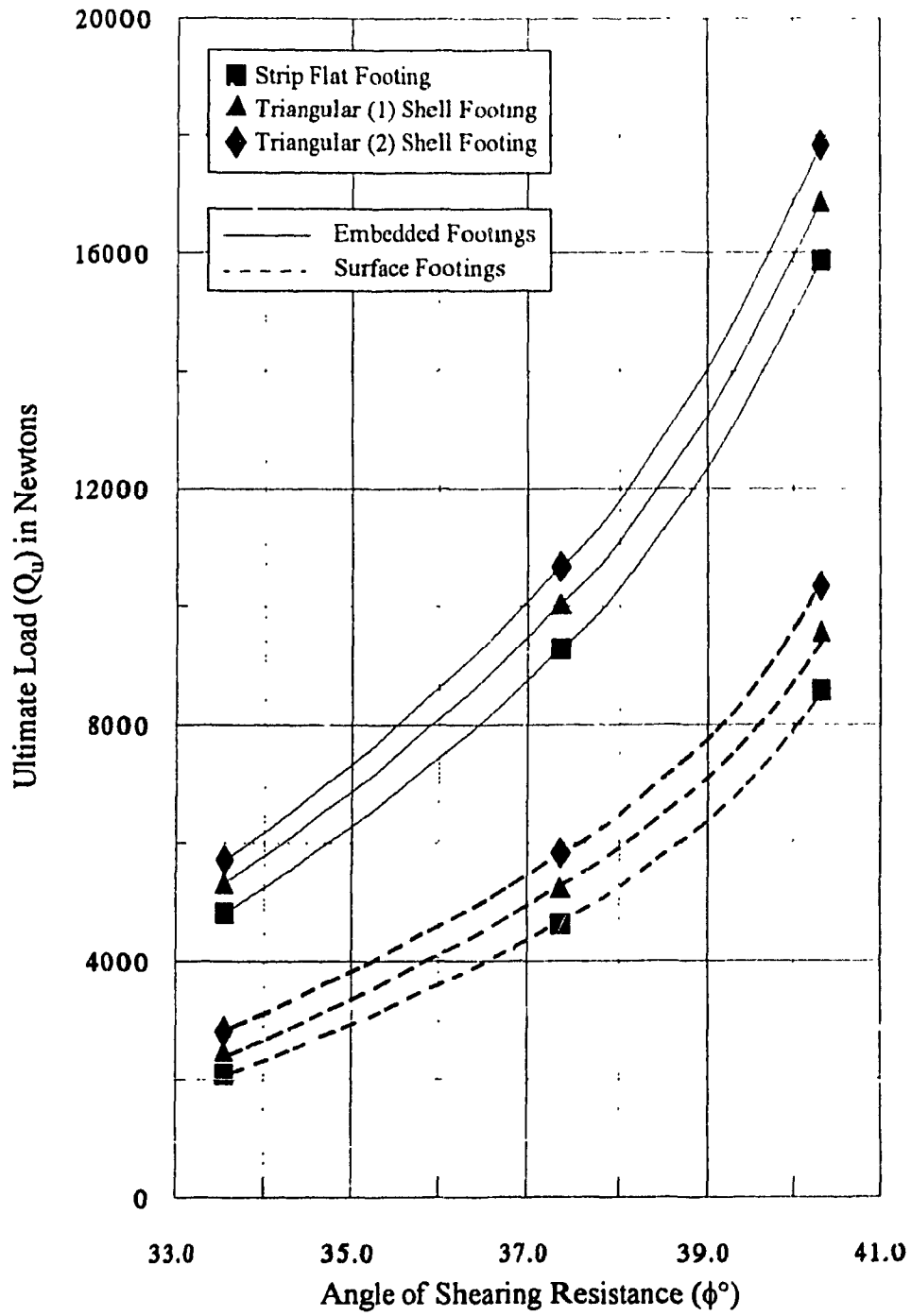


Figure 3.32 Ultimate Loads ( $Q_u$ ) for Plane Strain Condition

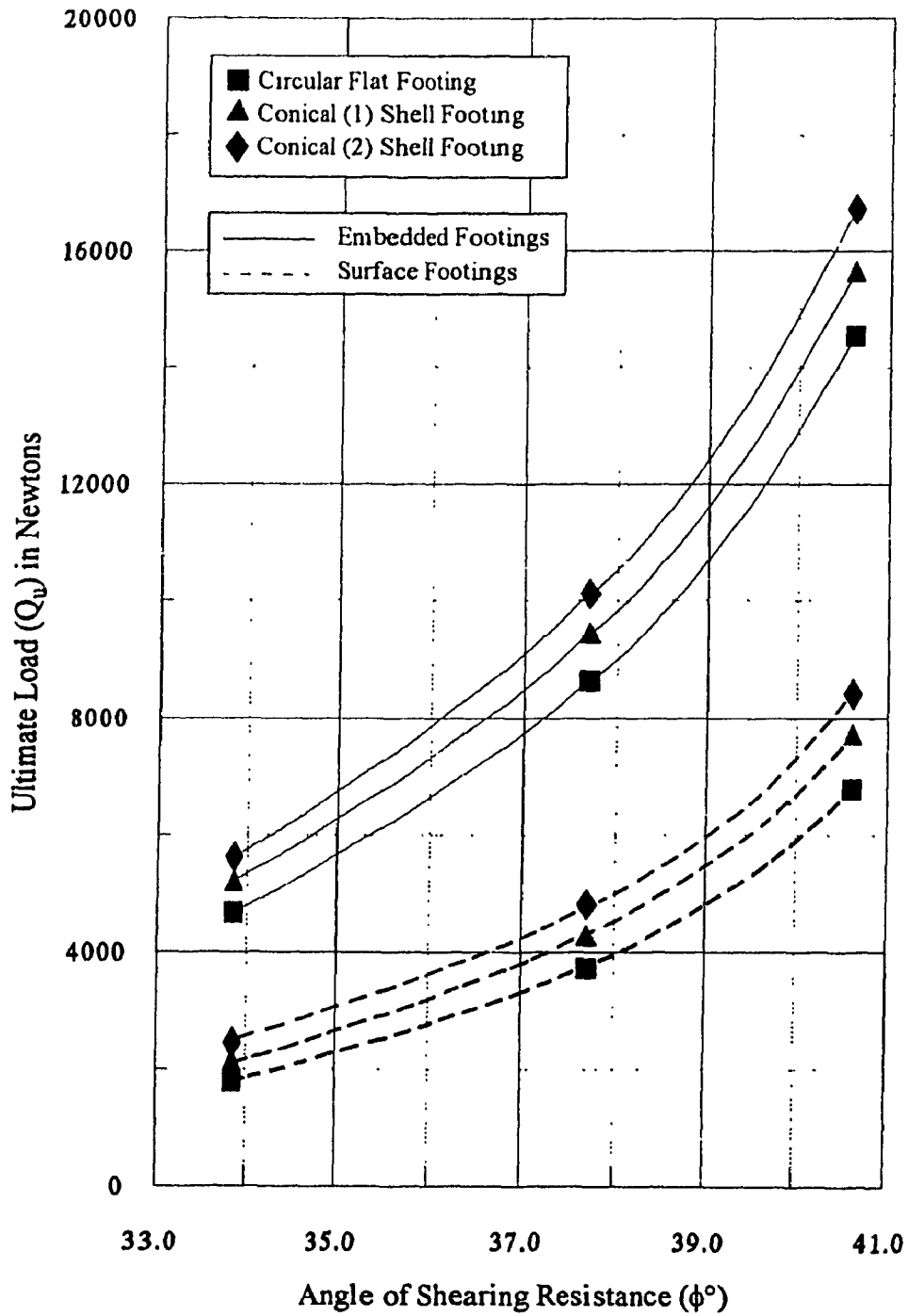


Figure 3.33 Ultimate Loads ( $Q_u$ ) for Axisymmetrical Condition

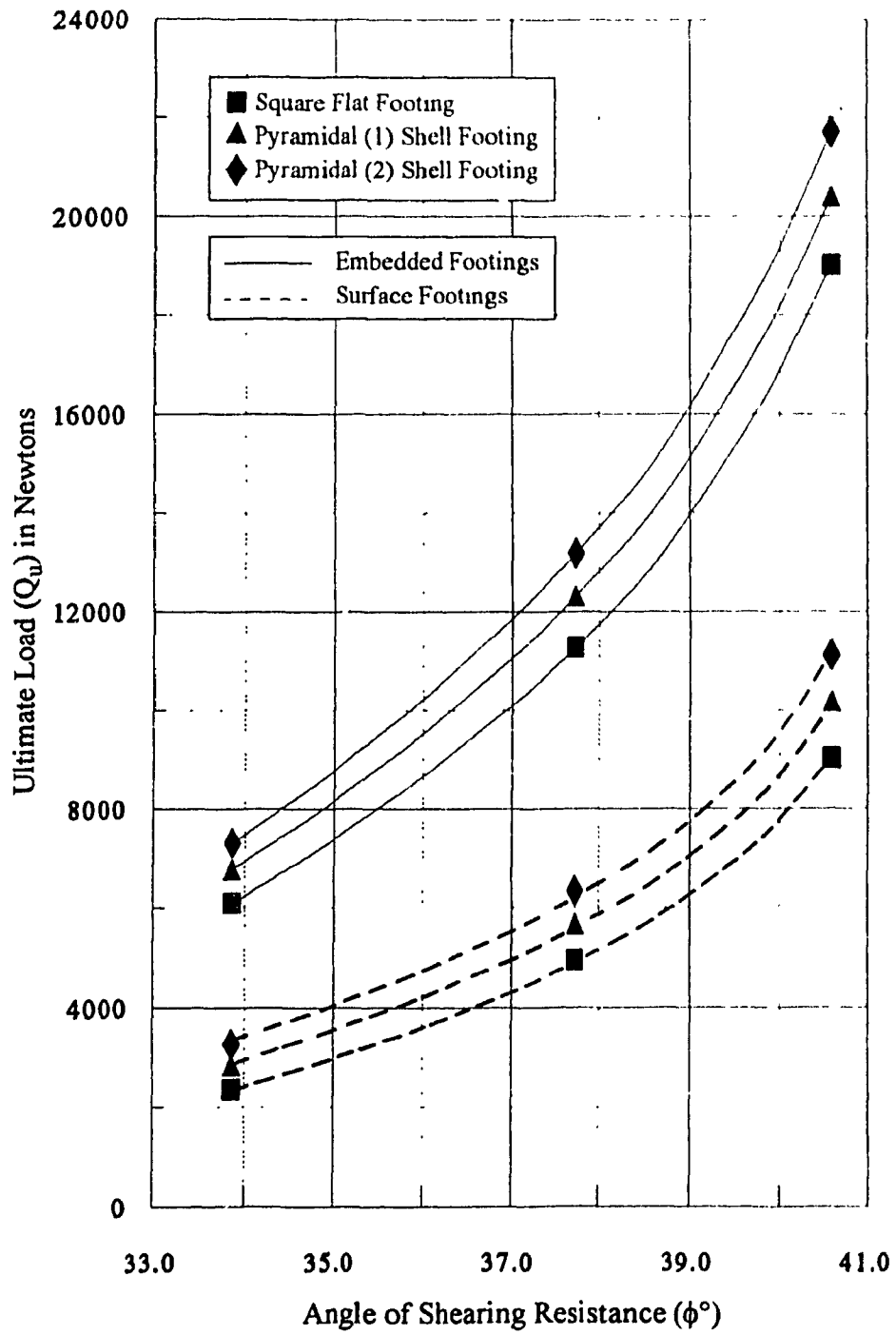


Figure 3.34 Ultimate Loads ( $Q_u$ ) for Three Dimensional Condition



the conical and pyramidal footings shows that the factors ( $\eta$ ) for the conical footings are slightly higher than that of the pyramidal ones for all tests except the ones conducted on the surface shell footings on loose sand.

In order to examine the settlement characteristics of the shell footings versus that of the conventional flat counterparts, a non-dimensional settlement factor ( $F_\delta$ ) was introduced. The settlement factor ( $F_\delta$ ) was calculated at the ultimate load ( $Q_u$ ) to reflect the settlement characteristics of the footings throughout the loading process. The settlement factor ( $F_\delta$ ) is presented in equation (3.7). It should be noted that a lower value of the settlement factor ( $F_\delta$ ) indicates better settlement characteristics.

$$F_\delta = \frac{\delta_u \gamma A_h}{Q_u} \quad (3.7)$$

Where:  $\delta_u$  : settlement at ultimate load;  
 $\gamma$  : soil unit weight;  
 $A_h$  : area of footing in horizontal projection;  
 $Q_u$  : ultimate load.

The calculated settlement factors ( $F_\delta$ ) deduced from the present experimental investigation are given in Table 3.12. In general, for any footing, the settlement factor ( $F_\delta$ ) decreases for denser sand. The comparison between the surface and embedded footings shows that the settlement factor ( $F_\delta$ ) decreases remarkably for the embedded footings specially for loose sand. The comparison between shell and flat footings for any a given sand state indicates that the shell footings possess lower settlement factor ( $F_\delta$ ) which demonstrates better settlement characteristics for shell footings. The relationships between the settlement factor ( $F_\delta$ ) and the angle of shearing resistance ( $\phi$ ) are presented in Figures 3.35, 3.36, and 3.37 for the plane strain, axisymmetrical, and three dimensional conditions, respectively.

Table 3.11 Shell Efficiency Factor ( $\eta$ )%

	surface Footings (D/B= 0)			Embedded Footings (D/B= 0.75)		
Plane Strain	Angle of Shearing Resistance ( $\phi^\circ$ )					
	33.56	37.37	40.31	33.56	37.37	40.31
Triangular (1)	19.03	13.61	11.61	10.55	8.17	6.33
Triangular (2)	35.08	26.08	20.58	18.41	14.96	12.36
Axisymm. & 3 Dimensional	Angle of Shearing Resistance ( $\phi^\circ$ )					
	33.86	37.73	40.61	33.86	37.73	40.61
Conical (1)	20.01	15.03	14.01	11.60	9.33	7.61
Conical (2)	36.96	29.22	24.10	20.24	17.18	14.93
Pyramidal (1)	20.42	14.66	12.66	11.26	9.15	7.22
Pyramidal (2)	38.06	28.07	22.98	19.91	16.85	14.14

Table 3.12 Settlement Factor ( $F_s$ ) at Ultimate Load ( $\times 10^{-3}$ )

	Surface Footings (D/B= 0)			Embedded Footings (D/B= 0.75)		
Plane Strain	Angle of Shearing Resistance ( $\phi^\circ$ )					
	33.56	37.37	40.31	33.56	37.37	40.31
Strip	2.51	1.92	1.20	1.56	1.19	0.93
Triangular (1)	2.21	1.47	0.95	1.30	1.00	0.83
Triangular (2)	2.11	1.40	0.91	1.20	0.93	0.78
Axisymm. & 3 Dimensional	Angle of Shearing Resistance ( $\phi^\circ$ )					
	33.86	37.73	40.61	33.86	37.73	40.61
Circular	2.14	1.63	1.16	1.22	1.06	0.83
Conical (1)	1.72	1.38	0.99	1.12	0.98	0.79
Conical (2)	1.63	1.23	0.92	1.03	0.89	0.75
Square	2.15	1.52	1.18	1.21	1.07	0.80
Pyramidal (1)	1.67	1.28	1.07	1.07	0.95	0.71
Pyramidal (2)	1.42	1.19	1.02	0.97	0.90	0.70

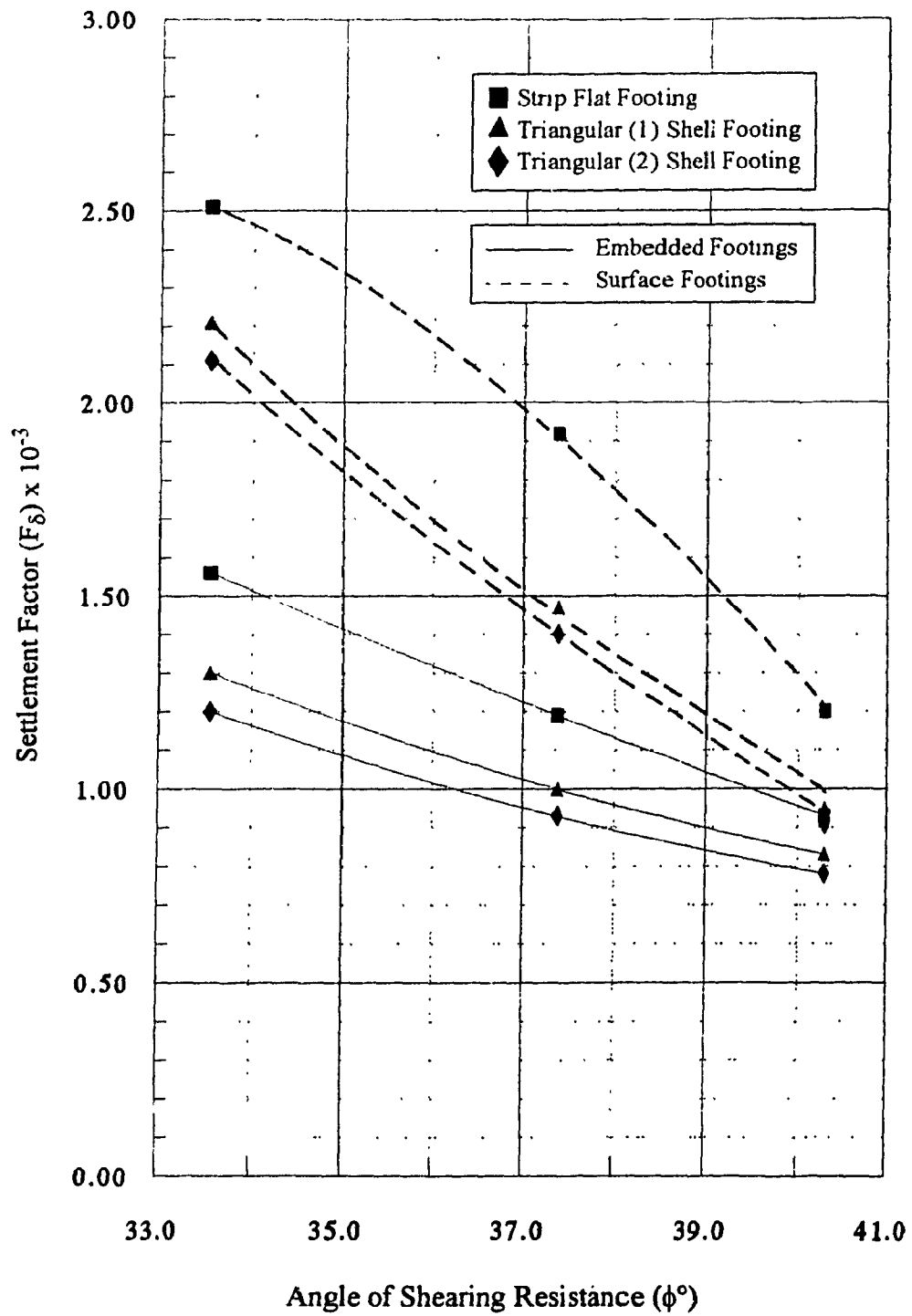


Figure 3.35 Settlement Factor ( $F_{\delta}$ ) for Plane Strain Condition

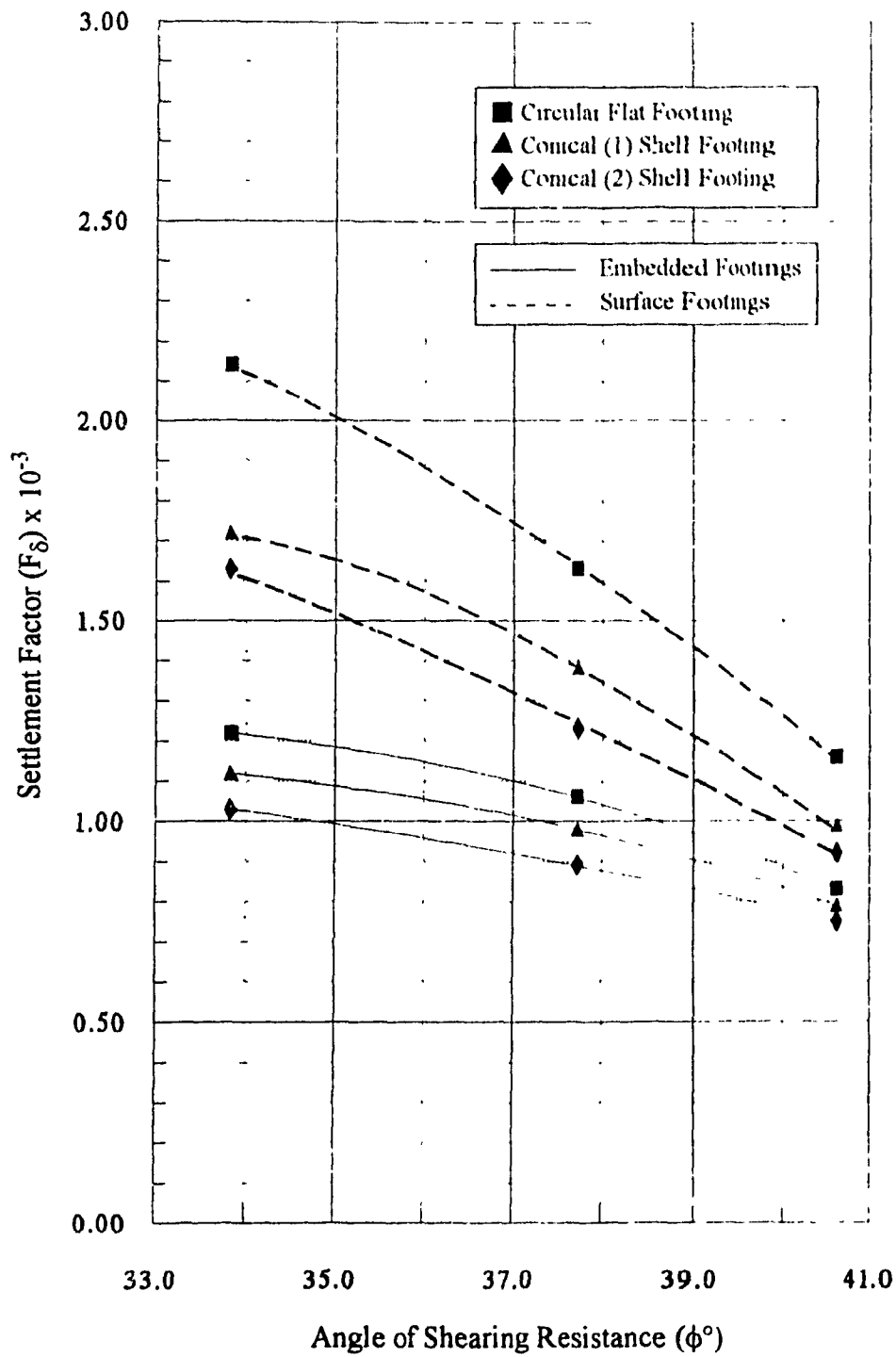


Figure 3.36 Settlement Factor ( $F_\delta$ ) for Axisymmetrical Condition

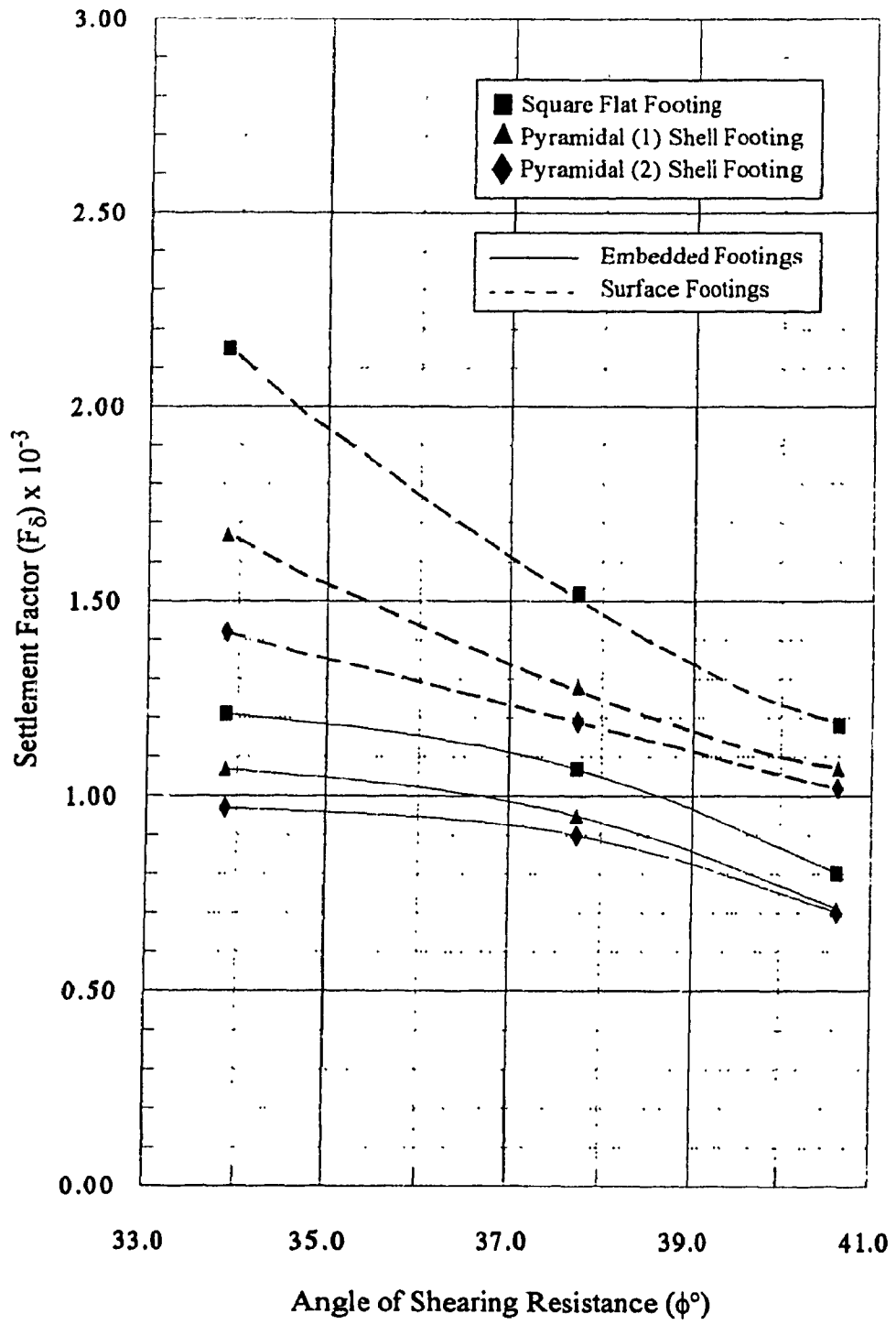


Figure 3.37 Settlement Factor ( $F_\delta$ ) for Three Dimensional Condition

### 3.8.3 Contact Pressure Distribution

In the present experimental investigation, the contact pressures were measured at predetermined locations on the soil-foundation interface by means of pressure transducers. The results of these measurements were recorded by the Data Acquisition System for each transducer. The contact pressures measured by each transducer were plotted versus the corresponding applied load for all tests. The pressure envelope, which is the domain enveloping the lower and upper limits of the recorded contact pressures, was established and shown on these plots.

The contact pressure measurements versus the applied load until the ultimate load are presented in Figures 3.38 through 3.40 for strip flat footing, in Figures 3.41 through 3.43 for triangular (1) shell footing, in Figures 3.44 through 3.46 for triangular (2) shell footing, in Figures 3.47 through 3.49 for circular flat footing, in Figures 3.50 through 3.52 for conical (1) shell footing, in Figures 3.53 through 3.55 for conical (2) shell footing, in Figures 3.56 through 3.58 for square shell footing, in Figures 3.59 through 3.61 for pyramidal (1) shell footing, and in Figures 3.62 through 3.64 for pyramidal (2) shell footing. A key plan of the soil-foundation interface including the pressure transducers is shown on these figures. Each pressure transducer ( $T_i$ ) is identified with a different symbol which is used in plotting the data.

In general, it can be observed from these figures that the contact pressures increase with the increase in the applied load in nearly a linear fashion. However, some curvature exists near the region of the ultimate load. The existence of a pressure envelope on these figures indicates that the contact pressure distribution is not a uniform one. A more confined domain for the pressure envelope demonstrates less variation in the contact pressures over the base of footing.

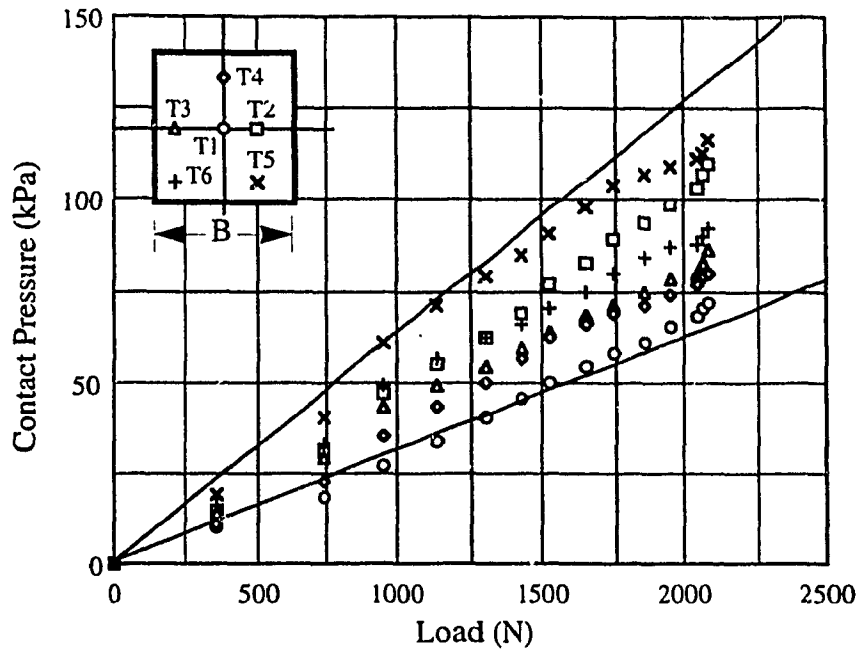
For the plane strain condition, the contact pressure envelopes of the embedded foot-

ings were generally more confined than that of the surface ones. The pressure envelope for a given footing was more confined for a denser sand state. The comparison between the strip flat and the triangular shell footings indicates that the later possessed relatively more confined pressure envelopes.

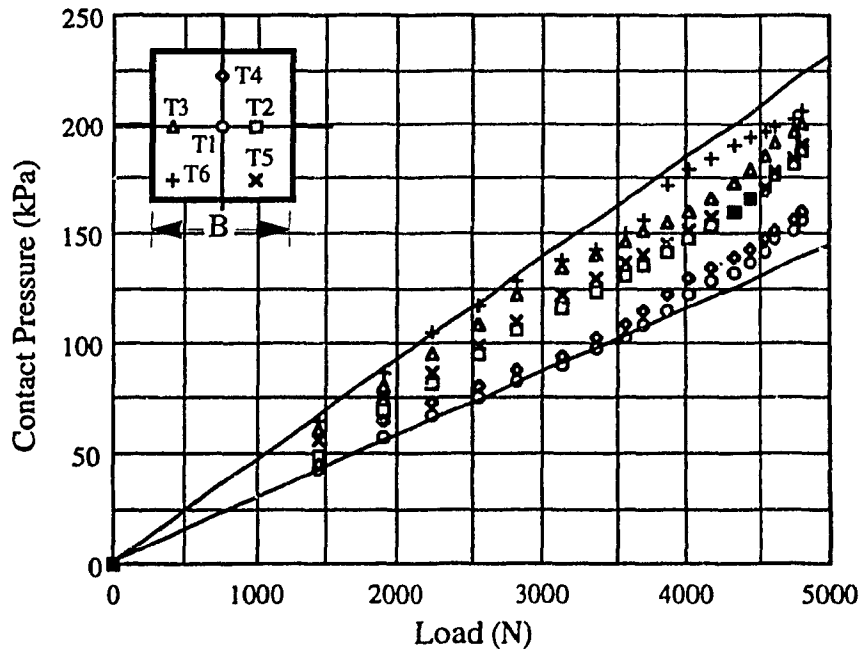
For the axisymmetrical condition, the pressure envelopes for the embedded and surface footings had almost the same degree of confinement. However, it can be seen that the pressure envelope of the embedded conical (2) shell footing was more confined than that of the surface one at any sand state. The pressure envelopes for the conical shell footings were more confined for a denser sand state. However, this trend was not satisfied for the circular flat footing, where the pressure envelope at the medium sand state was less confined than that at the loose sand state. The conical shell footings possessed relatively more confined pressure envelopes than that of the circular flat counterpart.

For the three dimensional condition, there was a significant difference as compared to the trend described for the plane strain and axisymmetrical conditions. The pressure envelopes of the surface square flat footing were more confined than that of the embedded one for the three sand states. The pressure envelopes for the dense sand state were less confined than that for the loose and medium sand states. The pressure envelopes of the surface pyramidal (1) shell footing at the loose and medium sand states were more confined than that of the embedded one. However, at the dense sand state, they had almost the same degree of confinement. The same trend applied for the pyramidal (2) shell footing with the exception that the pressure envelope of the embedded footing at the dense sand state was remarkably more confined than that of the surface one.

It can be concluded from the above that the picture of the contact pressure distribution for the axisymmetrical and three dimensional conditions is not well defined. However, some general trends were deduced for the plane strain condition which might help in understanding the overall behavior with respect to contact pressure distribution.



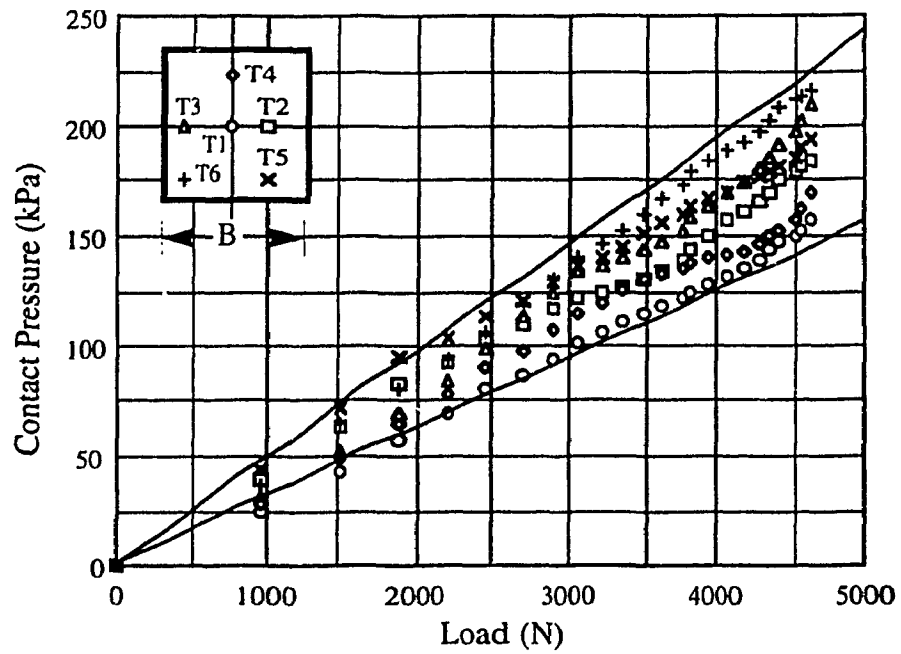
a) Surface Footing



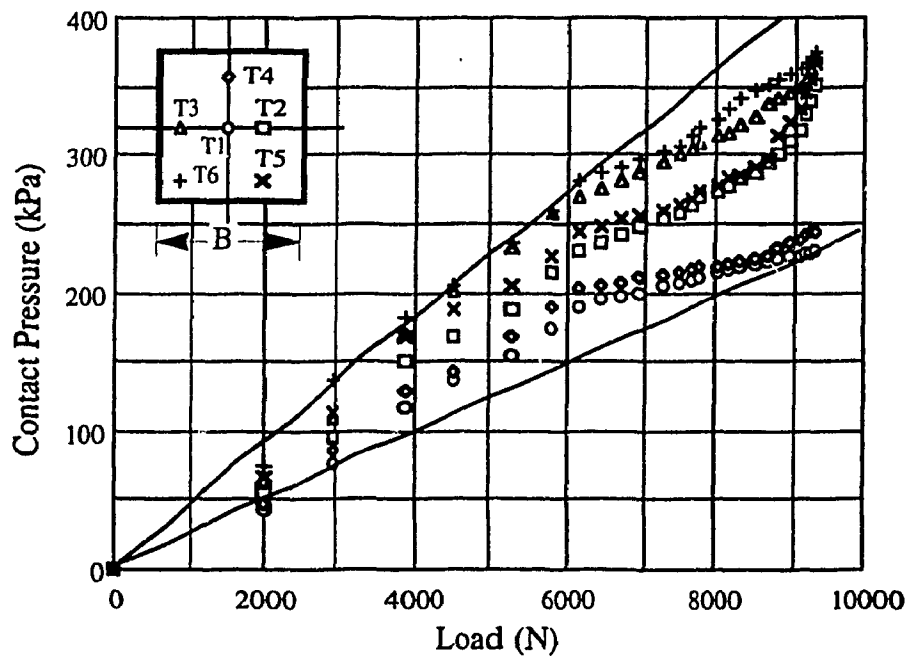
b) Embedded Footing

Figure 3.38 Contact Pressure Envelopes for Strip Flat Footing on Loose Sand



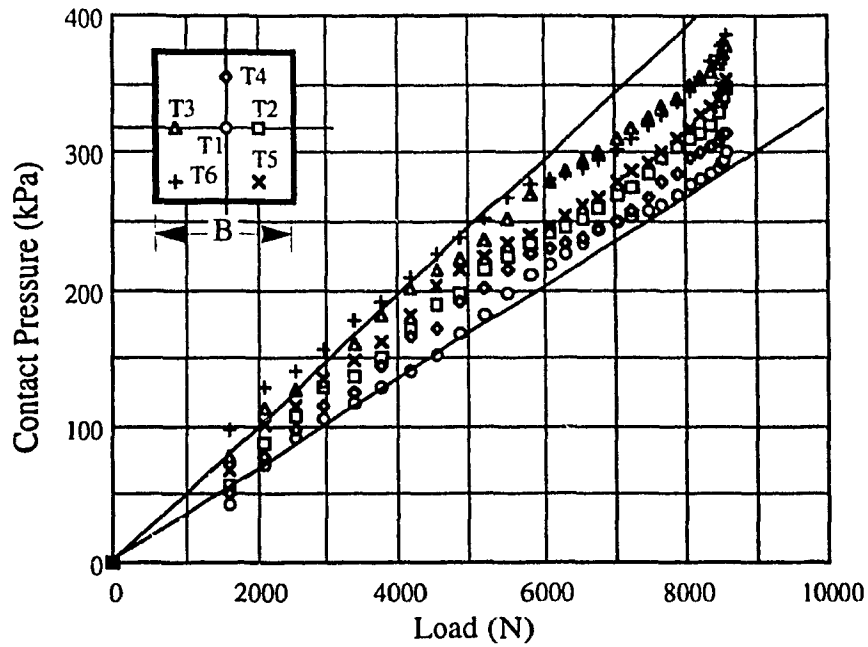


a) Surface Footing

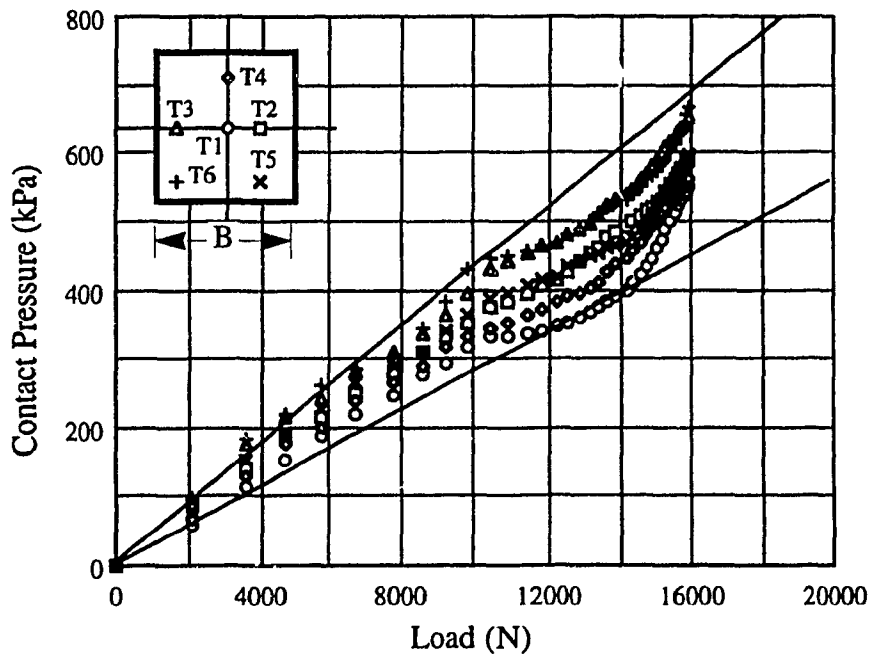


b) Embedded Footing

Figure 3.39 Contact Pressure Envelopes for Strip Flat Footing on Medium Sand

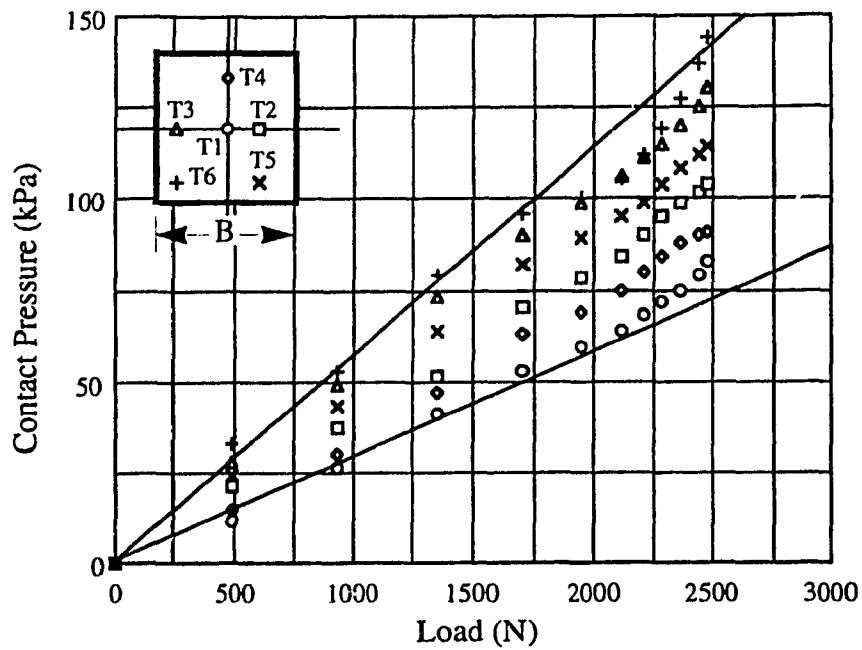


a) Surface Footing

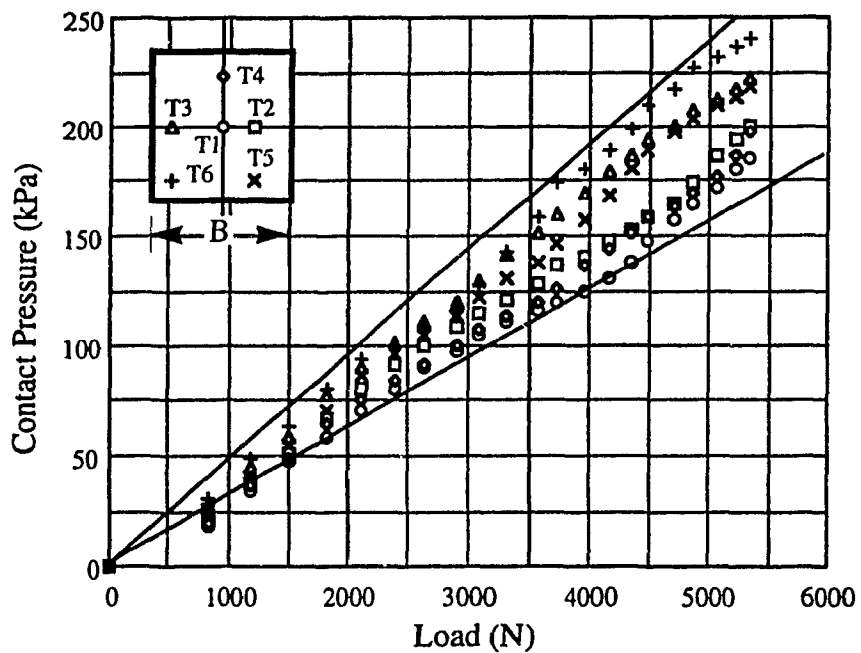


b) Embedded Footing

Figure 3.40 Contact Pressure Envelopes for Strip Flat Footing on Dense Sand

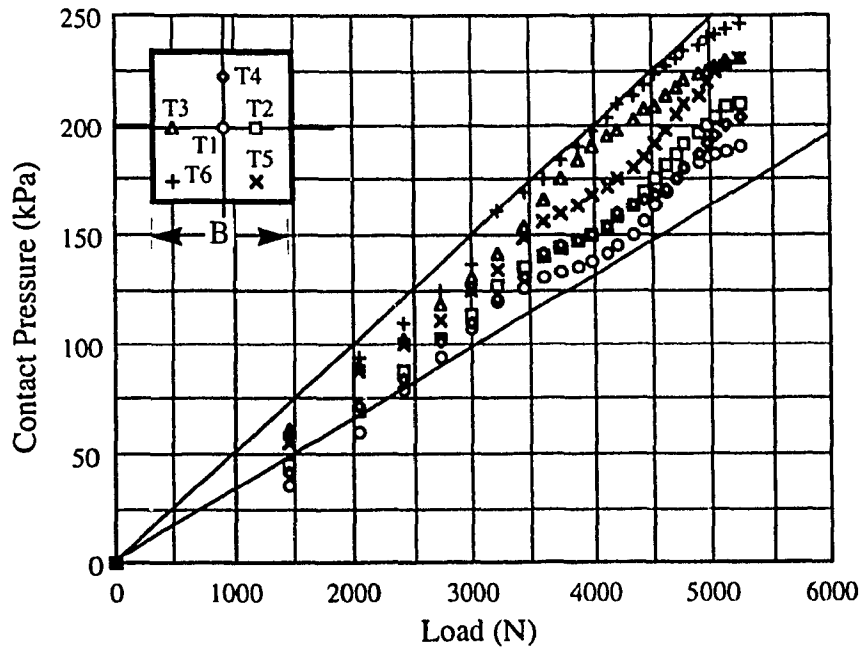


a) Surface Footing

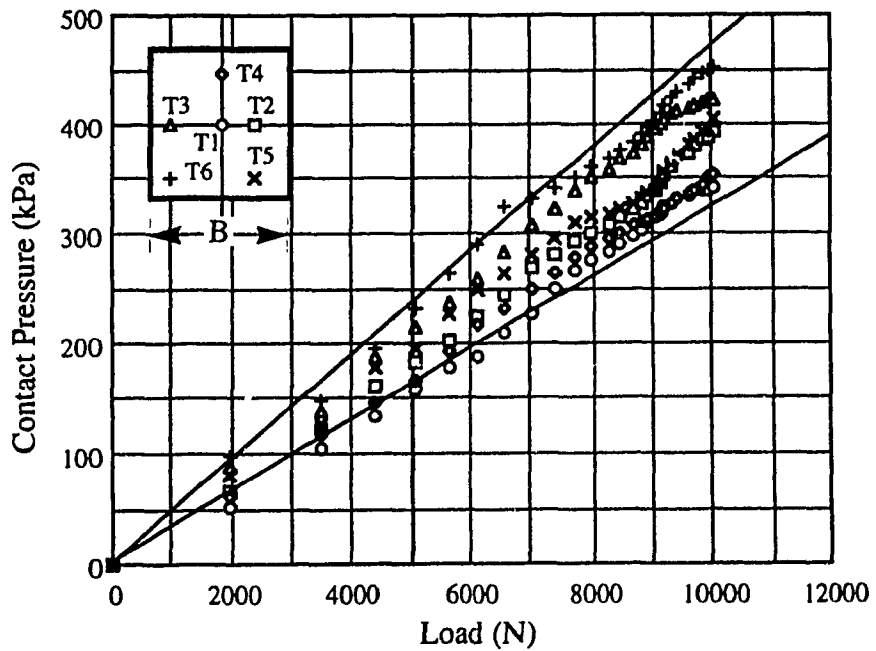


b) Embedded Footing

Figure 3.41 Contact Pressure Envelopes for Triangular (1) Footing on Loose Sand

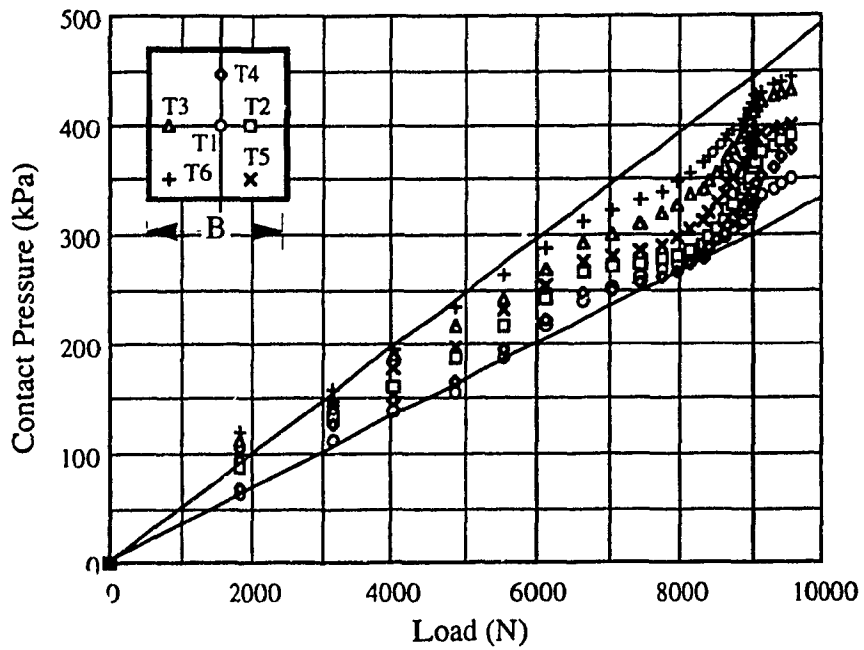


a) Surface Footing

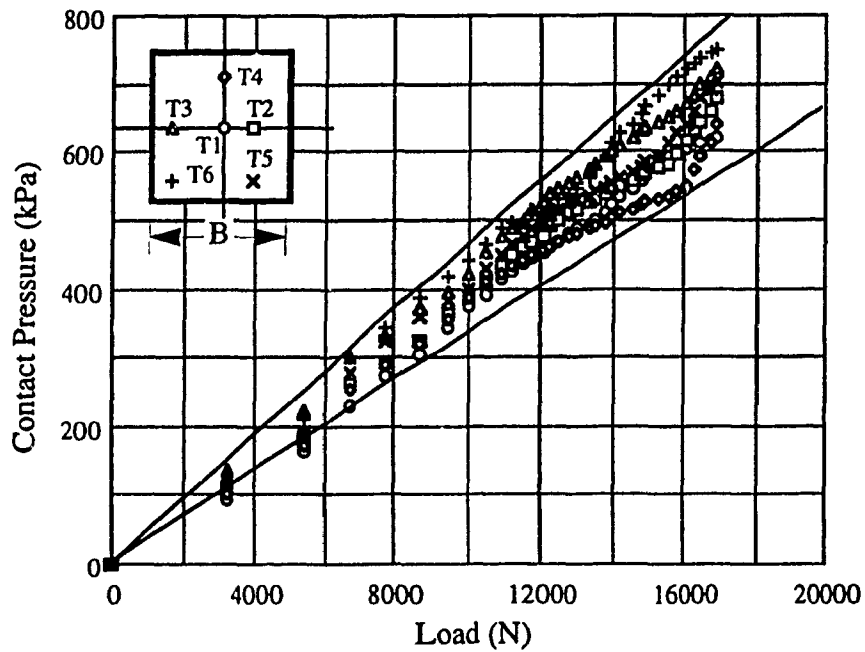


b) Embedded Footing

Figure 3.42 Contact Pressure Envelopes for Triangular (1) Footing on Medium Sand

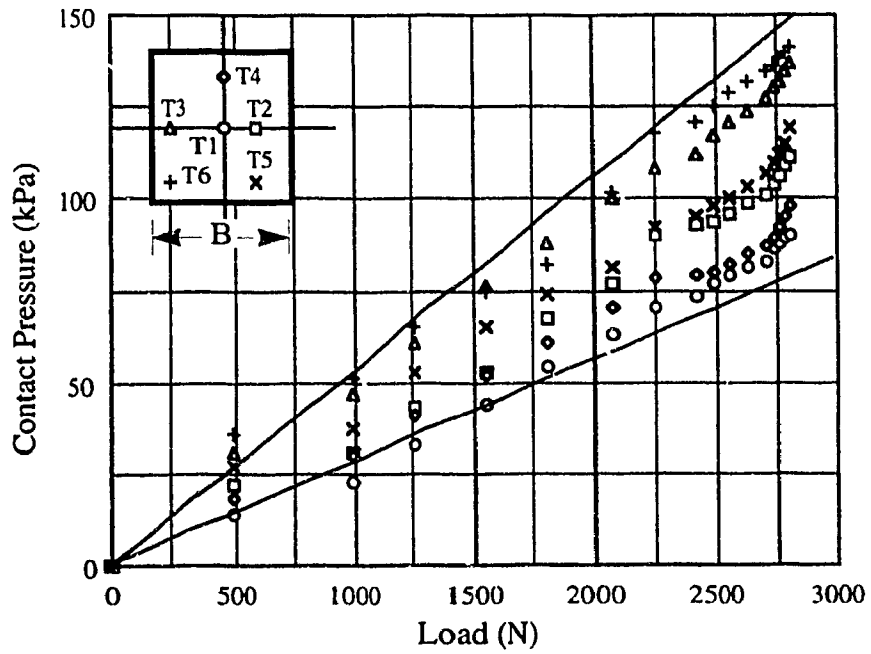


a) Surface Footing

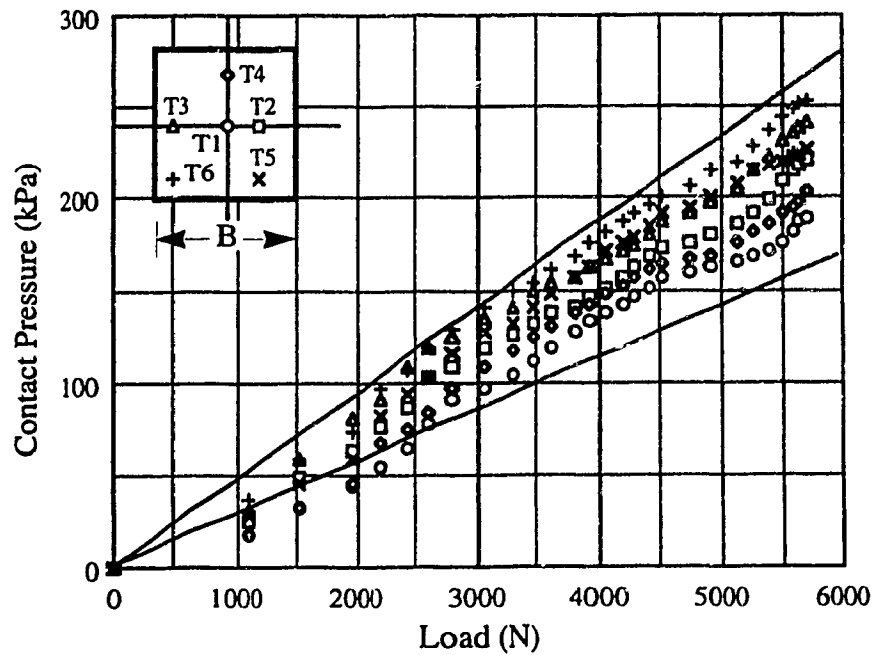


b) Embedded Footing

Figure 3.43 Contact Pressure Envelopes for Triangular (1) Footing on Dense Sand

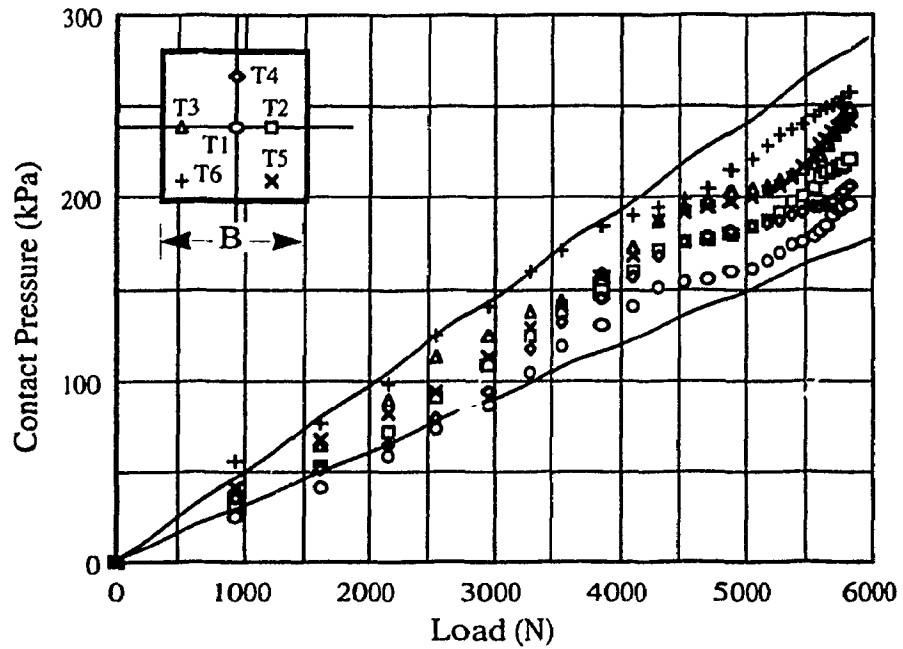


a) Surface Footing

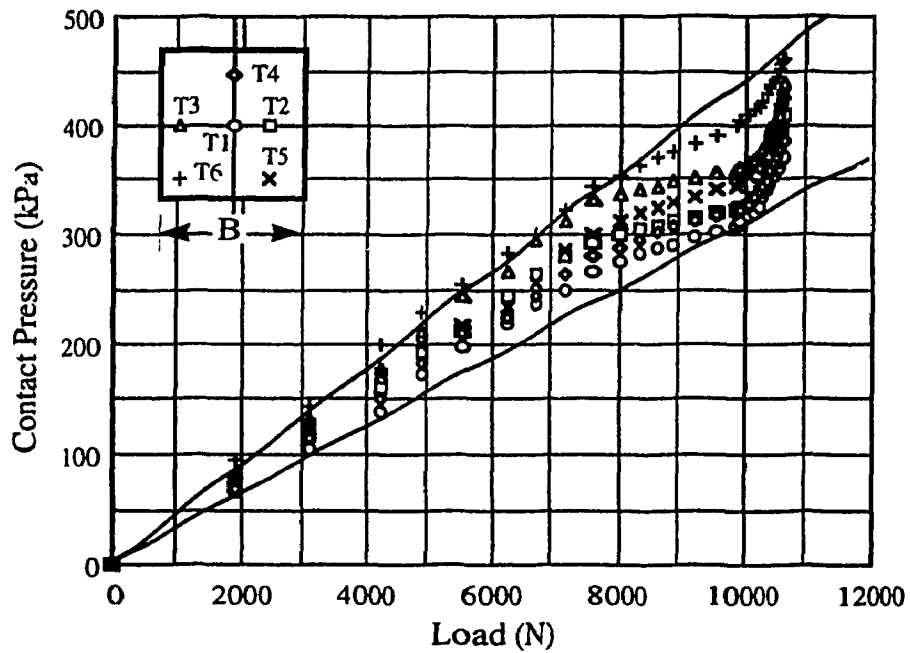


b) Embedded Footing

Figure 3.44 Contact Pressure Envelopes for Triangular (2) Footing on Loose Sand

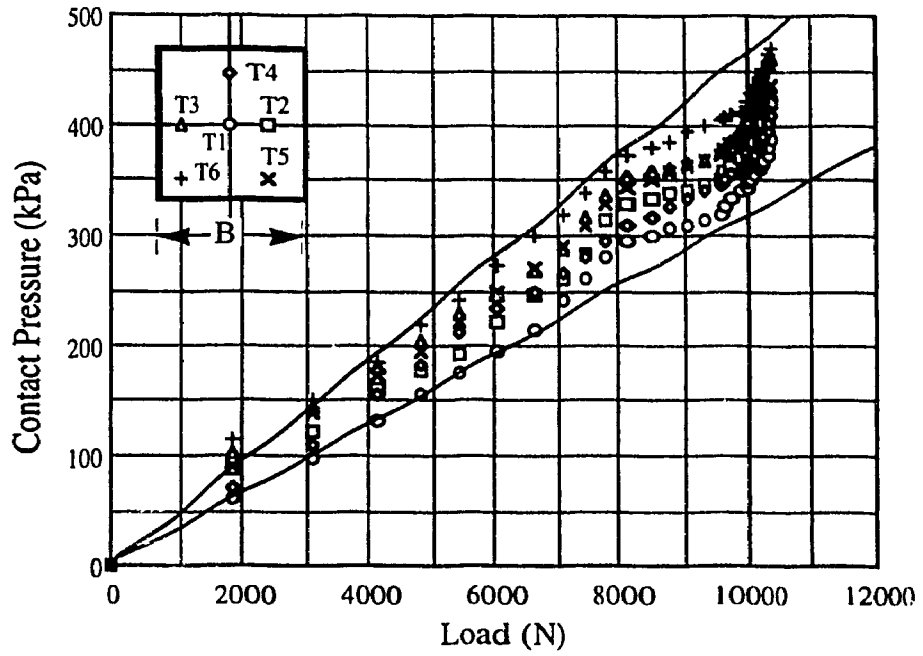


a) Surface Footing

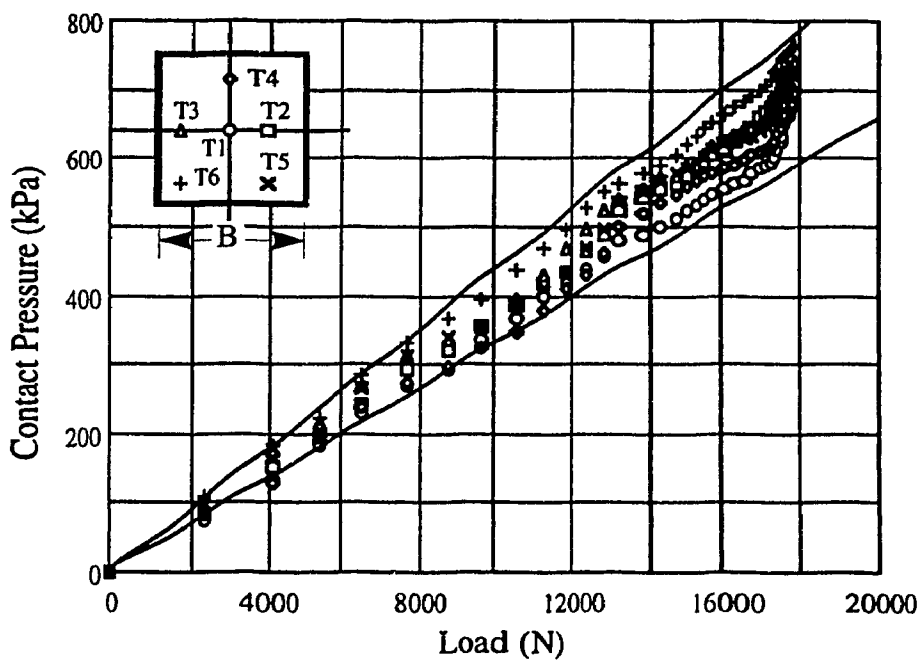


b) Embedded Footing

Figure 3.45 Contact Pressure Envelopes for Triangular (2) Footing on Medium Sand



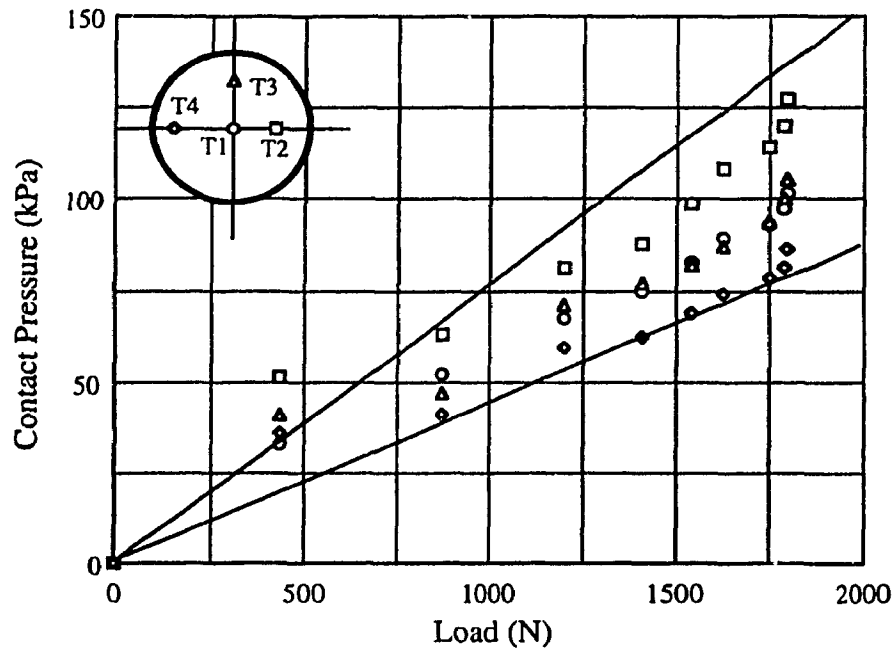
a) Surface Footing



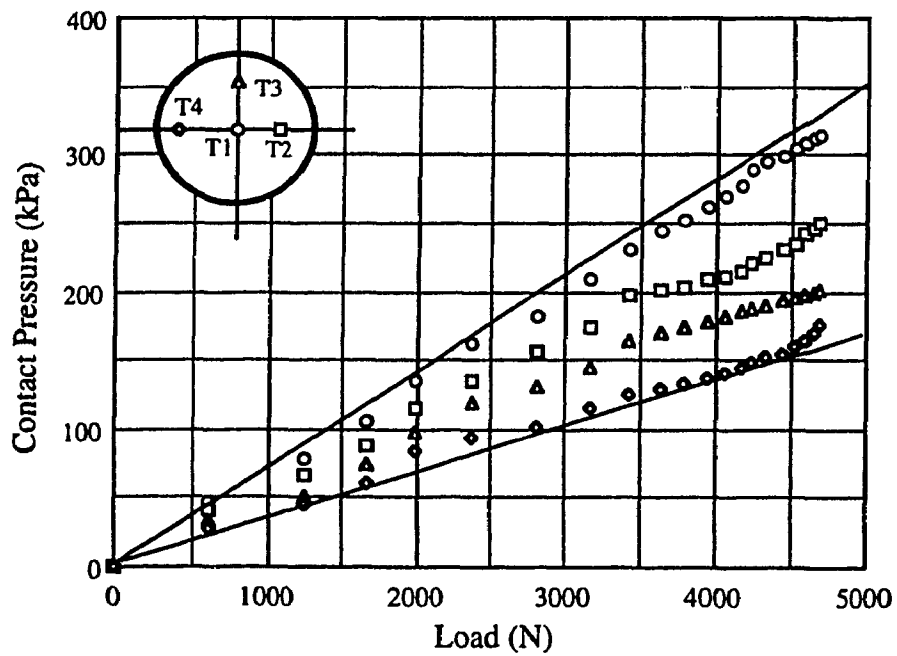
b) Embedded Footing

Figure 3.46 Contact Pressure Envelopes for Triangular (2) Footing on Dense Sand



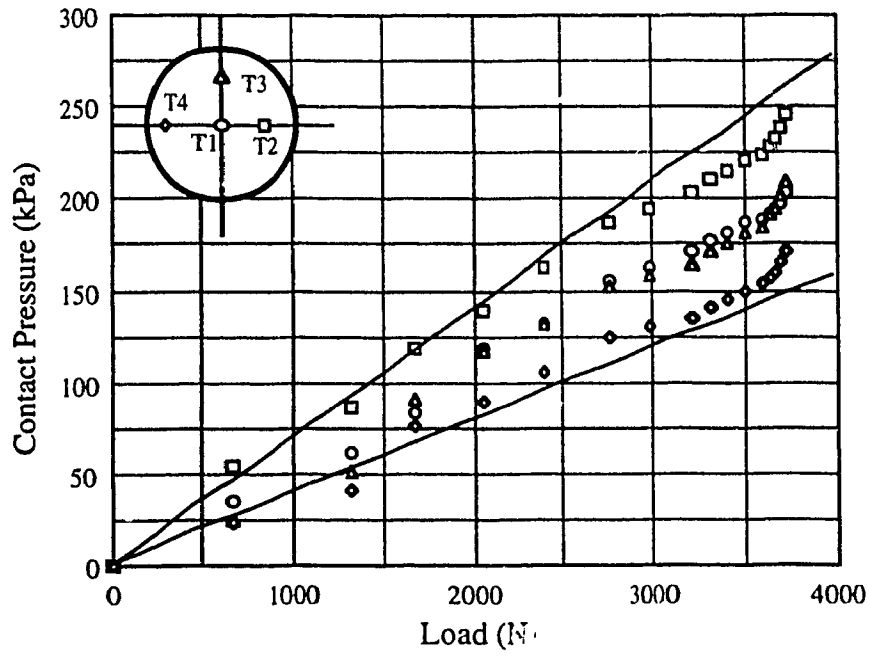


a) Surface Footing

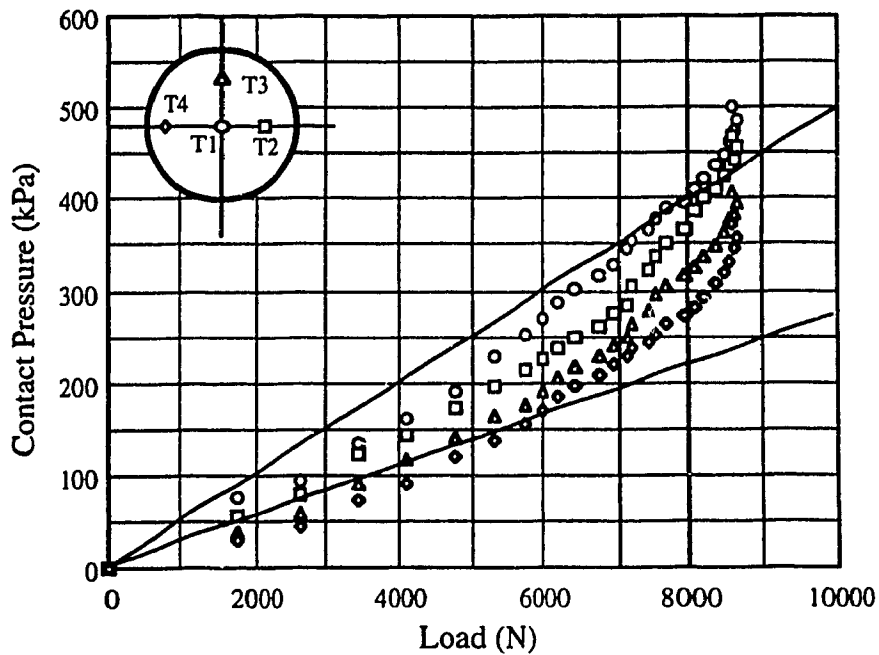


b) Embedded Footing

Figure 3.47 Contact Pressure Envelopes for Circular Flat Footing on Loose Sand

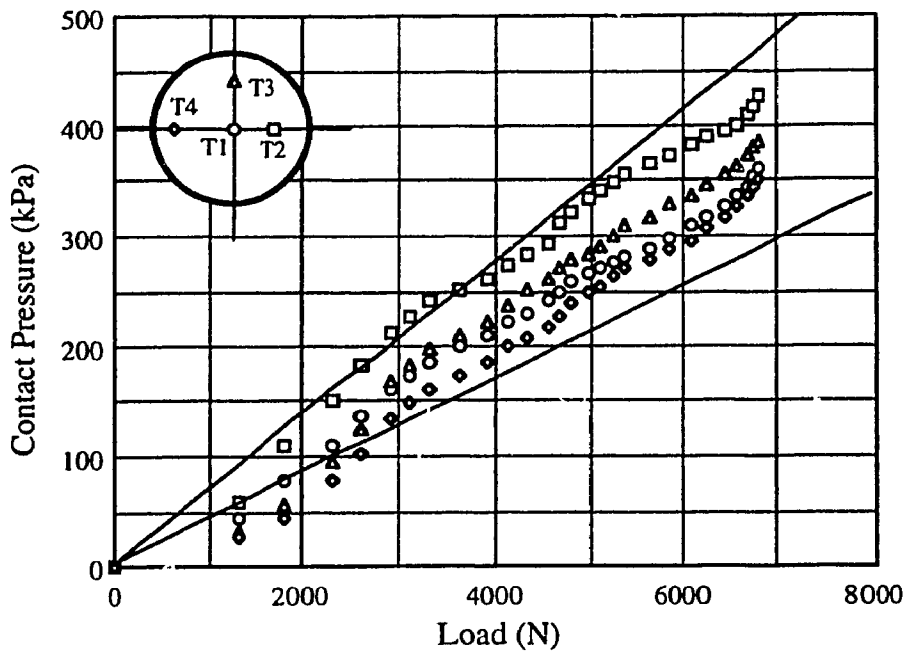


a) Surface Footing

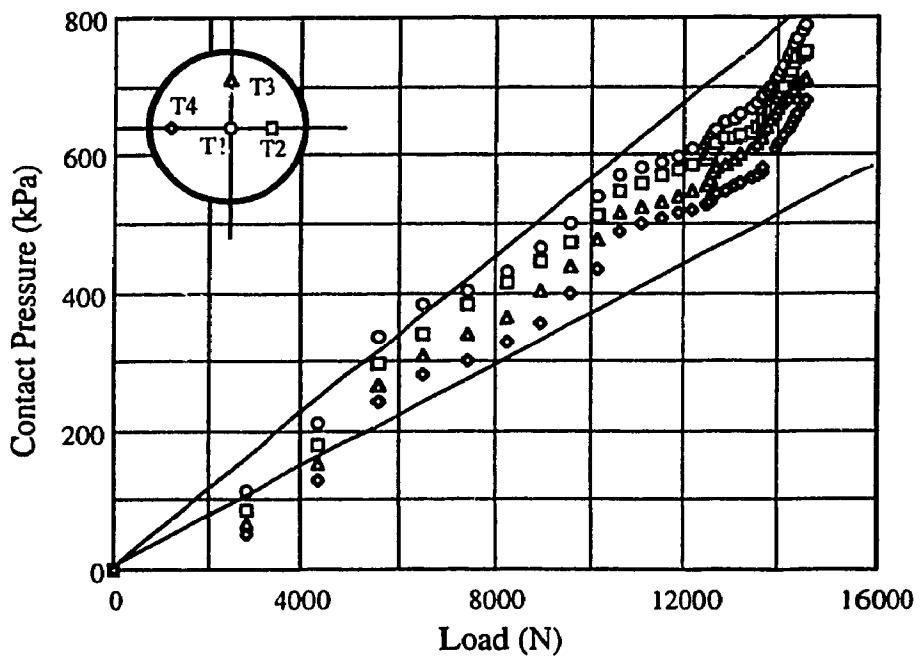


b) Embedded Footing

Figure 3.48 Contact Pressure Envelopes for Circular Flat Footing on Medium Sand

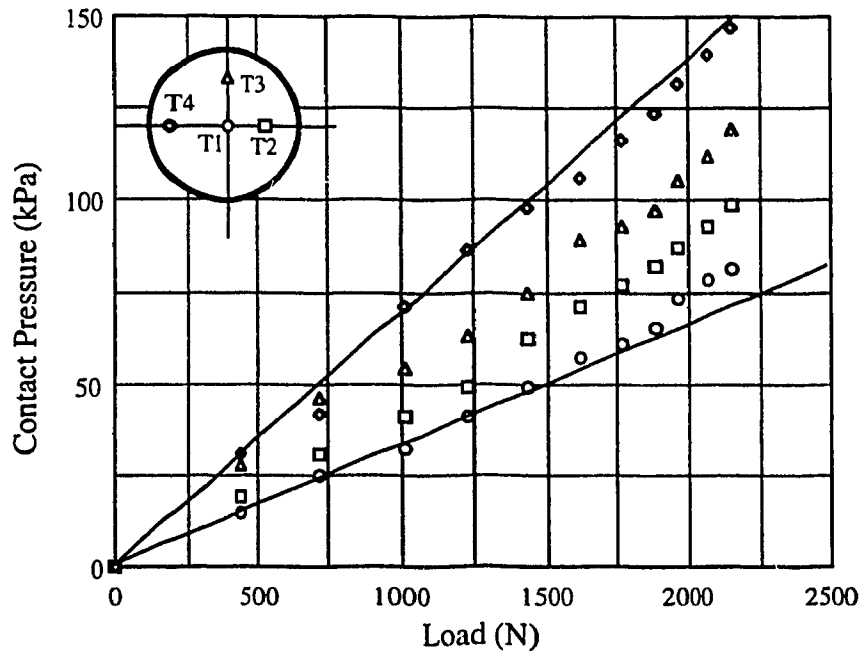


a) Surface Footing

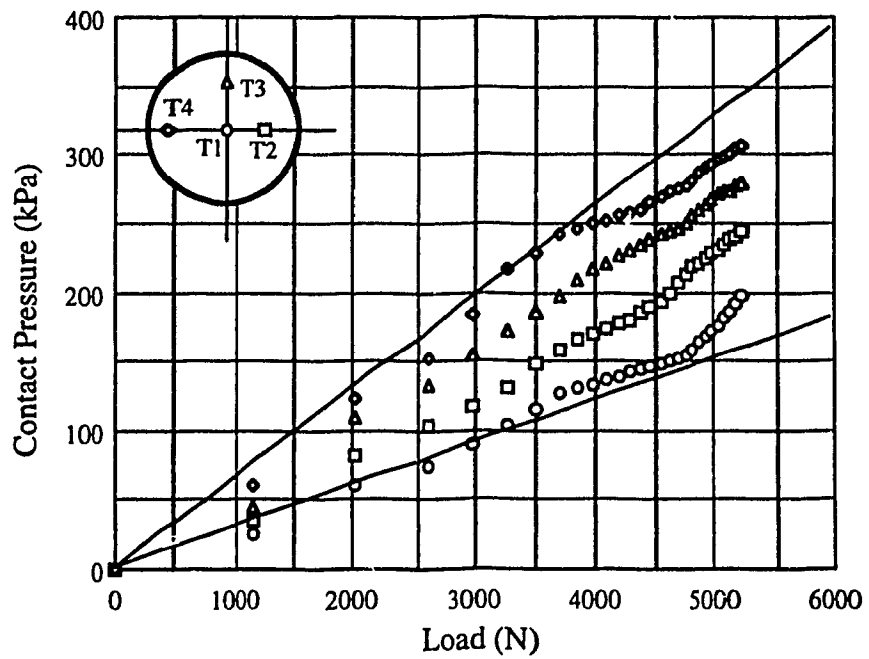


b) Embedded Footing

Figure 3.49 Contact Pressure Envelopes for Circular Flat Footing on Dense Sand

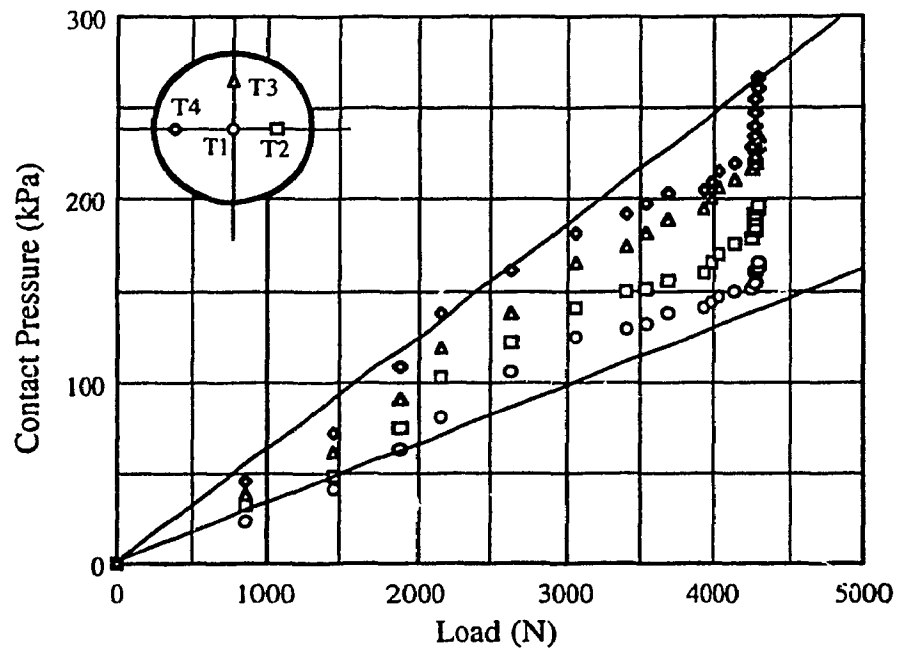


a) Surface Footing

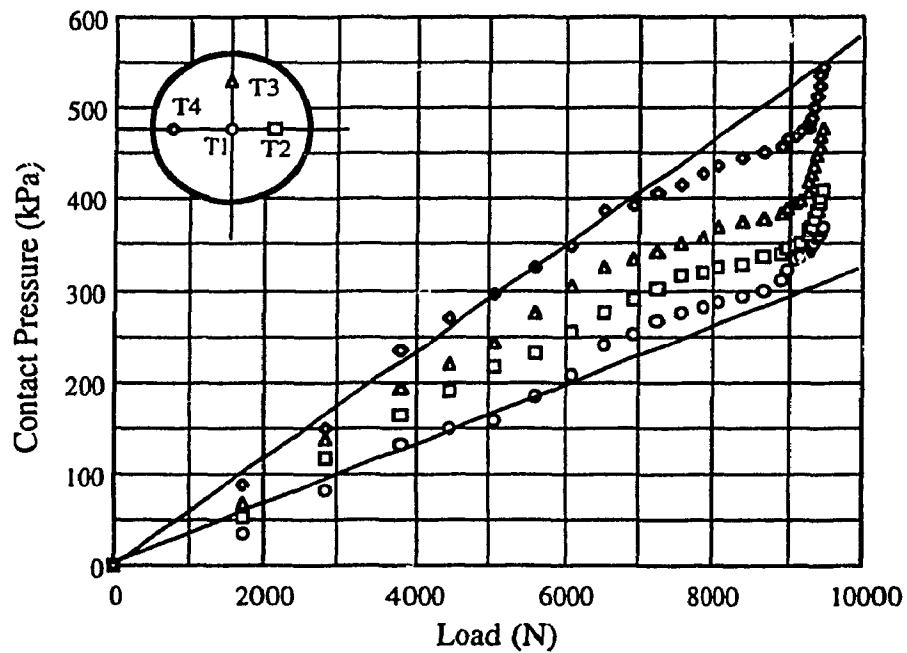


b) Embedded Footing

Figure 3.50 Contact Pressure Envelopes for Conical (1) Footing on Loose Sand

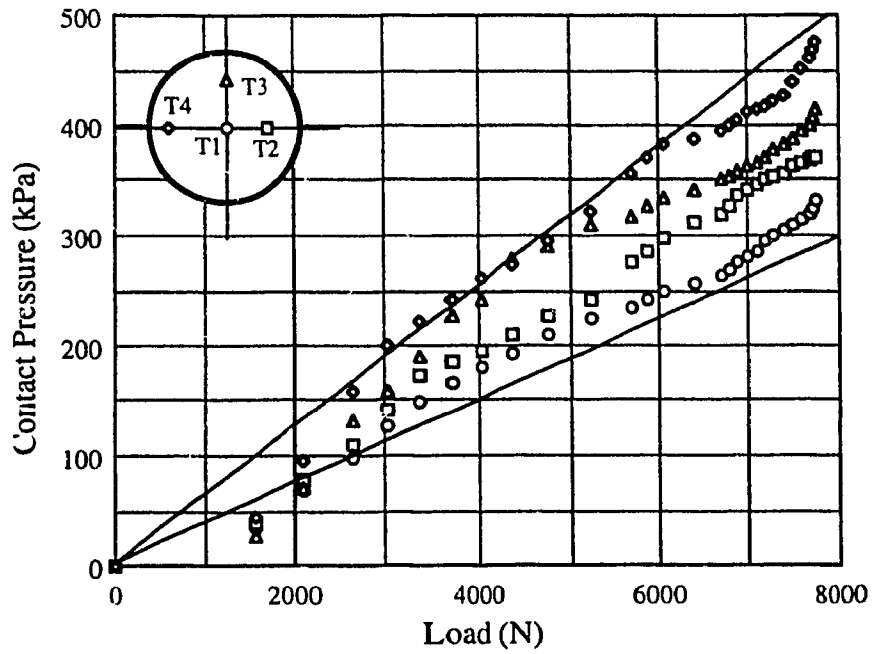


a) Surface Footing

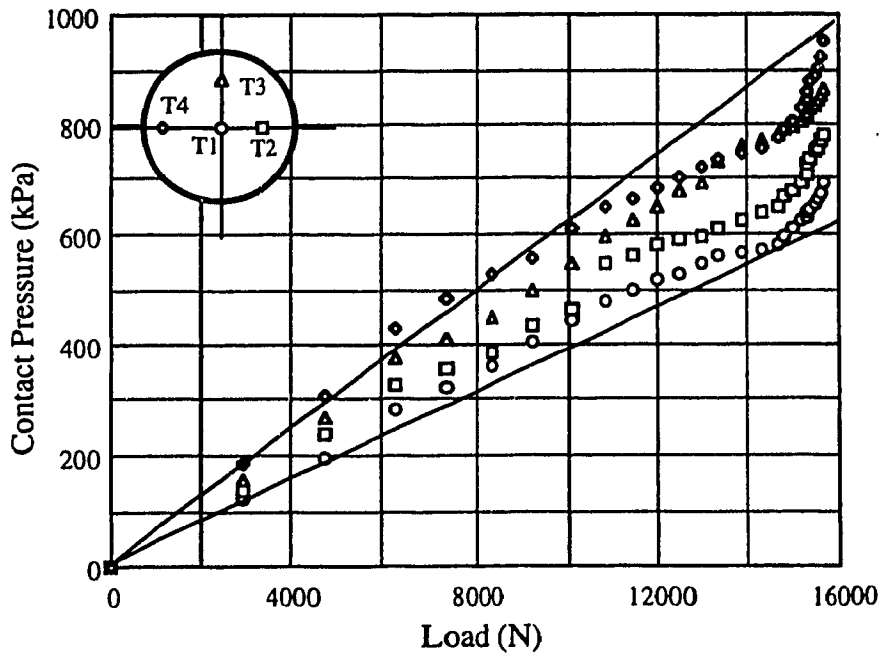


b) Embedded Footing

Figure 3.51 Contact Pressure Envelopes for Conical (1) Footing on Medium Sand

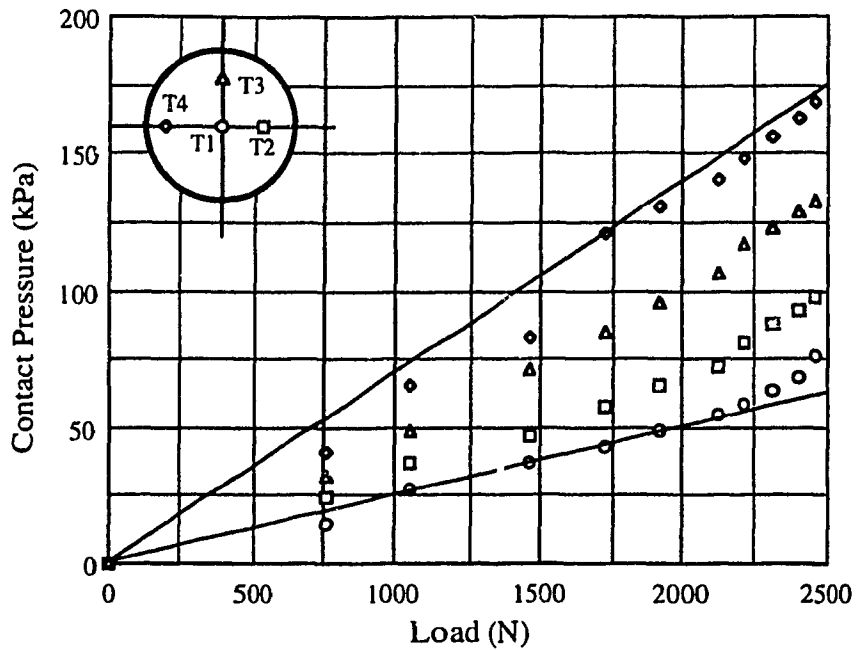


a) Surface Footing

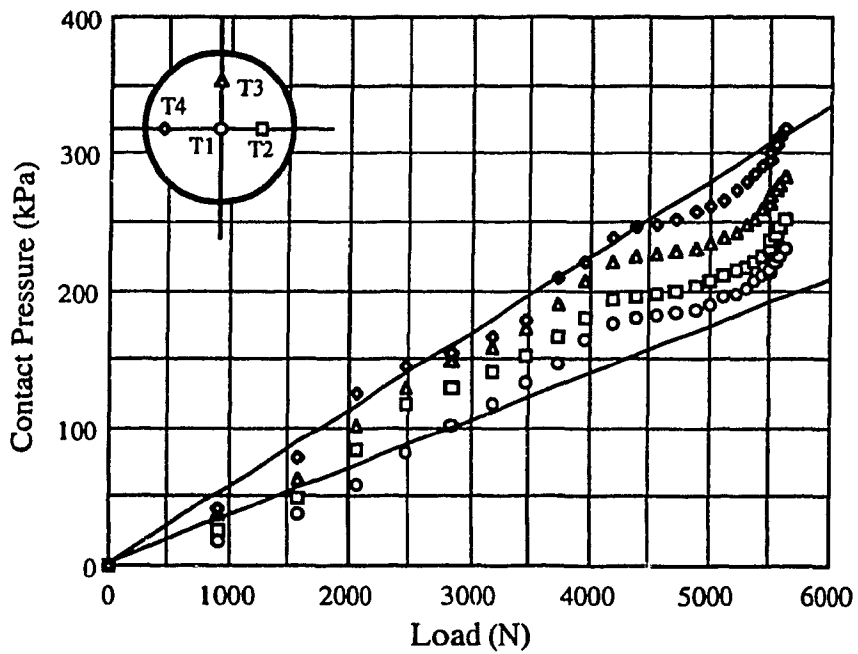


b) Embedded Footing

Figure 3.52 Contact Pressure Envelopes for Conical (1) Footing on Dense Sand

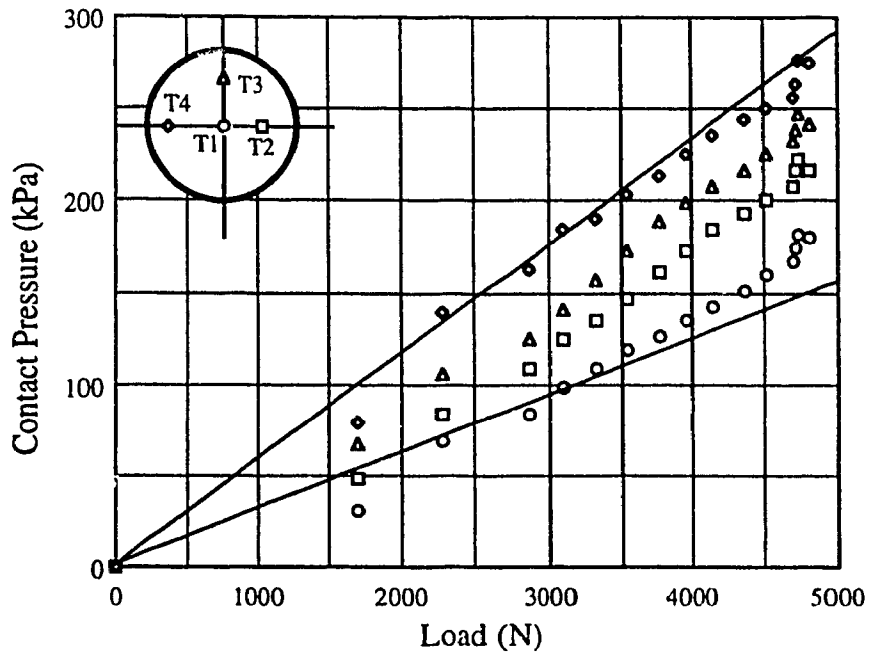


a) Surface Footing

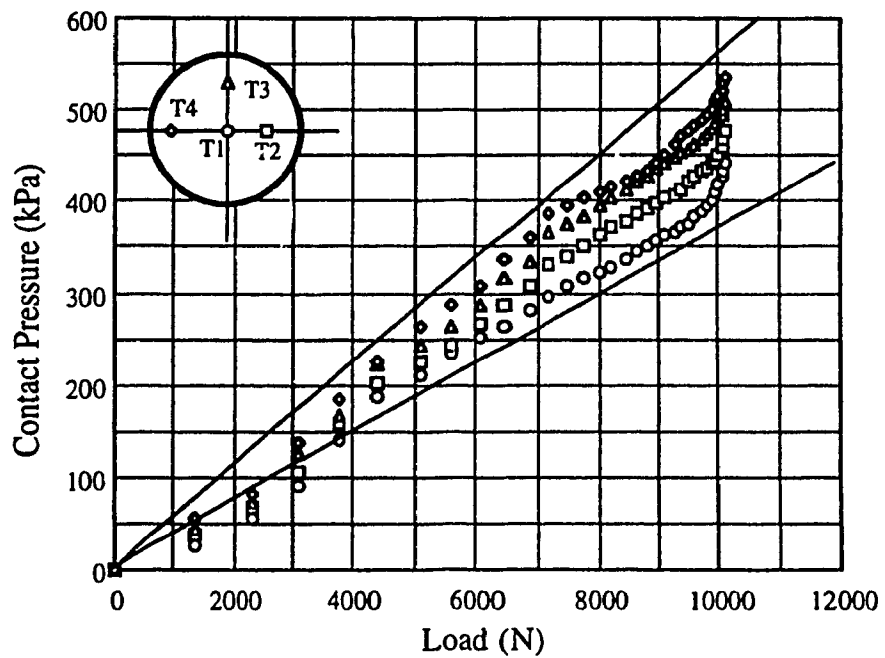


b) Embedded Footing

Figure 3.53 Contact Pressure Envelopes for Conical (2) Footing on Loose Sand



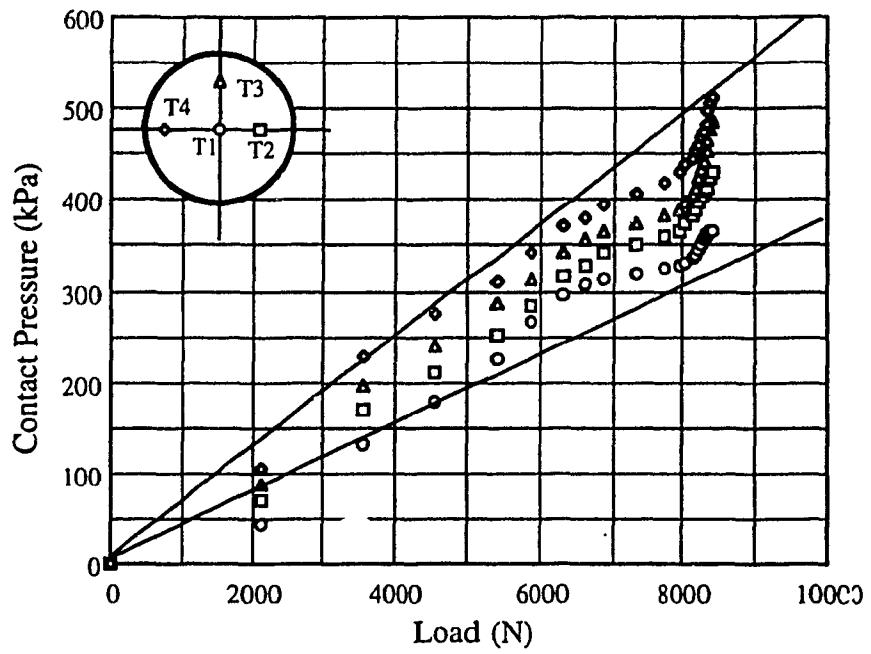
a) Surface Footing



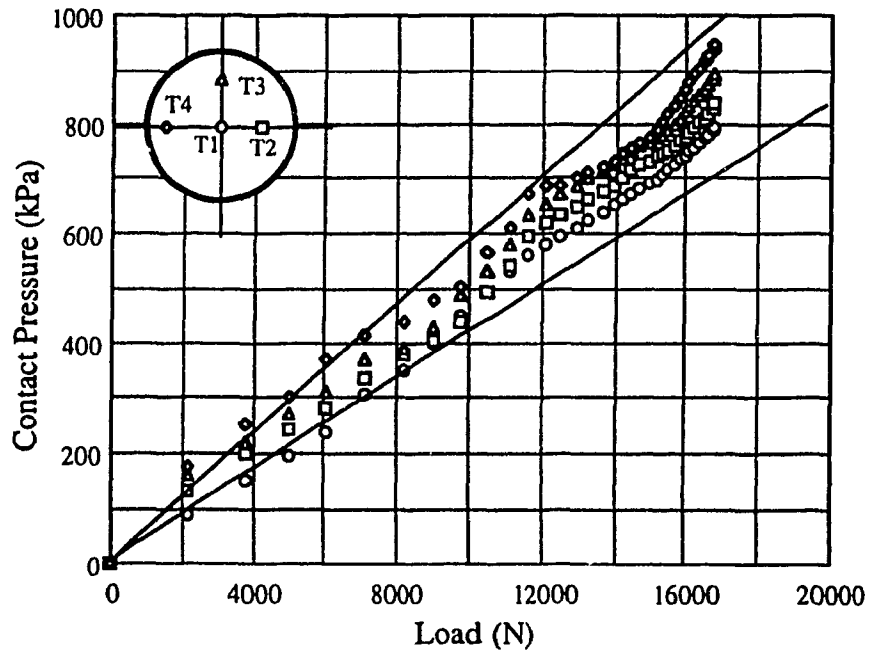
b) Embedded Footing

Figure 3.54 Contact Pressure Envelopes for Conical (2) Footing on Medium Sand



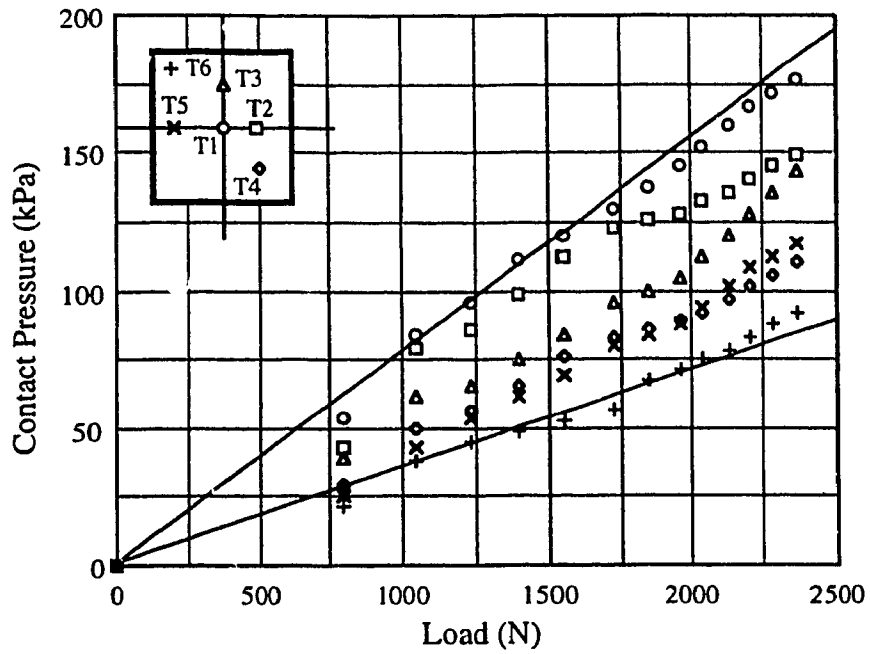


a) Surface Footing

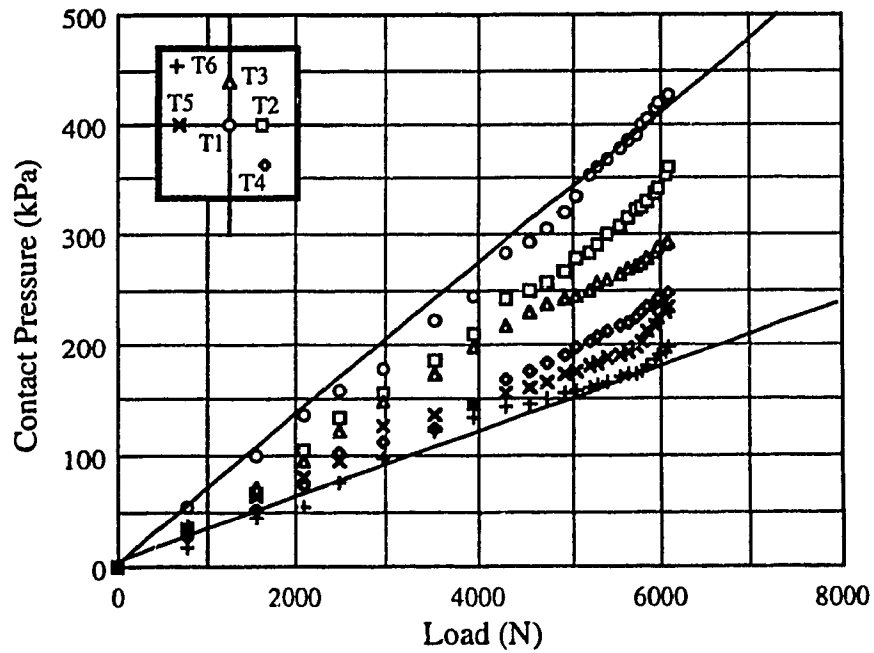


b) Embedded Footing

Figure 3.55 Contact Pressure Envelopes for Conical (2) Footing on Dense Sand

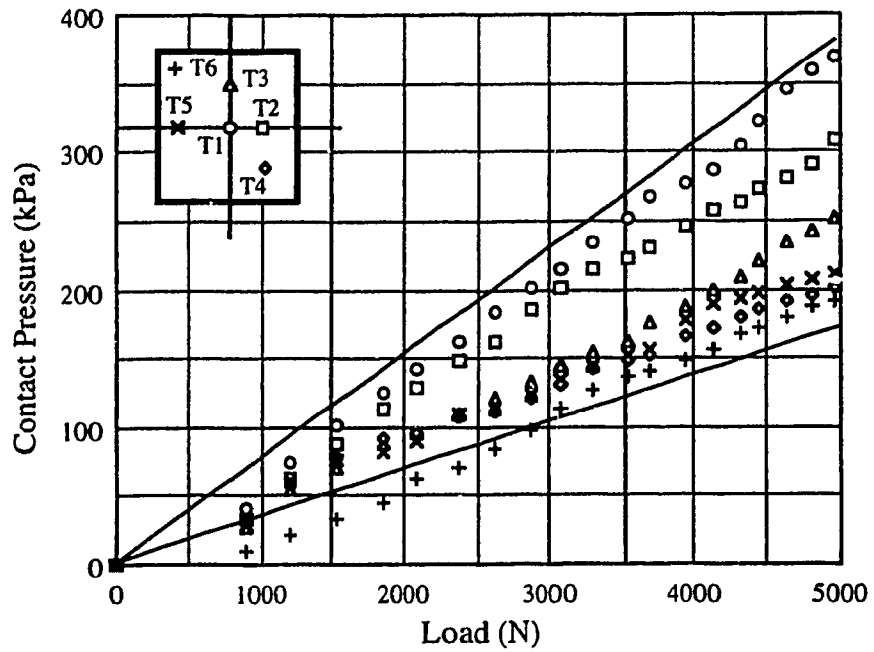


a) Surface Footing

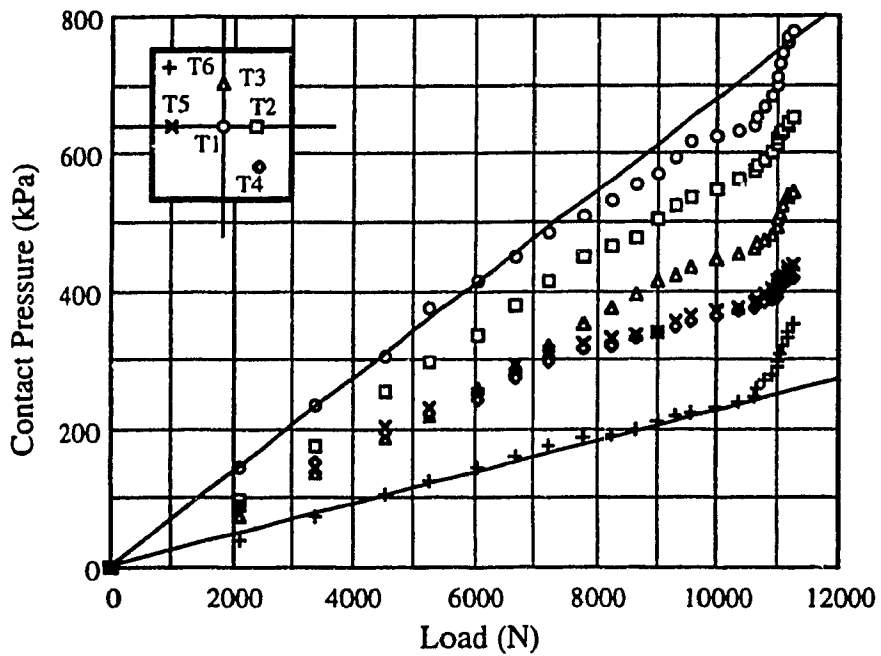


b) Embedded Footing

Figure 3.56 Contact Pressure Envelopes for Square Flat Footing on Loose Sand

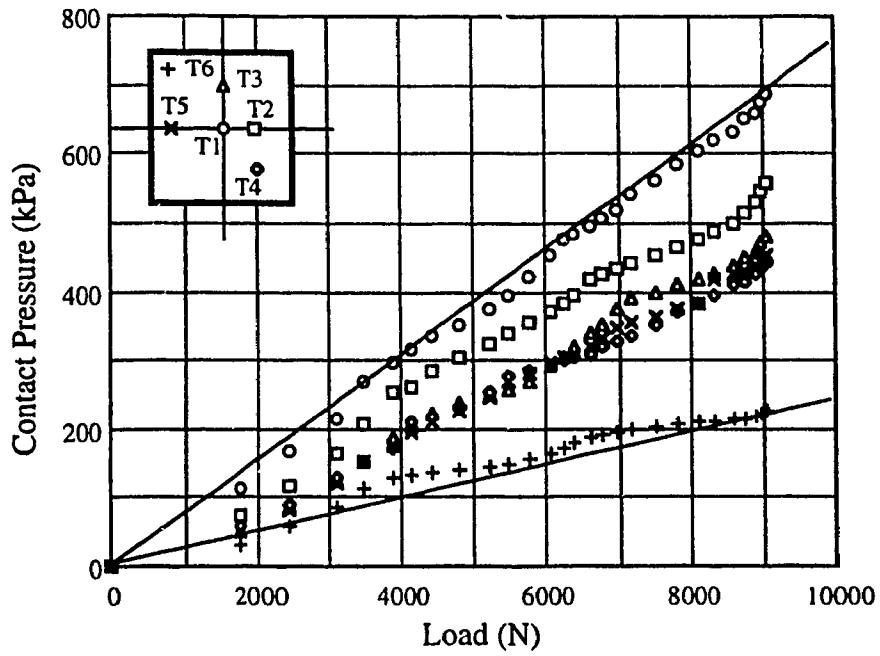


a) Surface Footing

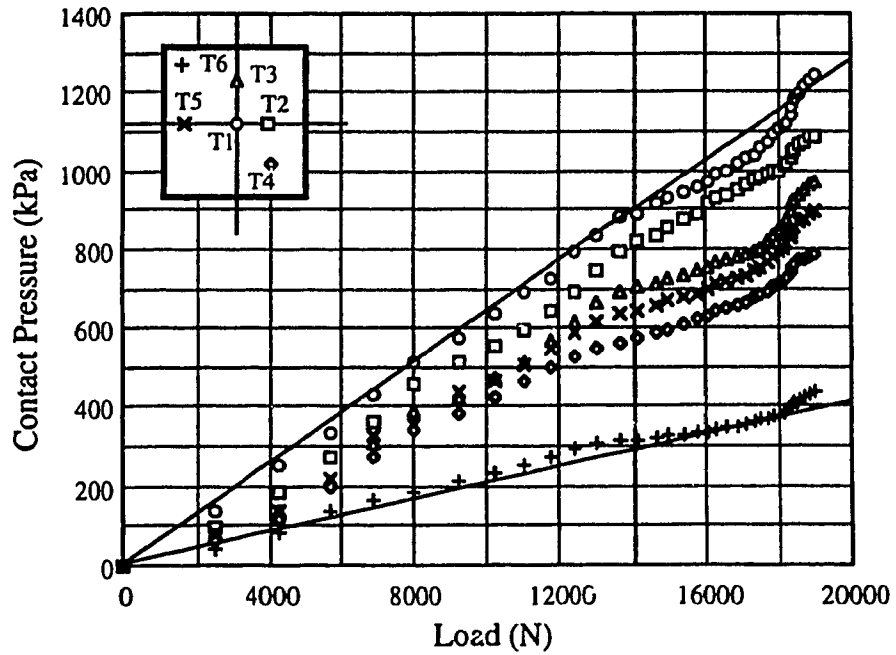


b) Embedded Footing

Figure 3.55 Contact Pressure Envelopes for Square Flat Footing on Medium Sand

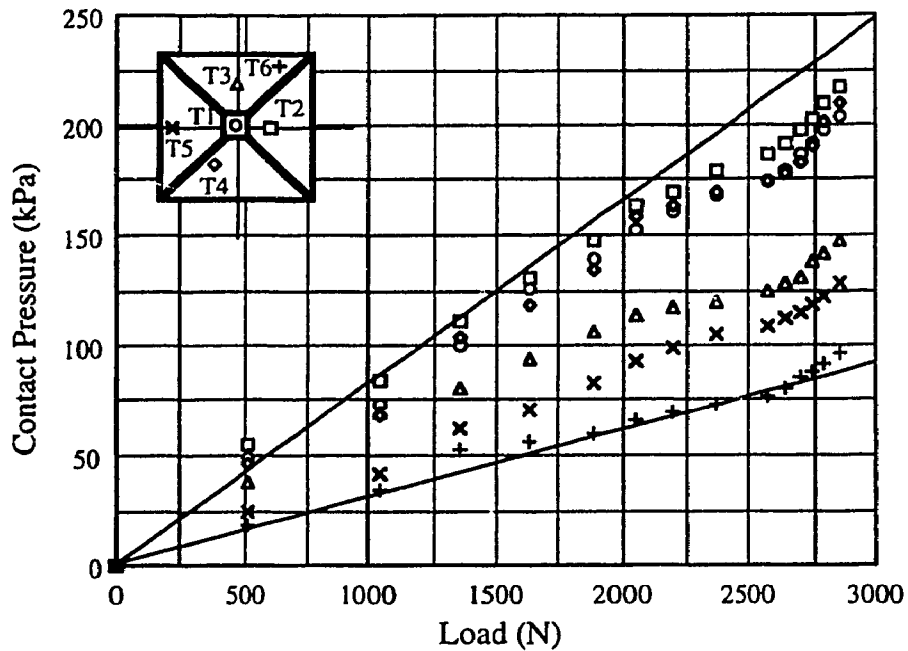


a) Surface Footing

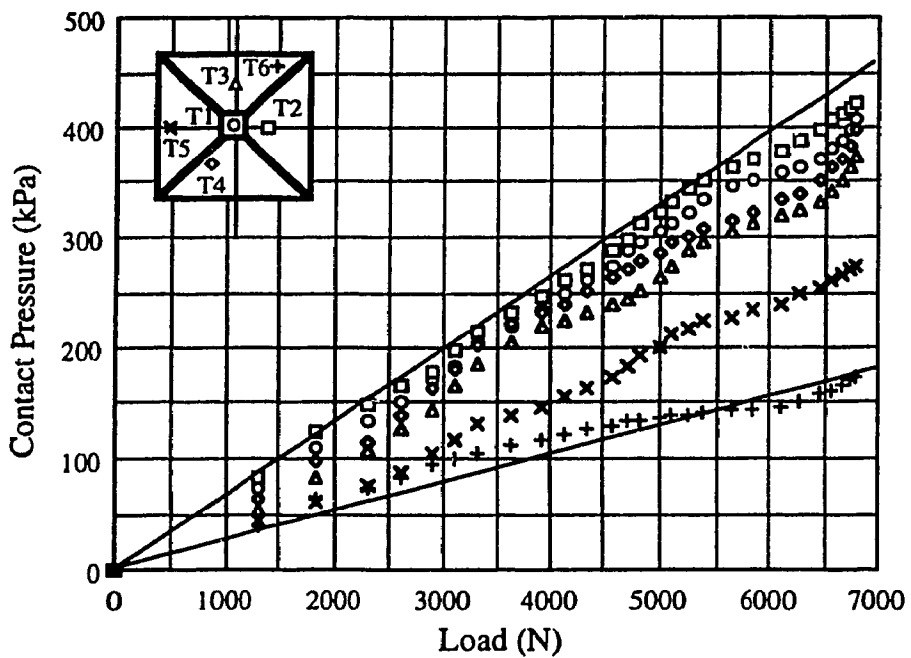


b) Embedded Footing

Figure 3.58 Contact Pressure Envelopes for Square Flat Footing on Dense Sand

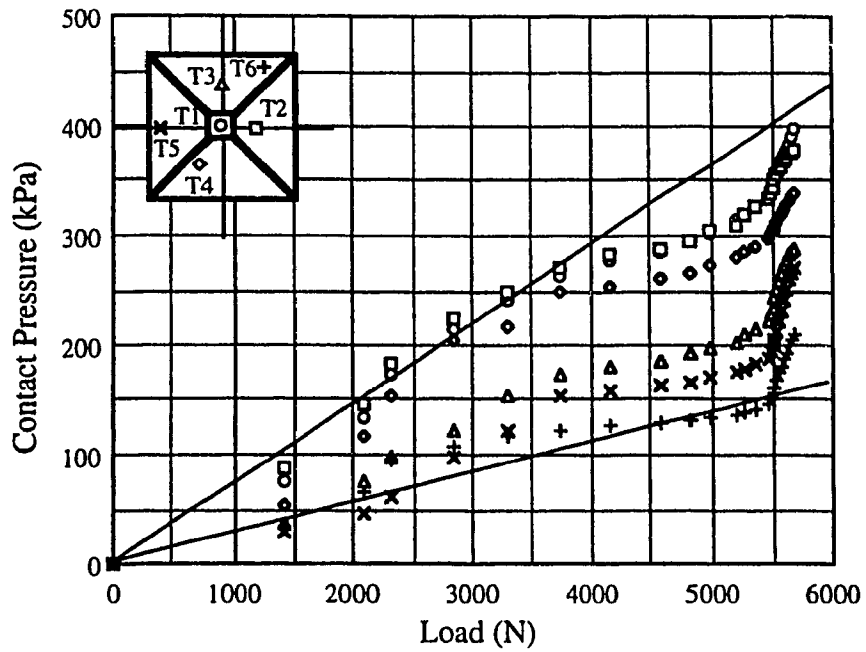


a) Surface Footing

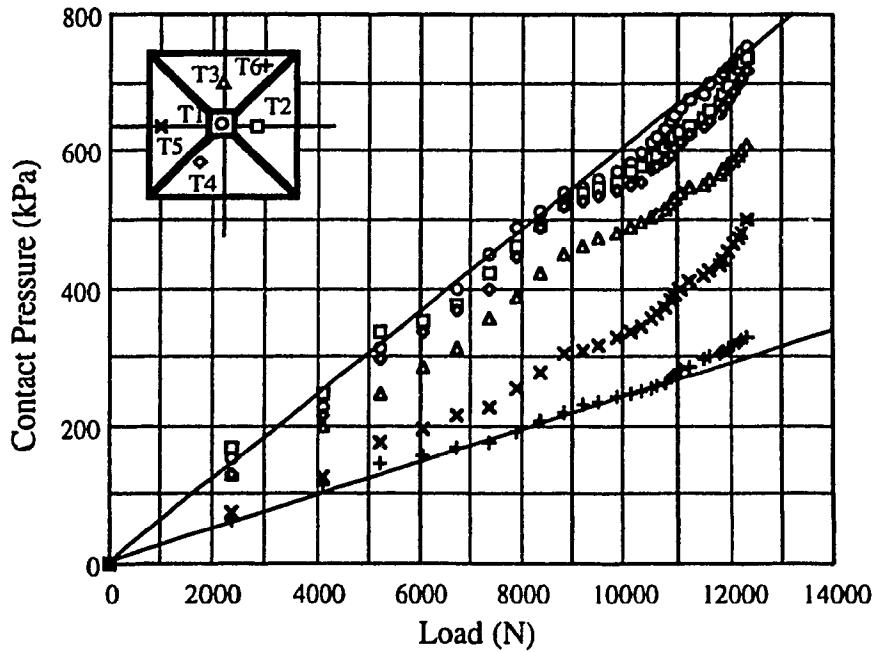


b) Embedded Footing

Figure 3.59 Contact Pressure Envelopes for Pyramidal (1) Footing on Loose Sand

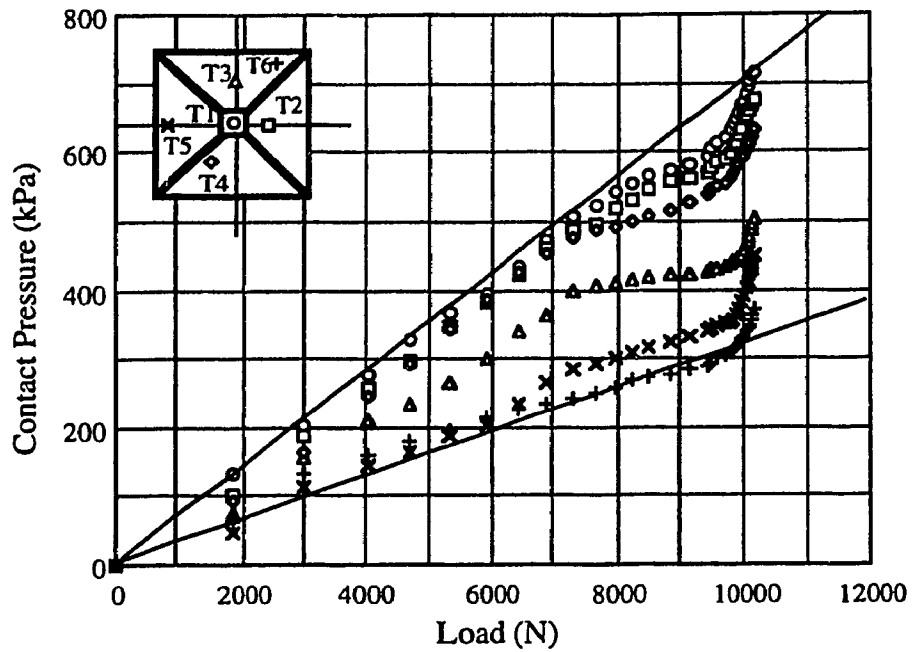


a) Surface Footing

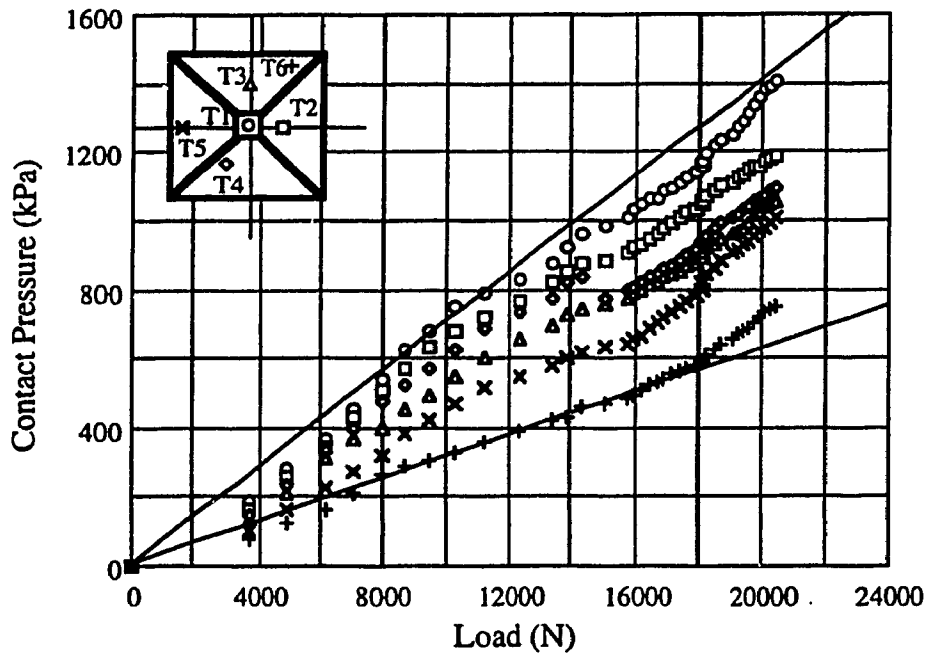


b) Embedded Footing

Figure 3.60 Contact Pressure Envelopes for Pyramidal (1) Footing on Medium Sand

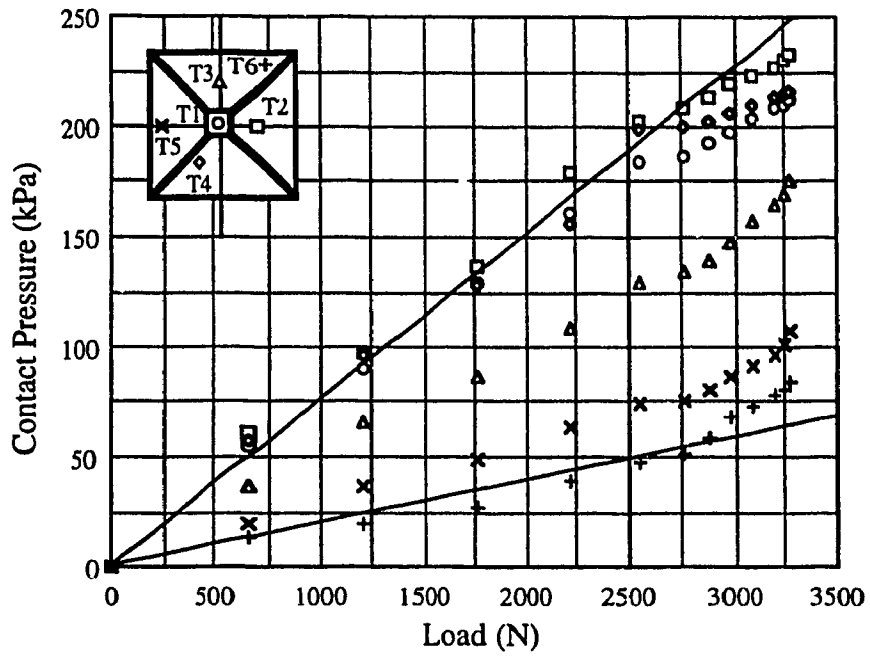


a) Surface Footing

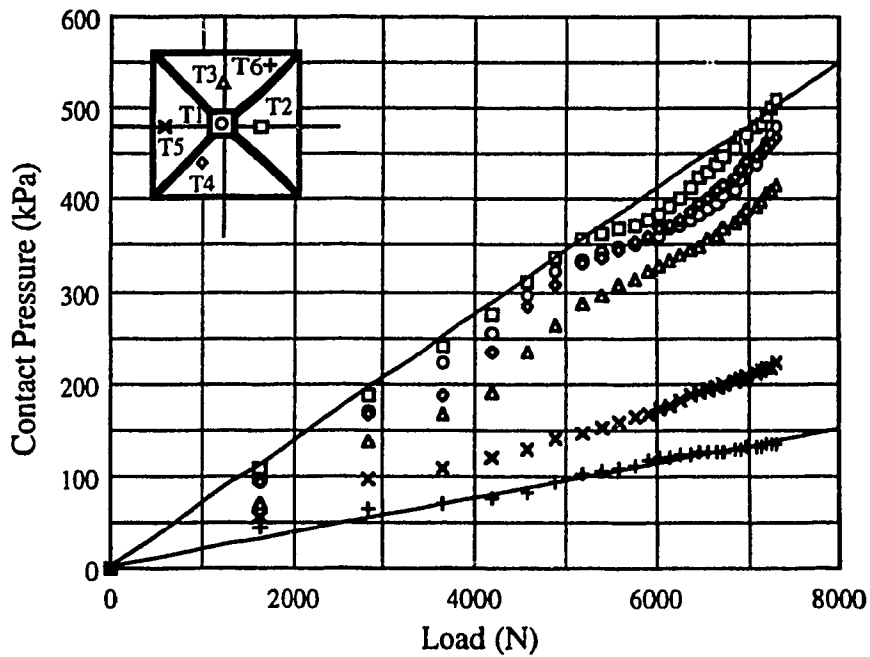


b) Embedded Footing

Figure 3.61 Contact Pressure Envelopes for Pyramidal (1) Footing on Dense Sand



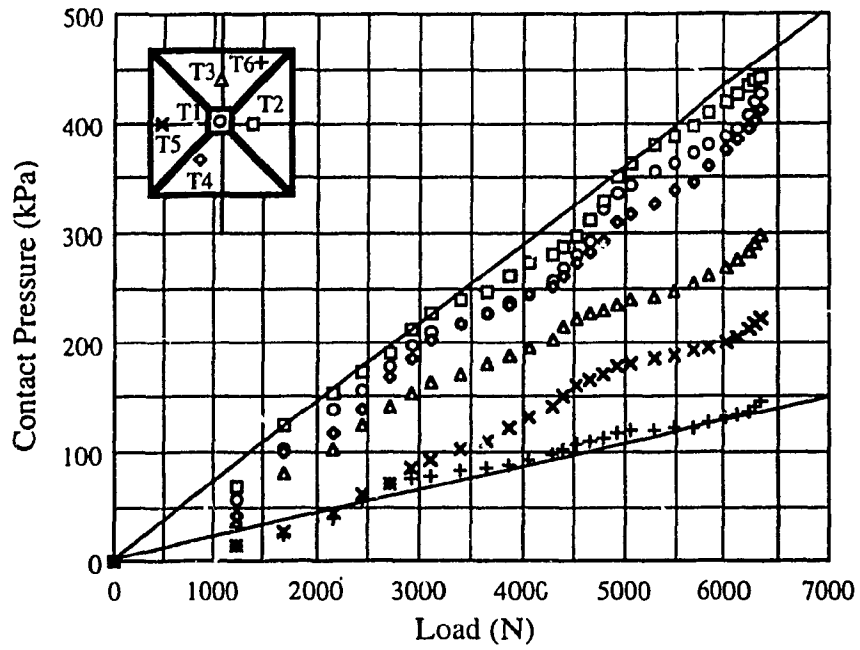
a) Surface Footing



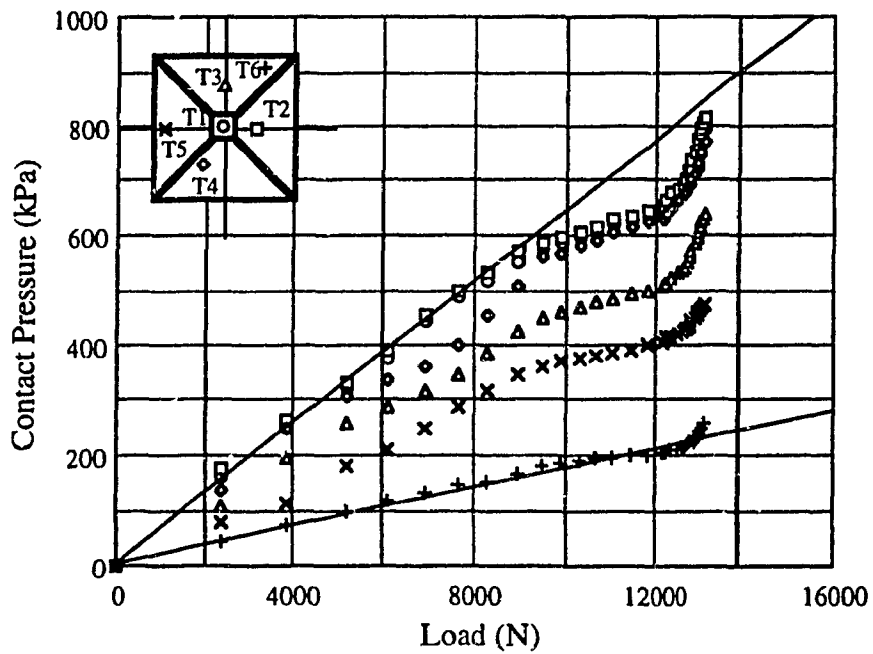
b) Embedded Footing

Figure 3.62 Contact Pressure Envelopes for Pyramidal (2) Footing on Loose Sand



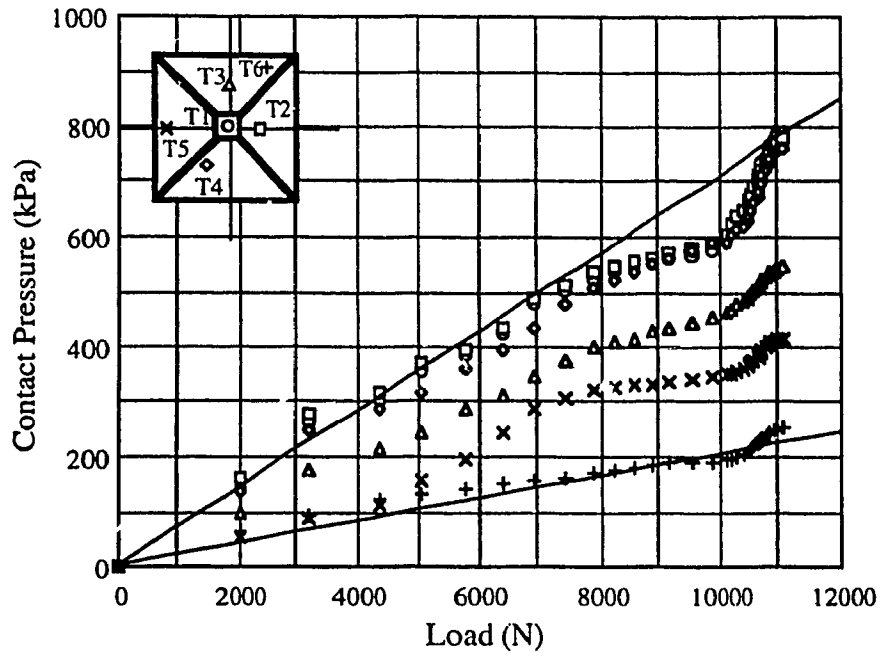


a) Surface Footing

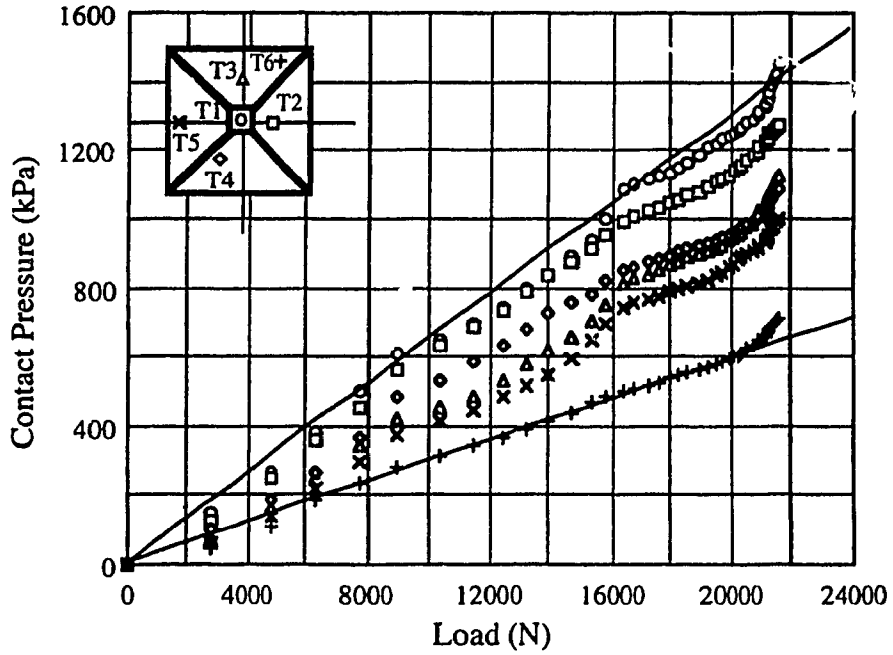


b) Embedded Footing

Figure 3.63 Contact Pressure Envelopes for Pyramidal (2) Footing on Medium Sand



a) Surface Footing



b) Embedded Footing

Figure 3.64 Contact Pressure Envelopes for Pyramidal (2) Footing on Dense Sand

In order to examine the development of the contact pressure distribution, the contact pressures were established at three different loading stages. The load-settlement curve for each test was divided into three main regions (Lambe and Whitman 1979). The first stage was defined at the load causing local shear failure ( $Q_1$ ) where major non-linearity appeared in the load-settlement curve. The second stage is at the bearing capacity load ( $Q_b$ ) which was defined where the slope of the load-settlement curve first reaches a steady minimum value, or in other terms, when the rate of settlement increases rapidly due to a gradual increase in the applied load. The third stage was defined at the prescribed ultimate load ( $Q_u$ ).

The values of  $Q_1$  and  $Q_b$  were determined from the load-settlement curves, and the ratios ( $Q_1/Q_u$ ) and ( $Q_b/Q_u$ ) were calculated to check the validity of the comparison between footings. The ratios ( $Q_1/Q_u$ ) are varied from 38% to 45% and the ratios ( $Q_b/Q_u$ ) are varied from 67% to 75%. The calculated ratios are given in Tables 3.13, 3.14, and 3.15 for the plane strain, axisymmetrical, and three dimensional conditions, respectively.

Table 3.13 Ratios of ( $Q_1 / Q_u$ ) & ( $Q_b / Q_u$ ) for Plane Strain Condition

Footing	Sand State	Surface Footings (D/B= 0)				Embedded Footings (D/B= 0.75)			
		$Q_1(N)$	$Q_1/Q_u$	$Q_b(N)$	$Q_b/Q_u$	$Q_1(N)$	$Q_1/Q_u$	$Q_b(N)$	$Q_b/Q_u$
Strip	Loose	845	0.41	1533	0.74	1903	0.40	3361	0.70
	Medium	1889	0.41	3225	0.70	3897	0.42	6454	0.70
	Dense	3380	0.39	5603	0.68	6685	0.42	10869	0.68
Triang. (1)	Loose	1034	0.42	1697	0.69	2107	0.40	3711	0.70
	Medium	2044	0.39	3596	0.69	4370	0.44	7373	0.73
	Dense	4036	0.42	6632	0.69	6718	0.40	11262	0.67
Triang. (2)	Loose	1265	0.45	2073	0.74	2192	0.38	3836	0.67
	Medium	2567	0.44	4332	0.75	4205	0.39	7661	0.72
	Dense	4106	0.40	7481	0.72	7589	0.43	13001	0.73

Table 3.14 Ratios of ( $Q_l / Q_u$ ) & ( $Q_b / Q_u$ ) for Axisymmetrical Condition

Footings	Sand State	Surface Footings (D/B= 0)				Embedded footings (D/B= 0.75)			
		$Q_l$ (N)	$Q_l/Q_u$	$Q_b$ (N)	$Q_b/Q_u$	$Q_l$ (N)	$Q_l/Q_u$	$Q_b$ (N)	$Q_b/Q_u$
Circular	Loose	800	0.45	1200	0.67	1972	0.42	3432	0.73
	Medium	1679	0.45	2749	0.74	3426	0.40	6233	0.72
	Dense	2899	0.43	4972	0.74	5581	0.38	10609	0.73
Conical (1)	Loose	862	0.40	1620	0.75	2014	0.39	3694	0.71
	Medium	1883	0.44	3060	0.71	3800	0.40	6536	0.69
	Dense	3385	0.44	5693	0.74	6287	0.40	10812	0.69
Conical (2)	Loose	1052	0.43	1730	0.70	2482	0.44	3970	0.71
	Medium	1982	0.41	3546	0.74	4376	0.43	7180	0.71
	Dense	3560	0.42	6324	0.75	7056	0.42	11577	0.69

Table 3.15 Ratios of ( $Q_l / Q_u$ ) & ( $Q_b / Q_u$ ) for Three Dimensional Condition

Footings	Sand State	Surface Footings (D/B=0)				Embedded Footings (D/B=0.75)			
		$Q_l$ (N)	$Q_l/Q_u$	$Q_b$ (N)	$Q_b/Q_u$	$Q_l$ (N)	$Q_l/Q_u$	$Q_b$ (N)	$Q_b/Q_u$
Square	Loose	1047	0.44	1724	0.73	2463	0.40	4287	0.70
	Medium	2088	0.42	3678	0.74	4526	0.40	7784	0.69
	Dense	3864	0.43	6628	0.73	7972	0.42	13656	0.72
Pyram. (1)	Loose	1200	0.42	2051	0.72	2611	0.38	4697	0.69
	Medium	2299	0.40	4157	0.73	5217	0.42	8803	0.72
	Dense	4012	0.39	7309	0.72	7973	0.39	14287	0.70
Pyram. (2)	Loose	1400	0.43	2300	0.70	2825	0.39	5182	0.71
	Medium	2718	0.43	4509	0.71	5195	0.39	9463	0.72
	Dense	4324	0.39	7878	0.71	8949	0.41	15797	0.73

The contact pressure at the edge of the footings was determined by equating the given applied load ( $Q_t$ ,  $Q_b$ , or  $Q_u$ ) with the integration of the contact pressure diagram over the surface area of the base of footings using the measured contact pressures at the predetermined locations of the pressure transducers. It should be admitted that the pressure diagram connecting any two points was assumed to be linear.

For the plane strain condition, an average reading of the contact pressures measured by pressure transducers located on the same axis was used in the pressure diagram. Since the contact pressure distribution for the three dimensional conditions is indeterminate, an assumption was made to determine the contact pressures at the edges. The total contact pressure at the edges was distributed according to the distance from the center of footing. A zero value at the edge indicates that the volume of the measured contact pressure diagram was greater than the total applied load. This suggests the existence of a lower pressure reading located in between two consecutive pressure transducers than that assumed due to the linear relationship. The locations of the points, at which the contact pressures are measured, are given in Table 3.16. The values of the contact pressure measured at the three loading stages and the calculated values at the edge of footings are presented in Tables 3.17 through 3.22 for all loading tests.

Table 3.16 Locations of Reference Points from The Center of Footing (in mm)

	Plane Strain			Axisymmetrical			Three Dimensional		
	Strip	Triang. (1)	Triang. (2)	Circular	Conical(1)	Conical(2)	Square	Pyram. 2)	Pyram. (1)
Point (1)	30	30	40	30	30	40	30	30	40
Point (2)	60	60	80	45	45	60	45	30*	40*
Point (3)	---	---	---	60	60	80	50	45	60
Point (4)	---	---	---	---	---	---	60	60	80
Point (5)	---	---	---	---	---	---	80	60*	80*

\* measured on the diagonal

Table 3.17 Contact Pressures for Plane Strain Condition for Surface Footings

Footing	Sand State	Surface Footings (D/B= 0)											
		Pressures at $Q_1$ (kPa)				Pressures at $Q_b$ (kPa)				Pressures at $Q_u$ (kPa)			
		Center	Point (1)	Point (2)	Edge	Center	Point (1)	Point (2)	Edge	Center	Point (1)	Point (2)	Edge
Strip	Loose	26	39	45	-----	56	84	67	-----	76	113	89	-----
	Medium	61	89	75	44	113	133	142	84	163	189	213	98
	Dense	121	143	169	23	218	237	273	93	308	351	383	207
Triang. (1)	Loose	30	44	57	15	58	76	93	10	87	109	137	12
	Medium	66	79	92	74	136	148	171	75	197	220	238	126
	Dense	143	169	193	90	243	271	303	176	364	396	437	230
Triang. (2)	Loose	37	48	63	38	67	79	101	60	94	115	139	61
	Medium	76	92	119	102	160	179	191	121	201	231	253	199
	Dense	144	167	183	123	271	297	327	240	398	429	466	248

Table 3.18 Contact Pressures for Plane Strain Condition for Embedded Footings

Footing	Sand State	Embedded Footings ( $D/B=0.75$ )											
		Pressures at $Q_1$ (kPa)				Pressures at $Q_b$ (kPa)				Pressures at $Q_u$ (kPa)			
		Center	Point (1)	Point (2)	Edge	Center	Point (1)	Point (2)	Edge	Center	Point (1)	Point (2)	Edge
Strip	Loose	61	72	83	80	100	126	142	167	158	189	203	193
	Medium	123	159	176	117	200	243	281	286	326	359	372	404
	Dense	229	258	283	264	343	389	446	601	557	593	659	699
Triang. (1)	Loose	73	83	92	74	123	141	167	135	191	209	231	182
	Medium	140	169	191	171	257	288	331	242	347	398	437	350
	Dense	243	269	301	201	431	458	491	325	631	692	735	498
Triang. (2)	Loose	61	79	93	108	125	143	157	173	196	224	247	201
	Medium	146	167	189	131	273	296	337	258	378	419	451	387
	Dense	271	301	321	269	460	493	536	527	687	719	753	562

Table 3.19 Contact Pressures for Axisymmetrical Condition for Surface Footings

Footing	Sand State	Surface Footings (D/B= 0)														
		Pressures at $Q_1$ (kPa)					Pressures at $Q_b$ (kPa)					Pressures at $Q_u$ (kPa)				
		Center	Point (1)	Point (2)	Point (3)	Edge	Center	Point (1)	Point (2)	Point (3)	Edge	Center	Point (1)	Point (2)	Point (3)	Edge
Circular	Loose	49	61	44	38	-----	67	81	71	59	-----	102	127	105	86	-----
	Medium	83	118	91	76	9	155	187	152	125	-----	204	246	209	171	11
	Dense	161	211	169	135	-----	265	333	284	248	-----	362	427	386	351	1
Conical (1)	Loose	29	36	50	57	40	71	89	106	81	74	81	99	119	147	77
	Medium	63	75	91	109	130	125	141	165	182	140	165	196	234	267	191
	Dense	149	173	191	223	85	235	276	317	355	211	332	371	415	475	300
Conical (2)	Loose	27	37	49	65	80	43	58	85	121	112	76	98	133	169	118
	Medium	50	66	80	109	182	118	147	172	203	236	180	216	241	275	275
	Dense	133	169	197	227	140	296	317	342	371	222	367	429	486	513	258



Table 3.20 Contact Pressures for Axisymmetrical Condition for Embedded Footings

Footings	Sand State	Embedded Footings ( $D/B = 0.75$ )														
		Pressures at $Q_1$ (kPa)					Pressures at $Q_b$ (kPa)					Pressures at $Q_u$ (kPa)				
		Center	Point (1)	Point (2)	Point (3)	Edge	Center	Point (1)	Point (2)	Point (3)	Edge	Center	Point (1)	Point (2)	Point (3)	Edge
Circular	Loose	135	116	97	83	31	231	198	164	125	109	315	249	201	175	219
	Medium	229	196	163	138	93	379	336	295	253	270	501	469	406	371	372
	Dense	336	298	267	243	220	569	547	515	488	510	787	751	710	678	670
Conical (1)	Loose	61	82	109	122	126	126	159	197	241	181	197	243	279	307	263
	Medium	131	163	192	233	218	239	276	325	386	390	369	409	478	545	536
	Dense	281	326	378	431	402	479	546	597	647	383	693	779	863	949	555
Conical (2)	Loose	82	117	128	144	141	163	180	206	221	210	231	252	283	319	299
	Medium	187	203	221	225	252	296	331	365	387	399	441	477	509	537	544
	Dense	308	339	371	416	294	561	593	632	671	378	797	839	892	947	635

Table 3.21 Contact Pressures for Three Dimensional Condition for Surface Footings

Footing	Sand State	Surface Footings (D/B= 0)																				
		Pressures at $Q_1$ (kPa)					Pressures at $Q_b$ (kPa)					Pressures at $Q_u$ (kPa)										
		Center	Point (1)	Point (2)	Point (3)	Point (4)	Point (5)	Edges	Center	Point (1)	Point (2)	Point (3)	Point (4)	Point (5)	Edges	Center	Point (1)	Point (2)	Point (3)	Point (4)	Point (5)	Edges
Square	Loose	84	79	61	50	43	38	---	130	123	96	83	80	57	---	177	149	143	110	117	92	---
	Medium	143	129	96	96	89	63	36	267	230	176	153	156	141	26	369	309	252	201	210	191	18
	Dense	298	253	186	173	177	130	---	496	417	341	308	319	188	2	686	559	481	440	451	226	---
Pyram. (1)	Loose	87	98	75	86	52	43	---	152	163	113	158	93	66	---	204	217	147	210	128	96	---
	Medium	174	183	97	153	62	96	---	278	282	180	254	159	126	20	398	377	289	339	270	210	---
	Dense	278	256	209	246	143	160	---	509	486	398	476	286	243	---	716	675	503	631	447	369	---
Pyram. (2)	Loose	110	118	76	112	43	23	---	173	191	119	178	69	43	---	212	233	176	216	107	84	79
	Medium	179	191	142	168	71	71	27	281	297	223	273	160	108	67	427	441	298	413	221	146	39
	Dense	304	317	215	287	112	120	---	524	537	398	506	320	173	4	791	780	547	763	415	253	---

Table 3.22 Contact Pressures for Three Dimensional Condition for Embedded Footings

Footings	Sand State	Embedded Footings ( $D/B=0.75$ )																				
		Pressures at $Q_1$ (kPa)					Pressures at $Q_b$ (kPa)					Pressures at $Q_u$ (kPa)										
		Center	Point (1)	Point (2)	Point (3)	Point (4)	Point (5)	Edges	Center	Point (1)	Point (2)	Point (3)	Point (4)	Point (5)	Edges	Center	Point (1)	Point (2)	Point (3)	Point (4)	Point (5)	Edges
Square	Loose	159	133	121	103	94	75	85	283	241	217	169	155	143	132	427	362	292	247	234	198	357
	Medium	303	255	187	197	202	105	165	507	449	351	315	324	187	300	776	652	543	419	437	352	344
	Dense	512	456	387	344	357	186	249	878	791	690	561	633	312	403	1242	1089	967	787	898	437	523
Pyram. (1)	Loose	150	166	127	139	87	84	63	287	298	244	271	182	133	53	407	423	373	398	273	172	76
	Medium	311	336	247	296	175	143	122	537	523	447	519	303	220	202	754	737	609	717	498	326	204
	Dense	542	505	398	476	323	263	-----	958	876	743	837	618	458	-----	1404	1187	1050	1090	1010	750	-----
Pyram.(2)	Loose	171	187	138	166	98	63	334	356	287	331	147	102	480	509	415	467	221	136			
	Medium	321	332	257	308	179	100	576	587	447	559	362	180	796	817	637	773	474	259			
	Dense	609	565	419	487	374	280	997	954	753	823	694	484	1452	1276	1127	1087	1002	708			

Figures 3.65 through 3.70 present the contact pressure distribution over the base of the footings at the three defined loading stages. For the plane strain and axisymmetrical conditions, the contact pressure distribution is presented only in two directions since it is constant in the third one. However, the contact pressure distribution for the three dimensional condition is presented in an isometric view showing the variation of the contact pressure over a triangular area representing one-eighth of the footing.

Figures 3.65, 3.66, and 3.67 show the contact pressure distribution for the plane strain condition: strip flat, triangular (1) shell, and triangular (2) shell footings, respectively. The surface strip flat footing had zero pressure at the edge throughout the three loading stages for the case of loose sand. However, for medium and dense sand, although the contact pressure decreased remarkably towards the edge, it did not reach a zero value at the edge. The maximum pressure occurred at  $(2/3B)$  from the center for medium and dense sand, and at  $(1/3B)$  for loose sand.

The contact pressure distribution for the embedded strip flat footing had different trend than that of the surface one. The maximum contact pressure occurred at the edge of footing at the bearing capacity and the ultimate loading stages. However, at the first loading stage, it reached the maximum pressure near the edge and then decreased again at the edge. The difference between the contact pressure at the center and at the edge for loose and medium sand was relatively small. However, for dense sand, the contact pressure at the edge was remarkably higher than that at the center, specially at the bearing capacity stage.

The contact pressure at the edge of the surface triangular (1) shell footing was nearly zero for the case of loose sand. The maximum contact pressure occurred at  $(2/3B)$  from the center. This trend also held true for both medium and dense sand states, however, the contact pressure at the edge was almost half the pressure at the center. However, for the first loading stage for medium sand, the contact pressure distribution was nearly uniform.

The contact pressure for the embedded triangular (1) shell footing on loose sand was nearly uniform at the first loading stage. Then, by increasing the applied load, the contact pressure increased with some concentration near the edge. The maximum contact pressure occurred at  $(2/3B)$  from the center. This trend was similar for both medium and dense sand, however, when the contact pressure reached its maximum value, it decreased remarkably at the edge, specially for dense sand.

The configuration of the contact pressure distribution for the surface and embedded triangular (2) shell footing was almost similar to the one described for the triangular (1) shell footing. The maximum contact pressure occurred at  $(2/3B)$  from the center for almost all cases, except for the contact pressure of the embedded footing on loose sand, which increased linearly from the center towards the edge for during first and second loading stages. The contact pressure at the edge was approximately equal to the one at the center, except at the ultimate stage, the contact pressure decreased remarkably at the edge.

Figures 3.68, 3.69, and 3.70 show the contact pressure distribution for the axisymmetrical condition: circular flat, conical (1) shell, and conical (2) shell footings, respectively. For the surface circular flat footing, the maximum contact pressure occurred at  $(1/3B)$  from the center and decreased gradually until it reached a zero value at the edge. This trend held true for all sand states at the three loading stages.

The maximum pressure for the embedded circular flat footing occurred at the center and decreased gradually towards the edge. However, it did not reach a zero value at the edge. The contact pressure at the edge was almost  $(2/3)$  the pressure at the center. The distribution for dense sand was nearly uniform and had a linear relationship.

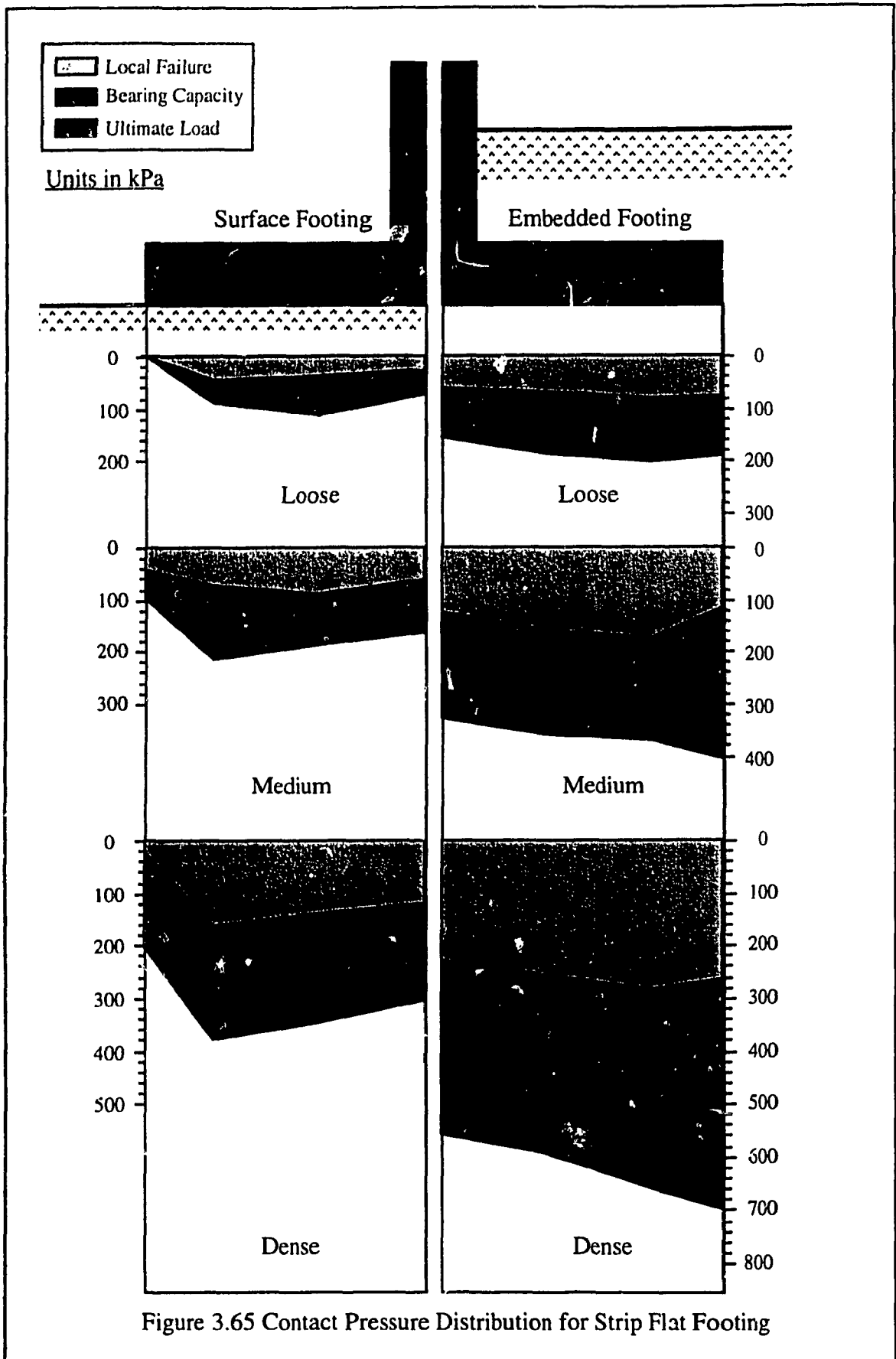
The maximum contact pressure for the surface conical (1) shell footing occurred at  $(2/3B)$  from the center for all cases, except for the first stage for medium sand, where the contact pressure increased linearly from the center towards the edge.

The contact pressure distribution of the embedded conical (1) shell footing varied according to the sand state. The maximum contact pressure occurred at the same location as for the surface footing. However, for loose sand, the pressure increased gradually until it reached the maximum value and then decreased again at the edge. The same trend applied for medium sand, however, the contact pressure remained constant from the point of maximum pressure until the edge. For dense sand, the contact pressure, after it reached its maximum value, decreased remarkably towards the edge. The contact pressure at the edge for loose and medium sand was higher than that at the center. This trend was reversed for dense sand, where the contact pressure at the center was relatively higher than that at the edge.

The behavior of the conical (2) shell footing was similar to that of the conical (1) shell footing. However, at the ultimate stage for the surface footing on medium sand, the contact pressure remained constant from the point of maximum pressure up to the edge. Also, the contact pressure at the edge of the embedded footing at the first loading stage was nearly the same as that occurred at the center.

Figures 3.71, 3.72, and 3.73 show the contact pressure distribution for the three dimensional condition: square flat, pyramidal (1) shell, and pyramidal (2) shell footings, respectively. For the surface and embedded square flat footing, the maximum contact pressure occurred at the centre and decreased towards the edge with more reduction on the diagonal. It can be noticed that the contact pressure at the edge of the surface footing reached a zero value for all sand states during all loading stages.

For the two pyramidal shell footings, the trend was almost the same. The maximum contact pressure occurred at the centre, however, there was an area around the centre of footing having the same contact pressure. The only exception case was the embedded footing on dense sand, which was similar to the square footing with maximum pressure at the centre and decreased towards the edge.



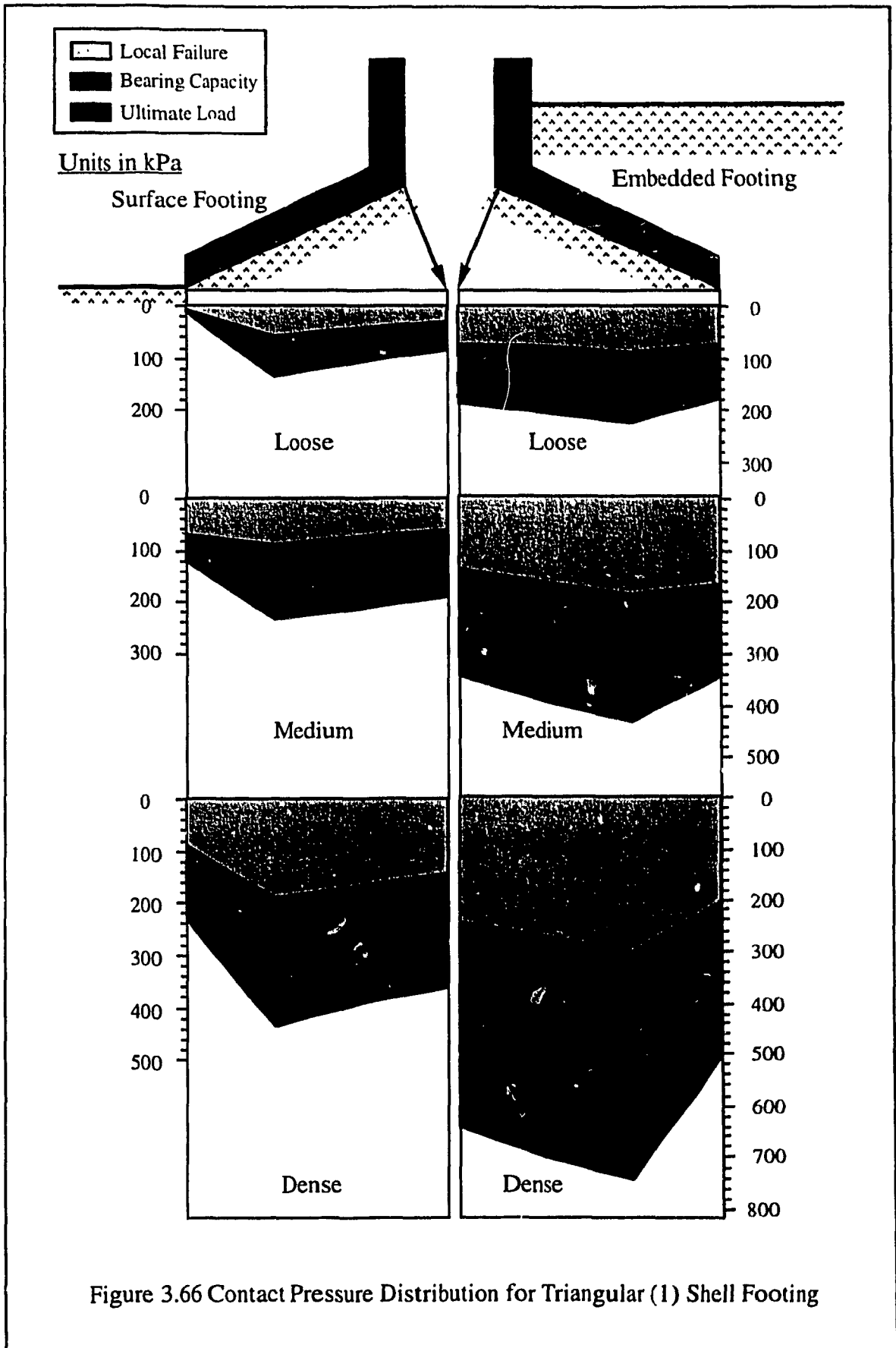


Figure 3.66 Contact Pressure Distribution for Triangular (1) Shell Footing



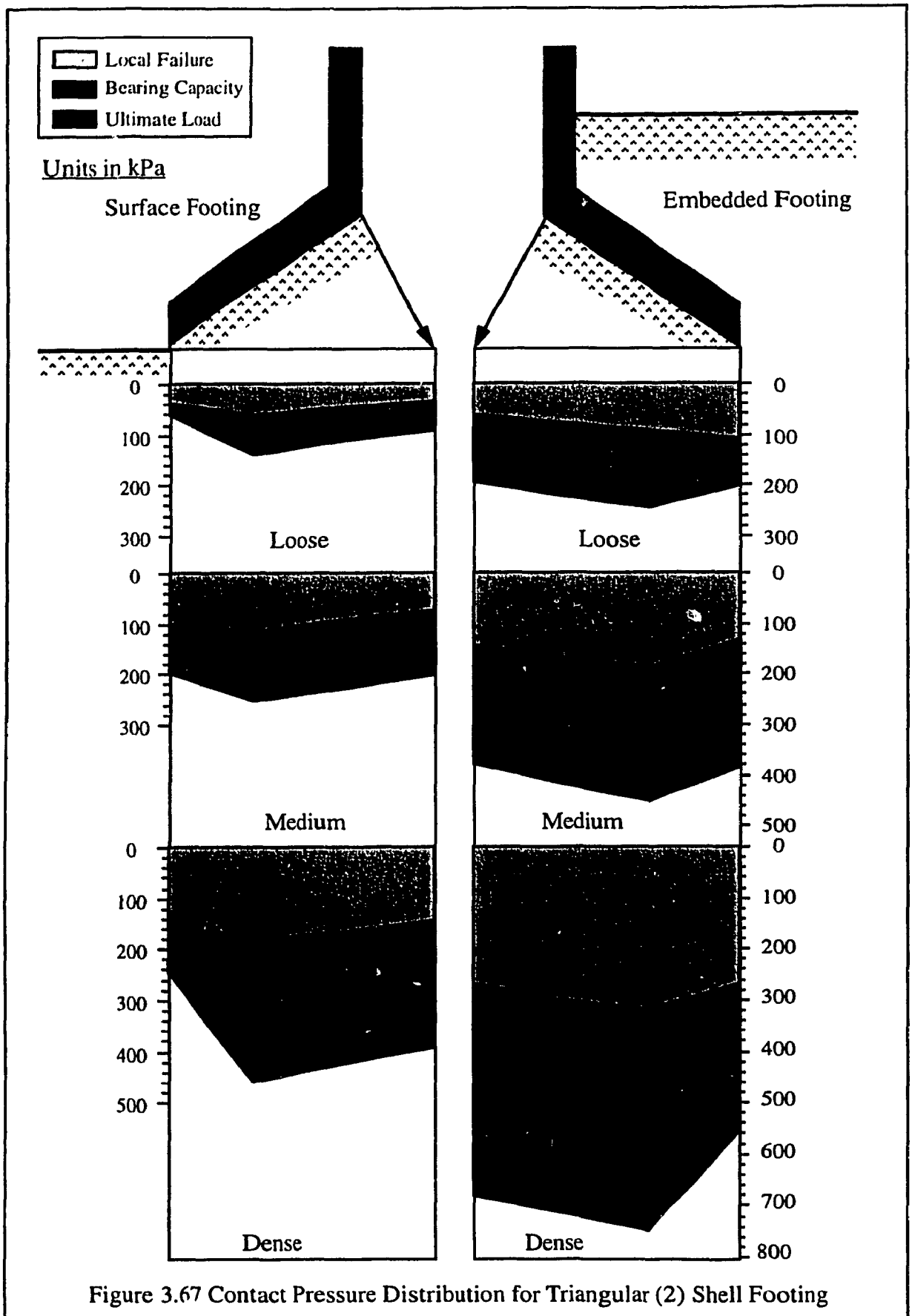


Figure 3.67 Contact Pressure Distribution for Triangular (2) Shell Footing

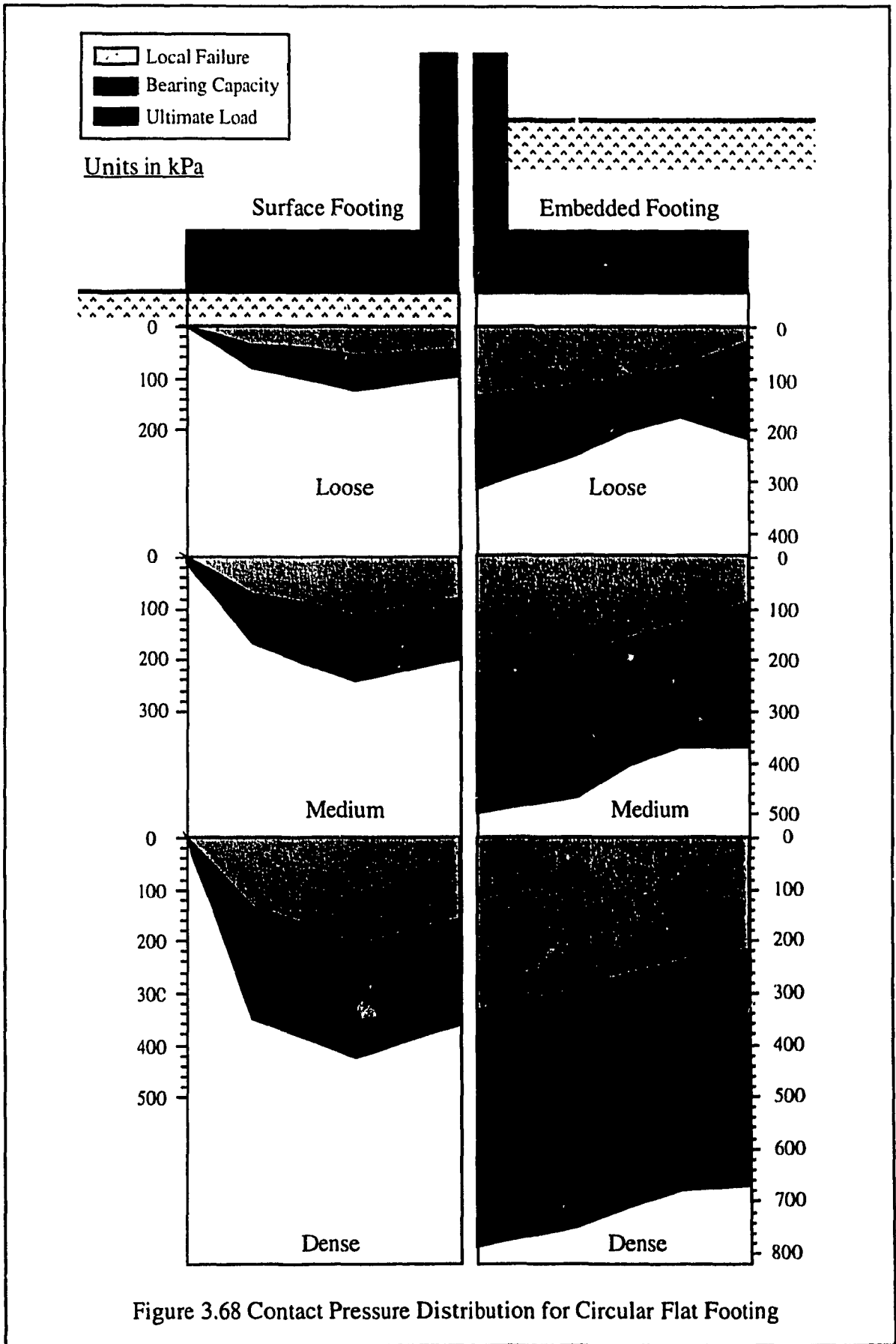
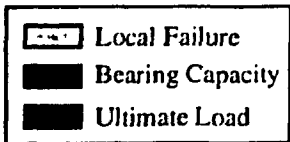


Figure 3.68 Contact Pressure Distribution for Circular Flat Footing



Units in kPa

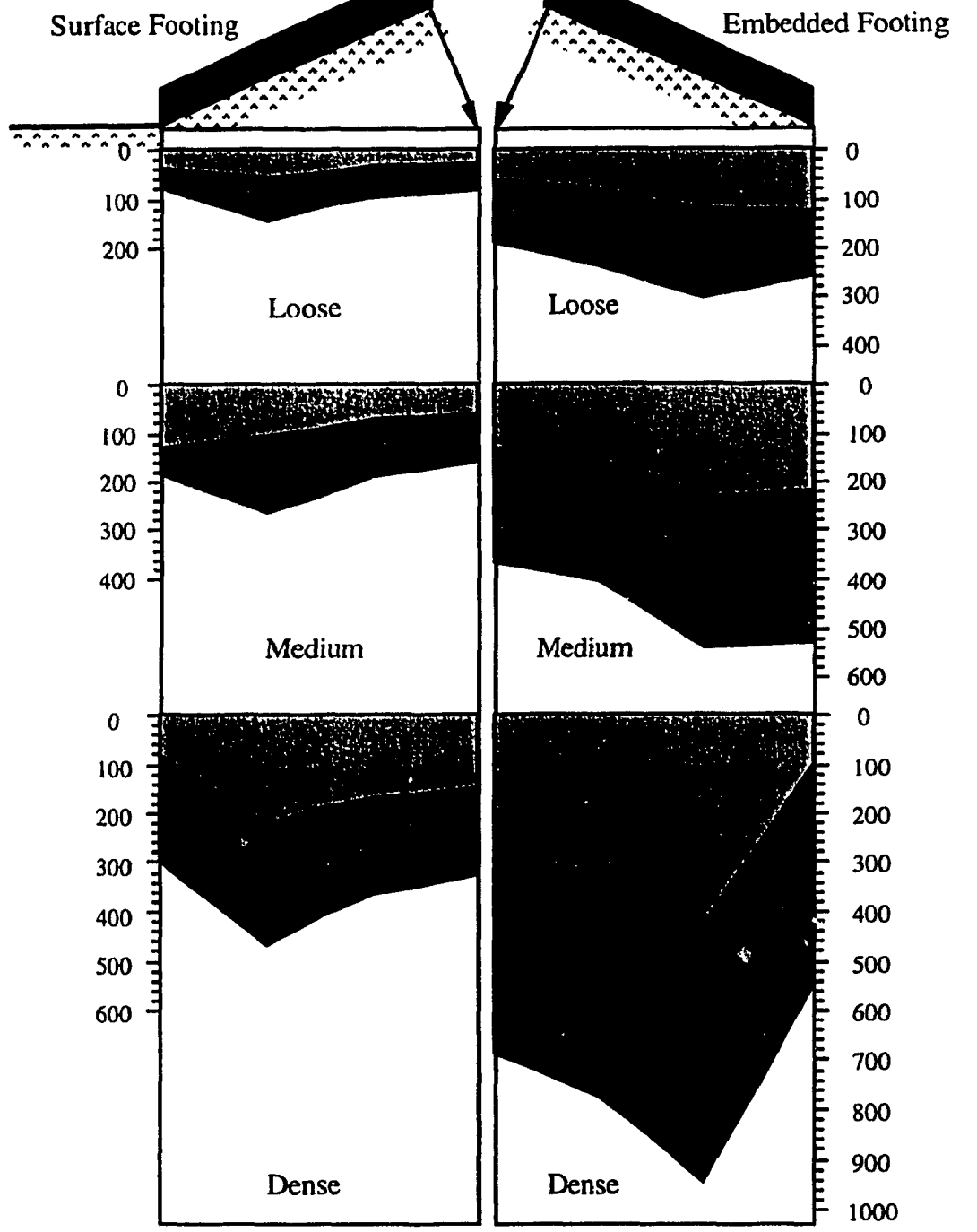
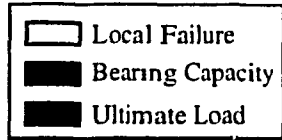


Figure 3.69 Contact Pressure Distribution for Conical (1) Shell Footing



Units in kPa

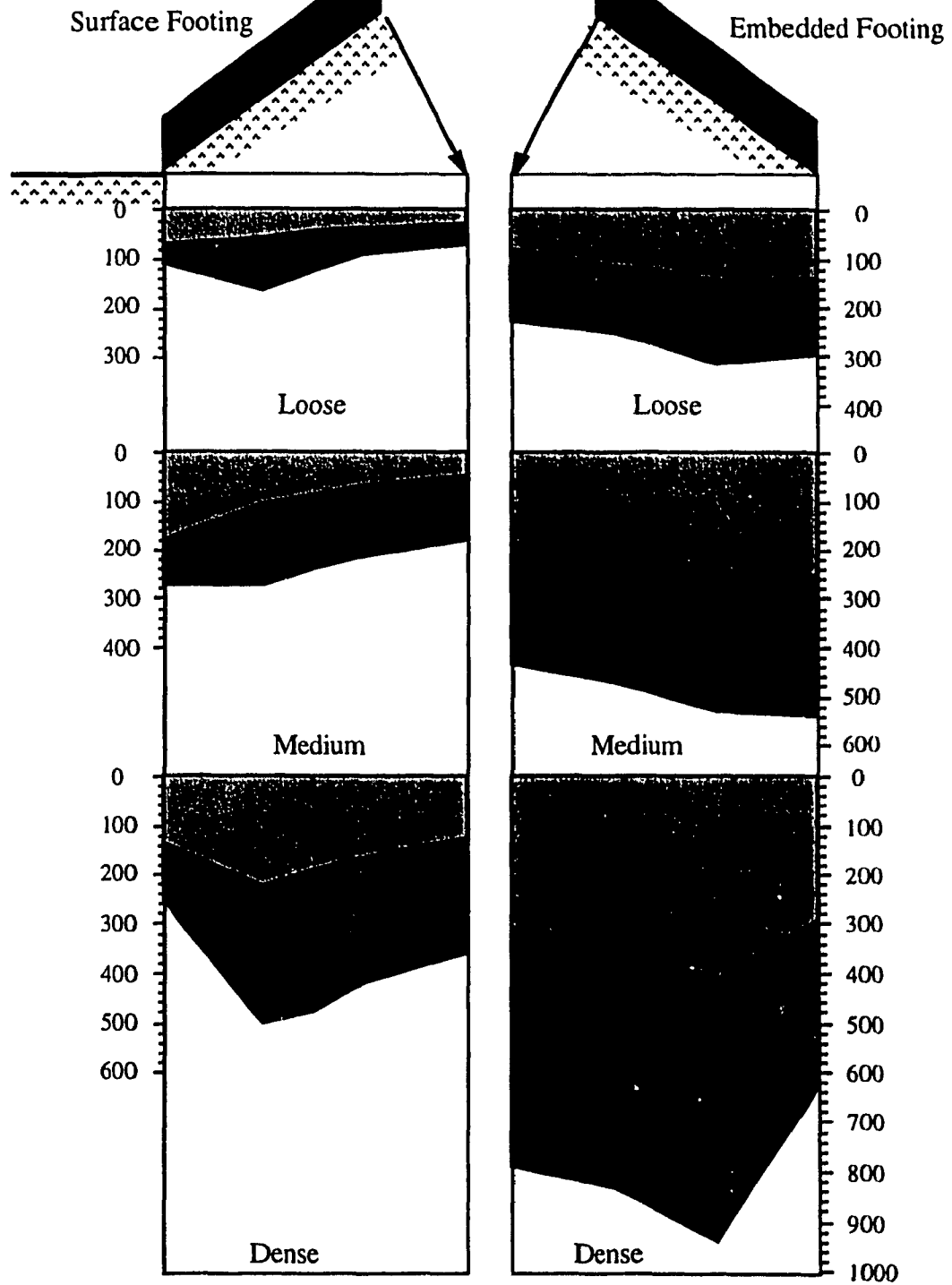
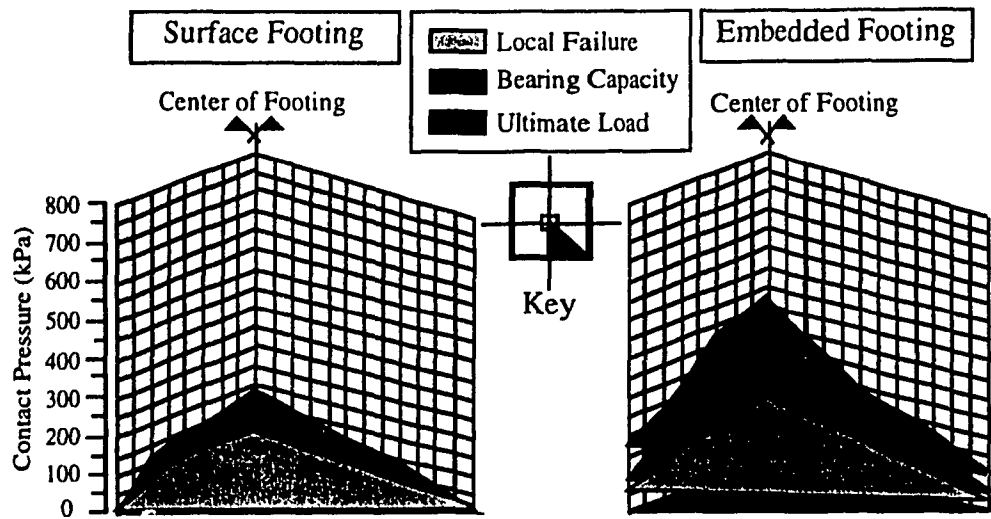
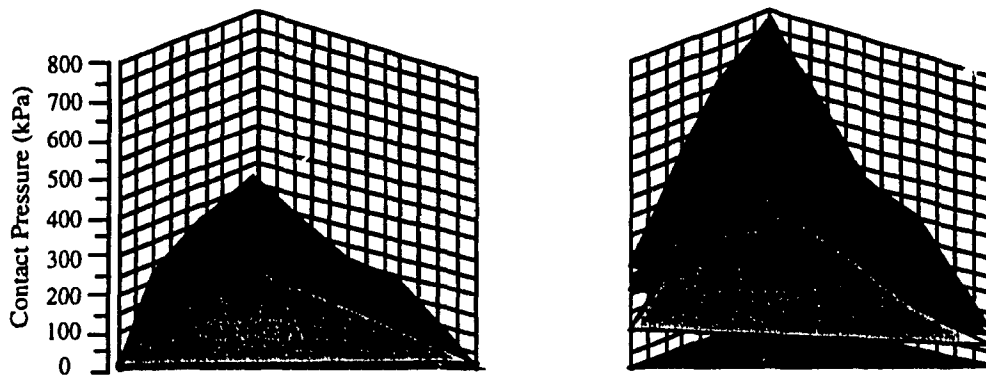


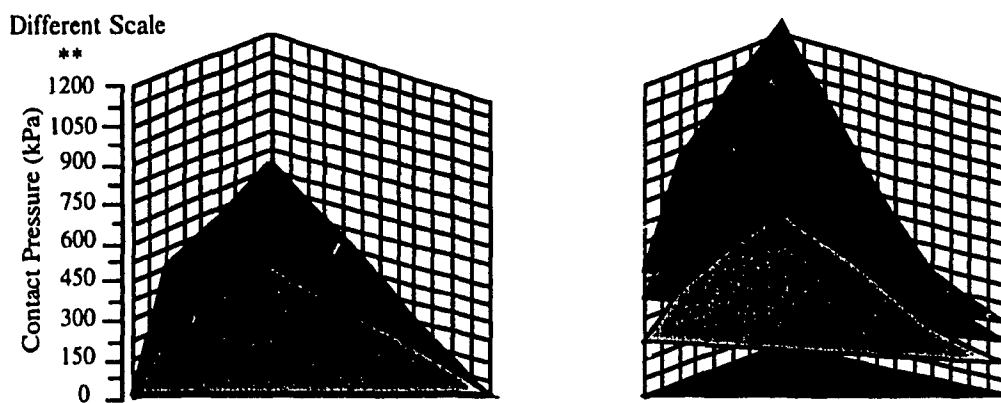
Figure 3.70 Contact Pressure Distribution for Conical (2) Shell Footing



Loose Sand State



Medium Sand State



Dense Sand State

Figure 3.71 Contact Pressure Distribution for Square Flat Footing

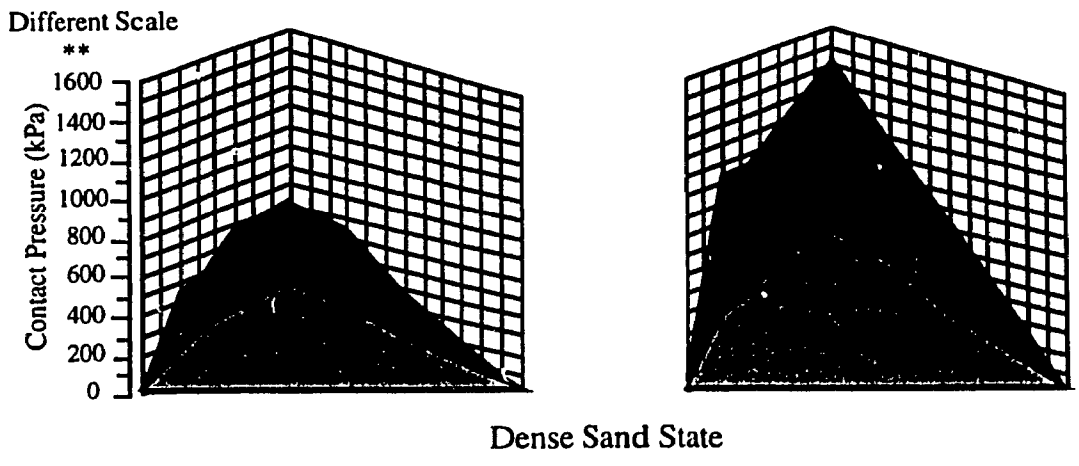
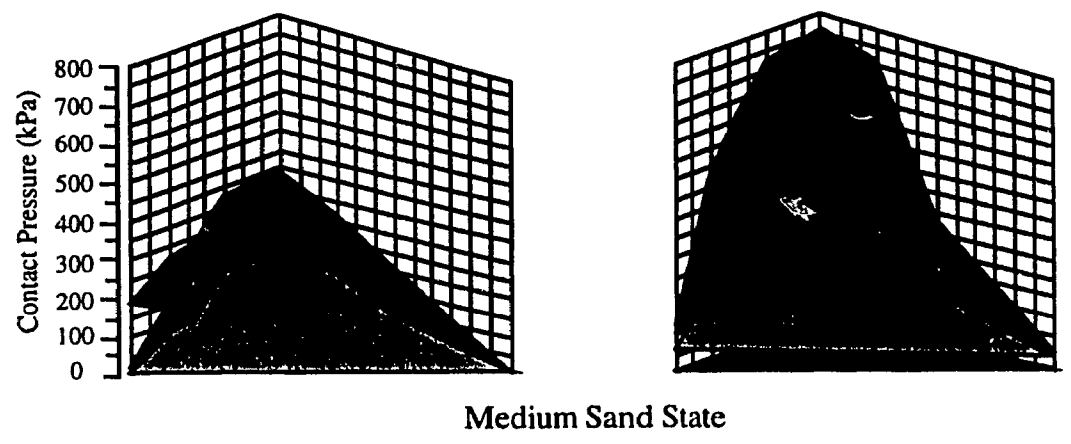
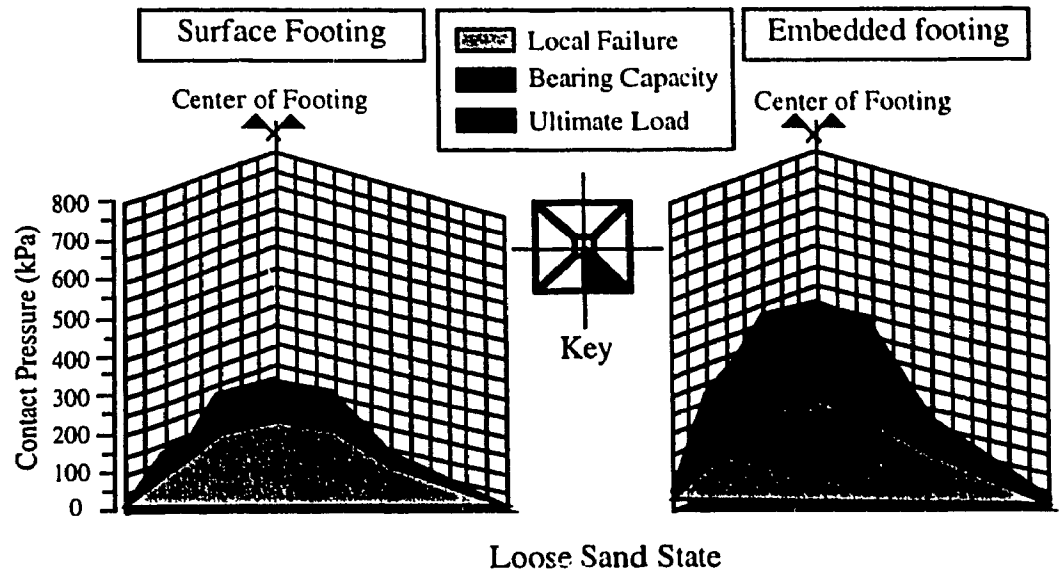
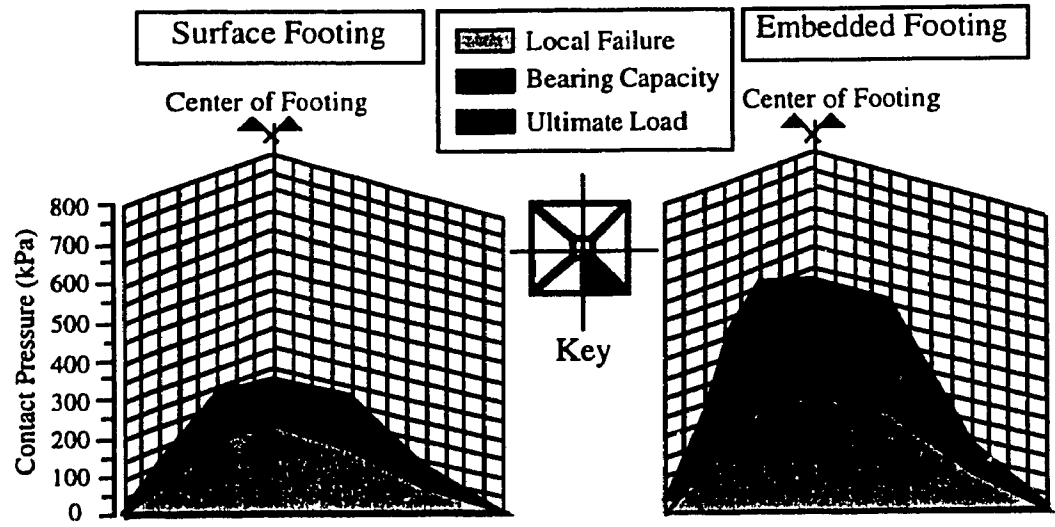
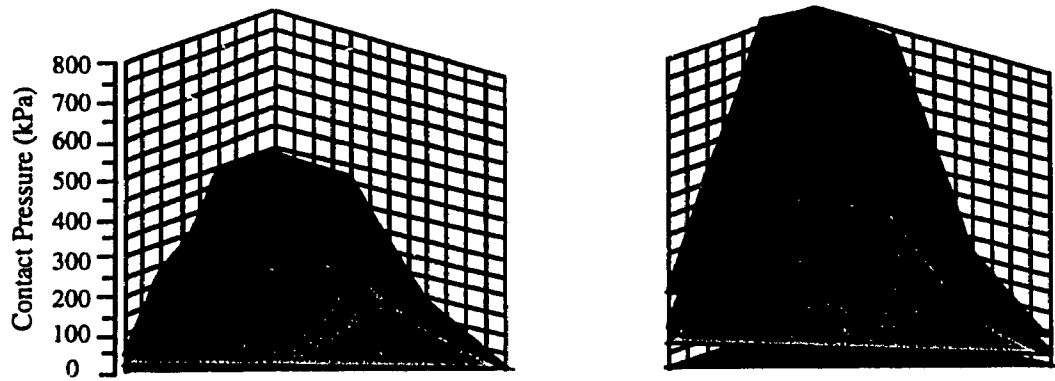


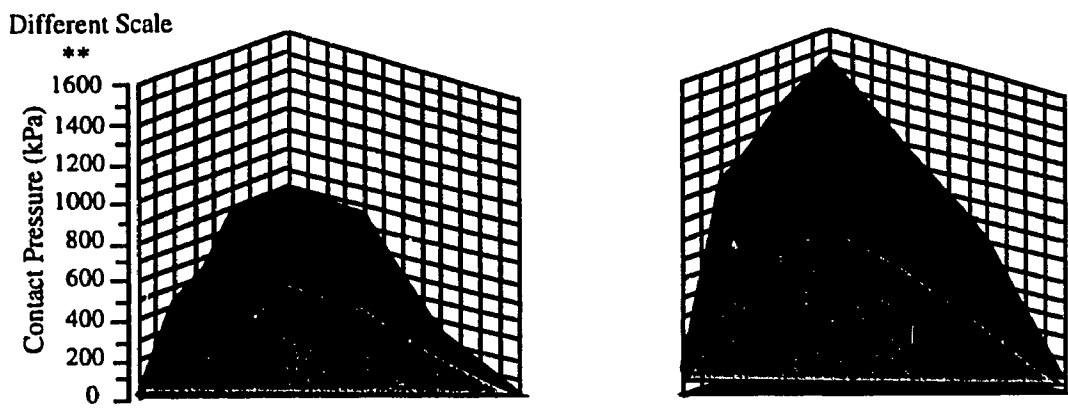
Figure 3.72 Contact Pressure Distribution for Pyramidal (1) Shell Footing



Loose Sand State



Medium Sand State



Dense Sand State

Figure 3.73 Contact Pressure Distribution for Pyramidal (2) Shell Footing

### 3.8.4 Vertical & Lateral Stresses

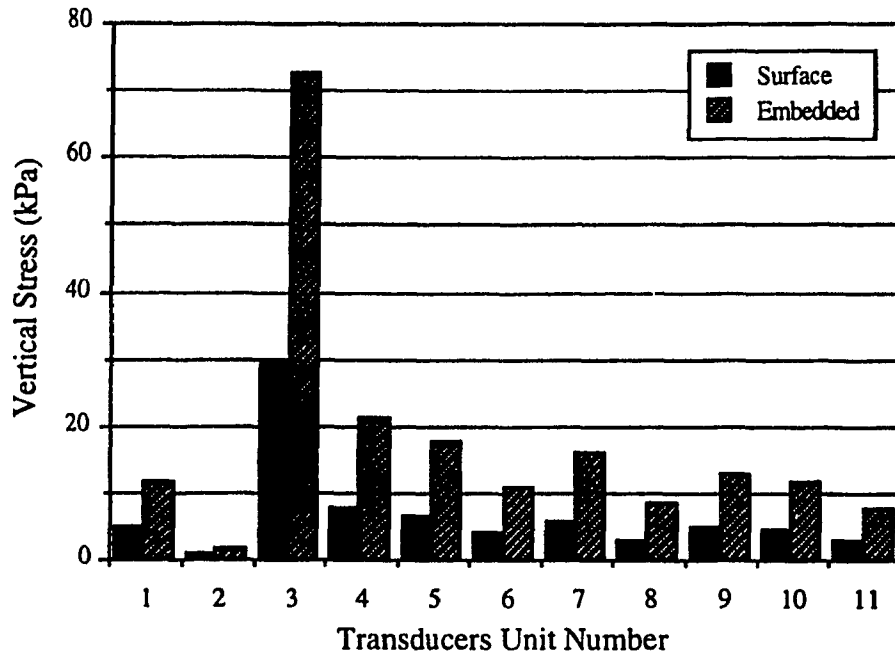
The vertical and lateral stresses induced within the sand mass during the loading process of the axisymmetrical footings (circular flat and conical shell footings) and the three dimensional footings (square flat and pyramidal shell footings) were measured by the pressure transducers located inside the box units. There are eleven box units (1 to 11) arranged in a staggered position inside the steel tank as shown in Figure 3.14. The coordinates of these box units inside the tank were given in Table 3.1. Each box unit contains two pressure transducers, one to measure the vertical stress and the other to measure the lateral stress acting perpendicular to the surface of the transducers. The measurements were recorded throughout the loading process and until failure occurred, i.e, at the ultimate load.

The vertical and lateral stresses acted on each pressure transducer are presented herein using vertical and horizontal bar charts, respectively. The test results at a particular sand state for each footing are grouped in one figure, which includes the tests conducted on the surface as well as the embedded footing. Each figure includes two charts: charts (a) and (b), showing the vertical and lateral stresses for each transducer at the ultimate load, respectively. Figures 3.74 to 3.76 show the tests results for the circular flat footing, Figures 3.77 to 3.79 for the conical (1) shell footing, Figures 3.80 to 3.82 for the conical (2) shell footing, Figures 3.83 to 3.84 for the square flat footing, Figures 3.86 to 3.88 for the pyramidal (1) shell footing, and Figures 3.89 to 3.91 for the pyramidal (2) shell footing.

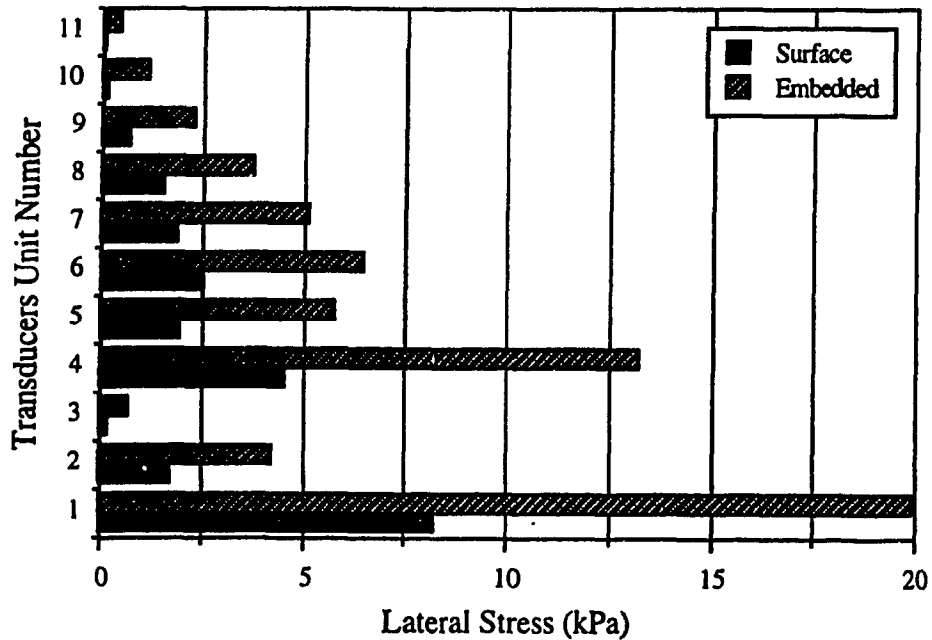
In general, it can be noticed from these figures that the vertical and lateral stresses for the embedded footing are higher than that for the surface one. The maximum vertical stress occurred at the pressure transducer unit number (3) for all tests, which is located at the center line of footing at depth equal to the width of footing. However, the maximum lateral stress occurred at the pressure transducer unit number (1) for all tests, which is located at a distance equal the width of footing from the center line at a depth equal to half the width of footing.



For Positions of Transducers Refer to Figure 3.14



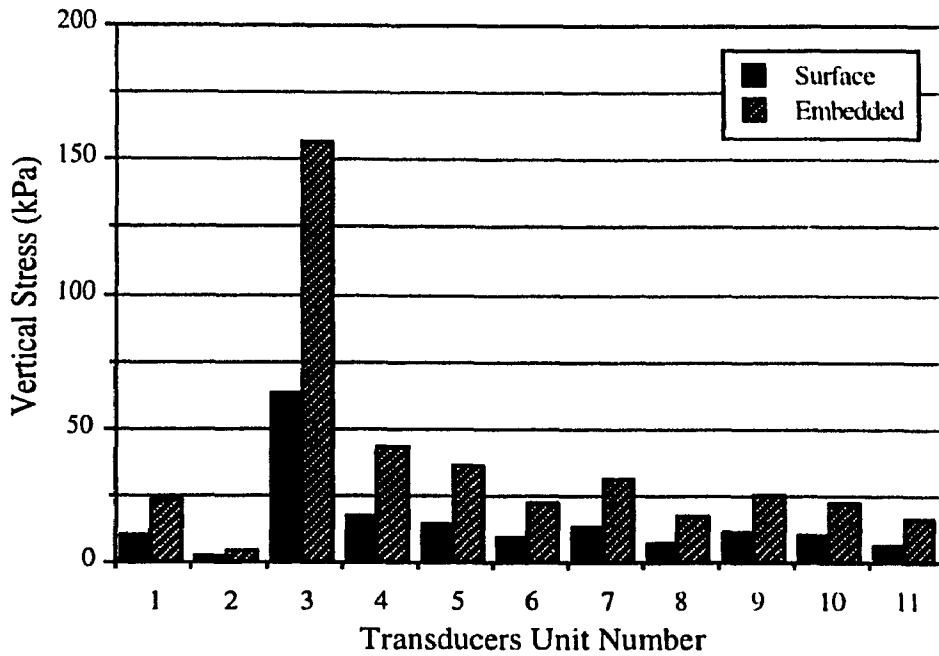
a) Vertical Stresses at Ultimate Load



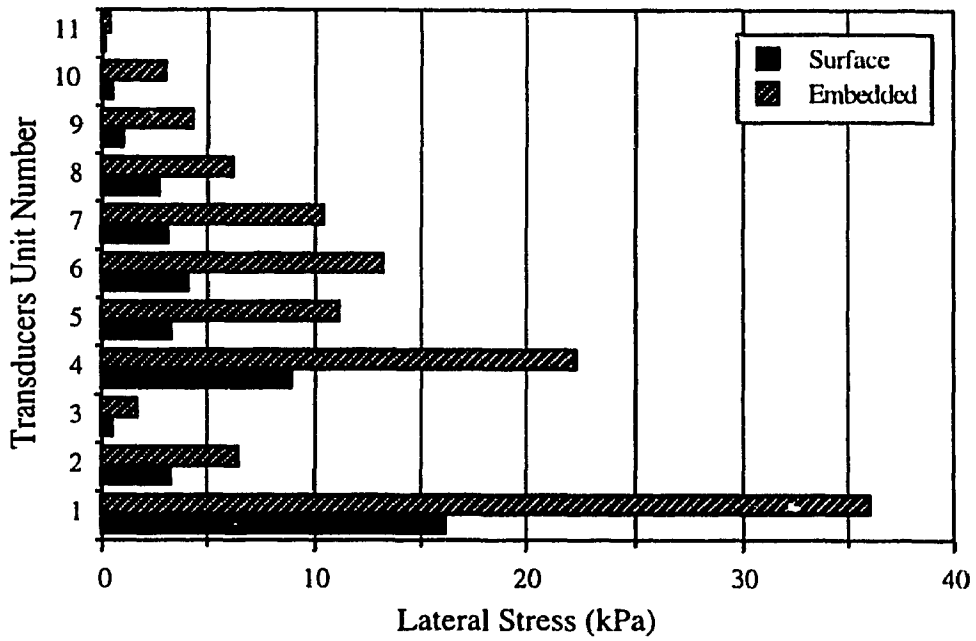
b) Lateral Stresses at Ultimate Load

Figure 3.74 Vertical & Lateral Stresses for Circular Flat Footing on Loose Sand

For Positions of Transducers Refer to Figure 3.14



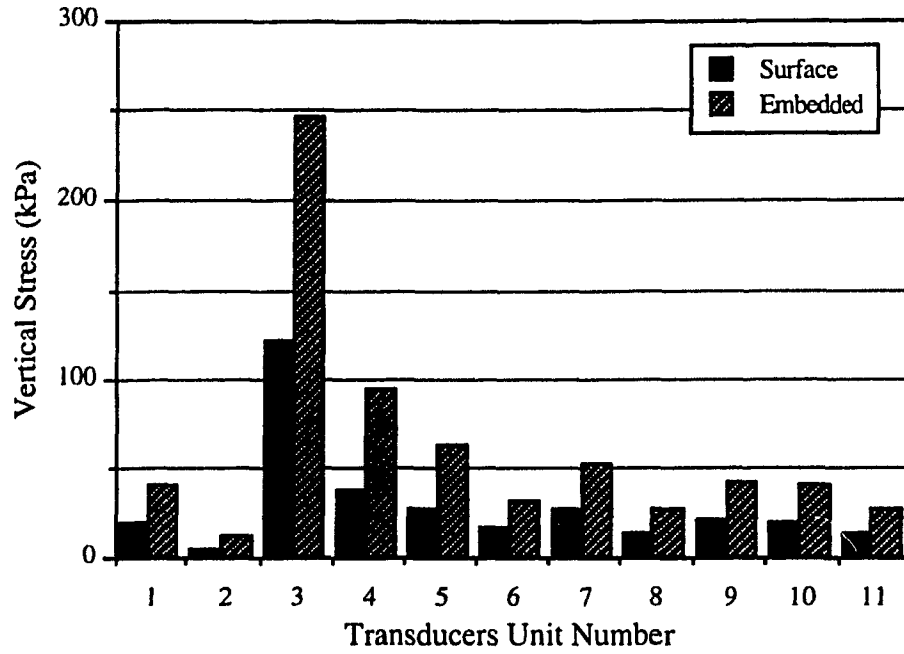
a) Vertical Stresses at Ultimate Load



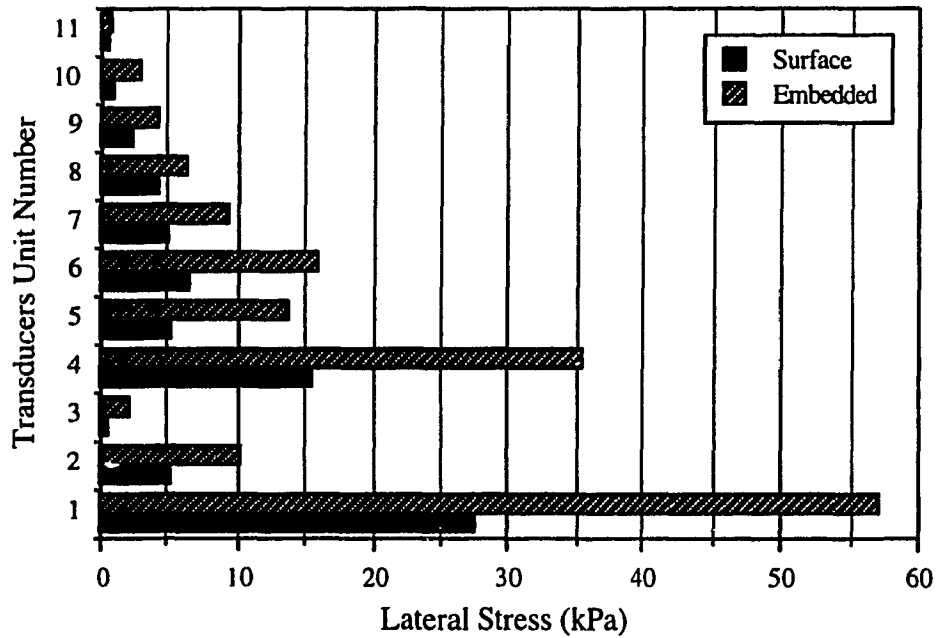
b) Lateral Stresses at Ultimate Load

Figure 3.75 Vertical & Lateral Stresses for Circular Flat Footing on Medium Sand

For Positions of Transducers Refer to Figure 3.14



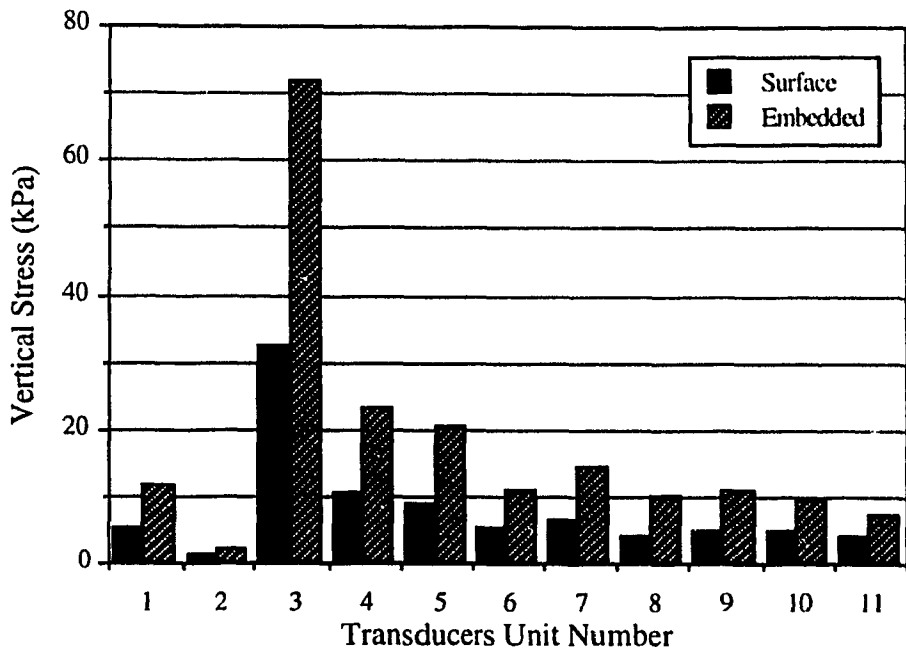
a) Vertical Stresses at Ultimate Load



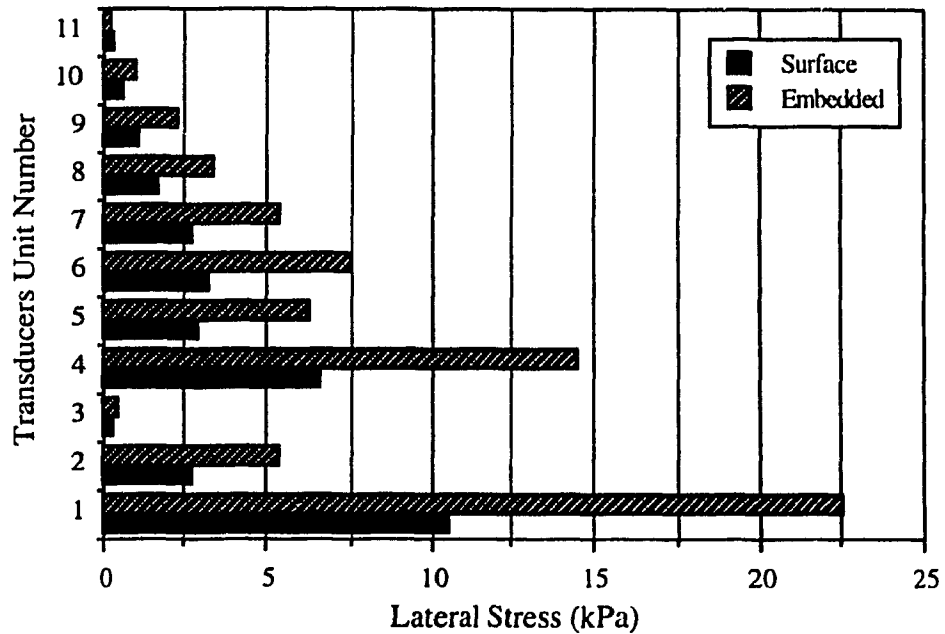
b) Lateral Stresses at Ultimate Load

Figure 3.76 Vertical & Lateral Stresses for Circular Flat Footing on Dense Sand

For Positions of Transducers Refer to Figure 3.14



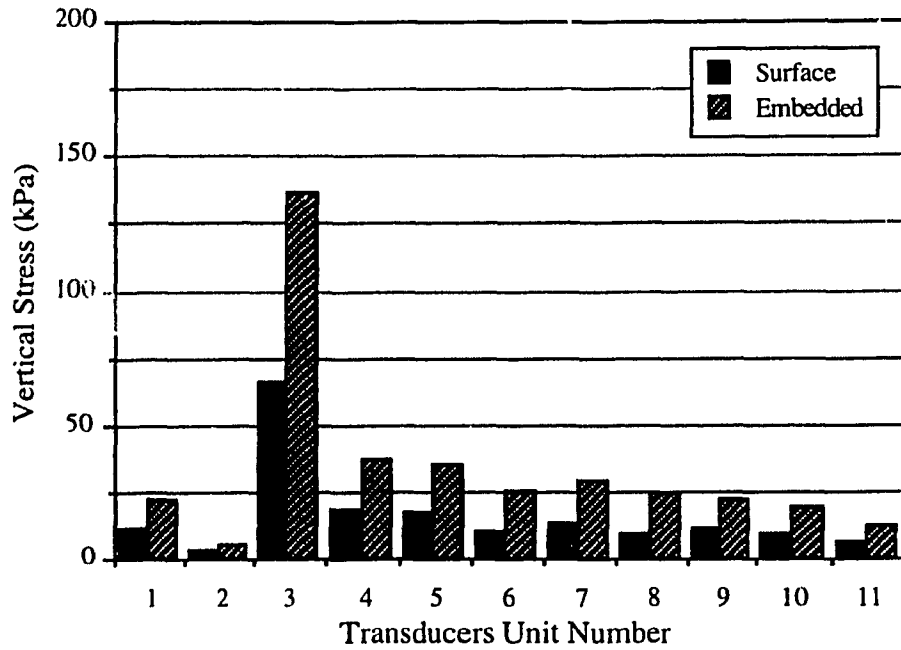
a) Vertical Stresses at Ultimate Load



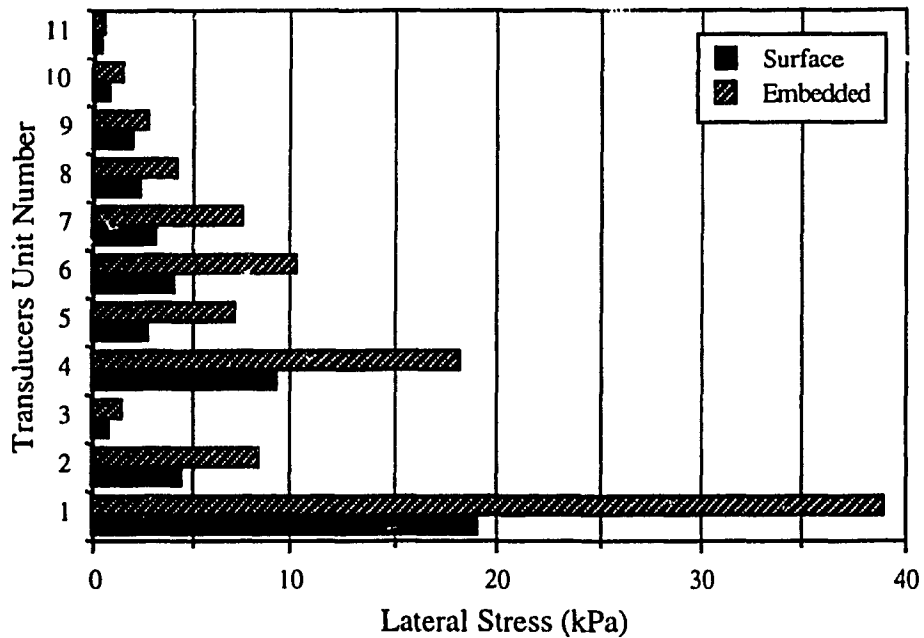
b) Lateral Stresses at Ultimate Load

Figure 3.77 Vertical & Lateral Stresses for Conical (1) Shell Footing on Loose Sand

For Positions of Transducers Refer to Figure 3.14



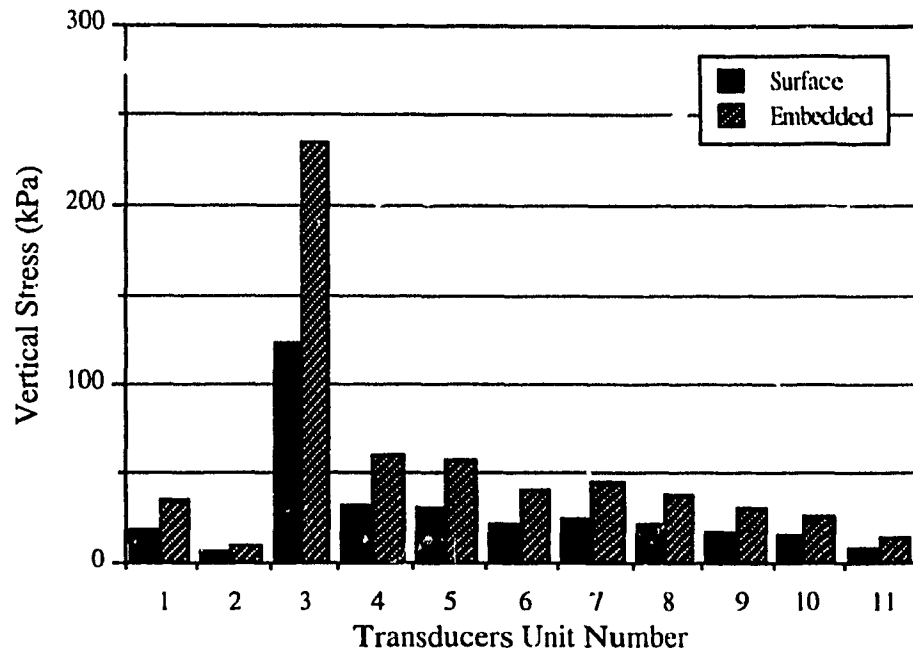
a) Vertical Stresses at Ultimate Load



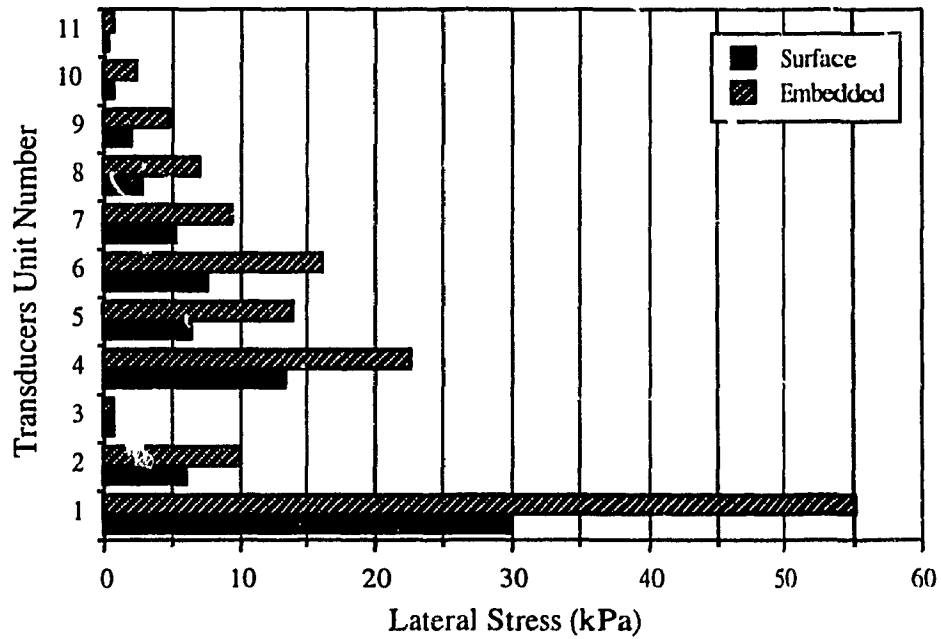
b) Lateral Stresses at Ultimate Load

Figure 3.78 Vertical & Lateral Stresses for Conical (1) Shell Footing on Medium Sand

For Positions of Transducers Refer to Figure 3.14



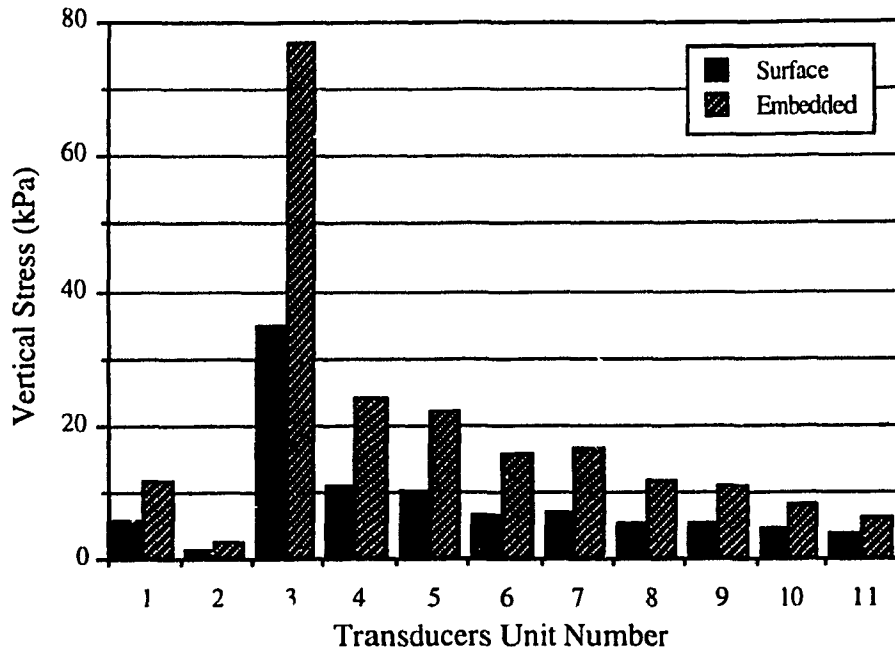
a) Vertical Stresses at Ultimate Load



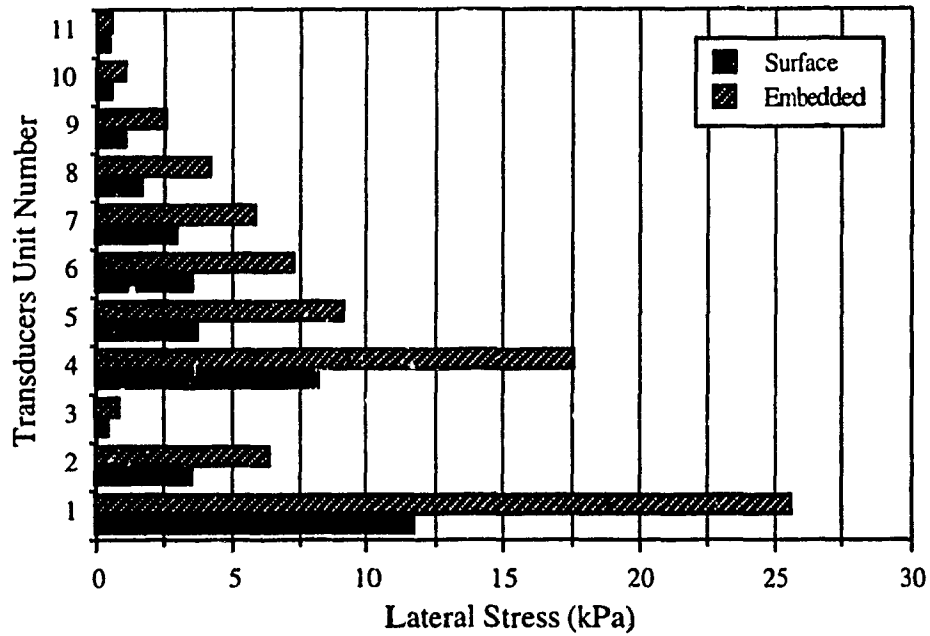
b) Lateral Stresses at Ultimate Load

Figure 3.79 Vertical & Lateral Stresses for Conical (1) Shell Footing on Dense Sand

For Positions of Transducers Refer to Figure 3.14



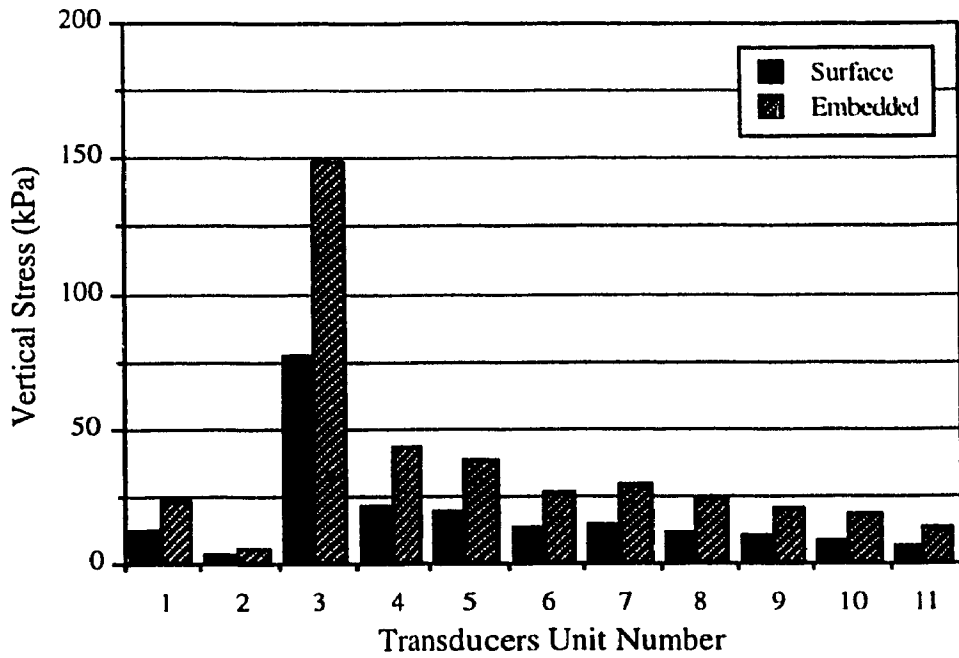
a) Vertical Stresses at Ultimate Load



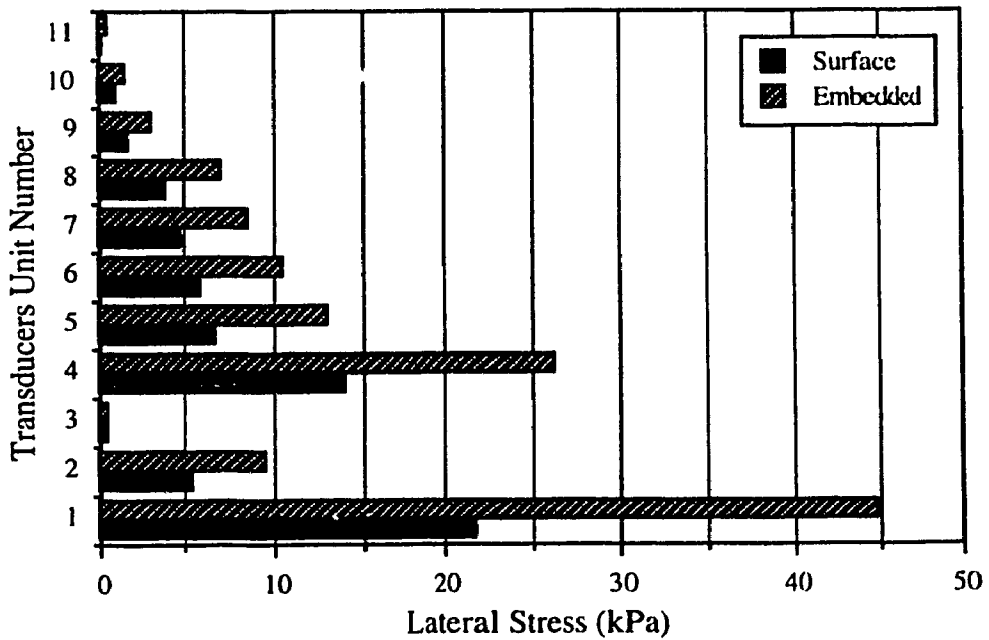
b) Lateral Stresses at Ultimate Load

Figure 3.80 Vertical & Lateral Stresses for Conical (2) Shell Footing on Loose Sand

For Positions of Transducers Refer to Figure 3.14



a) Vertical Stresses at Ultimate Load

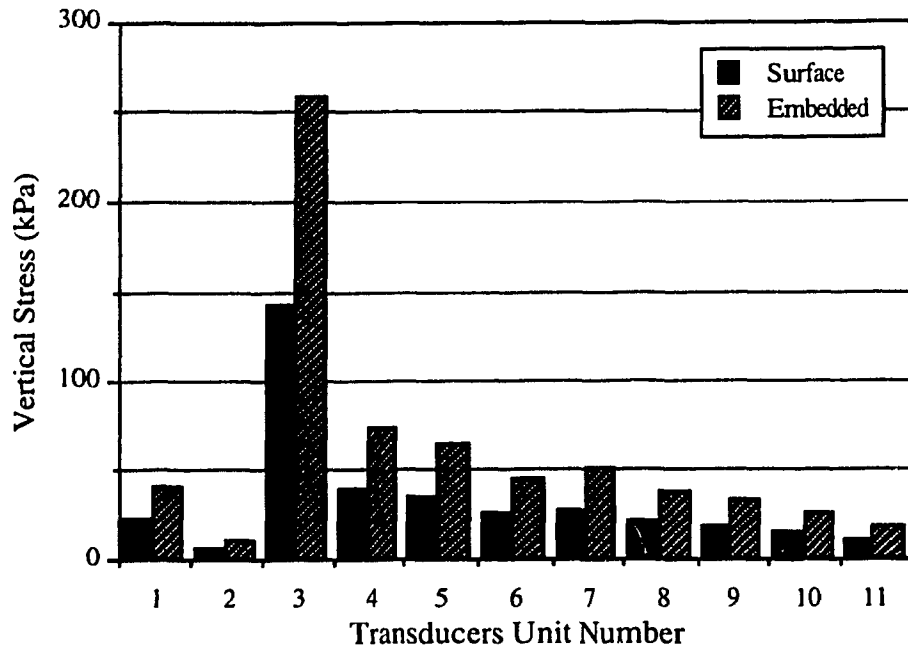


b) Lateral Stresses at Ultimate Load

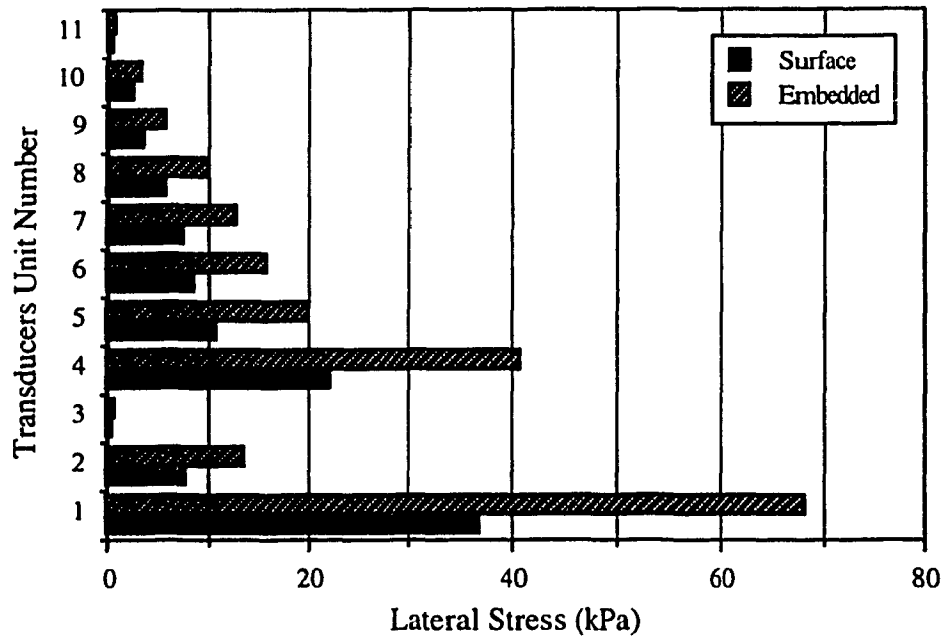
Figure 3.81 Vertical & Lateral Stresses for Conical (2) Shell Footing on Medium Sand



For Positions of Transducers Refer to Figure 3.14



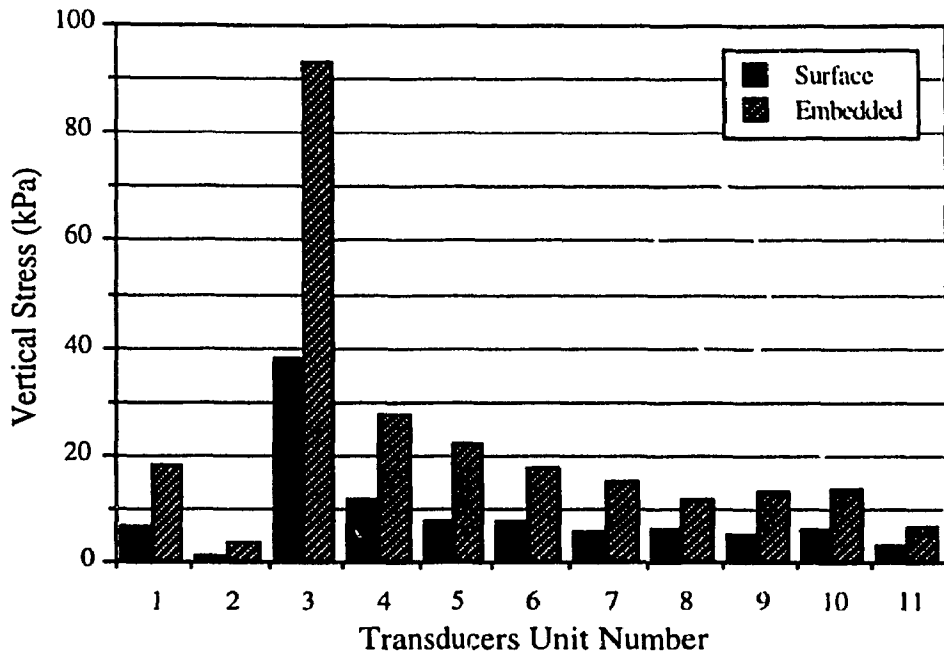
a) Vertical Stresses at Ultimate Load



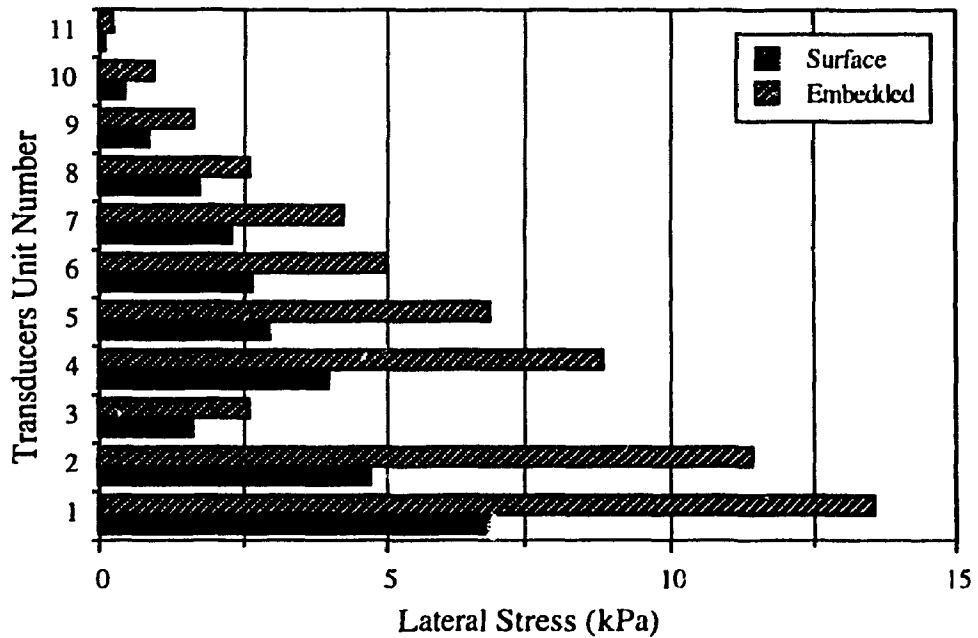
b) Lateral Stresses at Ultimate Load

Figure 3.82 Vertical & Lateral Stresses for Conical (2) Shell Footing on Dense Sand

For Positions of Transducers Refer to Figure 3.14



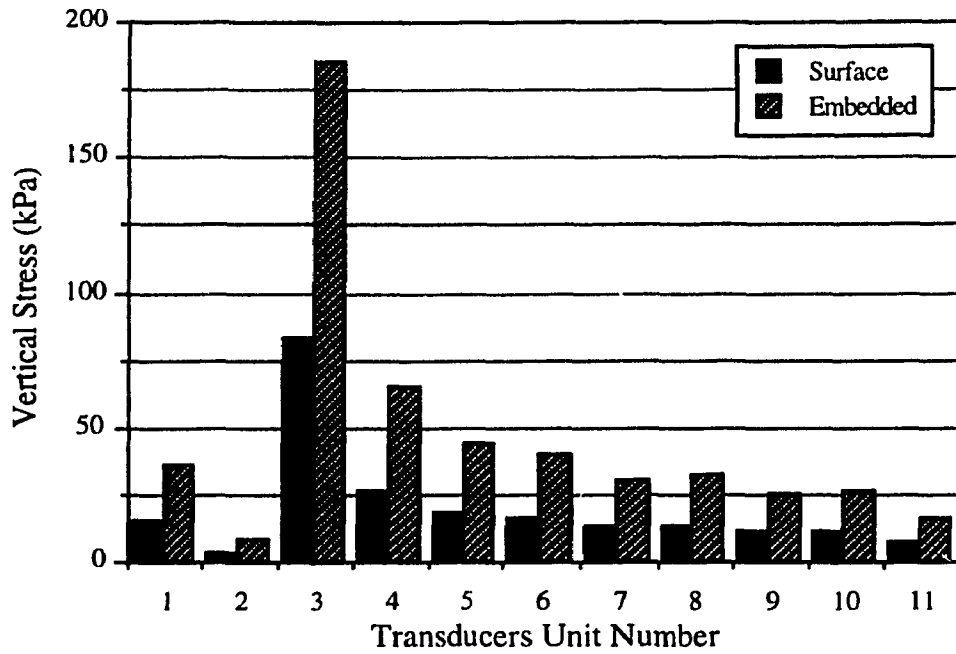
a) Vertical Stresses at Ultimate Load



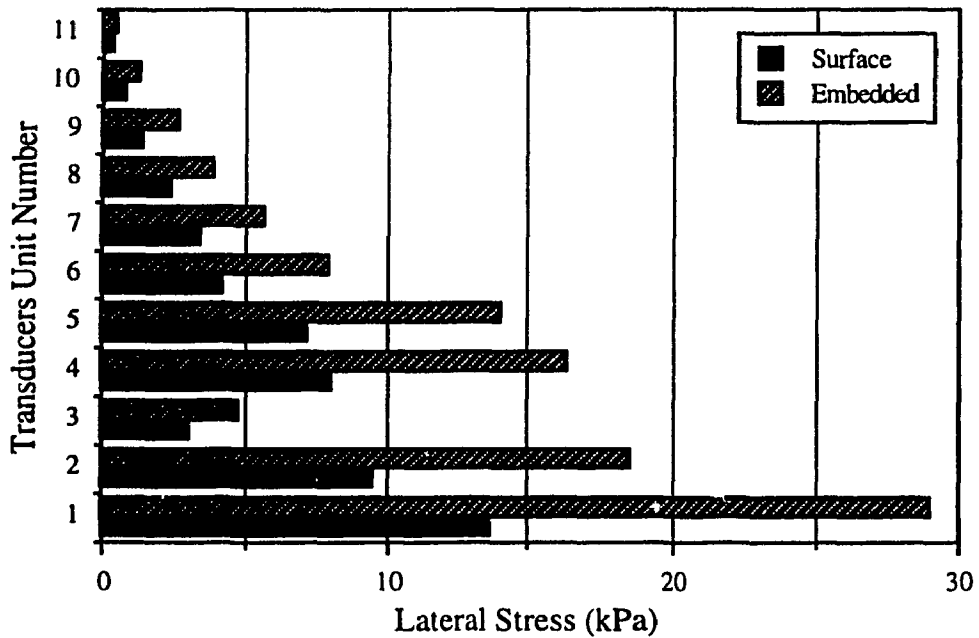
b) Lateral Stresses at Ultimate Load

Figure 3.83 Vertical & Lateral Stresses for Square Flat Footing on Loose Sand

For Positions of Transducers Refer to Figure 3.14



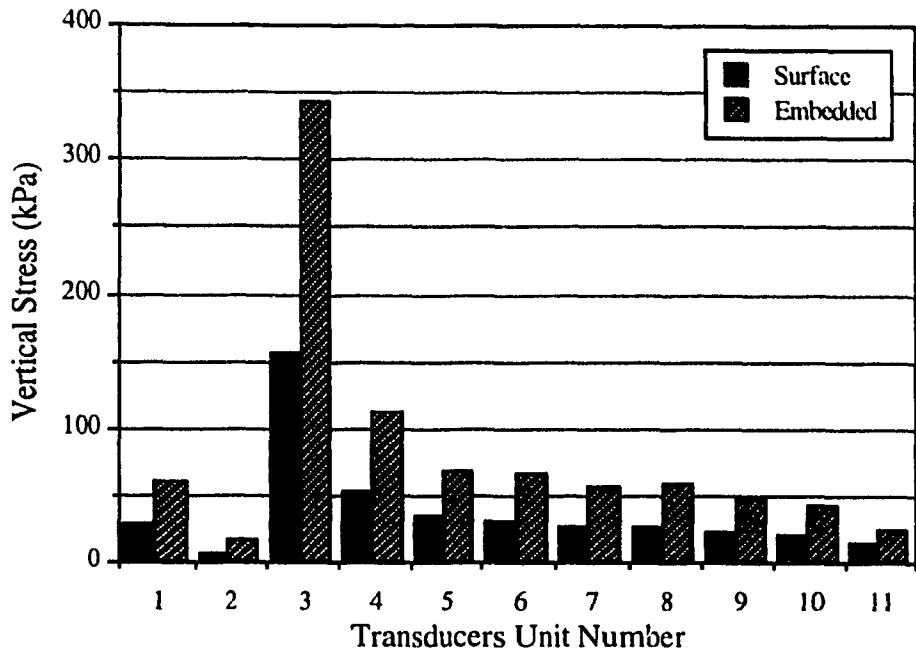
a) Vertical Stresses at Ultimate Load



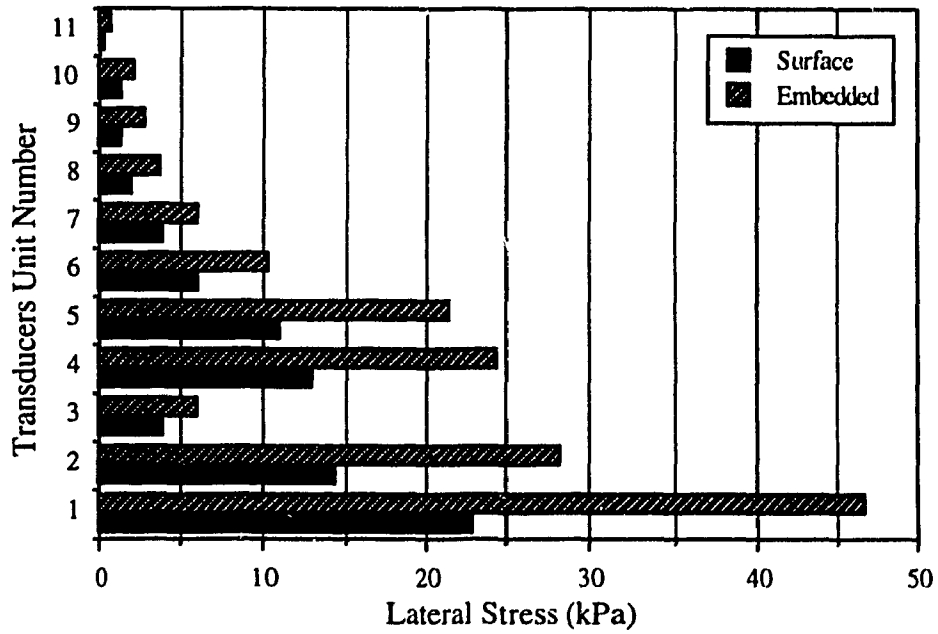
b) Lateral Stresses at Ultimate Load

Figure 3.84 Vertical & Lateral Stresses for Square Flat Footing on Medium Sand

For Positions of Transducers Refer to Figure 3.14



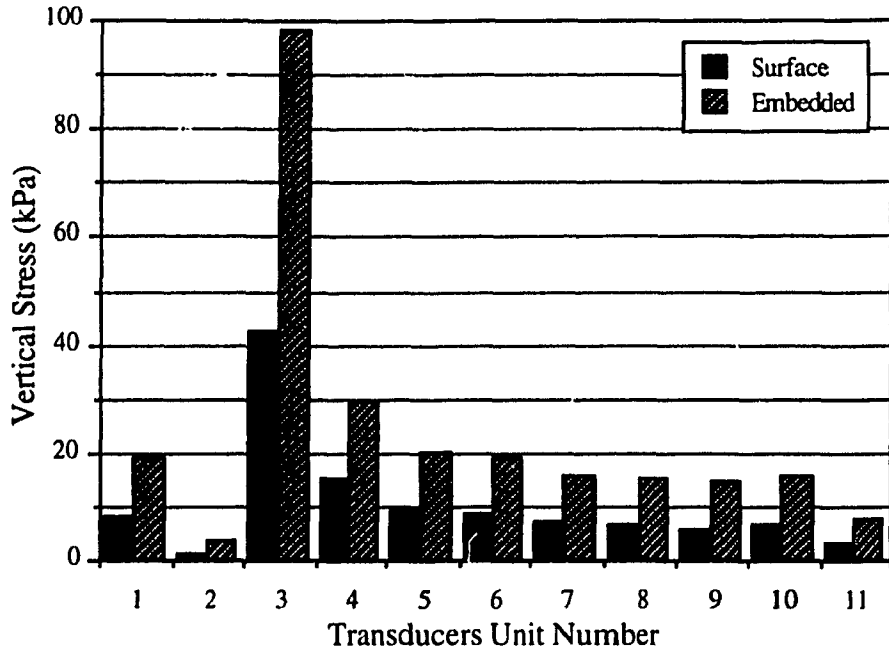
a) Vertical Stresses at Ultimate Load



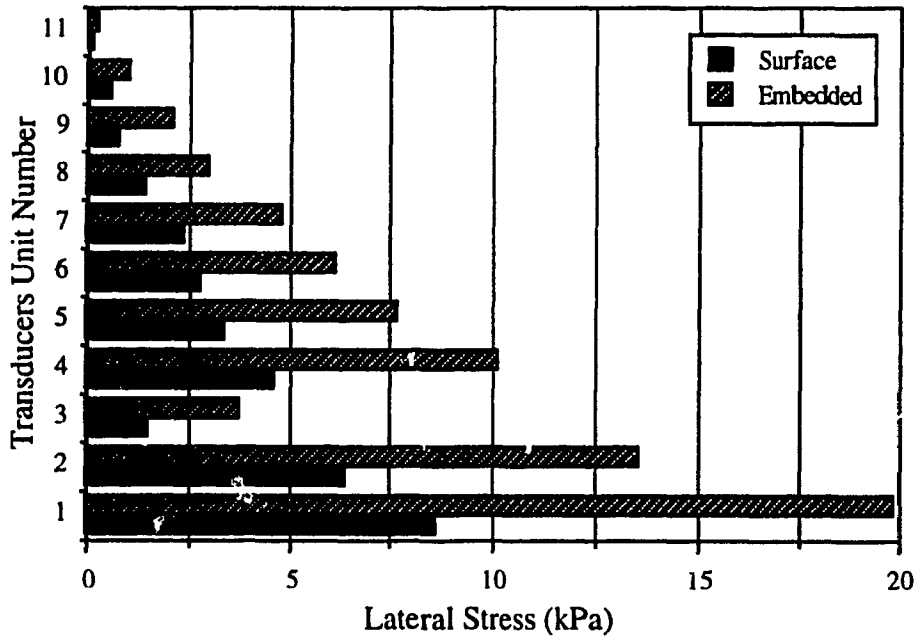
b) Lateral Stresses at Ultimate Load

Figure 3.85 Vertical & Lateral Stresses for Square Flat Footing on Dense Sand

For Positions of Transducers Refer to Figure 3.14



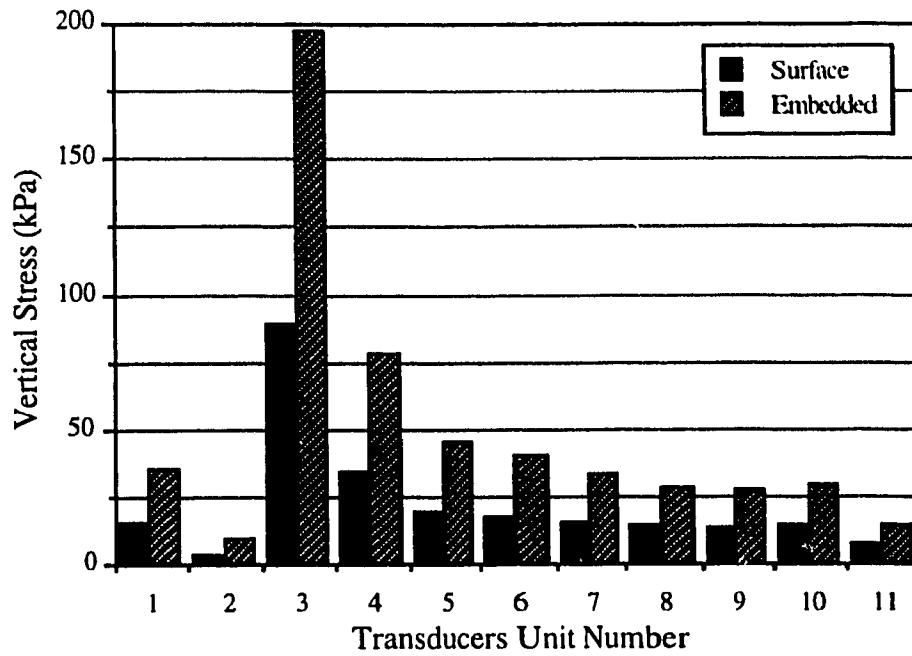
a) Vertical Stresses at Ultimate Load



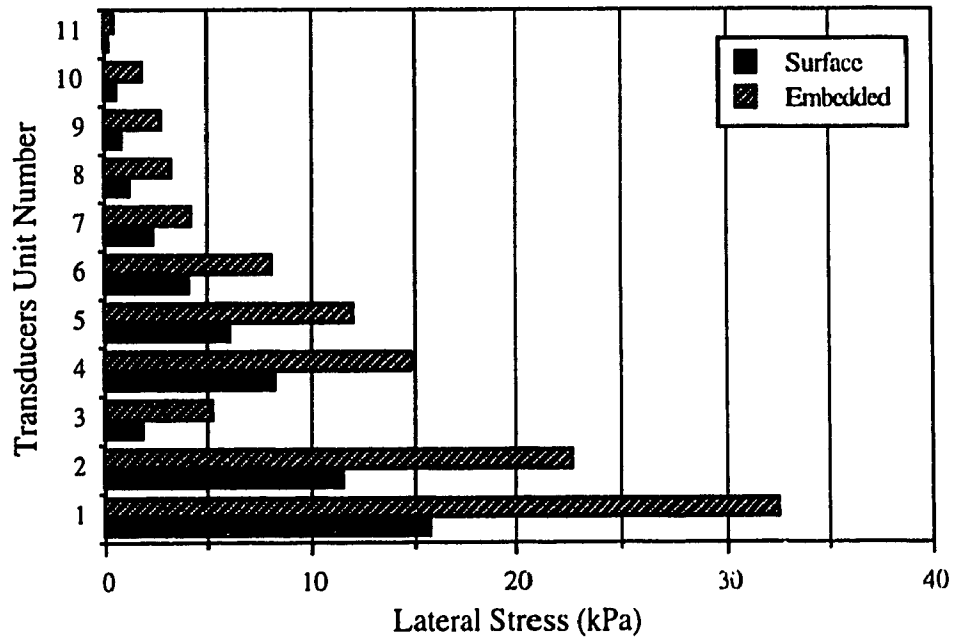
b) Lateral Stresses at Ultimate Load

Figure 3.86 Vertical & Lateral Stresses for Pyramidal (1) Shell Footing on Loose Sand

For Positions of Transducers Refer to Figure 3.14



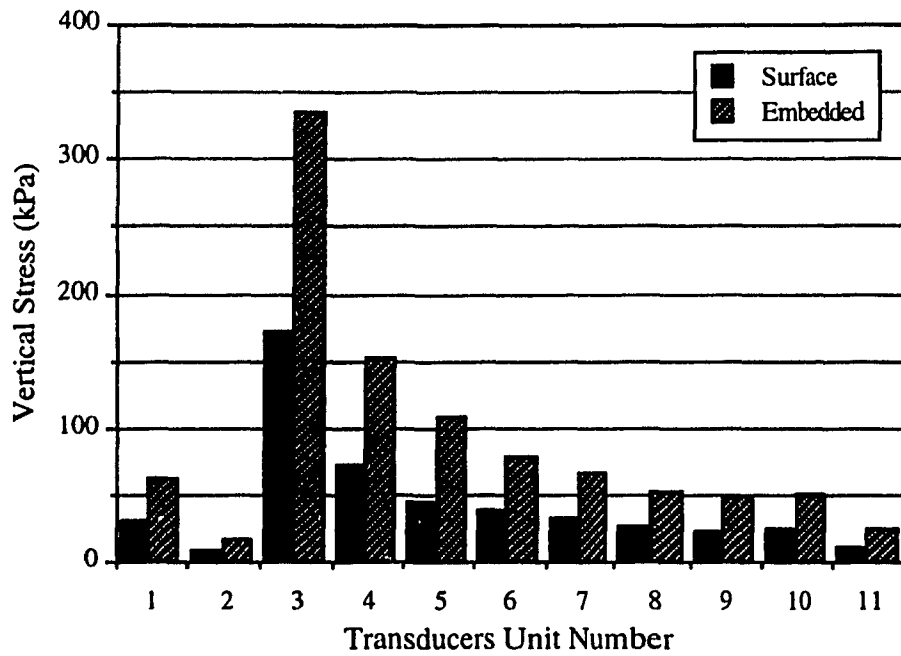
a) Vertical Stresses at Ultimate Load



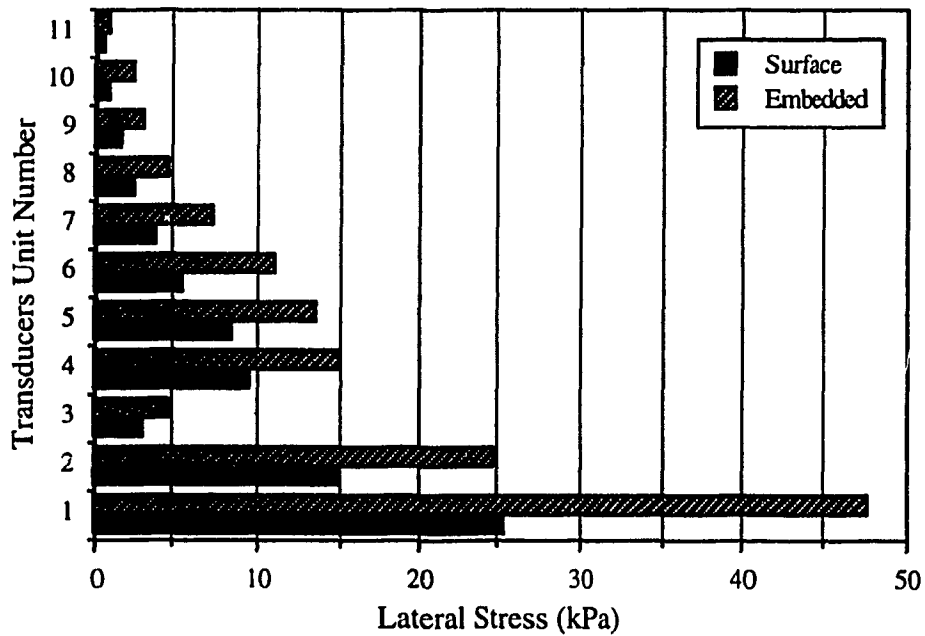
b) Lateral Stresses at Ultimate Load

Figure 3.87 Vertical & Lateral Stresses for Pyramidal (1) Shell Footing on Medium Sand

For Positions of Transducers Refer to Figure 3.14



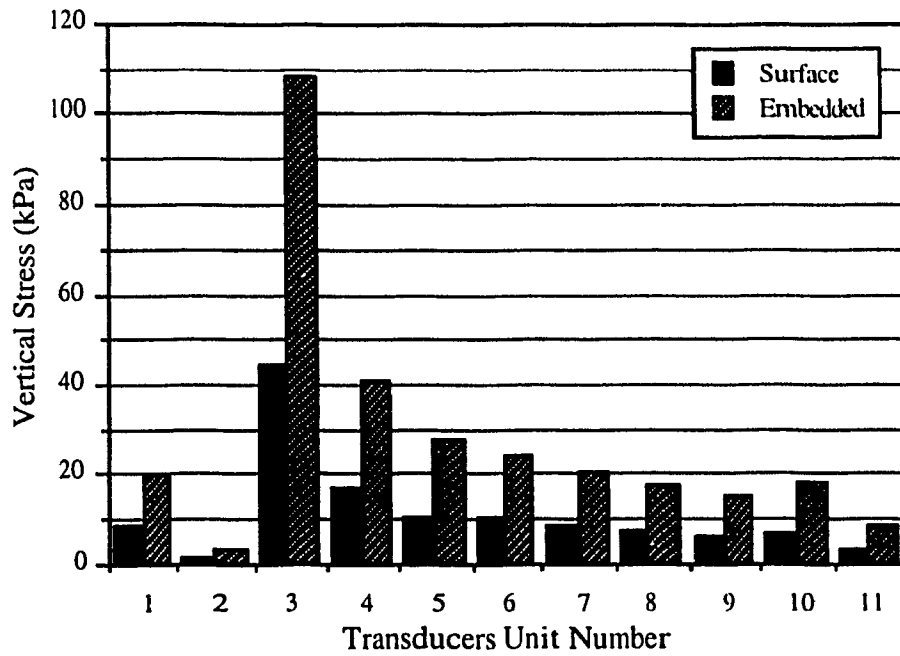
a) Vertical Stresses at Ultimate Load



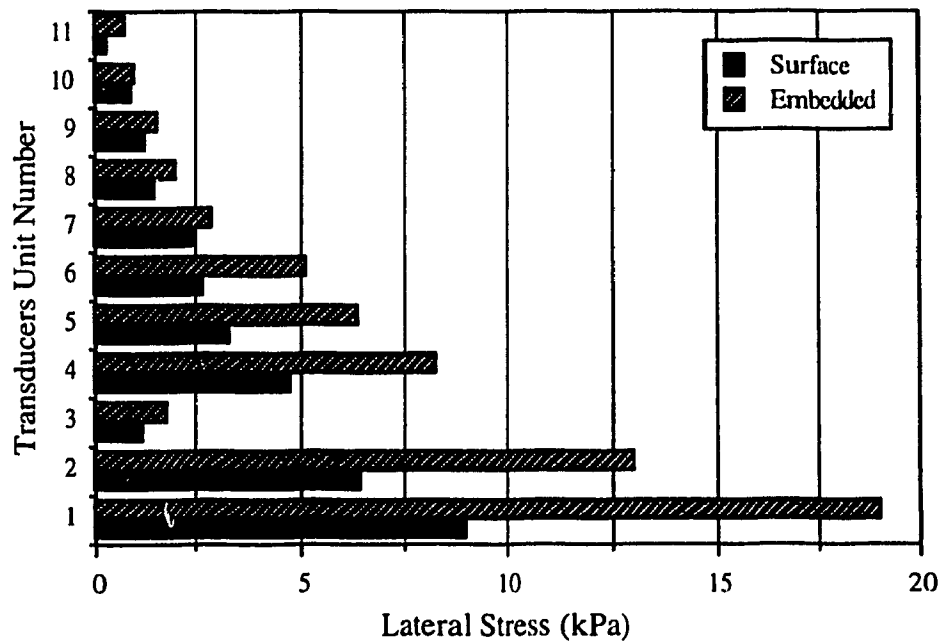
b) Lateral Stresses at Ultimate Load

Figure 3.88 Vertical & Lateral Stresses for Pyramidal (1) Shell Footing on Dense Sand

For Positions of Transducers Refer to Figure 3.14



a) Vertical Stresses at Ultimate Load

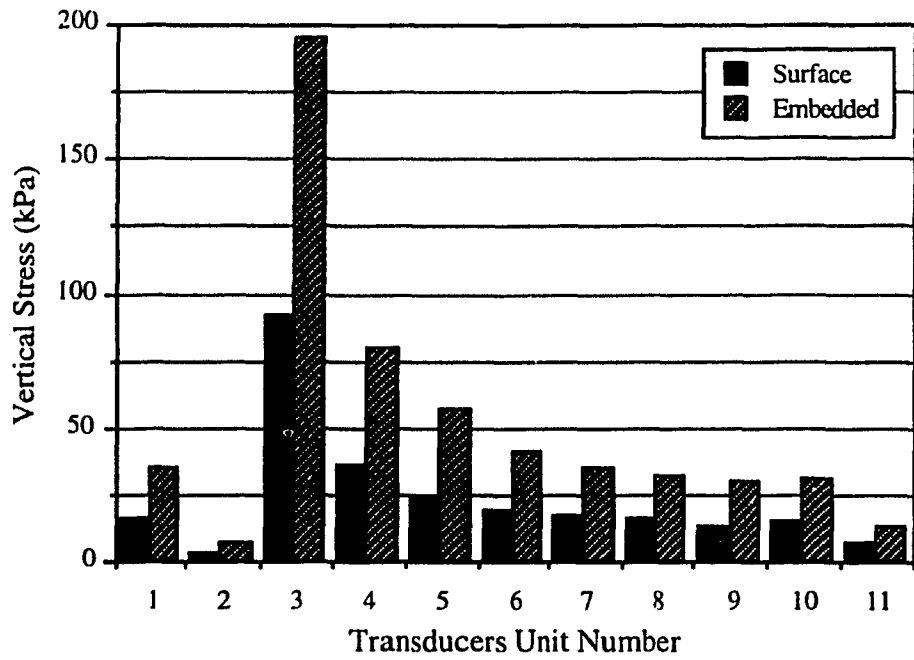


b) Lateral Stresses at Ultimate Load

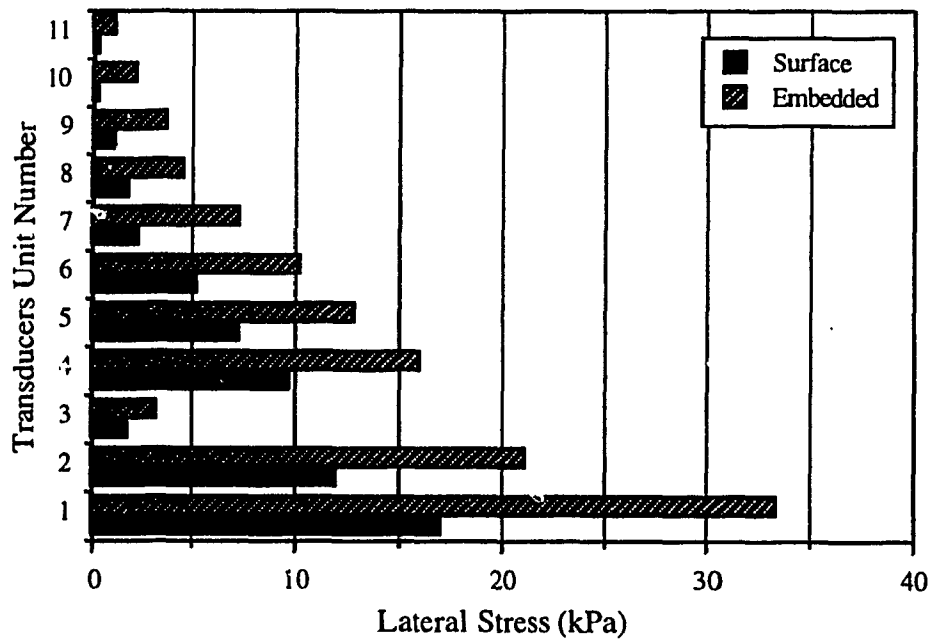
Figure 3.89 Vertical & Lateral Stresses for Pyramidal (2) Shell Footing on Loose Sand



For Positions of Transducers Refer to Figure 3.14



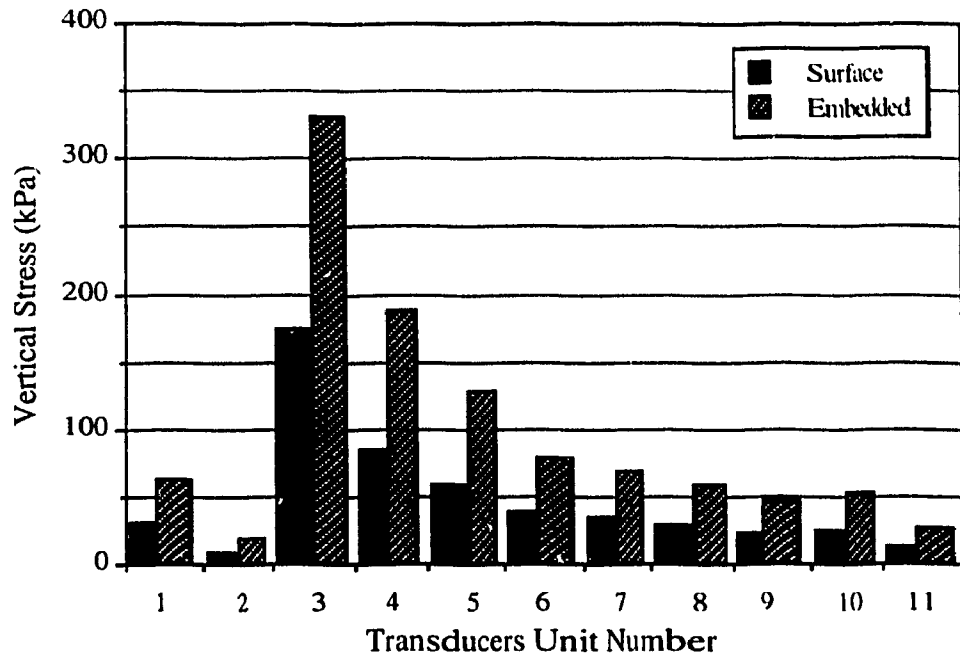
a) Vertical Stresses at Ultimate Load



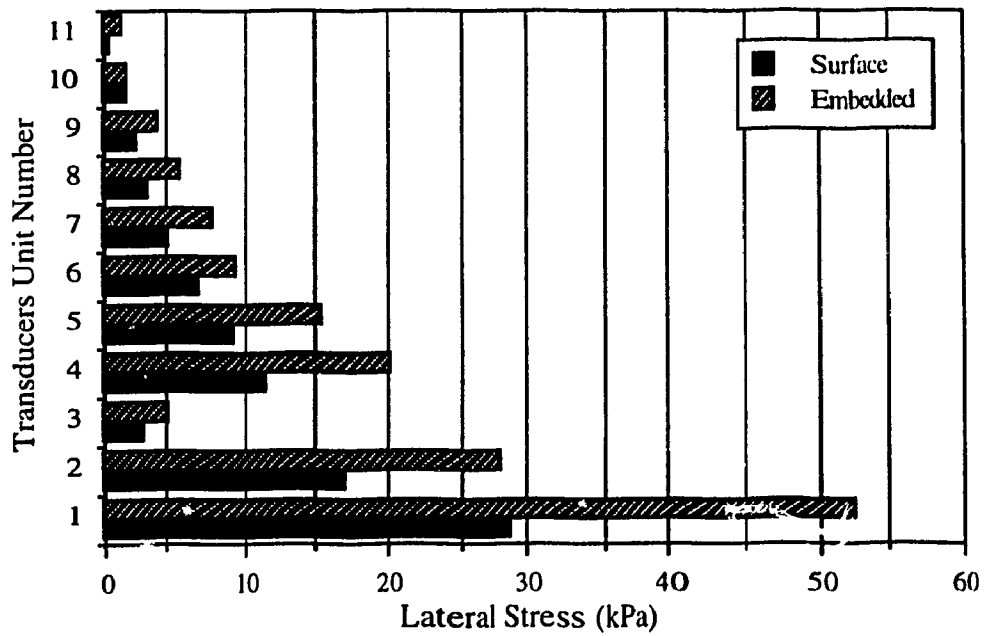
b) Lateral Stresses at Ultimate Load

Figure 3.90 Vertical & Lateral Stresses for Pyramidal (2) Shell Footing on Medium Sand

For Positions of Transducers Refer to Figure 3.14



a) Vertical Stresses at Ultimate Load



b) Lateral Stresses at Ultimate Load

Figure 3.91 Vertical & Lateral Stresses for Pyramidal (2) Shell Footing on Dense Sand

### 3.9 Special Loading Tests

In order to predict the shape of the rupture surface for flat and shell footings, special loading tests were conducted for the plane strain condition. The strip flat and the two triangular shell footings were tested in a plexiglass tank using colored loose sand layers. The results were captured by time limit exposure photographs throughout the loading process. Plates 3.20 through 3.22 show the test in progress up to the ultimate stage for the strip flat footing, and Plates 3.23 and 3.24 show the tests for the triangular shell footings at the ultimate stage. The predicted rupture surfaces were idealized and represented using circular and plane surfaces as shown on the transparencies over the photographs. It can be noticed that the wedge of the rupture surface for the triangular (1) shell footing is deeper than that for the flat footing, and shallower than that for the triangular (2) shell footing, which indicates that the shell footings have higher bearing capacity than the flat one.

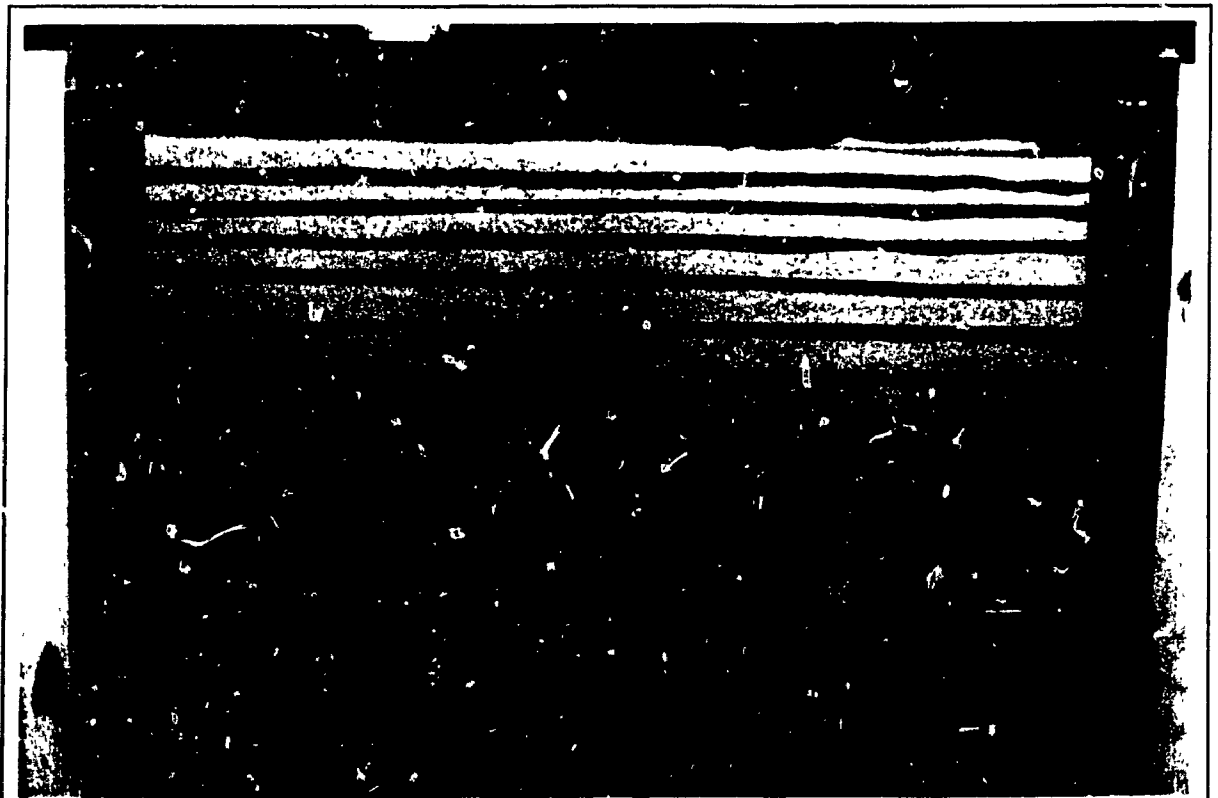


Plate 3.20 Strip Flat Footing before Testing

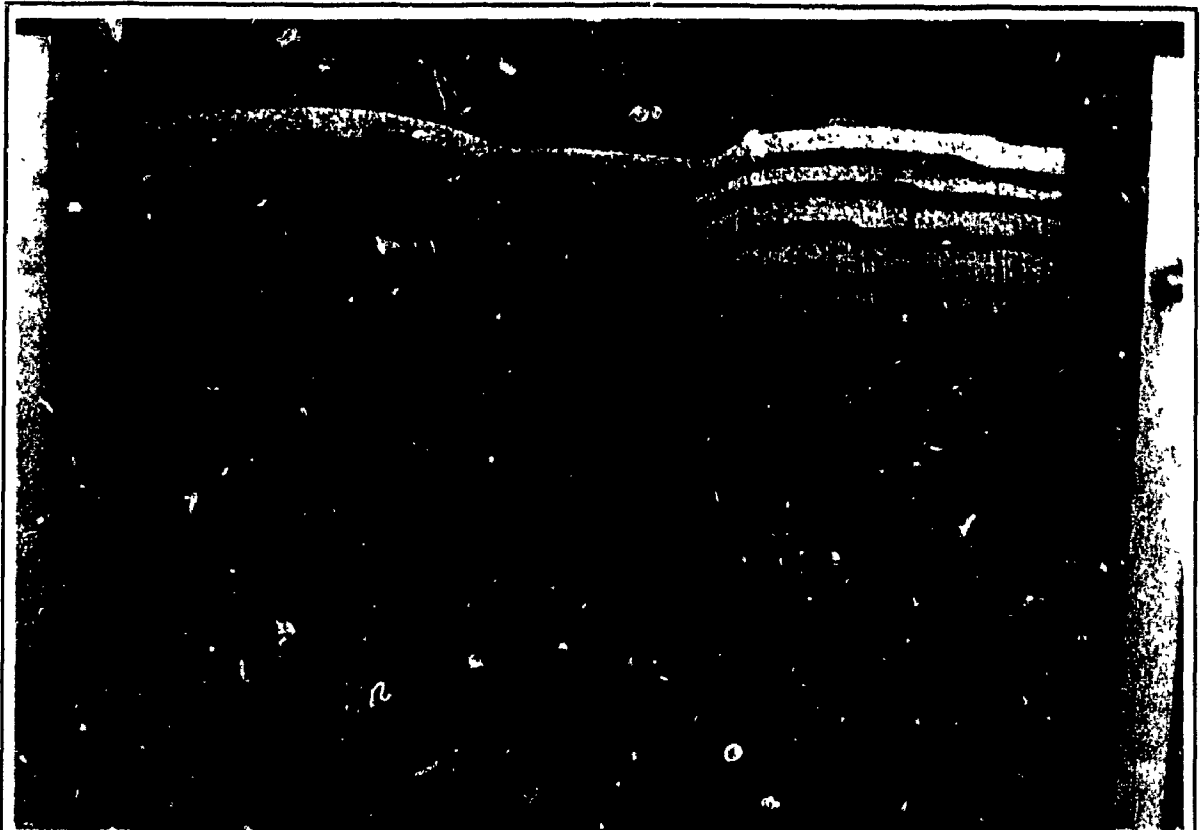


Plate 3.21 Strip Flat Footing during Testing

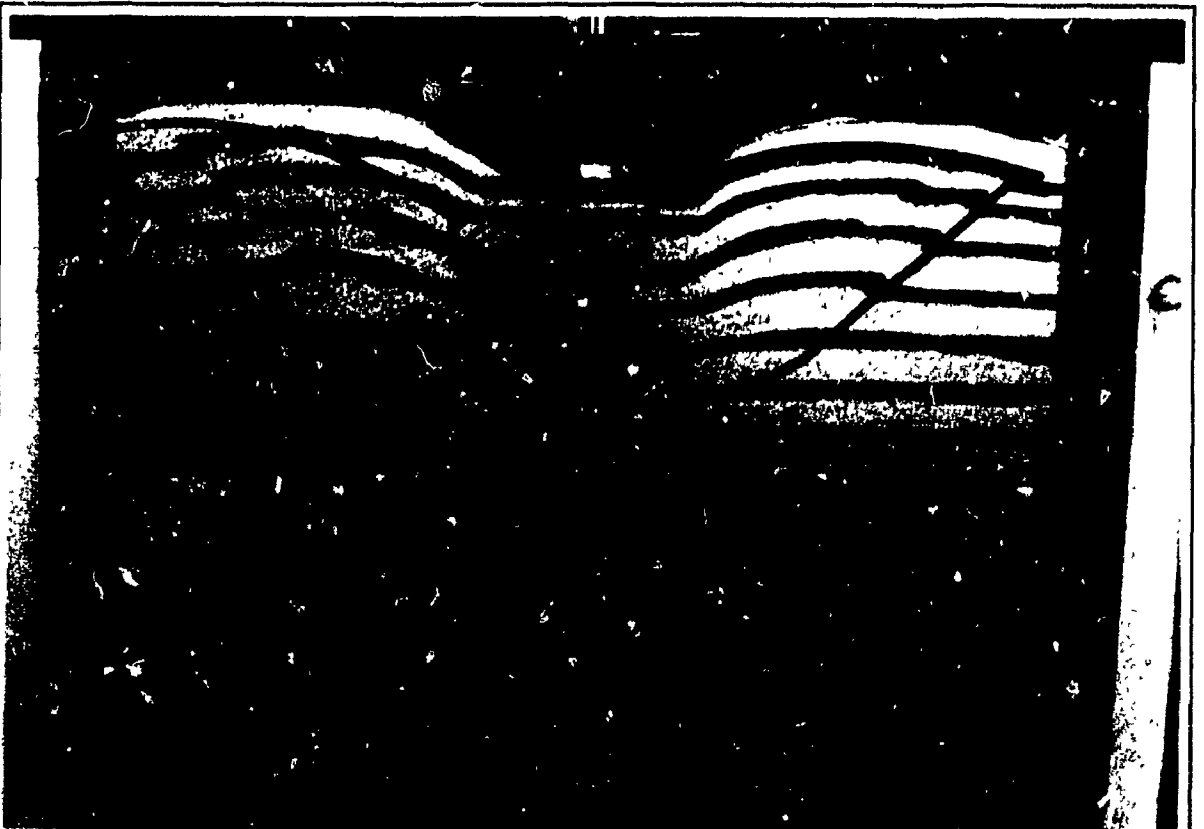


Plate 3.22 Strip Flat Footing at Ultimate Stage



Plate 3.23 Triangular (1) Shell Footing at Ultimate Stage



Plate 3.24 Triangular (2) Shell Footing at Ultimate Stage

## CHAPTER 4

### NUMERICAL MODELLING

#### 4.1 General

In this investigation, numerical modelling was conducted to examine the failure mechanism of strip shell foundations. Numerical analyses were performed for the cases of strip flat, triangular (1) shell, and triangular (2) shell footings using the finite element package, CRITICAL State Program "CRISP", developed by the geotechnical group at Cambridge University (Britto and Gunn 1987). Mesh deformations, displacement vectors, distributions of strains, stresses, and displacements were recorded during loading process and at failure.

The program "CRISP" uses the incremental tangent stiffness approach in the analysis, in which the load is divided into a number of small increments, which are applied simultaneously. During each load increment, the stiffness properties appropriate for the current stress level are employed in the numerical calculations. The linear simultaneous stiffness equations are solved using the frontal solution method.

#### 4.2 Mesh Design

The geometry of the mesh for the plane strain condition is symmetrical about the centre line, so the proposed mesh in the present investigation represents only one half of the cross section passing through the axis of symmetry of the footing. The nodes along the bottom boundary were considered as pinned supports, i.e., no movement was allowed in both vertical and horizontal directions, whereas the nodes along the vertical boundary and the axis of symmetry were considered to be rollers, i.e., free to move only in the vertical

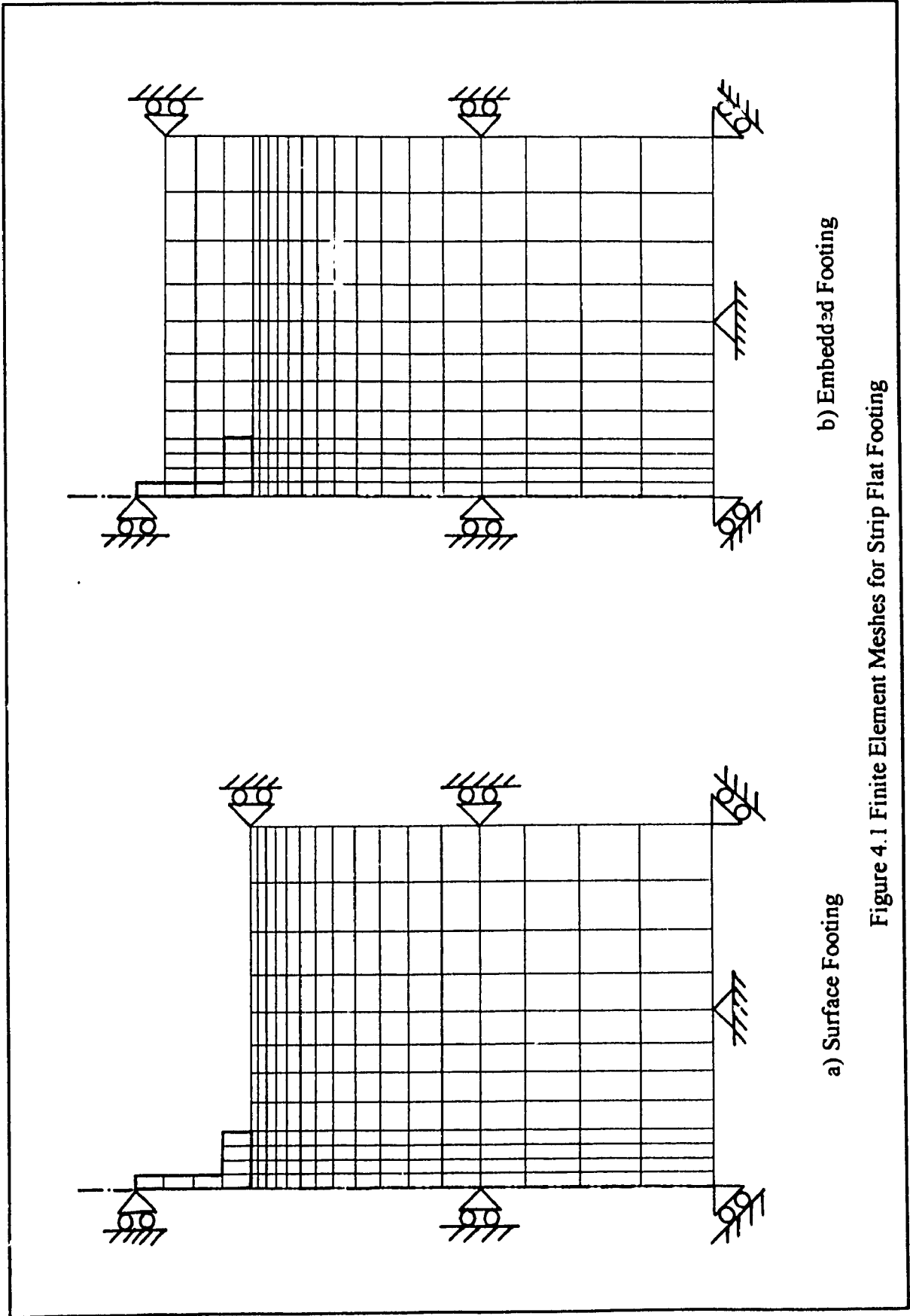
direction. The soil and the footings were modelled using eight-noded Linear Strain Quadrilateral elements "LSQ" with quadratic variation for the displacement along the sides of the element. Smaller size elements for the soil were selected in the vicinity of the footings where the variations in stresses and strains are expected to be more significant. Figures 4.1, 4.2, and 4.3 show the finite element meshes of the surface and embedded footings; strip flat, triangular (1) shell, and triangular (2) shell footings, respectively. Table 4.1 presents the number of nodes and elements employed for each mesh in the analysis.

Table 4.1 Number of Nodes & Elements in F.E. Meshes

Footing	Surface Footings		Embedded Footings	
	No. of Nodes	No. of Elements	No. of Nodes	No. of Elements
Strip Flat	232	199	262	229
Triangular (1) Shell	250	214	280	244
Triangular (2) Shell	250	214	280	244

#### 4.3 Soil & Foundation Modelling

In this study, in order to simulate the laboratory conditions for all sand states, extensive investigation was performed to select the appropriate soil model. Critical state soil models such as: cam-clay, modified cam-clay, and Schofield model, and elastic perfectly plastic models using different yield criteria such as: Mohr-Coulomb, Von Mises, Drucker-Prager, and Tresca, were examined. The tested sand was properly represented and idealized using an elastic perfectly plastic soil model employing Mohr-Coulomb's yield criterion. The numerical results showed that the critical state soil models resulted in mesh deformations far from the ones deduced from the experimental investigation. The foundation models were modelled by a linear elastic model using the elastic properties of Atlas alloy. The physical and mechanical properties of the three sand states: loose, medium, and dense, were determined from the experimental phase as presented in Table 3.3.

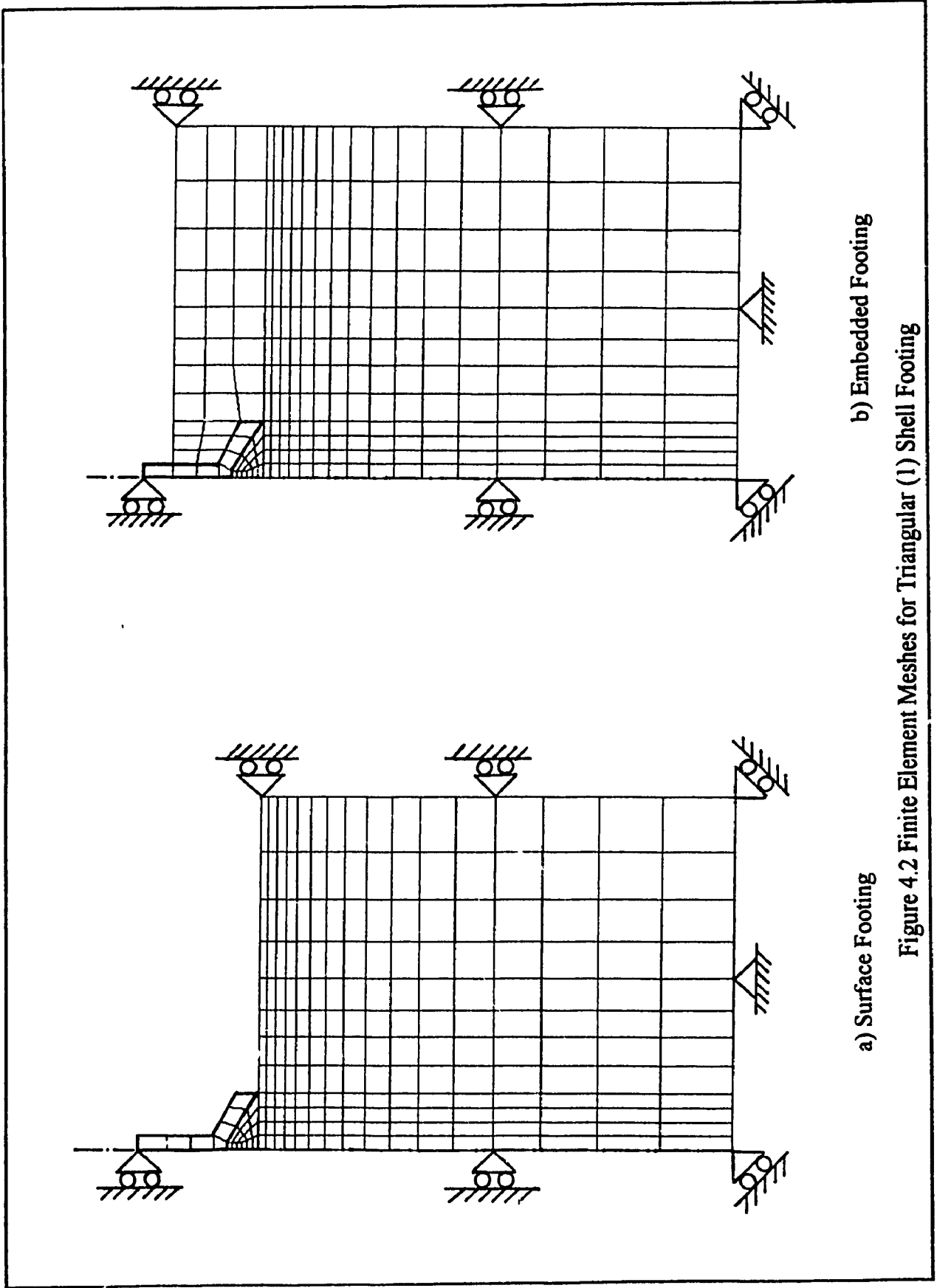


b) Embedded Footing

a) Surface Footing

Figure 4.1 Finite Element Meshes for Strip Flat Footing

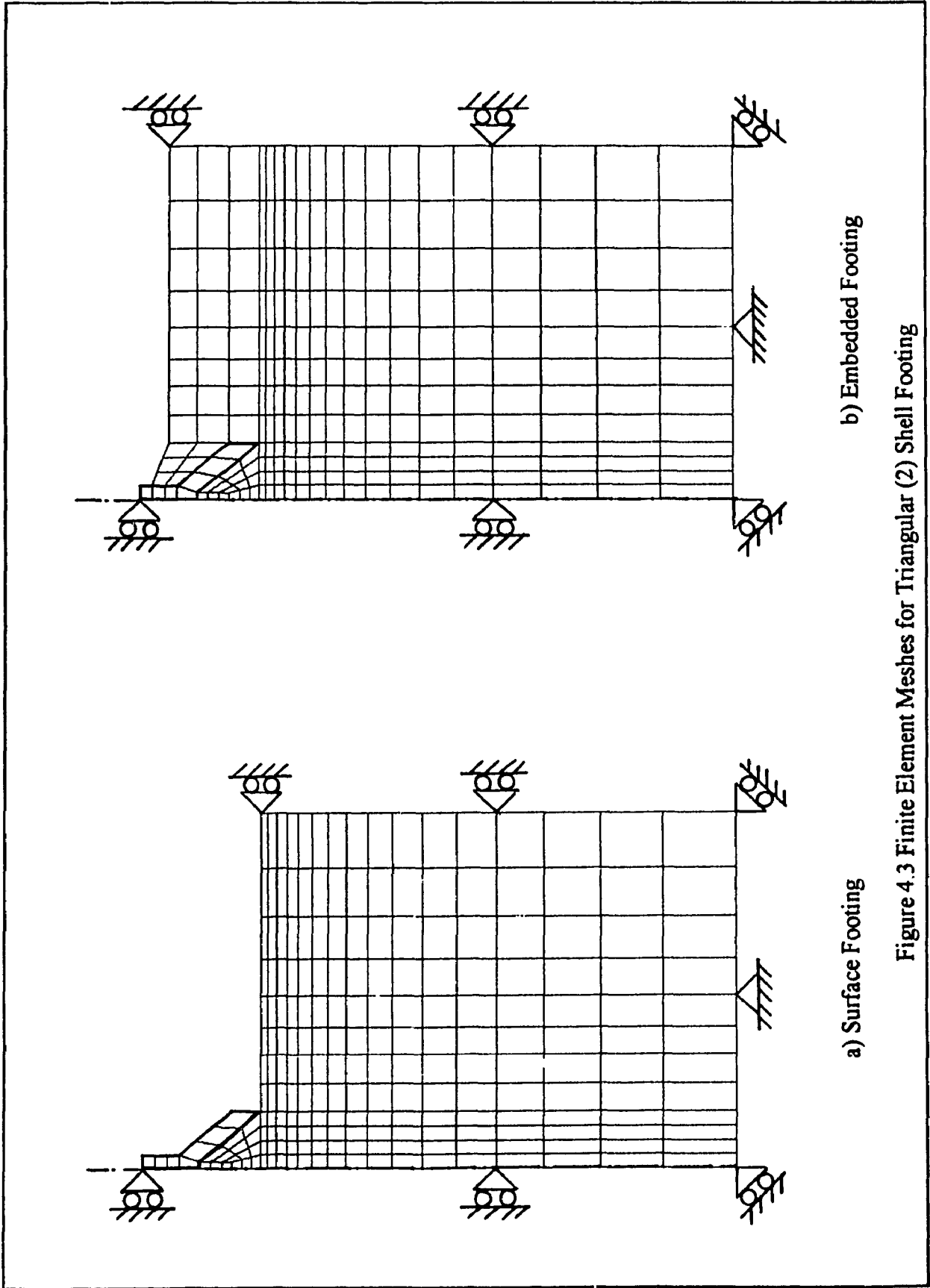




b) Embedded Footing

a) Surface Footing

Figure 4.2 Finite Element Meshes for Triangular (1) Shell Footing



b) Embedded Footing

a) Surface Footing

Figure 4.3 Finite Element Meshes for Triangular (2) Shell Footing

#### **4.4 Loading Scheme**

The loading scheme used in this investigation consisted of two main loading stages (load blocks). The first stage simulates the construction of a footing which was considered in the analysis as a single load increment. In case of the embedded footings, the first loading stage also included the backfilling, i.e., the embedment depth, until the final ground surface was reached. This additional load was incorporated in the first loading stage in the form of three load increments. The second loading stage simulates the loading on the footings up to the failure which substituted by a uniformly distributed vertical pressure acted over the top of the footings. This stage was incorporated in the form of several load increments (10.00 kPa each) which depends on the ultimate load of the testing footing.

#### **4.5 Finite Element's Output**

The results of this numerical investigation were introduced through the post processing feature of the program "CRISP" in the form of several plots and contour lines for the following parameters:

1. Deformed/undeformed mesh
2. Displacement vectors
3. Horizontal strain ( $\epsilon_{xx}$ )
4. Vertical strain ( $\epsilon_{yy}$ )
5. Horizontal stress ( $\sigma_{xx}$ )
6. Vertical stress ( $\sigma_{yy}$ )
7. Horizontal displacement ( $\delta_x$ )
8. Vertical displacement ( $\delta_y$ )

Typical plots for the numerical results are presented for the case of surface and embedded triangular (1) shell footing in Figures 4.4 through 4.7, and in Figures 4.8 through 4.11, respectively.

The deformed mesh and displacement vectors for the surface footing are presented in Figure 4.4. The figure shows that the footing moves downwards with the soil below while the soil outside the footing specially near the ground surface moves upwards. The rupture surface is shown in the figure according to the deformed mesh. It can be seen that the shape of the rupture surface has the same configuration as the one predicted experimentally from the photographs taken for the special loading test (see Plates 3.22 to 3.24). The comparison between the flat strip and shell footings indicated that the rupture surfaces for the shell footings are deeper than that for the strip flat counterpart.

The contour lines for the distribution of the horizontal and vertical strains are presented in Figure 4.5. The horizontal strain distribution is presented by contour lines (A) to (L) for the negative strain region and by contour lines (M) to (V) for the positive region. The maximum negative strain occurred at the edge of footing and reduced for lower soil depth. The region for the positive horizontal strains existed outside the footing region with a maximum value near the edge of footing and the ground surface.

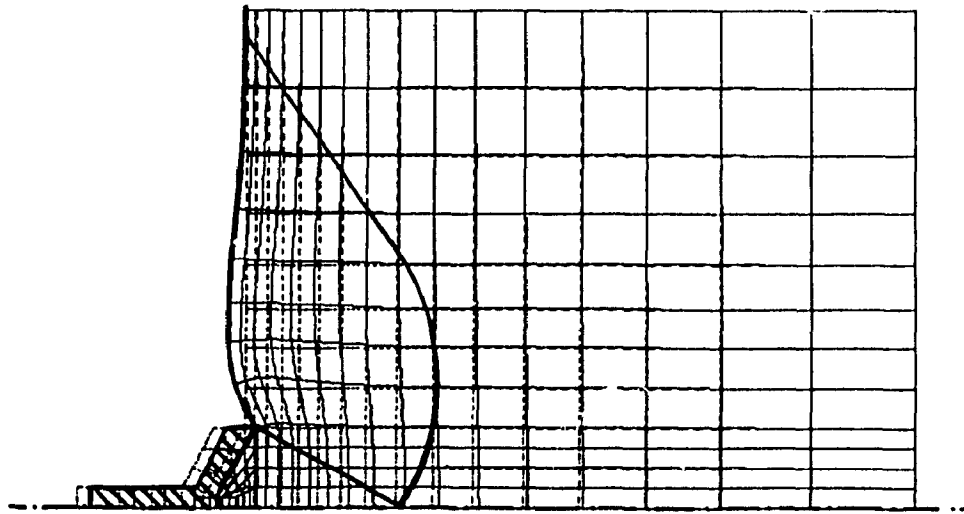
The vertical strain distribution is presented by contour lines (A) to (N) representing the positive strain region and by contour lines (O) to (Z) for the negative region. The maximum positive strain occurred at the edge of footing and reduced for lower soil depth. The region for negative vertical strain existed at the same region for positive horizontal strain.

The distribution of the horizontal and vertical stresses are presented by contour lines (A) to (N) in Figure 4.6. The maximum horizontal and vertical stresses are located at the edge of footing. The horizontal and vertical displacements are presented by contour lines (A) to (N) in Figure 4.7. The maximum horizontal displacement occurred near the edge of footing. The vertical displacement of the footing and the soil below were downwards (negative), while the vertical displacement of the region outside the footing and near the ground surface were upwards.

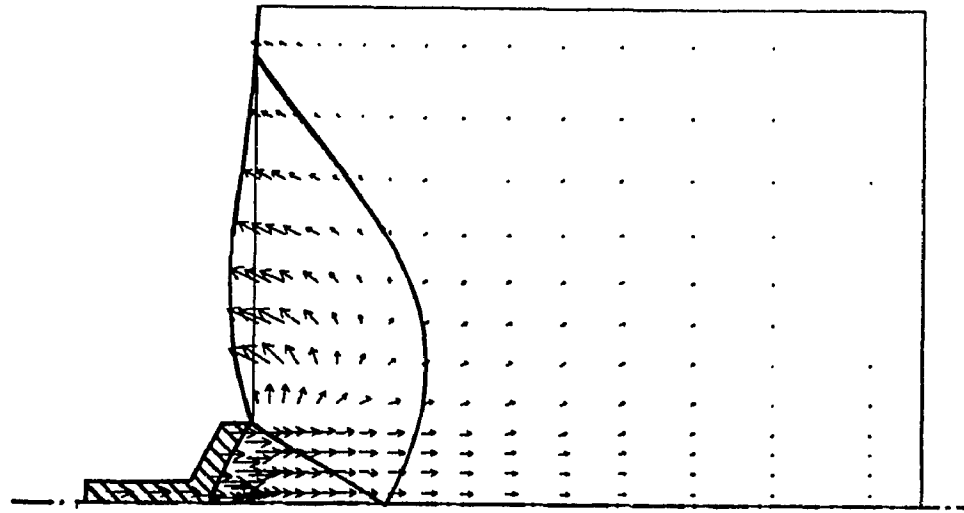
There is a major difference between the mesh deformation and displacement vectors for the embedded footings and that for the surface ones. The deformed mesh and displacement vectors for the embedded footing are presented in Figure 4.8. The soil particles in case of the embedded footing at the ground surface moved downwards with the footing, while for the surface footing it moved upwards. This confirms what was observed during the experimental phase for the case of embedded footings.

The contour lines for the horizontal and vertical strains of embedded footing are presented in Figure 4.9. The horizontal strain distribution is presented by contour lines (A) to (I) representing the negative strain region and by contour lines (J) to (N) for the positive region. The maximum negative strain occurred at the edge of footing and reduced for lower soil depth. The region for the positive horizontal strains existed outside the footing and the soil below with a maximum value at the region above the footing. The vertical strain distribution is presented by contour lines (A) to (H) to represent the negative strain region and by contour lines (G) to (N) for the positive region. The maximum negative strain occurred at the edge of footing and reduced for lower soil depth. The region for positive vertical strains existed at the same region for negative horizontal strains.

The distribution of the horizontal and vertical stresses are presented by contour lines (A) to (N) in Figure 4.10. The maximum horizontal and vertical stresses occurred at the edge of footing. The horizontal and vertical displacements are presented by contour lines (A) to (N) in Figure 4.11. The negative horizontal displacement are presented by contour lines (A) to (H) and the positive one by contour lines (I) to (N). The maximum negative displacement occurred at the ground surface and the maximum positive displacement near the edge of footing, occurred near the edge of footing. The vertical displacement of the footing and the soil in the mesh were all downwards (negative). Summary of the numerical results for the prescribed parameters are presented in Tables 4.2 through 4.7. The tables present the governing limits for the contour lines.

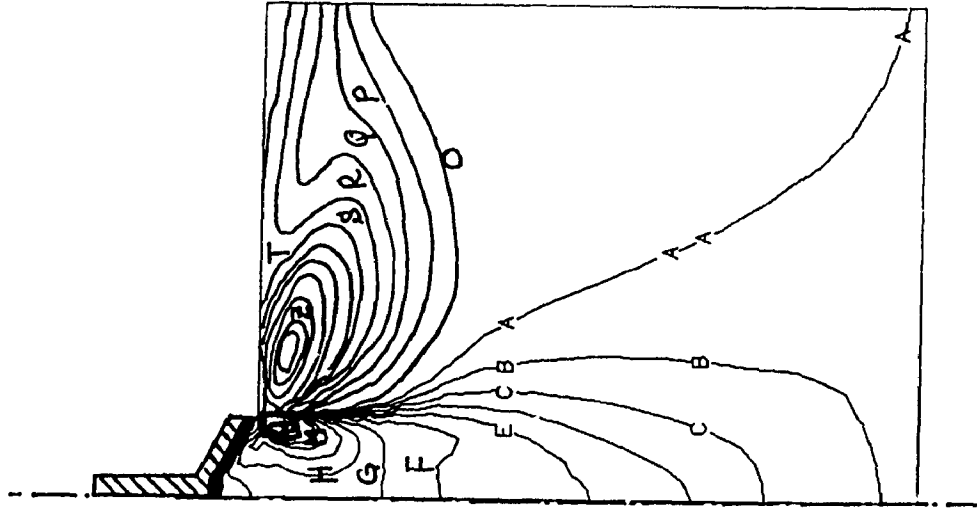


a) Undeformed/Deformed Mesh

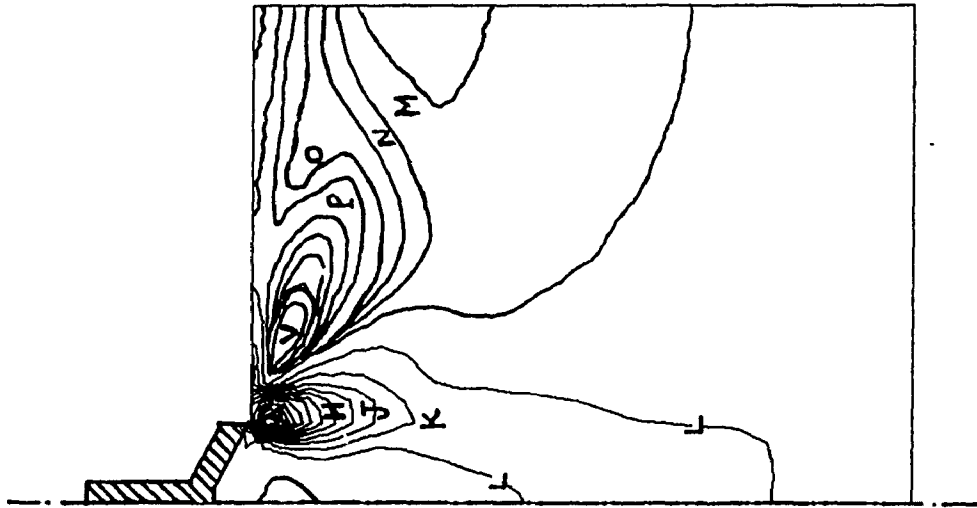


b) Displacement Vectors

Figure 4.4 Typical Undeformed/Deformed Mesh & Displacement Vectors for Triangular (1) Shell Surface Footing

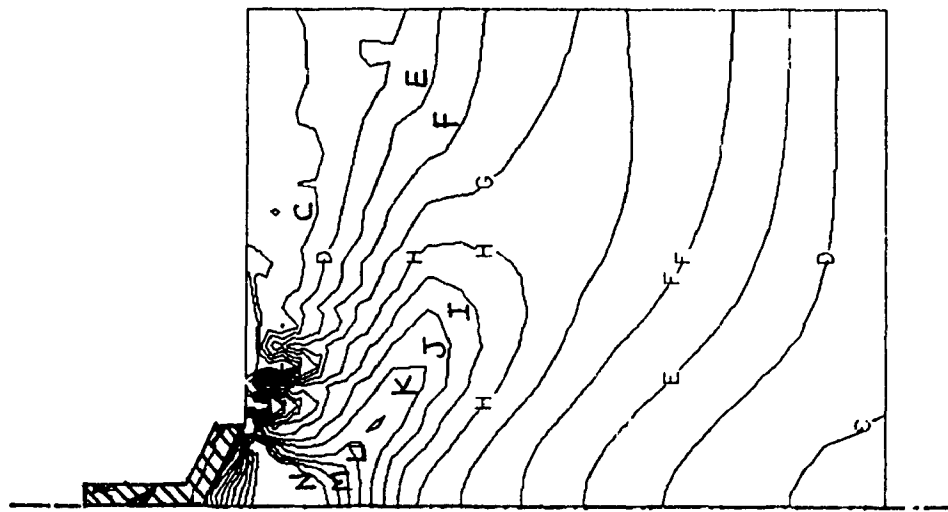


b) Vertical Strain ( $\epsilon_{yy}$ )

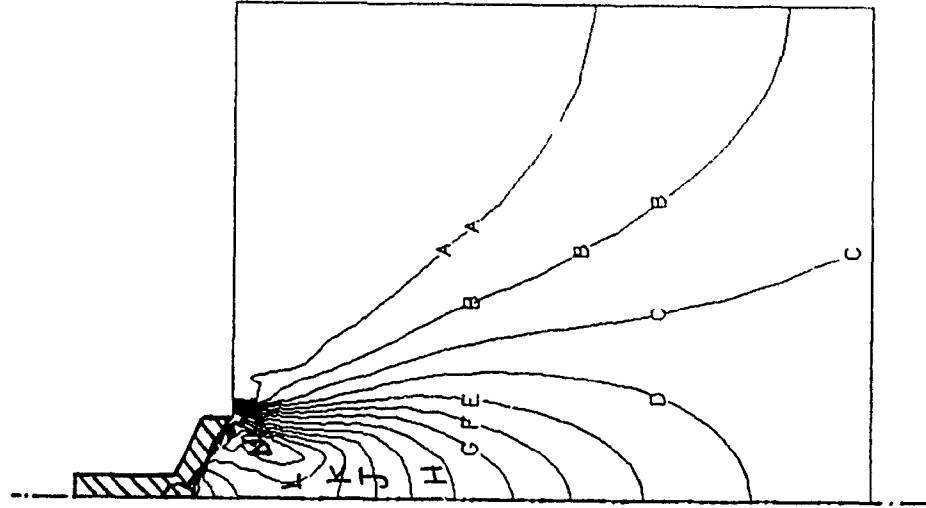


a) Horizontal Strain ( $\epsilon_{xx}$ )

Figure 4.5 Typical Distribution for Horizontal & Vertical Strains for Triangular (1) Shell Surface Footing



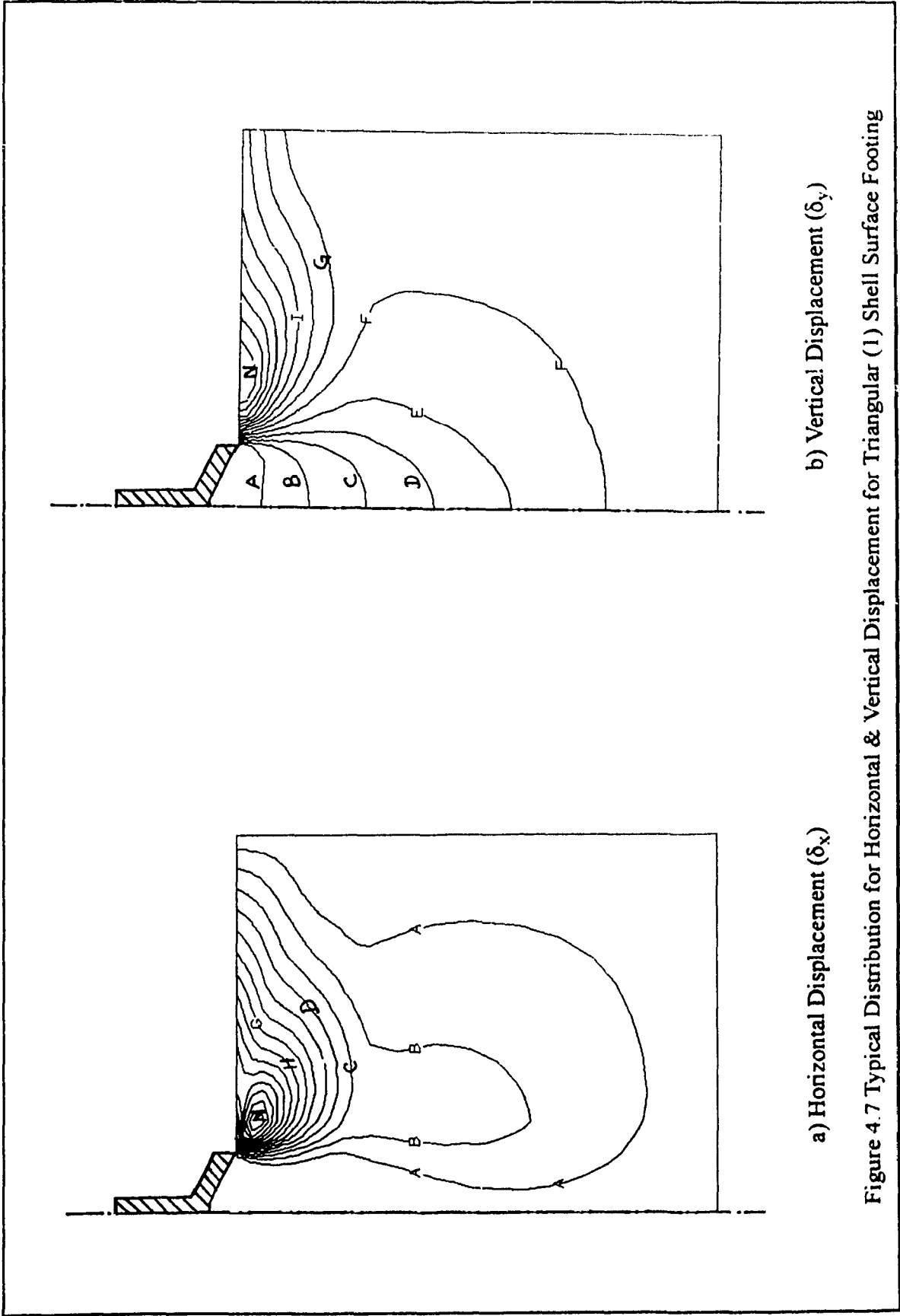
a) Horizontal Stress ( $\sigma_{xx}$ )



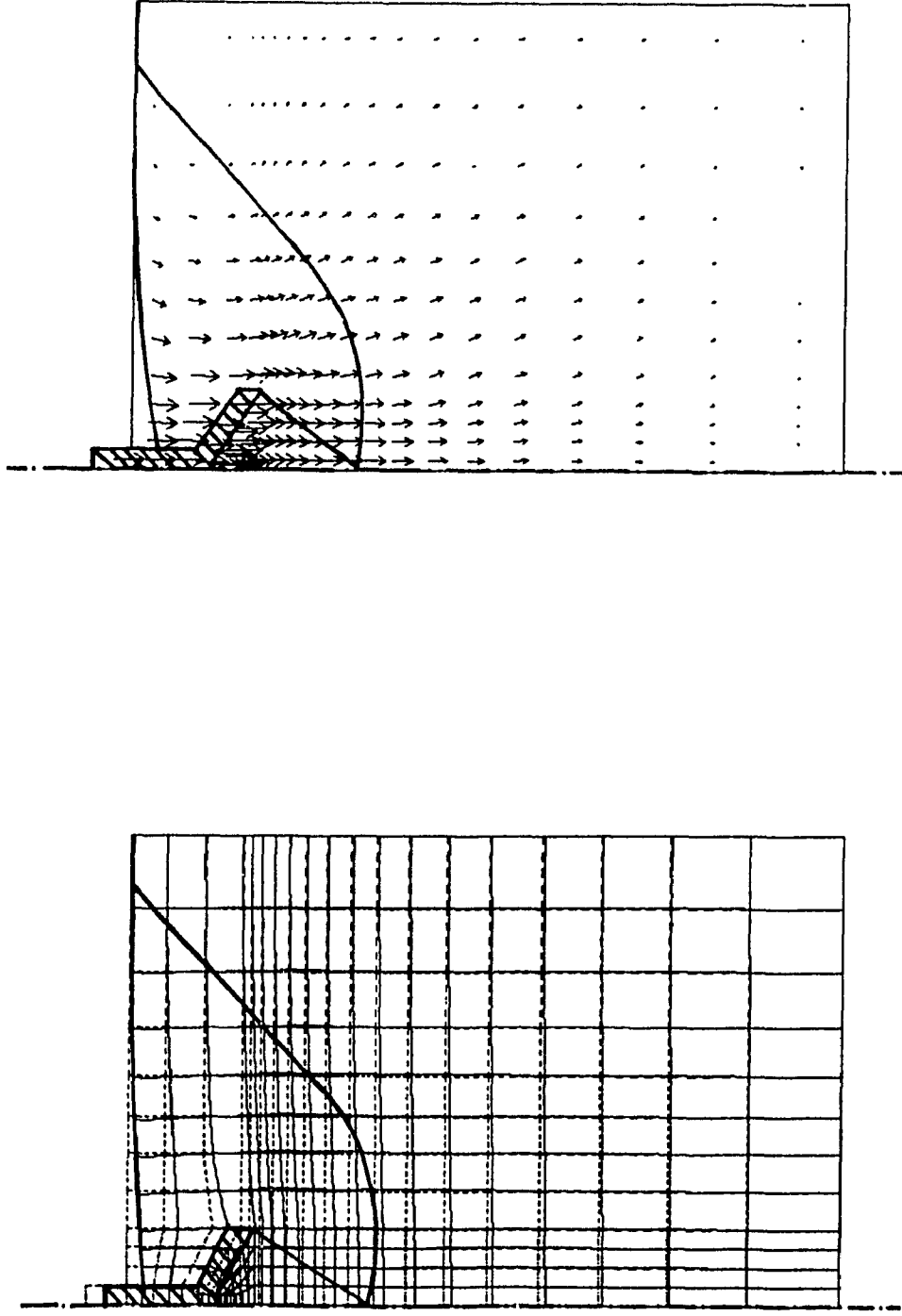
b) Vertical Stress ( $\sigma_{yy}$ )

Figure 4.6 Typical Distribution for Horizontal & Vertical Stresses for Triangular (1) Shell Surface Footing





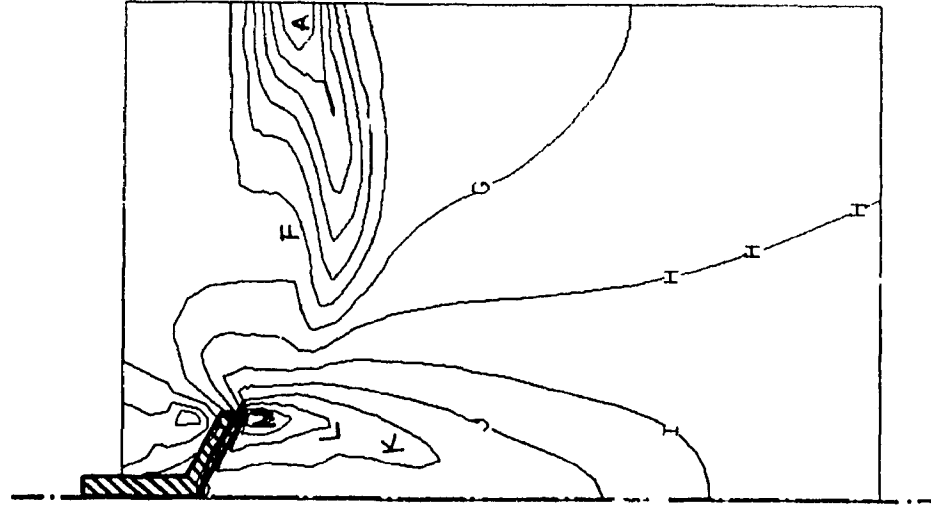
a) Horizontal Displacement ( $\delta_x$ )  
 b) Vertical Displacement ( $\delta_y$ )  
 Figure 4.7 Typical Distribution for Horizontal & Vertical Displacement for Triangular (1) Shell Surface Footing



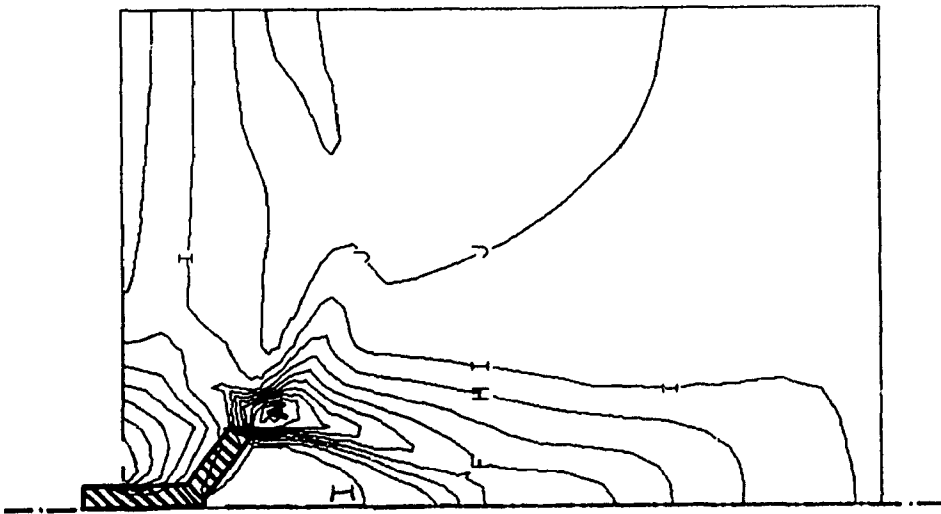
b) Displacement Vectors

a) Undeformed/Deformed Mesh

Figure 4.8 Typical Undeformed/Deformed Mesh & Displacement Vectors for Triangular (1) Shell Embedded Footing

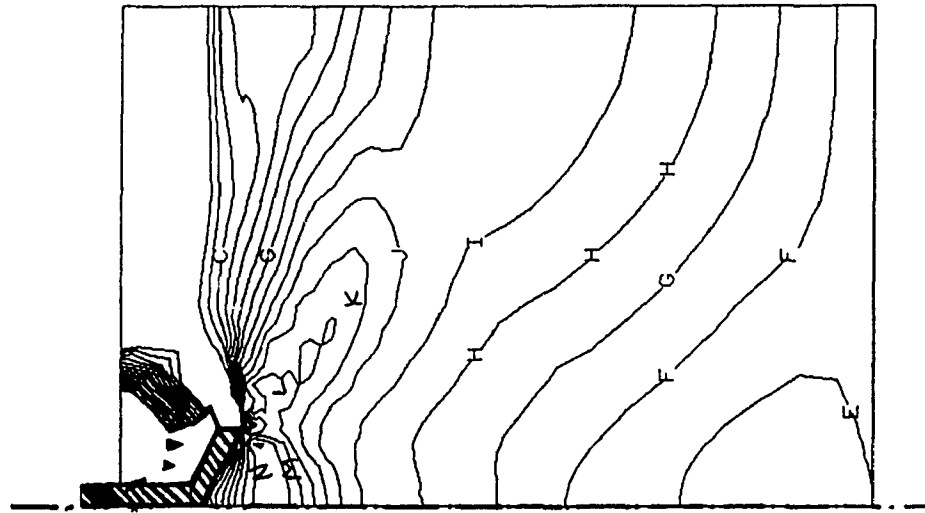


b) Vertical Strain ( $\epsilon_{yy}$ )

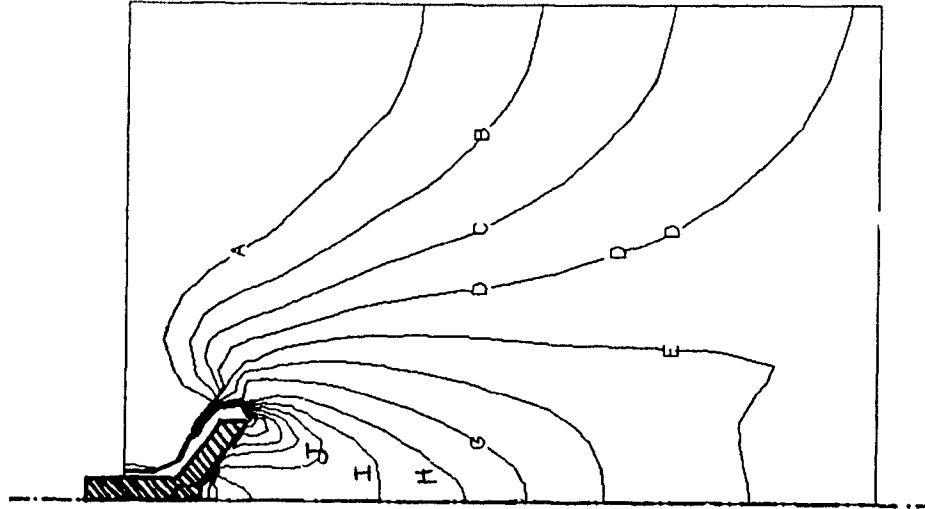


a) Horizontal Strain ( $\epsilon_{xx}$ )

Figure 4.9 Typical Distributions for Horizontal & Vertical Strain for Triangular (1) Shell Embedded Footing



a) Horizontal Stress ( $\sigma_{xx}$ )



b) Vertical Stress ( $\sigma_{yy}$ )

Figure 4.10 Typical Distributions for Horizontal & Vertical Stress for Triangular (1) Shell Embedded Footing

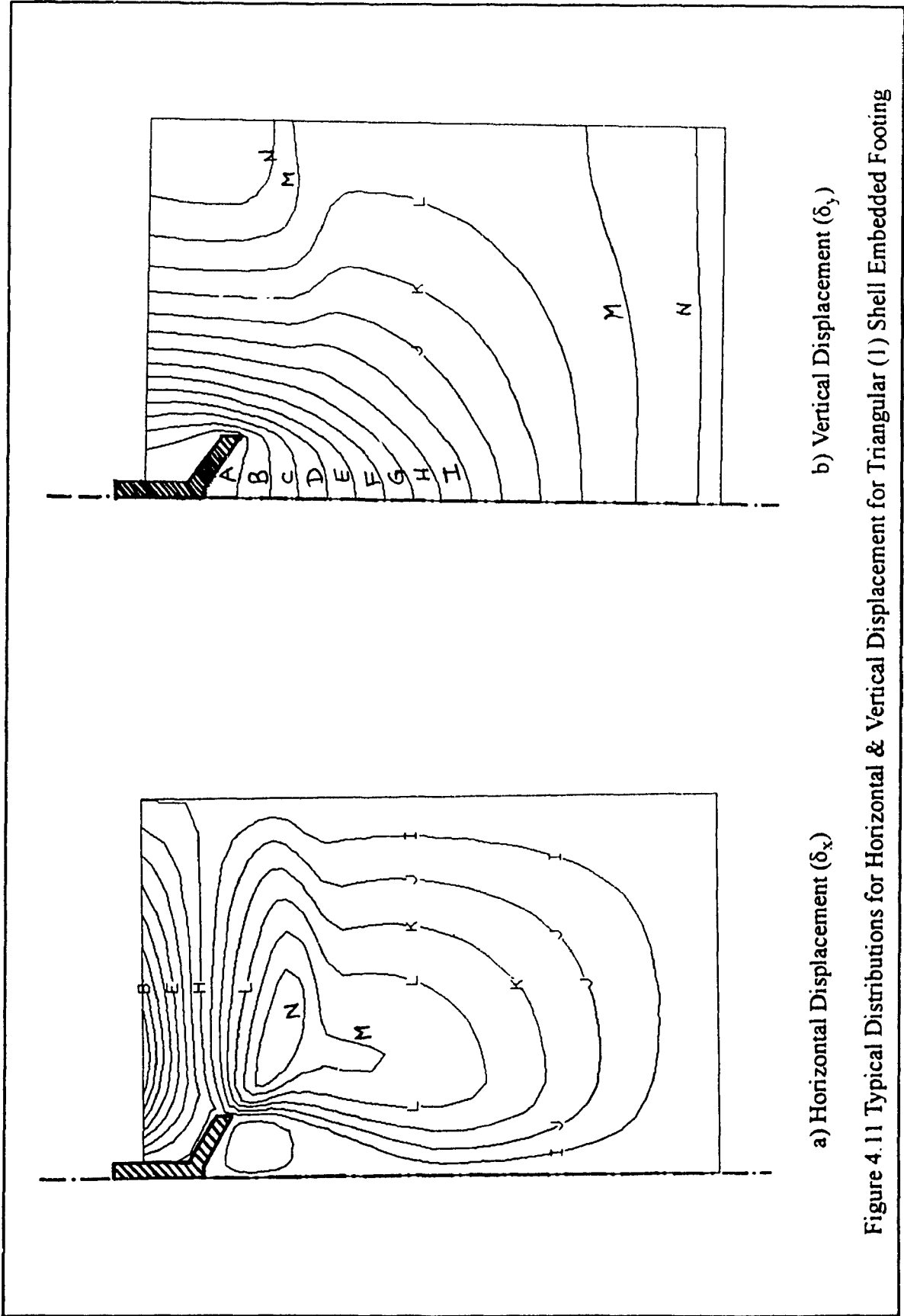


Figure 4.11 Typical Distributions for Horizontal & Vertical Displacement for Triangular (1) Shell Embedded Footing

Table 4.2 Summary of Numerical Results for The Distribution of Horizontal Strain ( $\epsilon_{xx}$ )

Sand	Footing	Contour Lines for Surface Footings					Contour Lines For Embedded Footings				
		A	L	M	V	A	I	N			
Loose	Strip Flat	-0.246	-0.000273	0.0000	0.0050	-0.0418	-0.00424	0.0280			
	Triangular (1) Shell	-0.272	-0.004390	0.0602	0.0043	-0.0596	-0.00152	0.0348			
	Triangular (2) Shell	-0.280	-0.000252	0.0666	0.0048	-0.0826	-0.00657	0.0410			
Medium	Strip Flat	-0.322	-0.029000	0.0053	0.0742	-0.0660	-0.00705	0.0435			
	Triangular (1) Shell	-0.341	-0.009350	0.0051	0.0714	-0.0818	-0.00174	0.0483			
	Triangular (2) Shell	-0.320	-0.025600	0.0058	0.0812	-0.0902	-0.00701	0.0450			
Dense	Strip Flat	-0.367	-0.001690	0.0062	0.0868	-0.0935	-0.01030	0.0610			
	Triangular (1) Shell	-0.361	-0.001880	0.0061	0.0854	-0.0989	-0.00172	0.0590			
	Triangular (2) Shell	-0.403	-0.001710	0.0068	0.0952	-0.0653	-0.00061	0.1030			

Table 4.3 Summary of Numerical Results for The Distribution of Vertical Strain ( $\epsilon_{yy}$ )

Sand	Footing	Contour Lines for Surface Footings						Contour Lines for Embedded Footings			
		A	N	O	Z	A	H	N			
Loose	Strip Flat	0.0048	0.0672	-0.0210	-0.2160	-0.0176	-0.00432	0.0399			
	Triangular (1) Shell	0.0053	0.0742	-0.0287	-0.2230	-0.0596	-0.00152	0.0348			
	Triangular (2) Shell	0.0055	0.0770	-0.0304	-0.2440	-0.0598	-0.00822	0.0743			
Medium	Strip Flat	0.0053	0.0742	-0.0390	0.0742	-0.0261	-0.00608	0.0607			
	Triangular (1) Shell	0.0056	0.0788	-0.0416	-0.3220	-0.0459	-0.000038	0.0733			
	Triangular (2) Shell	0.0056	0.0788	-0.0478	-0.3770	-0.0590	-0.003870	0.0843			
Dense	Strip Flat	0.0056	0.0784	-0.0500	-0.4790	-0.0350	-0.007620	0.0838			
	Triangular (1) Shell	0.0060	0.0840	-0.0664	-0.5070	-0.0561	-0.001410	0.0861			
	Triangular (2) Shell	0.0066	0.0924	-0.0738	-0.5650	-0.0653	-0.000613	0.1030			

Table 4.4 Summary of Numerical Results for The Distribution of Horizontal Stress ( $\sigma_{hx}$ ) (in kPa)

Sand	Footing	Contour Lines for Surface Footings		Contour Lines for Embedded Footings	
		A	N	A	N
Loose	Strip Flat	2.00	28.00	3.00	42.00
	Triangular (1) Shell	3.00	42.00	3.00	42.00
	Triangular (2) Shell	3.00	42.00	4.00	56.00
Medium	Strip Flat	4.00	56.00	5.00	70.00
	Triangular (1) Shell	6.00	84.00	6.00	84.00
	Triangular (2) Shell	6.00	84.00	6.00	84.00
Dense	Strip Flat	7.00	98.00	8.00	112.00
	Triangular (1) Shell	22.00	308.00	8.00	112.00
	Triangular (2) Shell	8.00	112.00	9.00	126.00



Table 4.5 Summary of Numerical Results for The Distribution of Vertical Stress ( $\sigma_{yy}$ ) (in kPa)

Sand	Footing	Contour Lines for Surface Footings		Contour Lines for Embedded Footings	
		A	N	A	N
Loose	Strip Flat	6.00	84.00	7.00	98.00
	Triangular (1) Shell	8.00	112.00	10.00	140.00
	Triangular (2) Shell	8.00	112.00	10.00	140.00
Medium	Strip Flat	14.00	196.00	15.00	210.00
	Triangular (1) Shell	15.00	210.00	20.00	280.00
	Triangular (2) Shell	20.00	280.00	20.00	280.00
Dense	Strip Flat	22.00	308.00	26.00	364.00
	Triangular (1) Shell	27.00	378.00	30.00	420.00
	Triangular (2) Shell	30.00	420.00	32.00	448.00

Table 4.6 Summary of The Distribution of Horizontal Displacement ( $\delta_x$ ) (in meters)

Sand	Footing	Contour Lines for Surface Footings		Contour Lines for Embedded Footing		
		A	N	A	H	N
Loose	Strip Flat	0.000663	0.0095	-0.00307	-0.000346	0.00199
	Triangular (1) Shell	0.000664	0.0105	-0.00342	-0.000033	0.00287
	Triangular (2) Shell	0.000476	0.0099	-0.00406	-0.000350	0.00398
Medium	Strip Flat	0.000808	0.0131	-0.00481	-0.000144	0.00277
	Triangular (1) Shell	0.000673	0.0131	-0.00466	-0.000284	0.00346
	Triangular (2) Shell	0.000344	0.0117	-0.00447	-0.000636	0.00334
Dense	Strip Flat	0.000866	0.0160	-0.00683	-0.000421	0.00358
	Triangular (1) Shell	0.000604	0.0149	-0.00561	-0.000515	0.00385
	Triangular (2) Shell	0.000534	0.0160	-0.00547	-0.000204	0.00431

Table 4.7 Summary of The Distribution for Vertical Displacement ( $\delta_y$ ) (in meters)

Sand	Footing	Contour Lines for Surface Footings		Contour Lines for Embedded Footings	
		A	N	A	N
Loose	Strip Flat	-0.0106	0.0119	-0.0131	-0.000933
	Triangular (1) Shell	-0.0108	0.0136	-0.0155	-0.000380
	Triangular (2) Shell	-0.0123	0.0121	-0.0189	-0.000662
Medium	Strip Flat	-0.0156	0.0175	-0.0201	-0.001440
	Triangular (1) Shell	-0.0142	0.0182	-0.0214	-0.001530
	Triangular (2) Shell	-0.0158	0.0149	-0.0216	-0.000648
Dense	Strip Flat	-0.0177	0.0236	-0.0280	-0.002000
	Triangular (1) Shell	-0.0173	0.0220	-0.0259	-0.000185
	Triangular (2) Shell	-0.0178	0.0235	-0.0273	-0.001950

## CHAPTER 5

### THEORETICAL MODELLING

#### 5.1 General

The ultimate bearing capacity of a flat strip foundation has been the subject of investigation of several researchers during the past century. The basic fundamentals of the ultimate bearing capacity theories are based on the work of Prandtl (1921) and Reissner (1924). They investigated the problem of penetrating a metal punch into another softer, homogenous, isotropic material by applying the theory of plastic equilibrium.

Terzaghi (1943) was the pioneer to develop the first generalized ultimate bearing capacity theory and applied it to the field of geotechnical engineering. Since then, several contributions and modifications have been made by other researchers to refine and improve the bearing capacity theory. The solution of the ultimate bearing capacity is theoretically correct only if the system is statically and kinematically admissible. Statics conditions are satisfied when all limit equilibrium equations are satisfied ( $\Sigma X=0, \Sigma Y=0, \Sigma M=0$ ), i.e., the shear stress on a soil element is equal to the shearing resistance of the said soil along the rupture surface. The conditions of Kinematics are satisfied if the movement and displacement of soil elements along the rupture plane are feasible.

The most common rupture surface used in the bearing capacity theories is composed of a soil wedge immediately located below the footing's base. The wedge is a rigid body which moves integrally with the footing during loading and remains in an elastic condition. A logarithmic spiral is originated from the point of intersection between the foundation's axis of symmetry and the elastic soil wedge. The logarithmic spiral is then connected with a plane surface until it intersects with the ground surface. The assumptions

used in these theories lead to that the final result does not satisfy the basic requirements for either statics or kinematics conditions. However, these shortcomings are probably justified due to the fact that there are still a lot of uncertainties in the evaluation of the basic soil parameters employed in the calculation process of the ultimate bearing capacity.

## 5.2 Theoretical Model for Shell Foundation

The rupture surfaces deduced from the experimental and the numerical modelling in the present investigation were idealized and represented by a rupture surface composed of circular and plane surfaces. This rupture surface should satisfy the requirements for both statics and kinematics conditions for shell foundations. It is of interest to note that this mechanism was used by Balla (1962) for strip flat foundation.

The proposed rupture surface originates from the apex of the soil wedge and intersects with the footing's axis of symmetry and the ground surface at angles which satisfied the statics equilibrium. In order for the rupture surface to be kinematically admissible, only circular and plane surfaces were considered in its formation. The proposed rupture surface shown in Figure 5.1 is composed of two parts, mainly a circular surface starts from point (h), which is the point of intersection of the foundation's axis of symmetry with the edge surface of soil wedge (eh), then connected with a plane surface (mn), which is tangent to the circular surface at point (m), and finally intersects with the ground surface at point (n).

The objective of the present theoretical analysis is to determine the circle which satisfy the equilibrium of all forces acting on the rupture surface. The deduced rupture surface will be used to determine the bearing capacity coefficients ( $N_c$ ,  $N_q$ , and  $N_\gamma$ ) and consequently the ultimate bearing capacity ( $q_u$ ).

In the present analysis, a Shell Ratio (SR) was introduced which represents the footing's configuration in the vertical direction as given in equation (5.1). This ratio is selected to reflect the effect of shell configuration on the failure angle ( $\alpha$ ). The two extreme limits

for (SR) are: SR= 1 for flat footings, i.e., ( $\theta = 0^\circ$ ) ; and SR= 2 for pile foundation, i.e., ( $\theta = 90^\circ$ ) . The values for (SR) which lie between 1 and 2 are for shell foundation.

$$SR = \frac{\pi + 2\theta}{\pi} \quad (5.1)$$

where:  $\theta$  is shell angle between shell surface (fe) and the horizontal level (ge).

The failure angle ( $\alpha$ ) depends on the shell configuration represented by the shell ratio (SR), and the angle of shearing resistance ( $\phi$ ). The following is a proposed empirical relationship for the failure angle ( $\alpha$ ) based on the experimental results deduced from the special loading tests conducted in the present investigation:

$$\alpha = \phi + (SR - 1) \left( \frac{\pi}{4} - \frac{2\phi}{3} \right) \quad (5.2)$$

where:  $\alpha$  is vertical angle between horizontal level (ge) and the surface (eh) of the soil wedge (egh).

According to equation (5.2), the failure angle ( $\alpha$ ) for the case of a flat footing, i.e., SR= 1, is equal to the angle of shearing resistance ( $\phi$ ); for shell footing with shell angle ( $\theta = 45^\circ$ ), i.e., SR= 1.5, the angle ( $\alpha$ ) is equal to ( $\pi/8 + 2\phi/3$ ); and for deep foundation, i.e., SR= 2 and ( $\theta = 90^\circ$ ), the angle ( $\alpha$ ) is equal to ( $\pi/4 + \phi/3$ ). However, the present investigation is limited to shallow foundation where the shell angle ( $\theta$ ) is less than  $90^\circ$ .

In order to determine the value of angle ( $\psi$ ), which satisfies the conditions of limit equilibrium, Mohr-Coulomb's envelope, (see Figure 5.2), is used to establish the slope of the tangent of the rupture surface at point (h) located on the axis of symmetry and point (n) on the ground surface. From the figure, the shear stress ( $\tau_{xy}$ ) can be presented as a function of the shear stress ( $\tau$ ) existed on Mohr's circle as follows:

$$\tau_{xy} = \tau \frac{\cos(\phi + 2\psi)}{\cos\phi} \quad (5.3)$$

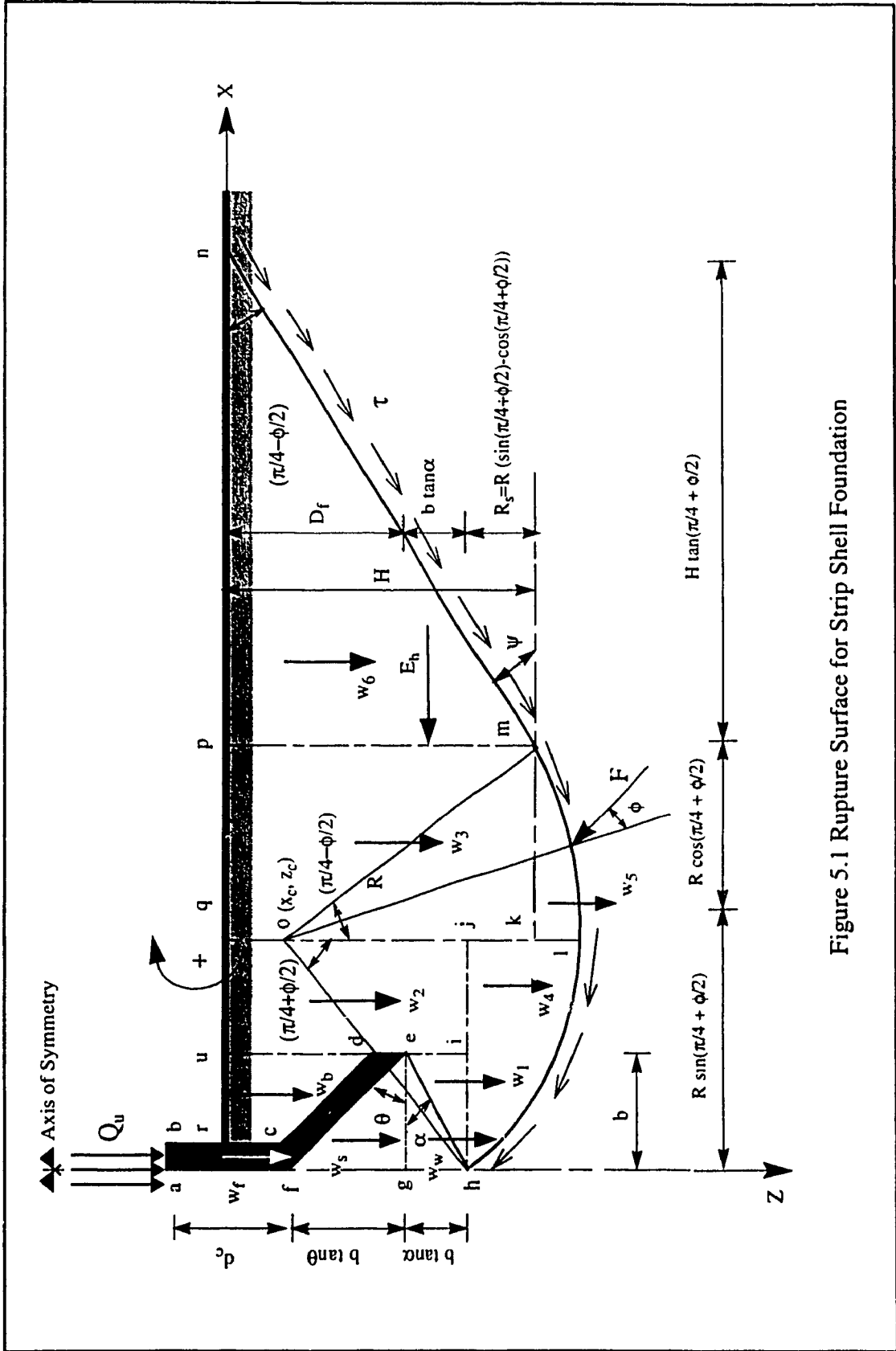


Figure 5.1 Rupture Surface for Strip Shell Foundation

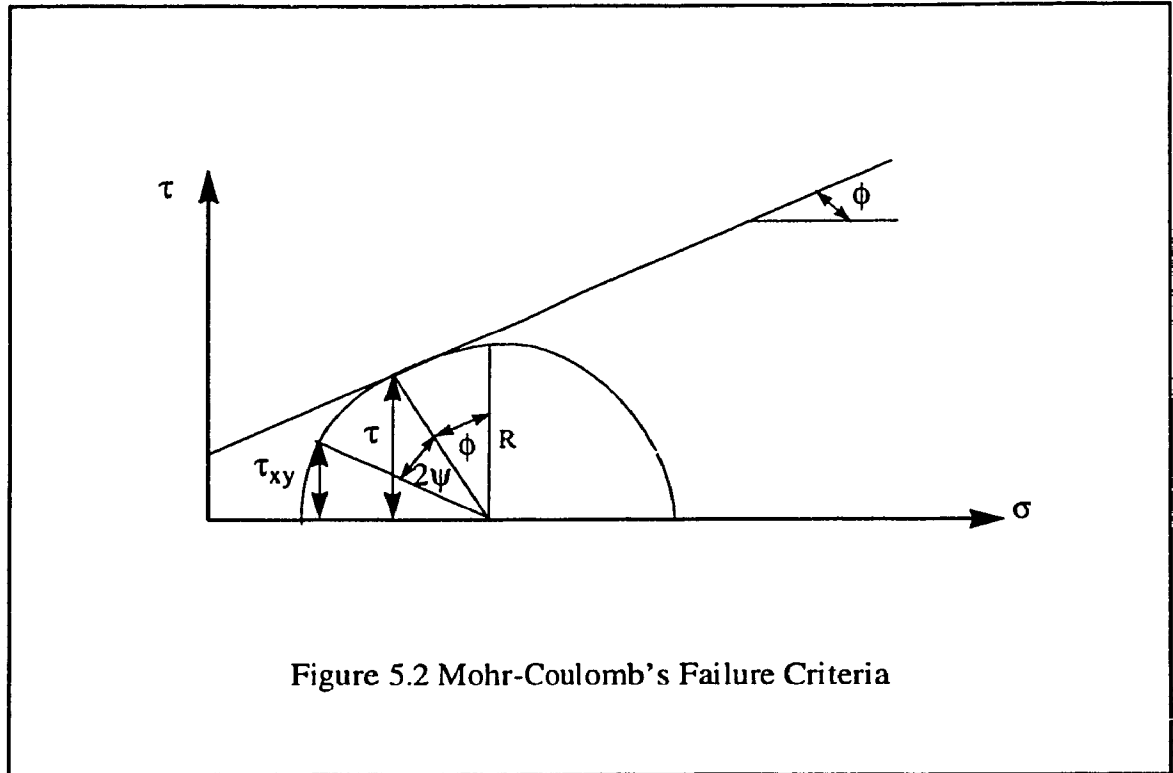


Figure 5.2 Mohr-Coulomb's Failure Criteria

The shear stress ( $\tau_{xy}$ ) on the axis of symmetry and on the ground surface, must be equal to zero, which is satisfied when  $\cos(\phi + 2\psi) = 0$ , i.e., when the angle  $(\phi + 2\psi)$  is equal to  $(\pm \pi/2)$ . According to the active and passive stress states, the slope of the tangent at points (h) and (n) can be given by the following:

$$\psi_1 = -\left(\frac{\pi}{4} + \frac{\phi}{2}\right) \quad (5.4)$$

$$\psi_2 = \left(\frac{\pi}{4} - \frac{\phi}{2}\right) \quad (5.5)$$

where:  $\psi_1$  and  $\psi_2$  are the slope of the tangent at point (h) and (n), respectively.

The distribution of soil pressure and shear stress along an arc of a given rupture surface was investigated by Kötter (1888). He derived a mathematical solution which can be employed for any rupture surface (plane or curve). This solution can be adopted to define more accurately the location and shape of the rupture surface. However, due to the rigorous mathematical formulation, Kötter's differential equation was rarely used by researchers in



predicting the ultimate bearing capacity of a foundation.

In the present investigation, in order to determine the distribution of shear stress acting along both parts of the rupture surface, Kötter's differential equation for the passive stress state will be utilized. Using the notations shown in Figure 5.3, Kötter's equation can be written as follows:

$$\frac{\partial \tau}{\partial s} + \frac{\partial \psi}{\partial s} (2 \tan \phi \tau) + \gamma \sin \phi \sin(\psi + \phi) = 0 \quad (5.6)$$

For the plane part (mn) of the rupture surface:  $\frac{\partial \psi}{\partial s} = 0$ . Substituting with this boundary condition in Kötter's differential equation, the following can be obtained:

$$\frac{\partial \tau_{pl}}{\partial s} - \gamma \sin \phi \sin(\psi + \phi) = 0 \quad (5.7)$$

$$\partial \tau_{pl} = \gamma \sin \phi \sin(\psi + \phi) \partial s \quad (5.8)$$

$$\tau_{pl} = \gamma \sin \phi \sin(\psi + \phi) s + \lambda_1 \quad (5.9)$$

where:  $\lambda_1$  is constant

From Figure (5.3a), and substitute by  $s = \frac{z}{\sin \psi}$ , thus:

$$\tau_{pl} = \gamma \sin \phi \frac{\sin(\psi + \phi)}{\sin \psi} z + \lambda_1 \quad (5.10)$$

Substitute for the angle  $\psi$  by  $\left(\frac{\pi}{4} - \frac{\phi}{2}\right)$ , as established from equation (5.5):

$$\tau_{pl} = \gamma \sin \phi \tan\left(\frac{\pi}{4} + \frac{\phi}{2}\right) z + \lambda_1 \quad (5.11)$$

Where  $\lambda_1$  is equal to the shear stress ( $\tau_{pl}$ ) at the ground surface, i.e., at  $z=0$ .

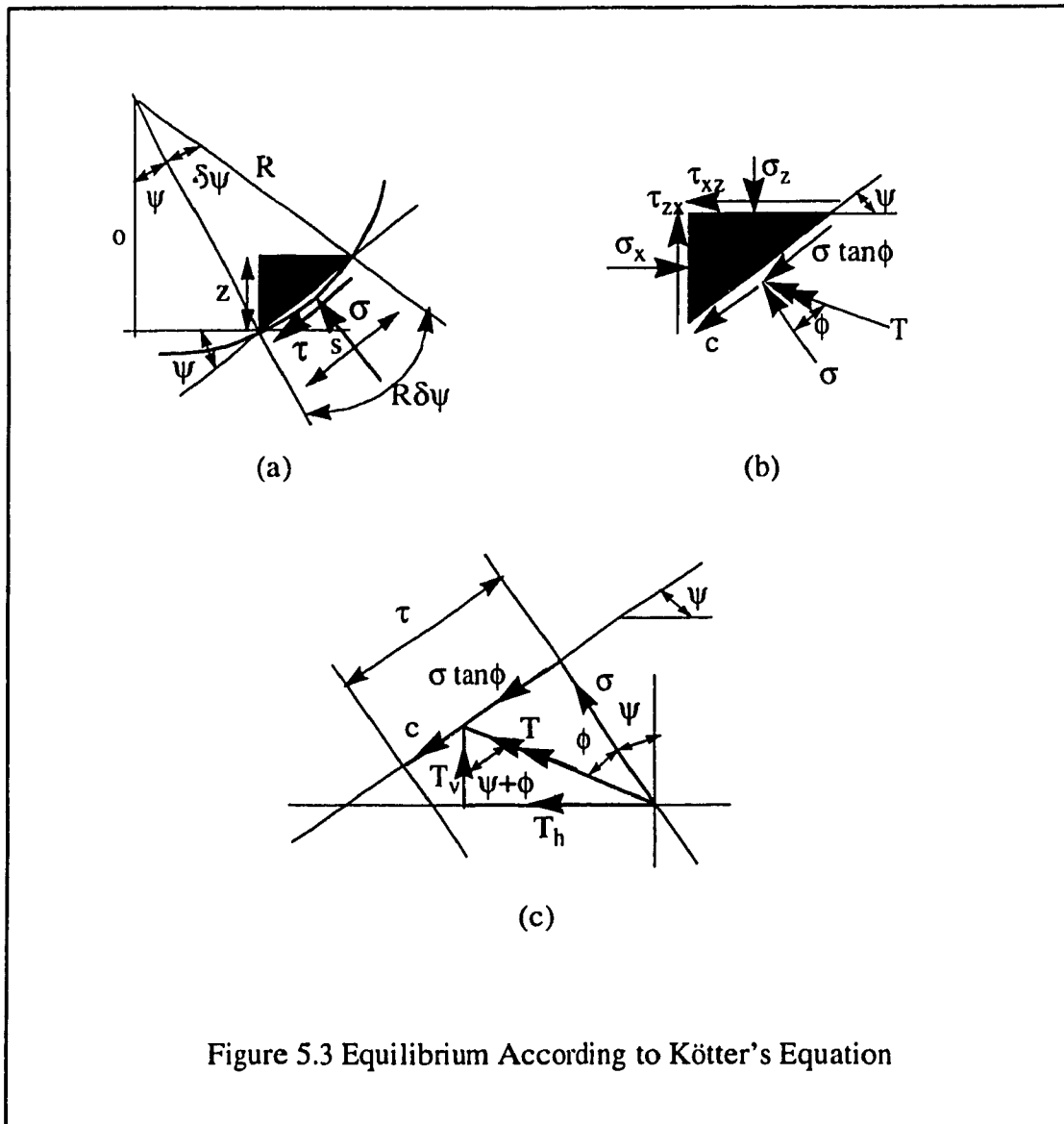


Figure 5.3 Equilibrium According to Kötter's Equation

$$\lambda_1 = \tau_{pl} = c(1 + \sin \phi) \quad (5.12)$$

$$\tau_{pl} = \gamma \sin \phi \tan\left(\frac{\pi}{4} + \frac{\phi}{2}\right) z + c(1 + \sin \phi) \quad (5.13)$$

For the circular surface:  $\frac{\partial s}{\partial \psi} = -R$ ; multiplying the first and second terms of Kötter's equation by  $\frac{\partial s}{\partial \psi}$  and the third term by  $(-R)$ , the following equation can be obtained:

$$\frac{\partial \tau_{cir}}{\partial \psi} + 2 \tan \phi \tau_{cir} = -R\gamma \sin \phi \sin(\psi + \phi) \quad (5.14)$$

In order to solve this equation, the following substitutions are employed:

$$M = 2 \tan \phi \quad (5.15)$$

$$N = -R\gamma \sin \phi \sin(\psi + \phi) \quad (5.16)$$

Substitute with equations (5.15) and (5.16) in equation (5.14):

$$\partial \tau_{cir} + (M\tau_{cir} - N)\partial \psi = 0 \quad (5.17)$$

Multiply equation (5.17) by  $\mu(\psi, \tau_{cir})$ .

$$\mu \partial \tau_{cir} + (M\tau_{cir} - N)\mu \partial \tau_{cir} = 0 \quad (5.18)$$

In order to obtain exact solution of equation (3.18), the following relationship must be satisfied:

$$\frac{\partial \mu}{\partial \psi} = \frac{\partial (M\tau_{cir} - N)}{\partial \tau_{cir}} \mu \quad (5.19)$$

$$\frac{\partial \mu}{\partial \psi} = M\mu = 2 \tan \phi \mu \quad (5.20)$$

$$\frac{\partial \mu}{\mu} = 2 \tan \phi \partial \psi \quad (5.21)$$

$$\ln(\mu) = 2 \tan \phi \psi ; \text{ i.e., } \mu = e^{2\psi \tan \phi} \quad (5.22)$$

The final solution of the differential equation can be obtained as follows:

$$\mu\tau_{cir} = \int \mu N \partial\psi \quad (5.23)$$

$$e^{2\psi \tan\phi} \tau_{cir} = -\int e^{2\psi \tan\phi} R\gamma \sin\phi \sin(\psi + \phi) \partial\psi \quad (5.24)$$

To determine the shear stress for the circular part of the rupture surface ( $\tau_{cir}$ ), the integration in the right-hand side of equation (5.24) is substituted by the following:

$$I = -\int e^{2\psi \tan\phi} R\gamma \sin\phi \sin(\psi + \phi) \partial\psi \quad (5.25)$$

To solve the integration (I) in equation (5.25), the following steps are performed:

$$I = \frac{e^{2\psi \tan\phi}}{2 \tan\phi} \sin(\psi + \phi) - \frac{1}{2 \tan\phi} \int e^{2\psi \tan\phi} \cos(\psi + \phi) \partial\psi \quad (5.26)$$

$$I = \frac{e^{2\psi \tan\phi}}{2 \tan\phi} \sin(\psi + \phi) - \frac{e^{2\psi \tan\phi}}{4 \tan^2\phi} \cos(\psi + \phi) - \frac{1}{4 \tan^2\phi} \int e^{2\psi \tan\phi} \sin(\psi + \phi) \partial\psi \quad (5.27)$$

$$I \left( 1 + \frac{1}{4 \tan^2\phi} \right) = \frac{e^{2\psi \tan\phi}}{2 \tan\phi} \sin(\psi + \phi) - \frac{e^{2\psi \tan\phi}}{4 \tan^2\phi} \cos(\psi + \phi) \quad (5.28)$$

$$I = \frac{e^{2\psi \tan\phi}}{4 \tan^2\phi} (2 \tan\phi \sin(\psi + \phi) - \cos(\psi + \phi)) + \lambda_2 \quad (5.29)$$

where:  $\lambda_2$  is constant

Substitute by the integration (I) in equation (5.24), the shear stress ( $\tau_{cir}$ ) can be presented in the following form:

$$\tau_{cir} = \lambda_2(e^{-2\psi \tan \phi}) - \frac{R\gamma \sin \phi}{1 + 4 \tan^2 \phi} (2 \tan \phi \sin(\psi + \phi) - \cos(\psi + \phi)) \quad (5.30)$$

In order to determine the constant ( $\lambda_2$ ), equate the shear stress from the plane part and the circular part, i.e.,  $\tau_{pl} = \tau_{cir}$ , at the junction point (m), where the slope of the tangent is equal to  $(\pi/4 - \phi/2)$ , and the depth (z) at point (m) is equal to (H).

$$\begin{aligned} \gamma \sin \phi \tan\left(\frac{\pi}{4} + \frac{\phi}{2}\right)H + c(1 + \sin \phi) &= \lambda_2 e^{-2\psi \tan \phi} \\ &- \frac{R\gamma \sin \phi}{1 + 4 \tan^2 \phi} (2 \tan \phi \sin(\psi + \phi) - \cos(\psi + \phi)) \end{aligned} \quad (5.31)$$

$$\begin{aligned} \lambda_2 &= e^{2\left(\frac{\pi}{4} - \frac{\phi}{2}\right) \tan \phi} \left( \gamma \sin \phi \tan\left(\frac{\pi}{4} + \frac{\phi}{2}\right)H + c(1 + \sin \phi) \right) + \\ &e^{2\left(\frac{\pi}{4} - \frac{\phi}{2}\right) \tan \phi} \frac{R\gamma \sin \phi}{1 + 4 \tan^2 \phi} \left( 2 \tan \phi \sin\left(\frac{\pi}{4} + \frac{\phi}{2}\right) - \cos\left(\frac{\pi}{4} + \frac{\phi}{2}\right) \right) \end{aligned} \quad (5.32)$$

To simplify the expressions used in the present analysis, constants which are function only of the angle of shearing resistance ( $\phi$ ) will be substituted by factors ( $\xi_i$ ), where:

$$\xi_1 = (1 + \sin \phi) \quad (5.33)$$

$$\xi_2 = \sin\left(\frac{\pi}{4} + \frac{\phi}{2}\right) - \cos\left(\frac{\pi}{4} + \frac{\phi}{2}\right) \quad (5.34)$$

$$\xi_3 = \sin \phi \tan \left( \frac{\pi}{4} + \frac{\phi}{2} \right) \quad (5.35)$$

$$\xi_4 = 1 + 4 \tan^2 \phi \quad (5.36)$$

$$\xi_5 = e^{2 \left( \frac{\pi}{4} + \frac{\phi}{2} \right) \tan \phi} \quad (5.37)$$

$$\xi_6 = \sin \phi \left( 2 \tan \phi \sin \left( \frac{\pi}{4} + \frac{\phi}{2} \right) - \cos \left( \frac{\pi}{4} + \frac{\phi}{2} \right) \right) \quad (5.38)$$

$$\xi_7 = \xi_2 \xi_3 + \frac{\xi_6}{\xi_4} \quad (5.39)$$

The soil depth (H) at point (m) on the rupture surface can be written as follows:

$$H = D_f + b \tan \alpha + R \left( \sin \left( \frac{\pi}{4} + \frac{\phi}{2} \right) - \cos \left( \frac{\pi}{4} + \frac{\phi}{2} \right) \right) \quad (5.40)$$

$$D_{fb} = D_f + b \tan \alpha \quad (5.41)$$

$$H = D_{fb} + R \xi_2 \quad (5.42)$$

The constant ( $\lambda_2$ ) can be presented in the following simplified form:

$$\lambda_2 = \xi_5 (\gamma D_{fb} \xi_3 + \gamma R \xi_7 + c \xi_1) \quad (5.43)$$

Figure 5.3c shows the vertical and horizontal components of the resultant force,  $T_v$  and  $T_h$ , respectively, which can be derived as follows:

$$\tau = c + \sigma \tan \phi \quad (5.44)$$

$$\tau - c = \sigma \tan \phi = \frac{\sigma}{\cos \phi} \sin \phi = T \sin \phi \quad (5.45)$$

$$T = \frac{\tau - c}{\sin \phi} \quad (5.46)$$

$$T_v = \frac{\tau - c}{\sin \phi} \cos(\psi + \phi) \quad (5.47)$$

$$T_h = \frac{\tau - c}{\sin \phi} \sin(\psi + \phi) \quad (5.48)$$

The partial derivative of the vertical component ( $\partial T_v$ ) acting on an element of the rupture surface as shown in Figure 5.3a can be presented as follows:

$$\partial T_v = \frac{\tau - c}{\sin \phi} \cos(\psi + \phi) R \partial \psi \quad (5.49)$$

For the plane part, substitute with the shear stress ( $\tau_{pl}$ ) in equation (5.49):

$$\partial T_{vp} = \left( \gamma \tan \left( \frac{\pi}{4} + \frac{\phi}{2} \right) z + c \right) R \cos(\psi + \phi) \partial \psi \quad (5.50)$$

$$\partial z = R \cos(\psi + \phi) \partial \psi \quad (5.51)$$

$$\partial T_{vp} = \left( \gamma \tan \left( \frac{\pi}{4} + \frac{\phi}{2} \right) z + c \right) \partial z \quad (5.52)$$

$$T_{vp} = \frac{\gamma}{2} \tan \left( \frac{\pi}{4} + \frac{\phi}{2} \right) z^2 + cz \quad (5.53)$$

where:  $T_{vp}$  is the vertical component of the resultant force acting on the plane part of the rupture surface.

For the circular part, substitute with the shear stress ( $\tau_{cir}$ ) in equation (5.49):

$$\partial T_{vc} = \int_{-\left(\frac{\pi}{4} + \frac{\phi}{2}\right)}^{\left(\frac{\pi}{4} - \frac{\phi}{2}\right)} \frac{(\tau_{c11} - c)}{\sin \phi} \cos(\psi + \phi) R \partial \psi \quad (5.54)$$

The integral given in equation (5.54) is divided to three parts  $I_1$ ,  $I_2$ , and  $I_3$  as follows:

$$T_{vc} = \sum_{n=1}^3 I_n \quad (5.55)$$

$$I_1 = \int \frac{\lambda_2 e^{-2\psi \tan \phi}}{\sin \phi} R \cos \psi + \phi \partial \psi \quad (5.56)$$

$$I_2 = -\int \frac{R^2 \gamma}{1 + 4 \tan^2 \phi} (2 \tan \phi \sin(\psi + \phi) - \cos(\psi + \phi)) \cos(\psi + \phi) \partial \psi \quad (5.57)$$

$$I_3 = -\int \frac{cR}{\sin \phi} \cos(\psi + \phi) \partial \psi \quad (5.58)$$

The solution of equations (5.56), (5.57), and (5.58) was performed as follows:

$$I_1 = \frac{\lambda_2 R}{\sin \phi} \left( \frac{e^{-2\psi \tan \phi}}{1 + 4 \tan^2 \phi} (\sin(\psi + \phi) - 2 \tan \phi \cos(\psi + \phi)) \right) \Bigg|_{-\left(\frac{\pi}{4} + \frac{\phi}{2}\right)}^{\left(\frac{\pi}{4} - \frac{\phi}{2}\right)} \quad (5.59)$$

$$I_1 = \frac{\lambda_2 R e^{-2\left(\frac{\pi}{4} - \frac{\phi}{2}\right) \tan \phi}}{\sin \phi (1 + 4 \tan^2 \phi)} \cos\left(\frac{\pi}{4} + \frac{\phi}{2}\right) \times$$

$$\left( e^{\pi \tan \phi} \tan^2\left(\frac{\pi}{4} + \frac{\phi}{2}\right) + \tan\left(\frac{\pi}{4} + \frac{\phi}{2}\right) - 2 \tan \phi \right) \quad (5.60)$$



$$I_2 = -\frac{\gamma R^2}{1 + 4 \tan^2 \phi} \left( \sin^2(\psi + \phi) + \psi + \frac{\sin 2(\psi + \phi)}{2} \right) \Bigg|_{\left(\frac{\pi}{4} - \frac{\phi}{2}\right)}^{\left(\frac{\pi}{4} + \frac{\phi}{2}\right)} \quad (5.61)$$

$$I_2 = -\frac{\gamma R^2}{1 + 4 \tan^2 \phi} \left( \frac{\pi}{4} + \frac{\cos \phi}{2} - \tan \phi \sin \phi \right) \quad (5.62)$$

$$I_3 = -\frac{cR}{\sin \phi} (\sin(\psi + \phi)) \Bigg|_{\left(\frac{\pi}{4} + \frac{\phi}{2}\right)}^{\left(\frac{\pi}{4} - \frac{\phi}{2}\right)} \quad (5.63)$$

$$I_3 = -\frac{cR\sqrt{2}}{\sin \phi} \cos\left(\frac{\phi}{2}\right) \quad (5.64)$$

Substitute with the values for  $I_1$ ,  $I_2$ , and  $I_3$  given in equations (5.60), (5.62), and (5.64), respectively, the expression for  $(T_{vc})$  can be presented as follows:

$$T_{vc} = \frac{\lambda_2 R e^{-2\left(\frac{\pi}{4} - \frac{\phi}{2}\right) \tan \phi}}{\sin \phi (1 + 4 \tan^2 \phi)} \cos\left(\frac{\pi}{4} + \frac{\phi}{2}\right) \times$$

$$\left( e^{\pi \tan \phi} \tan^2\left(\frac{\pi}{4} + \frac{\phi}{2}\right) + \tan\left(\frac{\pi}{4} + \frac{\phi}{2}\right) - 2 \tan \phi \right) +$$

$$\frac{\gamma R^2}{1 + 4 \tan^2 \phi} \left( \frac{\pi}{4} + \frac{\cos \phi}{2} - \tan \phi \sin \phi \right) - \frac{cR\sqrt{2}}{\sin \phi} \cos\left(\frac{\phi}{2}\right) \quad (5.65)$$

$$\xi_8 = \cos\left(\frac{\pi}{4} + \frac{\phi}{2}\right) e^{-2\left(\frac{\pi}{4} - \frac{\phi}{2}\right) \tan \phi} \quad (5.66)$$

$$\xi_9 = e^{\pi \tan \phi} \tan^2\left(\frac{\pi}{4} + \frac{\phi}{2}\right) + \tan\left(\frac{\pi}{4} + \frac{\phi}{2}\right) - 2 \tan \phi \quad (5.67)$$

$$\xi_{10} = \frac{\pi}{4} + \frac{\cos\phi}{2} - \sin\phi \tan\phi \quad (5.68)$$

$$\xi_{11} = -\frac{\sqrt{2} \cos\left(\frac{\phi}{2}\right)}{\sin\phi} \quad (5.69)$$

Substitute with ( $\xi_8$ ) through ( $\xi_{11}$ ) in equation (5.65), the following can be obtained:

$$T_{vc} = \frac{\lambda_2 R \xi_8 \xi_9}{\sin\phi \xi_4} + \frac{\gamma R^2 \xi_{10}}{\xi_4} + c R \xi_{11} \quad (5.70)$$

$$\xi_{12} = \frac{\xi_3 \xi_5 \xi_8 \xi_9}{\sin\phi \xi_4} \quad (5.71)$$

$$\xi_{13} = \frac{\xi_5 \xi_7 \xi_8 \xi_9}{\sin\phi \xi_4} + \frac{\xi_{10}}{\xi_4} \quad (5.72)$$

$$\xi_{14} = \frac{\xi_1 \xi_5 \xi_8 \xi_9}{\sin\phi \xi_4} + \xi_{11} \quad (5.73)$$

The vertical component of the resultant force acting on the circular part of rupture surface ( $T_{vc}$ ) can be represented by the following expression:

$$T_{vc} = \gamma R D_{fb} \xi_{12} + \gamma R^2 \xi_{13} + c R \xi_{14} \quad (5.74)$$

The rupture surface shown in Figure 5.1 was divided into soil prisms, with the notation ( $w_n$ ) to represent the soil weight, and ( $lw_n$ ) for the corresponding lever arm from the center of gravity of the soil prism to the center of the sliding circle, point (o). The expressions for the soil weights and the corresponding lever arms can be given as follows:

$$w_1 = \frac{1}{2}\gamma b^2 \tan\alpha : \text{for soil prism (hie)} \quad (5.75)$$

$$lw_1 = R \sin\left(\frac{\pi}{4} + \frac{\phi}{2}\right) - \frac{2}{3}b \quad (5.76)$$

$$w_2 = \gamma D_{fb} \left( R \sin\left(\frac{\pi}{4} + \frac{\phi}{2}\right) - b \right) ; \text{for soil prism (ijqu)} \quad (5.77)$$

$$lw_2 = \frac{1}{2} \left( R \sin\left(\frac{\pi}{4} + \frac{\phi}{2}\right) - b \right) \quad (5.78)$$

$$w_3 = \gamma HR \cos\left(\frac{\pi}{4} + \frac{\phi}{2}\right) ; \text{for soil prism (kmpq)} \quad (5.79)$$

$$lw_3 = \frac{1}{2} R \cos\left(\frac{\pi}{4} + \frac{\phi}{2}\right) \quad (5.80)$$

$$w_4 = \frac{1}{2}\gamma R^2 \left( \frac{\pi}{4} + \frac{\phi}{2} - \sin\left(\frac{\pi}{4} + \frac{\phi}{2}\right) \cos\left(\frac{\pi}{4} + \frac{\phi}{2}\right) \right) ; \text{for soil prism (hlj)} \quad (5.81)$$

$$lw_4 = \frac{2}{3} R \frac{\left( 1 - \frac{3}{2} \cos\left(\frac{\pi}{4} + \frac{\phi}{2}\right) + \frac{1}{2} \cos^3\left(\frac{\pi}{4} + \frac{\phi}{2}\right) \right)}{\left( \frac{\pi}{4} + \frac{\phi}{2} - \sin\left(\frac{\pi}{4} + \frac{\phi}{2}\right) \cos\left(\frac{\pi}{4} + \frac{\phi}{2}\right) \right)} \quad (5.82)$$

$$w_5 = \frac{1}{2}\gamma R^2 \left( \frac{\pi}{4} - \frac{\phi}{2} - \sin\left(\frac{\pi}{4} - \frac{\phi}{2}\right) \cos\left(\frac{\pi}{4} - \frac{\phi}{2}\right) \right) ; \text{for soil prism (lmk)} \quad (5.83)$$

$$lw_5 = \frac{2}{3} R \frac{\left( 1 - \frac{3}{2} \cos\left(\frac{\pi}{4} - \frac{\phi}{2}\right) + \frac{1}{2} \cos^3\left(\frac{\pi}{4} - \frac{\phi}{2}\right) \right)}{\left( \frac{\pi}{4} - \frac{\phi}{2} - \sin\left(\frac{\pi}{4} - \frac{\phi}{2}\right) \cos\left(\frac{\pi}{4} - \frac{\phi}{2}\right) \right)} \quad (5.84)$$

$$w_6 = \frac{1}{2}\gamma H^2 \tan\left(\frac{\pi}{4} + \frac{\phi}{2}\right); \text{ for soil prism (mnp)} \quad (5.85)$$

$$lw_6 = R \cos\left(\frac{\pi}{4} + \frac{\phi}{2}\right) + \frac{1}{3}H \tan\left(\frac{\pi}{4} + \frac{\phi}{2}\right) \quad (5.86)$$

The total weight ( $w_t$ ) of the soil prism (uehlmn), and the corresponding moment ( $Mw_t$ ) at the center of the circle (o) are given by the following equations:

$$w_t = \sum_{n=1}^6 w_n \quad (5.87)$$

$$Mw_t = \sum_{n=1}^5 w_n lw_n \quad (5.88)$$

In order to normalize the effect of the foundation width (B) on the calculation of the radius of the rupture circle, a factor ( $\rho$ ) is introduced as follows:

$$\rho = \frac{R}{b} \quad (5.89)$$

where: R is the radius of the circle  
b is half of the foundation width

Employing the factor ( $\rho$ ) in the calculation and solving equation (5.88), the moment ( $Mw_t$ ) at the center of the circle (o) can be presented in the following form:

$$Mw_t = \left( \frac{-\gamma b^3}{6\sqrt{2}} (4 - \cos\phi) \sin\left(\frac{\phi}{2}\right) + \frac{\sqrt{2}}{2} \gamma b^3 \sin^2\left(\frac{\pi}{4} - \frac{\phi}{2}\right) \sin\left(\frac{\phi}{2}\right) \right) \rho^3 +$$

$$\begin{aligned}
& \left( \frac{1}{2} \gamma b^2 (D_f + b \tan \alpha) \left( \sin^2 \left( \frac{\pi}{4} - \frac{\phi}{2} \right) - \sin^2 \left( \frac{\pi}{4} + \frac{\phi}{2} \right) \right) \right) \rho^2 + \\
& \left( \gamma b^2 \sin \left( \frac{\pi}{4} + \frac{\phi}{2} \right) \left( D_f + \frac{b}{2} \tan \alpha \right) \right) \rho \\
& - \frac{\gamma b^2}{2} \left( D_f + \frac{b}{3} \tan \alpha \right)
\end{aligned} \tag{5.90}$$

The weight of the foundation ( $w_f$ ) is divided into three parts ( $w_{f1}$ ,  $w_{f2}$ , and  $w_{f3}$ ) having lever arms ( $lw_{f1}$ ,  $lw_{f2}$ , and  $lw_{f3}$ ), respectively. The notations used for the following calculations are shown in Figure 5.4.

$$w_{f1} = d_c a \gamma_f \tag{5.91}$$

where:  $d_c$  is the height of column  
 $a$  is the width of column  
 $\gamma_f$  is the unit weight of the foundation

$$lw_{f1} = R \sin \left( \frac{\pi}{4} + \frac{\phi}{2} \right) - \frac{1}{2} a \tag{5.92}$$

$$w_{f2} = \frac{a^2}{2} \tan \theta \gamma_f \tag{5.93}$$

$$lw_{f2} = R \sin \left( \frac{\pi}{4} + \frac{\phi}{2} \right) - \frac{2}{3} a \tag{5.94}$$

$$w_{f3} = b r \gamma_f \tag{5.95}$$

$$lw_{f3} = R \sin \left( \frac{\pi}{4} + \frac{\phi}{2} \right) - \frac{1}{2} b \tag{5.96}$$

$$w_f = \sum_{n=1}^3 w_{fn} \quad (5.97)$$

The moment resulting from the weight of footing can be determined as follows:

$$Mw_f = \sum_{n=1}^3 w_{fn} l w_{fn} \quad (5.98)$$

$$Mw_f = \left( -a\gamma_f b \sin\left(\frac{\pi}{4} + \frac{\phi}{2}\right) \left( d_c + \frac{a}{2} \tan\theta + \frac{t}{a} b \right) \rho + a^2 \gamma_f \left( \frac{d_c}{2} + \frac{a(\tan\theta)}{3} + \frac{tb^2}{2a^2} \right) \right) \quad (5.99)$$

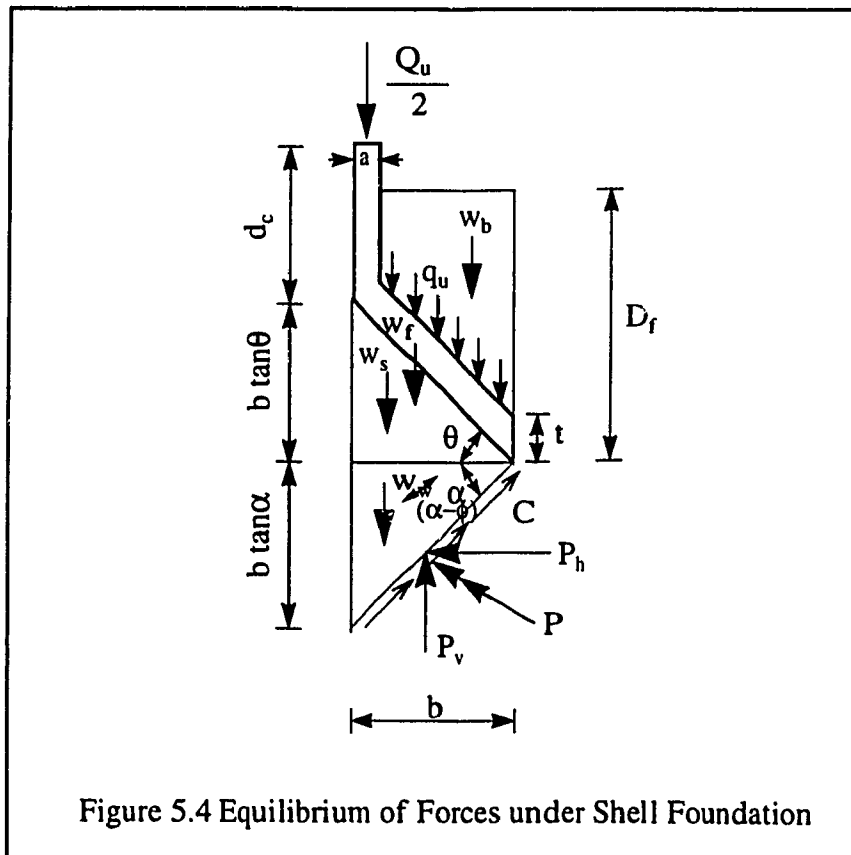


Figure 5.4 Equilibrium of Forces under Shell Foundation

In the present investigation, an embedment ratio (ER) was introduced as follows:

$$ER = \frac{D_f}{2b} \quad (5.100)$$

For footings located directly on the ground surface, i.e.,  $D_f = 0$ , the embedment ratio (ER) will be equal to zero. However, for (ER > 0), the weight of the backfill ( $w_b$ ), resulting from the soil prism (cdur) shown in Figure 5.1, will be divided into two zones ( $w_{b1}$  and  $w_{b2}$ ) having lever arms ( $lw_{b1}$  and  $lw_{b2}$ ), respectively. Thus, the following relationships can be introduced:

$$d_b = D_f - t - (b - a)\tan\theta \quad (5.101)$$

$$w_{b1} = d_b(b - a)\gamma \quad (5.102)$$

$$lw_{b1} = R \sin\left(\frac{\pi}{4} + \frac{\phi}{2}\right) - \frac{1}{2}(a + b) \quad (5.103)$$

$$w_{b2} = \frac{1}{2}\gamma(b - a)^2 \tan\theta \quad (5.104)$$

$$lw_{b2} = R \sin\left(\frac{\pi}{4} + \frac{\phi}{2}\right) - \frac{1}{3}(a + 2b) \quad (5.105)$$

$$w_b = \sum_{n=1}^2 w_{bn} \quad (5.106)$$

The moment resulting from the weight of backfilling can be determined as follows:

$$Mw_b = \sum_{n=1}^2 w_{bn}lw_{bn} \quad (5.107)$$

$$M_{w_b} = \left( -(b-a)\gamma b \sin\left(\frac{\pi}{4} + \frac{\phi}{2}\right) \left( d_b + \frac{(b-a)}{2} \tan\theta \right) \right) \rho + (b-a)\gamma d_b \left( \frac{a}{2} + \frac{b}{2} + (b-a) \tan\theta \left( \frac{a}{6} + \frac{b}{3} \right) \right) \quad (5.108)$$

The horizontal earth pressure ( $E_h$ ) acting on surface (pm) shown in Figure 5.1 consists of two components,  $E_c$  which is due to the cohesion, and  $E_\gamma$  which is due to the soil unit weight, having  $lE_c$  and  $lE_\gamma$  as the lever arms from the horizontal forces  $E_c$  and  $E_\gamma$  to the center of the circle (o), respectively.

$$E_c = 2cH \tan\left(\frac{\pi}{4} + \frac{\phi}{2}\right) \quad (5.109)$$

$$lE_c = R \sin\left(\frac{\pi}{4} + \frac{\phi}{2}\right) - \frac{1}{2}H \quad (5.110)$$

$$E_\gamma = \frac{1}{2}\gamma H^2 \tan^2\left(\frac{\pi}{4} + \frac{\phi}{2}\right) \quad (5.111)$$

$$lE_\gamma = R \sin\left(\frac{\pi}{4} + \frac{\phi}{2}\right) - \frac{1}{3}H \quad (5.112)$$

$$E_h = E_c + E_\gamma \quad (5.113)$$

The moment resulting from the lateral earth pressure can be determined as follows:

$$ME_h = E_c lE_c + E_\gamma lE_\gamma \quad (5.114)$$

$$ME_h = \left( \frac{\sin^2\left(\frac{\pi}{4} + \frac{\phi}{2}\right)}{\cos\left(\frac{\pi}{4} + \frac{\phi}{2}\right)} \left( 2c + \frac{\gamma}{2}H \tan\left(\frac{\pi}{4} + \frac{\phi}{2}\right) \right) \right) \rho$$



$$-H^2 \tan\left(\frac{\pi}{4} + \frac{\phi}{2}\right) \left(c + \frac{\gamma}{6} H \tan\left(\frac{\pi}{4} + \frac{\phi}{2}\right)\right) \quad (5.115)$$

$$\begin{aligned} ME_h = & \left(\frac{\gamma}{2} b^3 \tan^2\left(\frac{\pi}{4} + \frac{\phi}{2}\right) \xi_2^2 \left(\sin\left(\frac{\pi}{4} + \frac{\phi}{2}\right) - \frac{\xi_2}{3}\right)\right) \rho^3 + \\ & \left(c b^2 \tan\left(\frac{\pi}{4} + \frac{\phi}{2}\right) \xi_2 \left(2 \sin\left(\frac{\pi}{4} + \frac{\phi}{2}\right) - \xi_2\right)\right) \rho^2 + \\ & \left(\gamma D_{fb} b^2 \tan^2\left(\frac{\pi}{4} + \frac{\phi}{2}\right) \xi_2 \left(\sin\left(\frac{\pi}{4} + \frac{\phi}{2}\right) - \frac{\xi_2}{2}\right)\right) \rho^2 + \\ & \left(2 c b D_{fb} \tan\left(\frac{\pi}{4} + \frac{\phi}{2}\right) \left(\sin\left(\frac{\pi}{4} + \frac{\phi}{2}\right) - \xi_2\right)\right) \rho + \\ & \left(\frac{\gamma}{2} (D_{fb}^2 b) \tan^2\left(\frac{\pi}{4} + \frac{\phi}{2}\right) \left(\sin\left(\frac{\pi}{4} + \frac{\phi}{2}\right) - \frac{\xi_2}{2}\right)\right) \rho \\ & - D_{fb}^2 \tan\left(\frac{\pi}{4} + \frac{\phi}{2}\right) \left(c + \frac{\gamma}{6} D_{fb} \tan\left(\frac{\pi}{4} + \frac{\phi}{2}\right)\right) \end{aligned} \quad (5.116)$$

While the normal stress acting on the circular part of the rupture surface has no moment at the center of the circle (o), the moment caused by the shear stress is given by the following equation:

$$MT = \int_{-\left(\frac{\pi}{4} + \frac{\phi}{2}\right)}^{\left(\frac{\pi}{4} - \frac{\phi}{2}\right)} R^2 \tau \partial \psi \quad (5.117)$$

$$MT = \frac{-R^2 \lambda_2}{2 \tan \phi} \left( e^{-2 \tan \phi \left(\frac{\pi}{4} - \frac{\phi}{2}\right)} - e^{2 \tan \phi \left(\frac{\pi}{4} + \frac{\phi}{2}\right)} \right)$$

$$-\frac{R^3 \gamma \sin \phi \sqrt{2}}{1 + 4 \tan^2 \phi} \left( 2 \tan \phi \sin \left( \frac{\phi}{2} \right) - \cos \left( \frac{\phi}{2} \right) \right) \quad (5.118)$$

Substitute in equation (5.118) for the terms which depend on  $(\phi)$  by the following:

$$\xi_{15} = -2 \tan \phi \quad (5.119)$$

$$\xi_{16} = \frac{1}{\xi_{15}} \left( e^{\xi_{15} \left( \frac{\pi}{4} - \frac{\phi}{2} \right)} - e^{-\xi_{15} \left( \frac{\pi}{4} + \frac{\phi}{2} \right)} \right) \quad (5.120)$$

$$\xi_{17} = \frac{-\sin \phi}{\xi_4} \sqrt{2} \left( 2 \tan \phi \sin \left( \frac{\phi}{2} \right) - \cos \left( \frac{\phi}{2} \right) \right) \quad (5.121)$$

$$MT = R^2 (\lambda_2 \xi_{16} + R \gamma \xi_{17}) \quad (5.122)$$

$$MT = R^2 \xi_{16} \xi_5 (\gamma D_{fb} \xi_3 + \gamma \rho b \xi_7 + c \xi_1) + R^3 \gamma \xi_{17} \quad (5.123)$$

$$\xi_{18} = \xi_{17} + \xi_5 \xi_7 \xi_{16} \quad (5.124)$$

$$\xi_{19} = \xi_3 \xi_5 \xi_{17} \quad (5.125)$$

$$\xi_{20} = \xi_1 \xi_5 \xi_{17} \quad (5.126)$$

The moment due to the shear stress can be presented in the following form:

$$MT = \gamma b^3 \xi_{18} \rho^3 + \gamma b^2 D_{fb} \xi_{19} \rho^2 + c b^2 \xi_{20} \rho^2 \quad (5.127)$$

Considering the vertical equilibrium of the soil prism (uehlmp), the following equilibrium equation can be obtained:

$$P_v = T_{vc} + T_{vp} - c_v - \sum_{n=1}^5 w_n \quad (5.128)$$

Substitute for all terms in the right-hand side of equation (5.128), and presenting additional constants ( $\xi_i$ ), the following expression for ( $P_v$ ) can be obtained:

$$\xi_{21} = \frac{\pi}{2} - 2 \sin\left(\frac{\pi}{4} + \frac{\phi}{2}\right) \cos\left(\frac{\pi}{4} + \frac{\phi}{2}\right) \quad (5.129)$$

$$\xi_{22} = \xi_{13} - \xi_2 \cos\left(\frac{\pi}{4} + \frac{\phi}{2}\right) - \frac{\xi_{21}}{2} \quad (5.130)$$

$$\xi_{23} = \xi_{12} - \sin\left(\frac{\pi}{4} + \frac{\phi}{2}\right) - \cos\left(\frac{\pi}{4} + \frac{\phi}{2}\right) \quad (5.131)$$

$$\xi_{24} = \xi_2 + \xi_{14} \quad (5.132)$$

$$P_v = \gamma R^2 \xi_{22} + \gamma R D_{fb} \xi_{23} + c R \xi_{24} + \gamma b D_{fb} - \frac{1}{2} \gamma b^2 \tan \alpha \quad (5.133)$$

Substitute for the radius of the circle (R) by ( $\rho b$ ) in equation (5.133), thus:

$$P_v = \gamma b^2 \left( \rho^2 \xi_{22} + \rho \tan \alpha \xi_{23} + \frac{1}{2} \tan \alpha \right) + \gamma b D_f (\rho \xi_{23} + 1) + c b (\rho \xi_{24}) \quad (5.134)$$

From Figure 5.4, the following relationship can be derived from the equilibrium in the vertical direction:

$$q_u b = P_v + cb \tan \alpha - \frac{1}{2} \gamma b^2 \tan \alpha - \frac{1}{2} \gamma b^2 \tan \theta \quad (5.135)$$

Substituting for ( $P_v$ ) in equation (5.135), thus:

$$q_u = \gamma b \left( \xi_{22} \rho^2 + \xi_{23} \tan \alpha \rho - \frac{1}{2} \tan \theta \right) + \gamma D (\xi_{23} \rho + 1) + c (\xi_{24} \rho + \tan \alpha) \quad (5.136)$$

The moment of the resultant force ( $P$ ) which is acting on the base of the footing can be presented as follows:

$$MP = -q_u b \left( R \sin \left( \frac{\pi}{4} + \frac{\phi}{2} \right) - \frac{b}{2} \right) - \frac{\gamma b^2}{2} \left( R \sin \left( \frac{\pi}{4} + \frac{\phi}{2} \right) - \frac{b}{3} \right) (\tan \alpha + \tan \theta) + cb R \left( \tan \alpha \sin \left( \frac{\pi}{4} + \frac{\phi}{2} \right) - \cos \left( \frac{\pi}{4} + \frac{\phi}{2} \right) \right) \quad (5.137)$$

$$MP = \left( -\gamma b^3 \sin \left( \frac{\pi}{4} + \frac{\phi}{2} \right) \xi_{22} \right) \rho^3 - \left( b^2 \sin \left( \frac{\pi}{4} + \frac{\phi}{2} \right) \right) \left( \gamma \xi_{23} (D + b \tan \alpha) + c \xi_{24} \right) + \frac{\gamma}{2} b^3 \xi_{22} \rho^2 - \left( \frac{\gamma}{2} b^3 \sin \left( \frac{\pi}{4} + \frac{\phi}{2} \right) \left( \tan \theta + \tan \alpha + 2 \frac{D}{b} \right) \right) \rho + \left( \frac{\gamma}{2} b^2 \xi_{22} (D + b \tan \alpha) + cb^2 \left( \frac{\xi_{24}}{2} - \cos \left( \frac{\pi}{4} + \frac{\phi}{2} \right) \right) \right) \rho + \frac{\gamma}{6} b^2 \left( 3D + b \tan \alpha - \frac{b}{2} \tan \theta \right) \quad (5.138)$$

In order to determine the rupture circle which satisfies the moment equilibrium of all forces acting on the system, the summation of the moments taken at the center of the circle (o) must be satisfied, thus:

$$Mw_l + Mw_f + Mw_b + ME_h + MT + MP = 0 \quad (5.139)$$

As shown from the formulation of  $Mw_l$ ,  $Mw_f$ ,  $Mw_b$ ,  $ME_h$ ,  $MT$ , and  $MP$ , equation (5.139) is a third degree equation in factor ( $\rho$ ), and when solved, the ultimate bearing capacity ( $q_u$ ) can be predicted. The coordinates ( $x_c$ ,  $z_c$ ) of the center of the rupture circle (o) can be calculated as follows:

$$x_c = \rho b \sin\left(\frac{\pi}{4} + \frac{\phi}{2}\right) \quad (5.140)$$

$$z_c = H - \rho b \sin\left(\frac{\pi}{4} + \frac{\phi}{2}\right) \quad (5.141)$$

Putting equation (5.136) in the form of the general bearing capacity equation,

$$q_u = cN_c + \gamma D_f N_q + \gamma b N_\gamma \quad (5.142)$$

The bearing capacity coefficients ( $N_c$ ,  $N_q$ , and  $N_\gamma$ ) can be substituted from equation (5.136) with the following:

$$N_c = \xi_{24}\rho + \tan \alpha \quad (5.143)$$

$$N_q = \xi_{23}\rho + 1 \quad (5.144)$$

$$N_\gamma = \xi_{22}\rho^2 + \xi_{23}\tan \alpha \rho - \frac{1}{2}\tan \theta \quad (5.145)$$

Equations (5.143), (5.144), and (5.145) indicate that the bearing capacity coefficients are not only a function of the angle of shearing resistance ( $\phi$ ) but also of the failure angle ( $\alpha$ ), the vertical shell angle ( $\theta$ ), and the factor ( $\rho$ ). The factor ( $\rho$ ) is a function of the radius of the rupture circle ( $R$ ) which depends on the cohesion of soil ( $c$ ), soil unit weight ( $\gamma$ ), embedment ratio ( $ER$ ), and shell ratio ( $SR$ ), and consequently the bearing capacity coefficients ( $N_c$ ,  $N_q$ , and  $N_\gamma$ ).

The above analysis proceeds by trial and error until a factor ( $\rho$ ) is obtained to satisfy the equilibrium conditions. Then utilize the value of factor ( $\rho$ ) to determine the bearing capacity coefficients ( $N_c$ ,  $N_q$ , and  $N_\gamma$ ) and the corresponding ultimate bearing capacity ( $q_u$ ).

However, in order to facilitate this procedure, the mathematical formulations were coded in a computer program “*BC-Shell*”, which stands for *Bearing Capacity of Shell Foundations*, to perform the calculations involved in the analysis. The listing of the program is presented in Appendix (I).

### **5.3 Program “*BC-Shell*”**

The program “*BC-Shell*” was designed for easy application to allow data input through an interactive session to determine the ultimate bearing capacity of shell foundations ( $q_u$ ). The parameters used in the data input are given in Table 5.1. The data input allows the user to predict the bearing capacity for a given case as well as for a given range of shell angle ( $\theta$ ), soil unit weight ( $\gamma$ ), cohesion of soil ( $c$ ), and angle of shearing resistance ( $\phi$ ). When the interactive session is completed, the program runs and locates the rupture surface which satisfies the equilibrium condition for the given data input, then utilizes the rupture surface to calculate the bearing capacity coefficients and the corresponding ultimate bearing capacity ( $q_u$ ). The program stores the final result of the analysis in an output file together with the data input.

Table 5.1 Data Input for Program "BC-Shell"

Total Width of Strip Shell Footing (B)	= -----	meters
Minimum Horizontal Shell Angle ( $\theta_{\min}$ )	= -----	degrees
Maximum Horizontal Shell Angle ( $\theta_{\max}$ )	= -----	degrees
Interval for Horizontal Shell Angle	= -----	degrees
Depth of Foundation Level ( $D_f$ )	= -----	meters
Minimum Unit Weight of Soil ( $\gamma_{\min}$ )	= -----	kN/m <sup>3</sup>
Maximum Unit Weight of Soil ( $\gamma_{\max}$ )	= -----	kN/m <sup>3</sup>
Interval for Unit Weight of Soil	= -----	kN/m <sup>3</sup>
Minimum Cohesion of Soil ( $c_{\min}$ )	= -----	kPa
Maximum Cohesion of Soil ( $c_{\max}$ )	= -----	kPa
Interval for Cohesion of Soil	= -----	kPa
Minimum Angle of Shearing Resistance ( $\phi_{\min}$ )	= -----	degrees
Maximum Angle of Shearing Resistance ( $\phi_{\min}$ )	= -----	degrees
Interval for Angle of Shearing Resistance	= -----	degrees

#### 5.4 Comparison between Theoretical & Experimental Results

In the present investigation, the theoretical results obtained from the theory described above using the program "BC-Shell" were compared with the experimental results given in Chapter 3 of this thesis. The comparison was conducted for the plane strain condition (flat strip, triangular (1) shell, and triangular (2) shell footings). The results are presented in Figures 5.5 and 5.6 for the surface and embedded footings, respectively. The two figures indicate that good agreement between both experimental and theoretical results was achieved. It can be noticed that the theoretical values calculated for the ultimate load are slightly conservative.

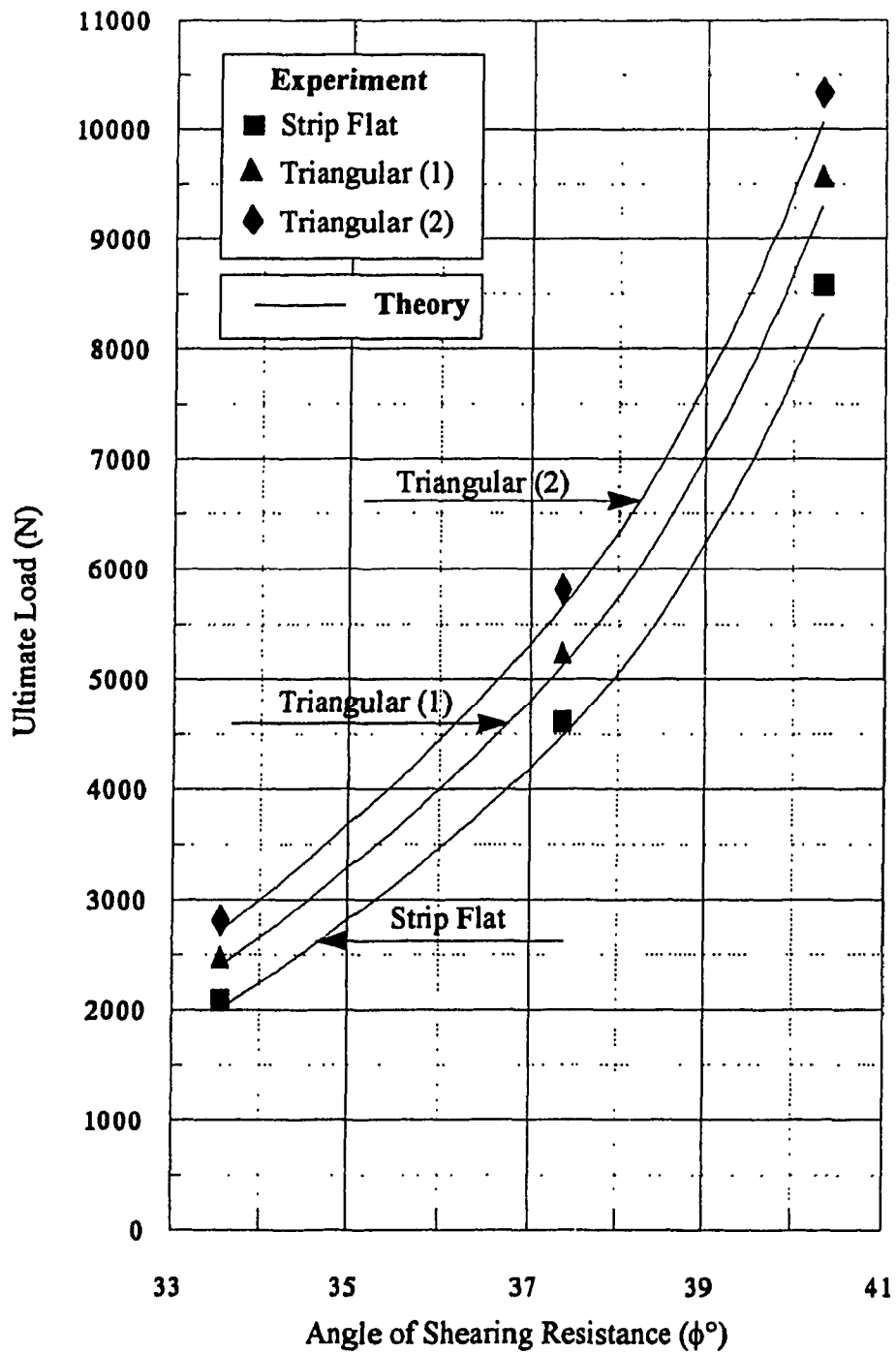


Figure 5.5 Theoretical & Experimental Results for Surface Strip Footings



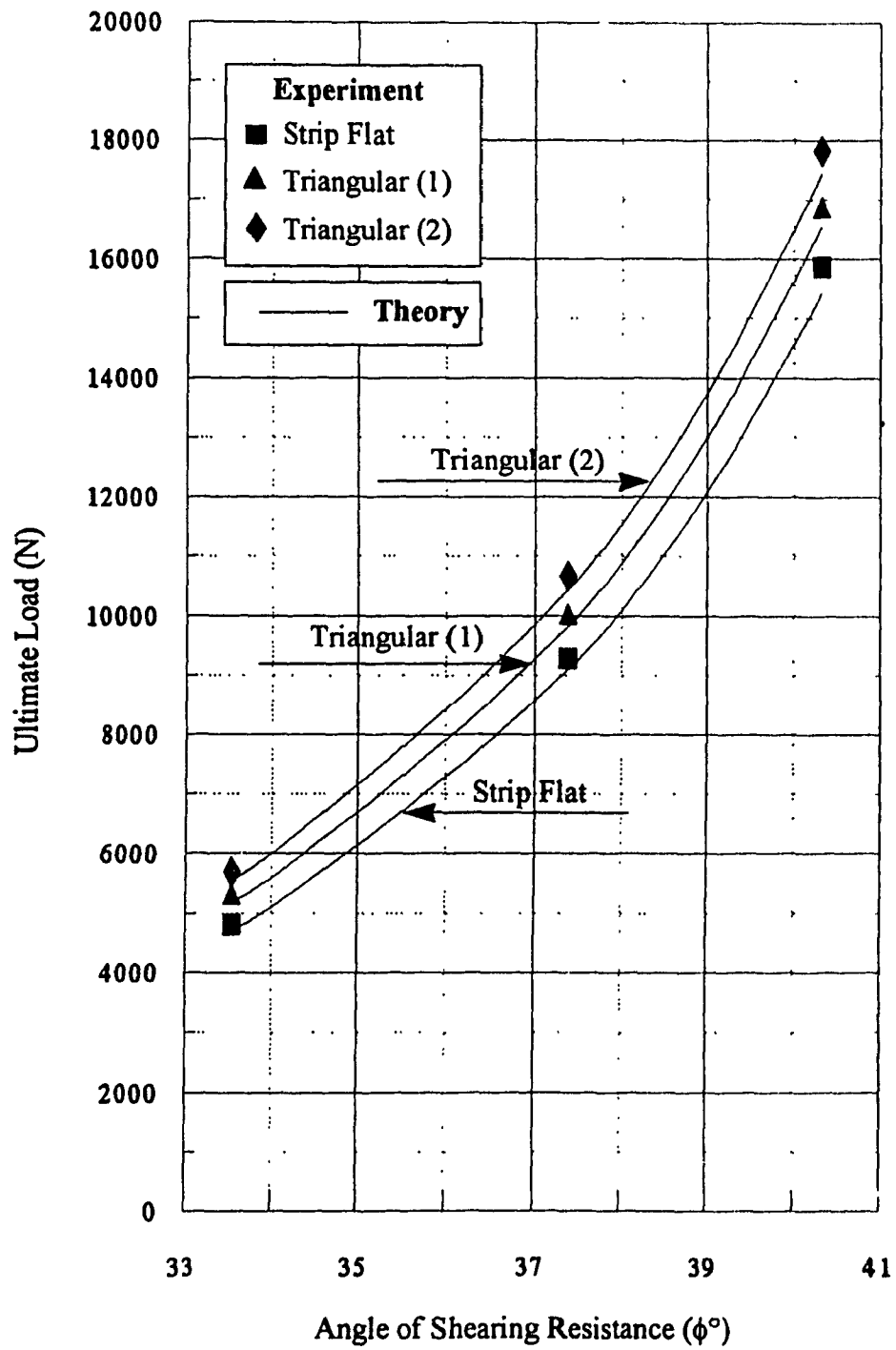


Figure 5.6 Theoretical & Experimental Results for Embedded Strip Footings

## 5.5 Parametric Study

A parametric study was conducted to examine the effect of the governing parameters on the factor ( $\rho$ ), which influences the bearing capacity coefficients ( $N_c$ ,  $N_q$ , and  $N_\gamma$ ). The description of these parameters and their limits are shown in Table 5.2. The parametric study was conducted on a flat strip footing, i.e.,  $SR= 1.0$ , to examine the effect of soil cohesion ( $c$ ), width of footing ( $B$ ), unit weight ( $\gamma$ ), and the embedment ratio (ER). The effect shell configuration was examined by the shell ratio (SR).

Figure 5.7 shows that the cohesion ( $c$ ) has insignificant effect on the factor ( $\rho$ ) specially for higher angles of shearing resistance ( $\phi$ ). Figure 5.8 shows that the factor ( $\rho$ ) increases due to an increase in the foundation width ( $B$ ) for lower values of ( $\phi$ ), however, at higher values of ( $\phi$ ), the effect of ( $B$ ) seems to be insignificant. Figure 5.9 shows that unit weight ( $\gamma$ ) has no effect on the factor ( $\rho$ ). Figure 5.10 shows that the effect of the embedment ratio (ER) is consistent for the entire range of ( $\phi$ ) and the factor ( $\rho$ ) increases for higher embedment ratio. The effect of shell configuration is demonstrated in Figure 5.11. Seven foundation models with different horizontal shell angle ( $\theta$ ), varied from  $0^\circ$ , i.e., flat footing, to  $60^\circ$ , were examined. The existence of shell action appears to increase the factor ( $\rho$ ) and consequently the bearing capacity coefficients, however, this contribution is decreased for soil with a higher angle of shearing resistance ( $\phi$ ).

Table 5.2 Parameters Used in The Parametric Study for Factor ( $\rho$ )

Parameter under Investigation	Units	Range of Parameter	
Cohesion of Soil ( $c$ )	kPa	0.00	2.00
Width of Footing ( $B$ )	meter	0.10	2.00
Unit Weight of Soil ( $\gamma$ )	kN/m <sup>3</sup>	15.00	21.00
Embedment Ratio (ER)		0.00	1.00
Shell Ratio (SR)		1.00	1.67

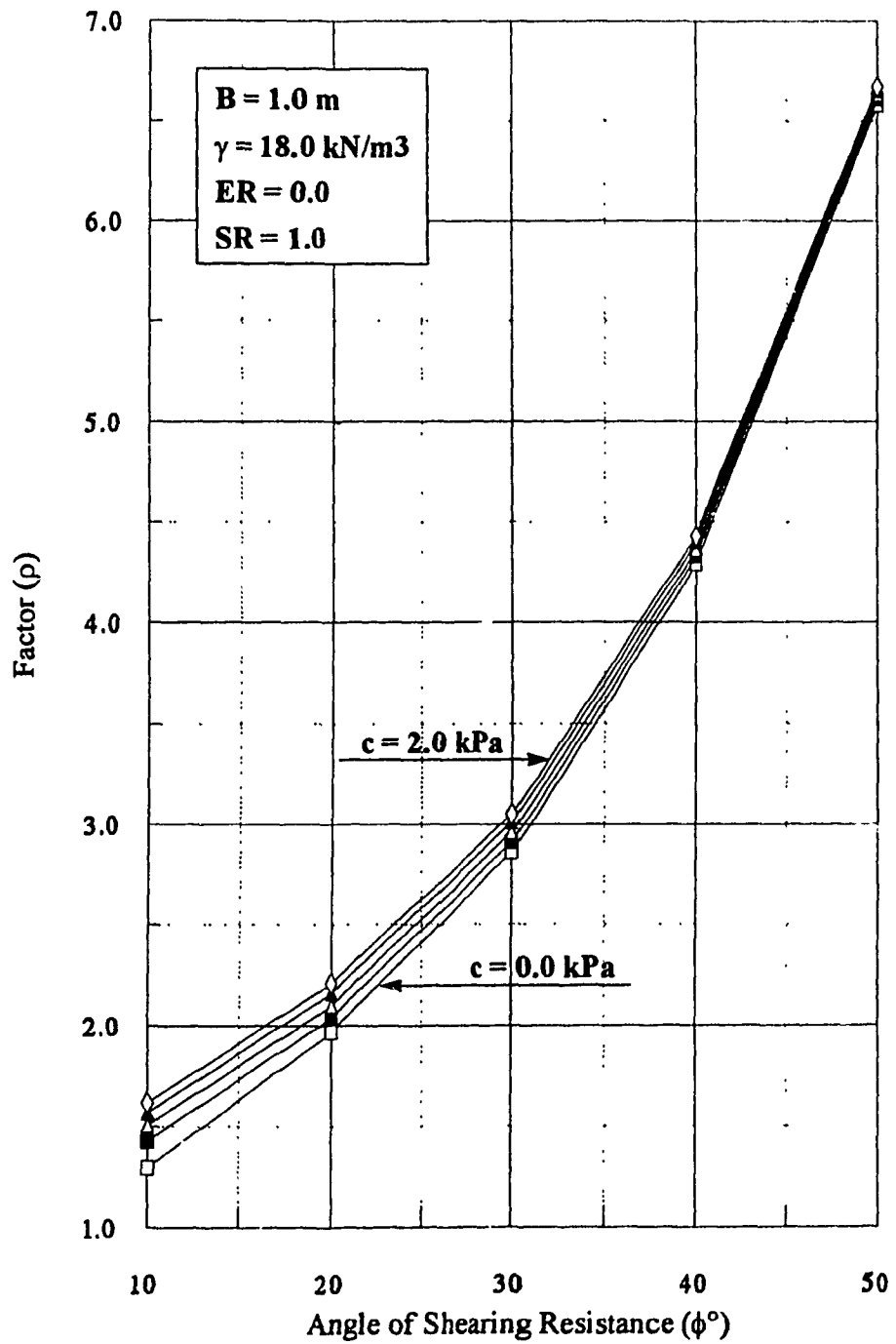


Figure 5.7 Effect of The Cohesion of Soil ( $c$ ) on Factor ( $\rho$ )

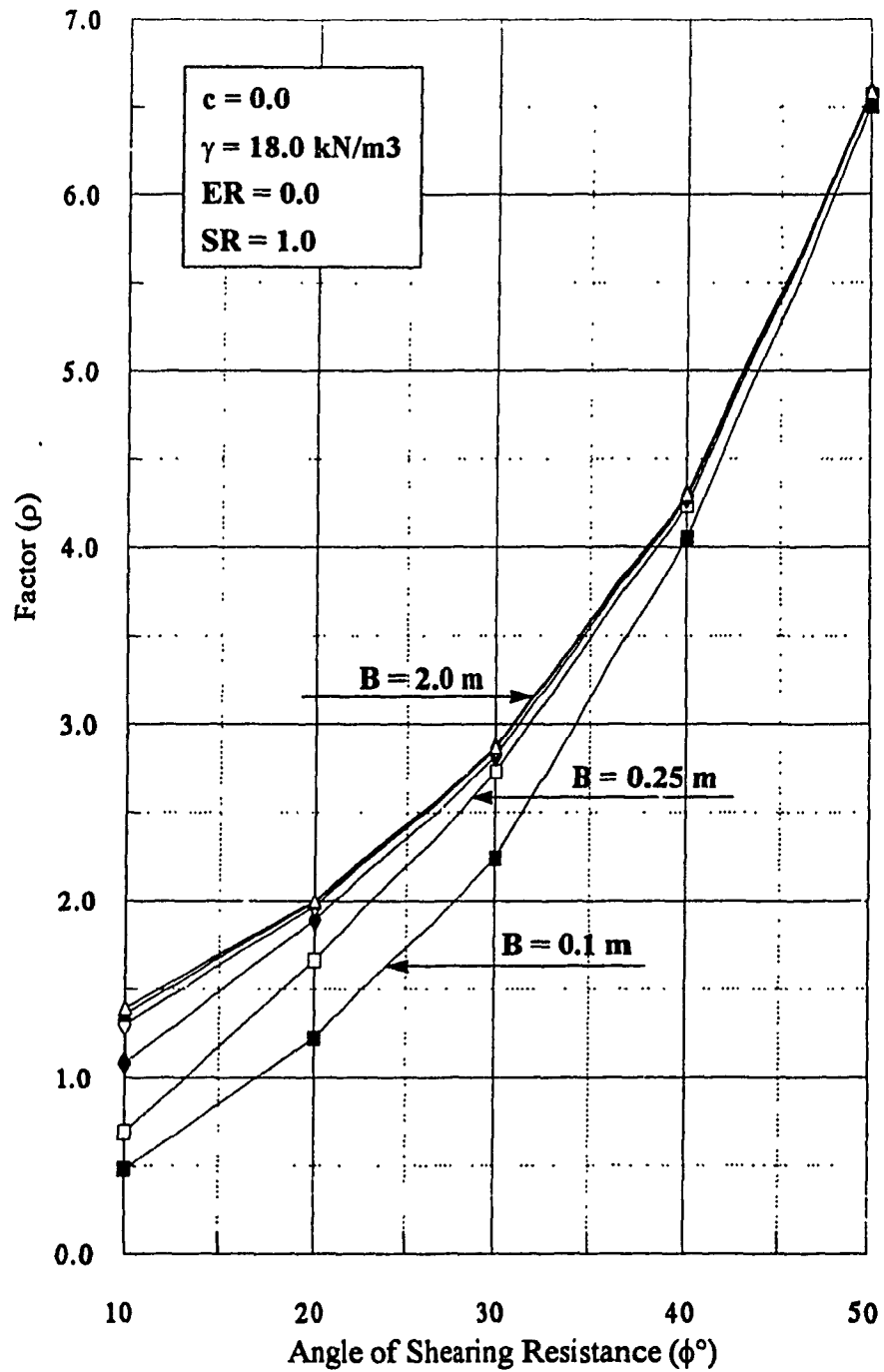


Figure 5.8 Effect of Foundation Width (B) on Factor ( $\rho$ )

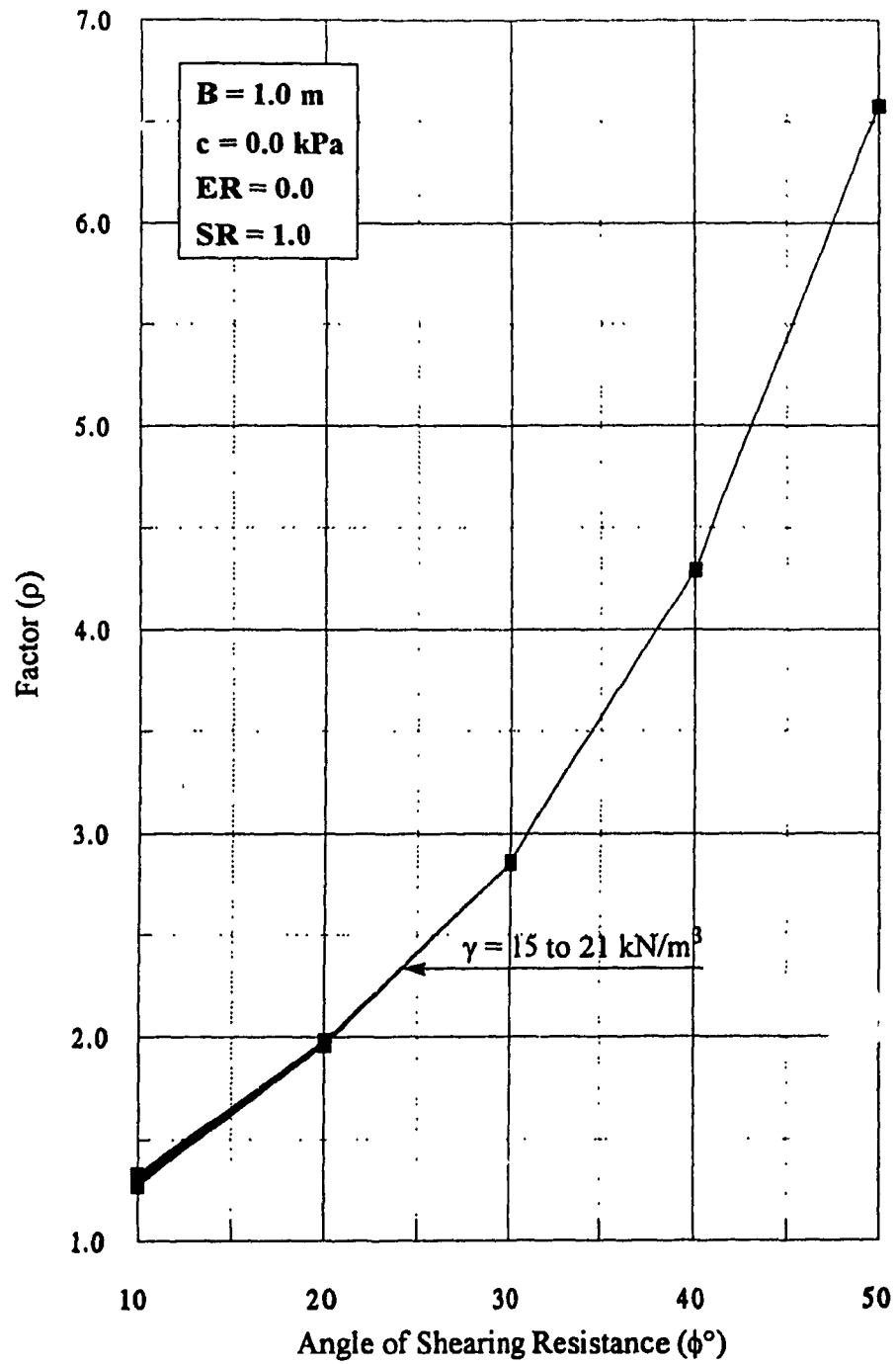


Figure 5.9 Effect of Unit Weight of Soil ( $\gamma$ ) on Factor ( $\rho$ )

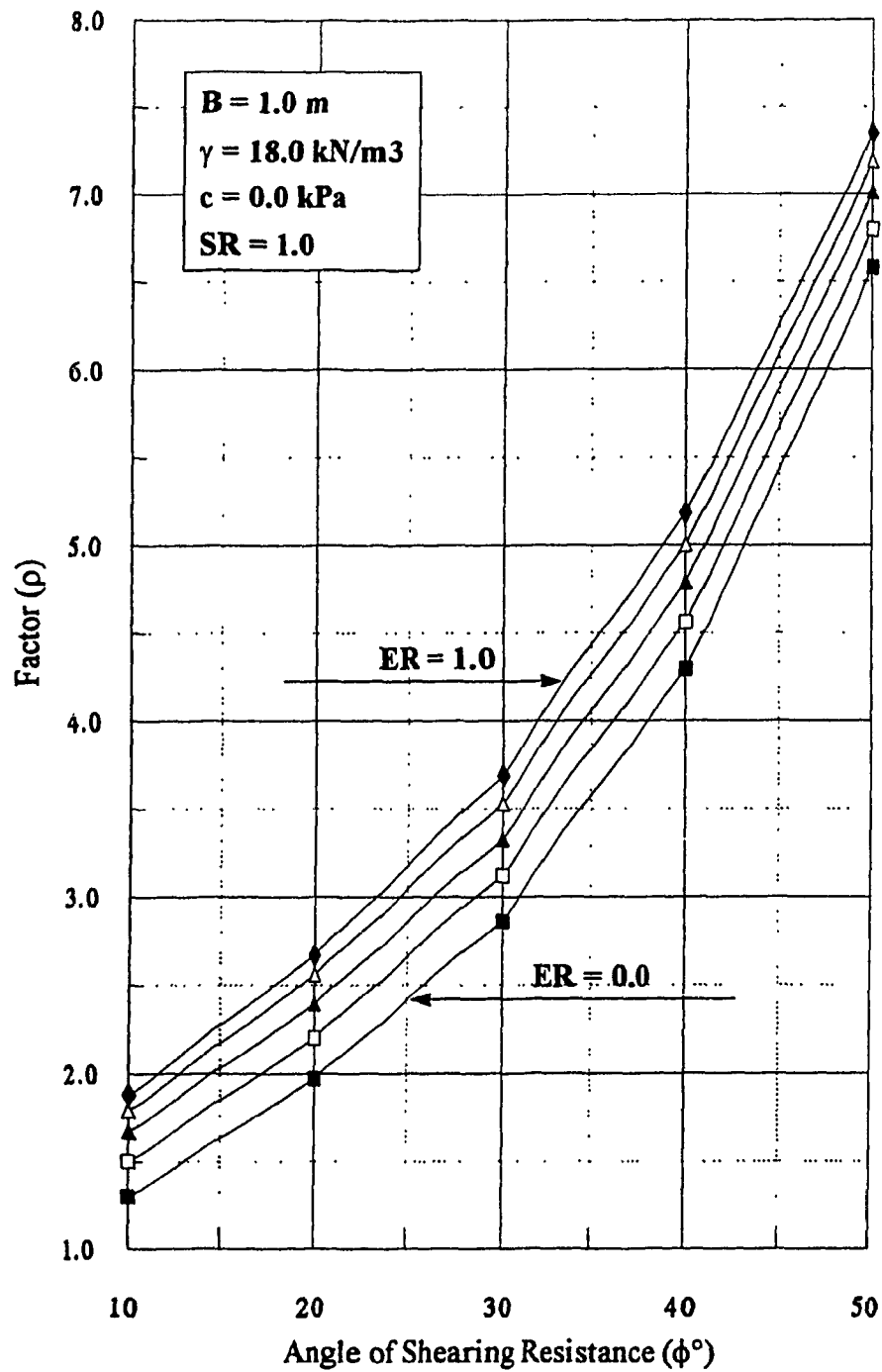


Figure 5.10 Effect of Embedment Ratio (ER) on Factor ( $\rho$ )

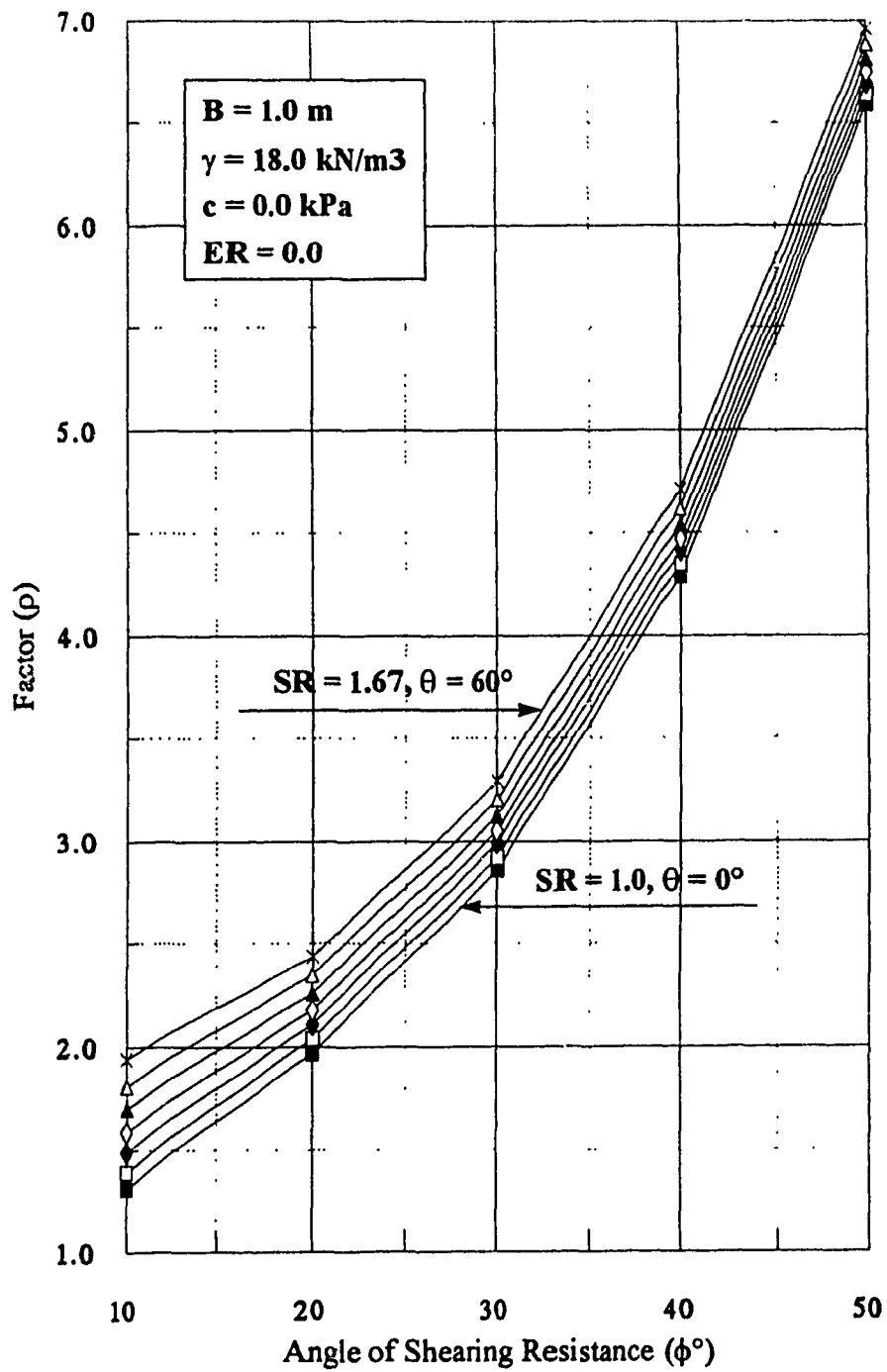


Figure 5.11 Effect of Shell Ratio (SR) on Factor ( $\rho$ )

## 5.6 Design Charts & Tables

In order to facilitate the use of the above theory for practical applications, the program "BC-Shell" was employed to develop design charts for the bearing capacity coefficients ( $N_c$ ,  $N_q$ ,  $N_\gamma$ ) for shell foundations. As concluded from the parametric study conducted in the present investigation, the width of foundation (B) for the range of practical use (0.50 to 2.00 m) and the unit weight of soil ( $\gamma$ ) have no effect on the factor ( $\rho$ ) and consequently on the bearing capacity coefficients, see Figures 5.8 and 5.9, respectively. The design charts were developed as a function of the angle of shearing resistance ( $\phi$ ), the shell angle ( $\theta$ ), and the Embedment Ratio (ER). Although the present investigation deals with cohesionless material, a small value for the cohesion of soil ( $c$ ) was used to incorporate the bearing capacity coefficient ( $N_c$ ). The data input used to develop the design charts are given in Table 5.3.

Table 5.3 Data Input Used for The Design Charts

Parameter	Units	Range		
		Min.	Max.	Interval
Foundation Width (B)	meters	1.00		
Shell Angle ( $\theta$ )	degrees	0°	60°	10°
Embedment Ratio (ER)		0.00	0.75	0.25
Unit Weight of Soil ( $\gamma$ )	kN/m <sup>3</sup>	18.00		
Angle of Shearing Resistance ( $\phi$ )	degrees	10°	50°	10°
Cohesion of Soil (c)	kPa	0.10		

The design charts for the bearing capacity coefficients ( $N_c$ ,  $N_q$ ,  $N_\gamma$ ) are presented in Figures 5.12 to 5.14 for Embedment Ratio ER= 0.0; in Figures 5.15 to 5.17 for ER= 0.25; in Figures 5.18 to 5.20 for ER= 0.50; and in Figures 5.21 to 5.23 for ER= 0.75. For precise values for the bearing capacity coefficients ( $N_c$ ,  $N_q$ ,  $N_\gamma$ ), design tables are also given in Appendix II. An interval of 1° for the angle of shearing resistance ( $\phi$ ) and 10° for the shell angle ( $\theta$ ) were used to produce these tables.



## 5.7 Depth & Shape Factors

The developed theoretical model together with the experimental results were employed to introduce depth factors ( $f_{dq}, f_{d\gamma}$ ) and shape factors ( $f_{sq}, f_{s\gamma}$ ) for the axisymmetrical and three dimension conditions. The depth factors ( $f_{dq}, f_{d\gamma}$ ) determined from the present experimental investigation are presented in Figure 5.24. By employing the calculated depth factors and the experimental results recorded for the plane strain condition, the corresponding bearing capacity coefficients ( $N_q, N_\gamma$ ) were determined. The experimental results for the axisymmetrical and three dimensions conditions were then used to calculate the shape factors ( $f_{sq}, f_{s\gamma}$ ). Figures 5.25 and 5.26 present the shape factors ( $f_{sq}, f_{s\gamma}$ ) for the axisymmetrical and three dimensional conditions, respectively.

In addition, the program “*BC-Shell*” was used to develop design charts for depth factors ( $f_{dq}, f_{d\gamma}$ ) for cohesionless material as a function of the angle of shearing resistance ( $\phi^\circ$ ), the shell angle ( $\theta^\circ$ ), and the embedment ratio (ER). The design charts for the depth factors ( $f_{dq}, f_{d\gamma}$ ) are presented for the shell angle ( $\theta$ ) equal to  $0^\circ$ ,  $30^\circ$ , and  $60^\circ$  in Figures 5.27, 5.28, and 5.29, respectively.

The ultimate bearing capacity equation for cohesionless material can be presented in the traditional form as follows:

$$q_u = qN_q f_{dq} f_{sq} + \gamma b N_\gamma f_{d\gamma} f_{s\gamma} \quad (5.146)$$

where:  $q_u$  is the ultimate bearing capacity  
 $N_q, N_\gamma$  are the bearing capacity coefficients for ER=0  
 $f_{dq}, f_{d\gamma}$  are the depth factors  
 $f_{sq}, f_{s\gamma}$  are the shape factors

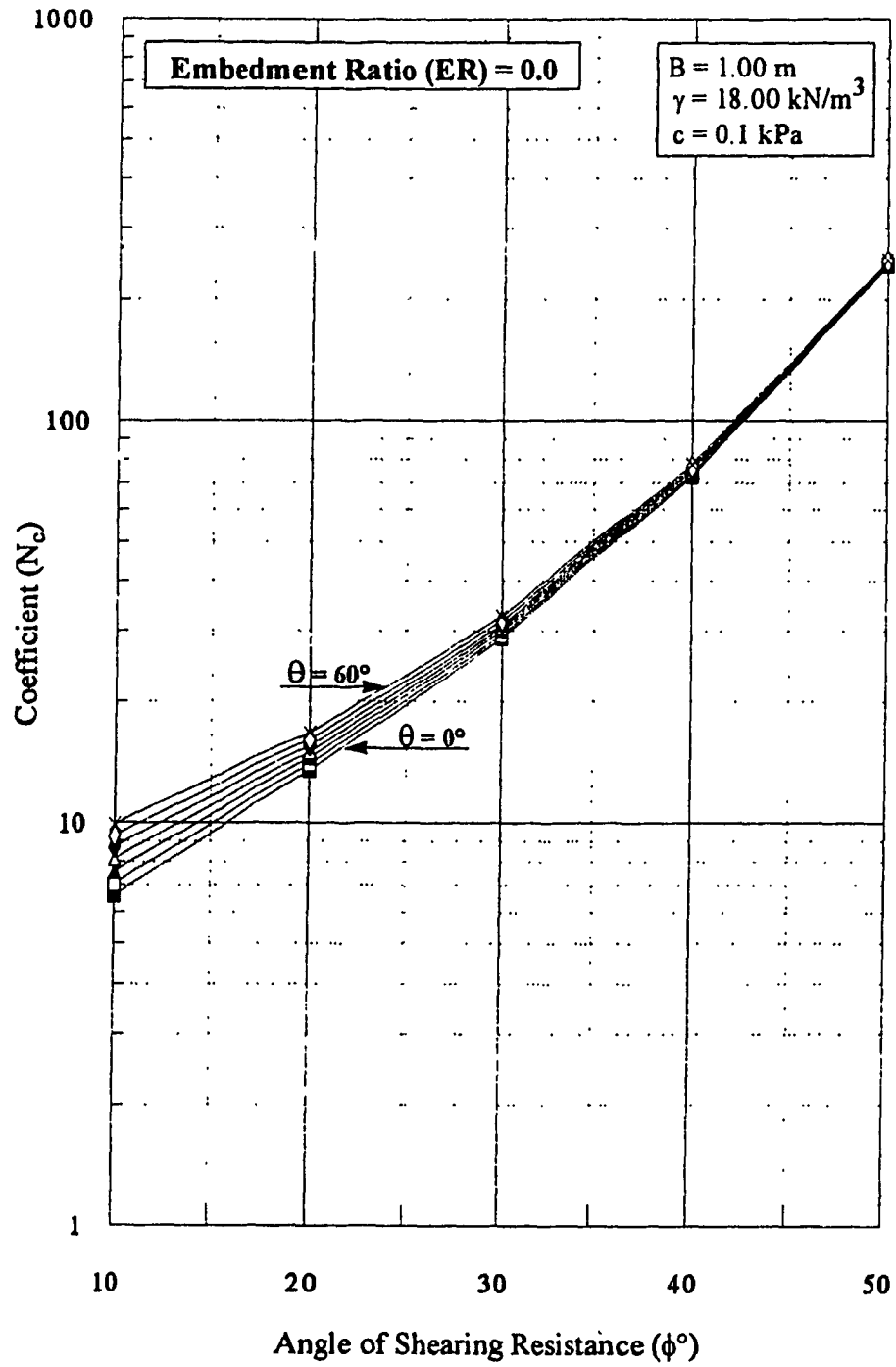


Figure 5.12 Design Chart for Bearing Capacity Coefficient ( $N_c$ ) for ER = 0.0

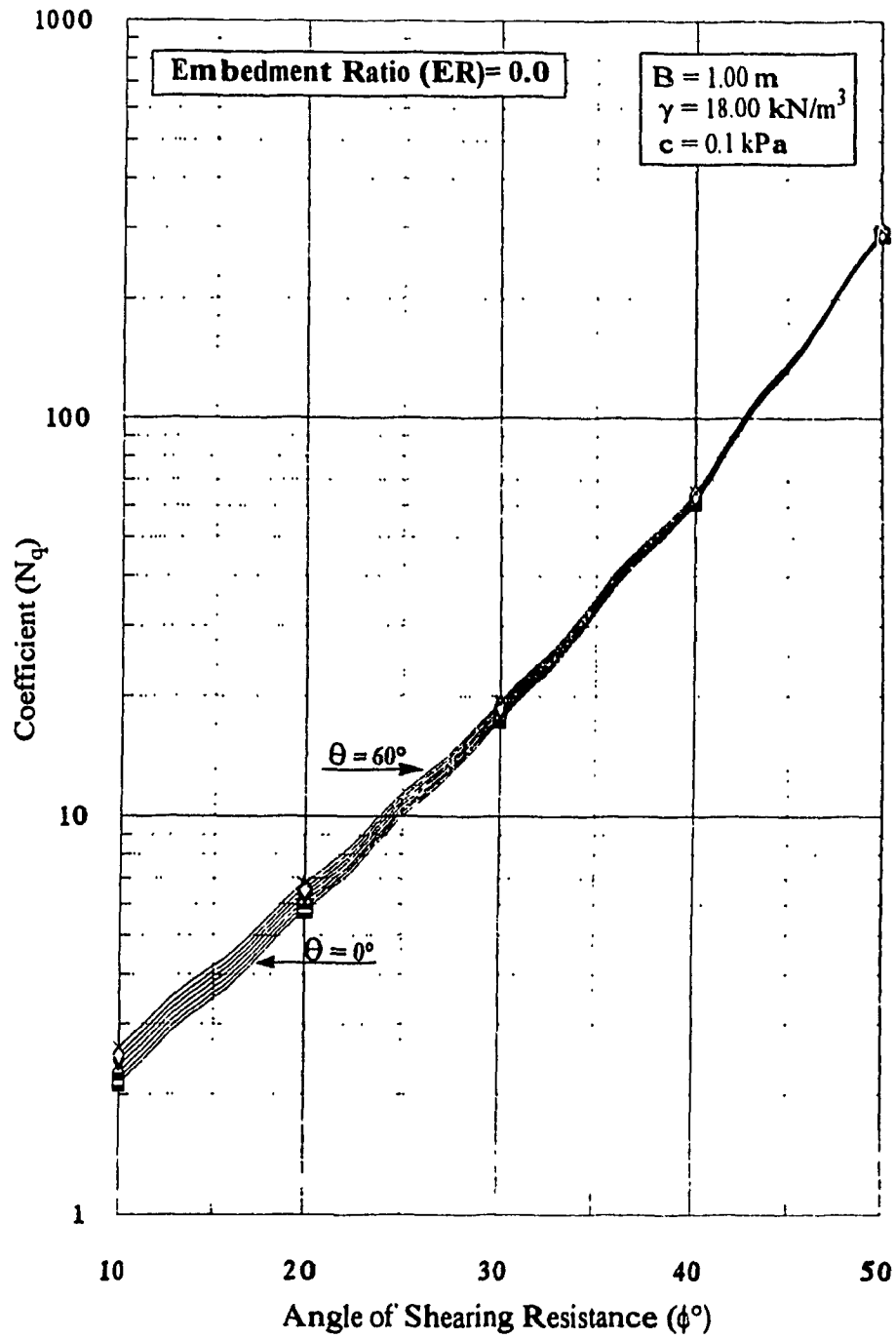


Figure 5.13 Design Chart for Bearing Capacity Coefficient ( $N_q$ ) for ER = 0.0

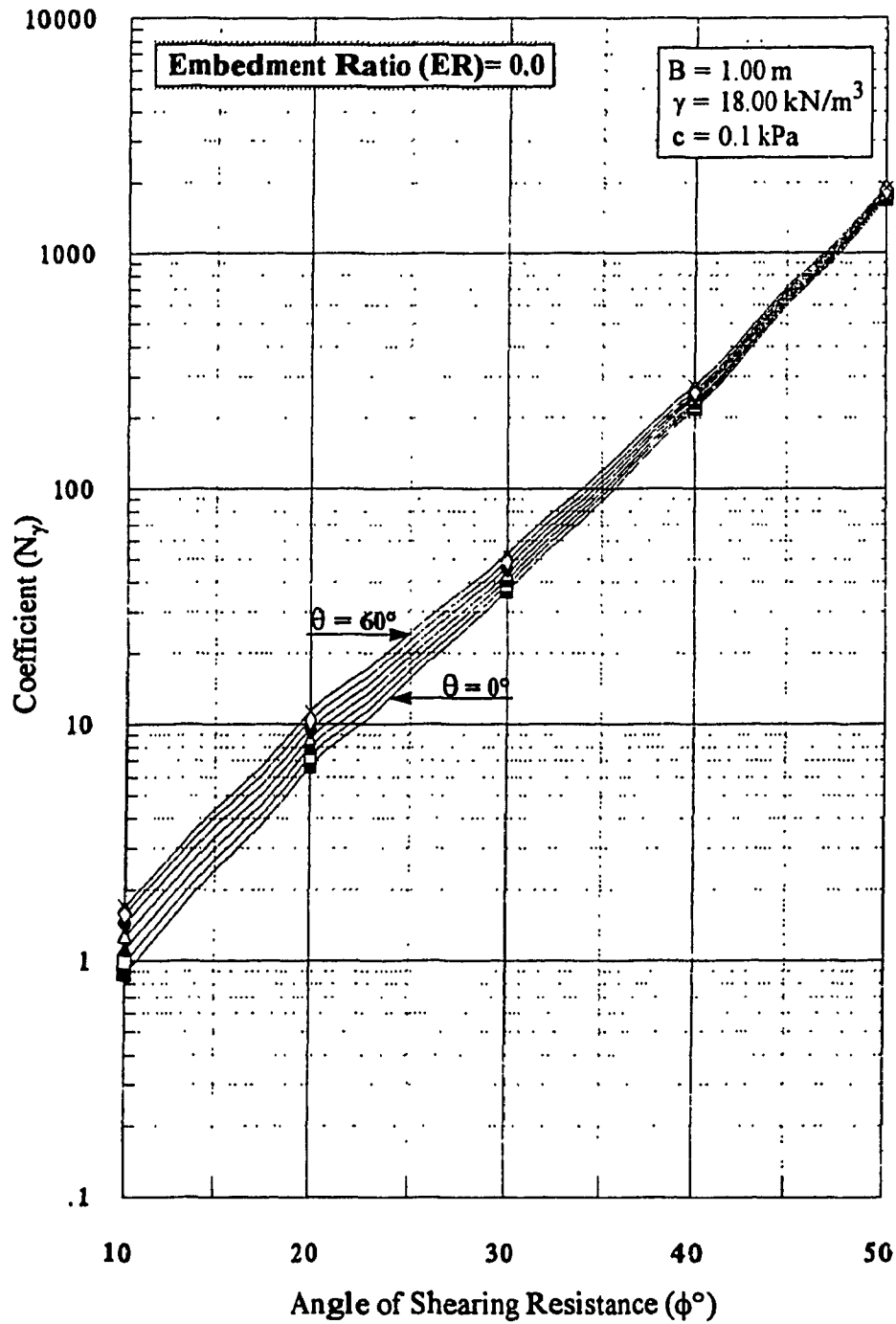


Figure 5.14 Design Chart for Bearing Capacity Coefficient ( $N_\gamma$ ) for ER = 0.0

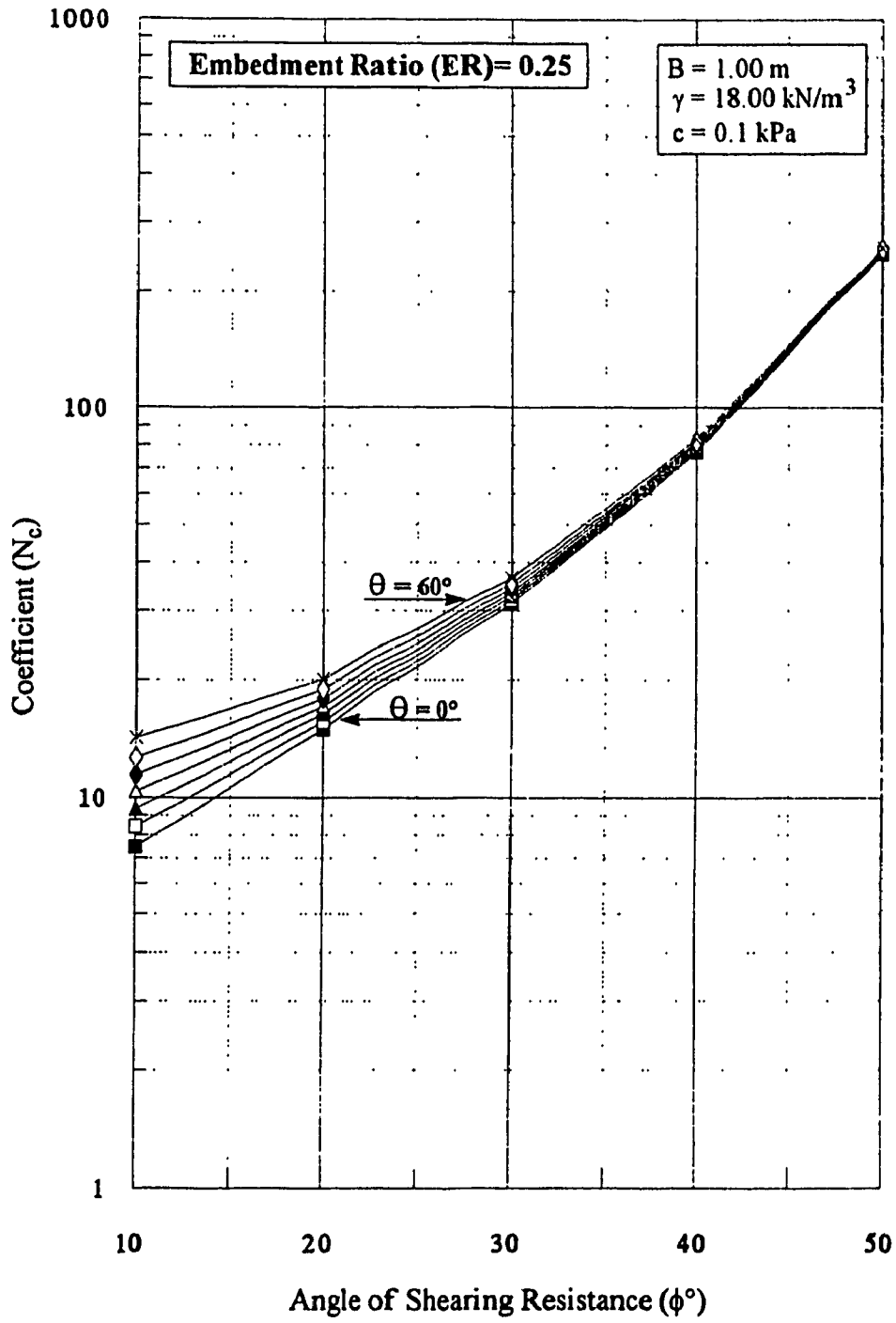


Figure 5.15 Design Chart for Bearing Capacity Coefficient ( $N_c$ ) for ER = 0.25

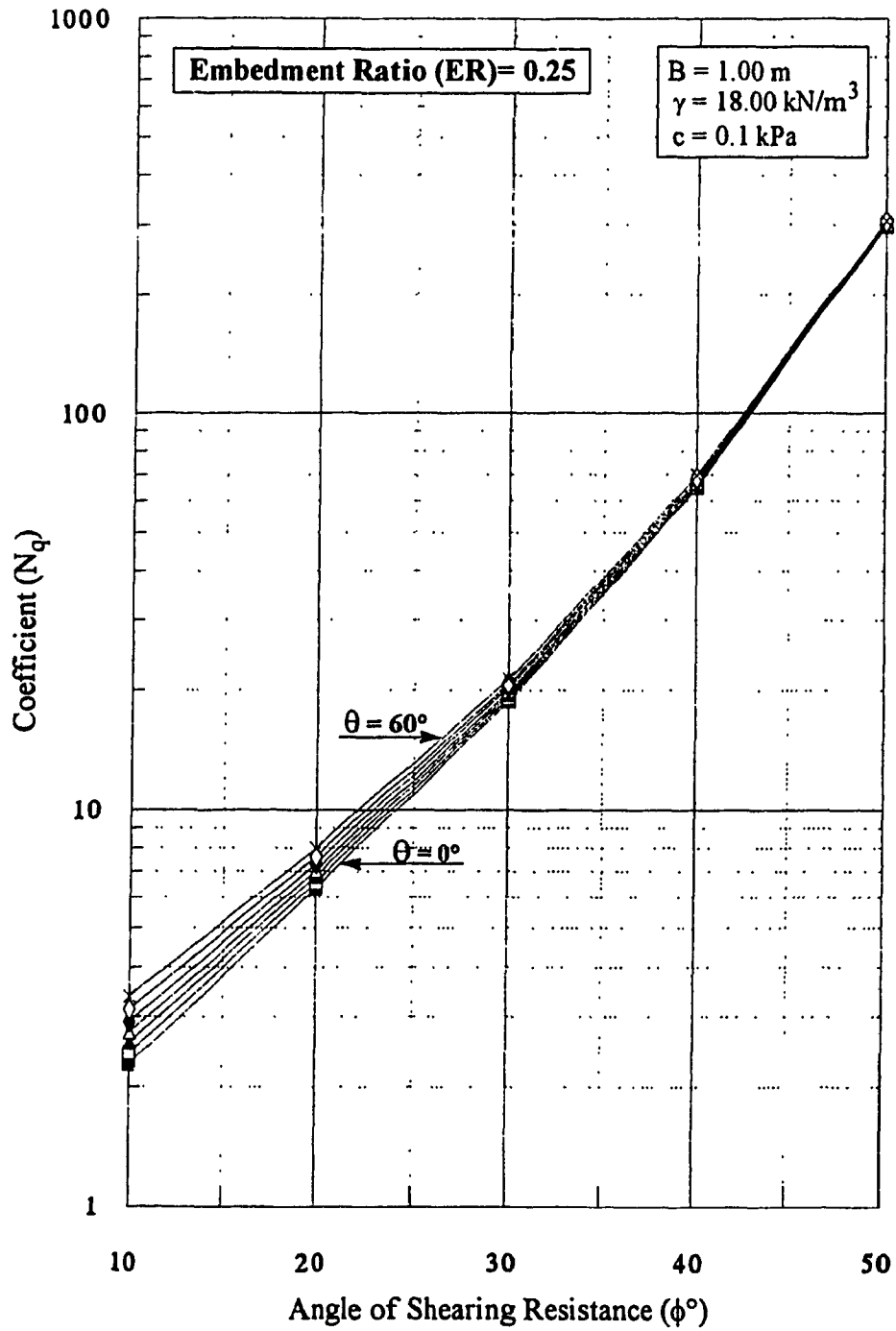


Figure 5.16 Design Chart for Bearing Capacity Coefficient ( $N_q$ ) for ER = 0.25

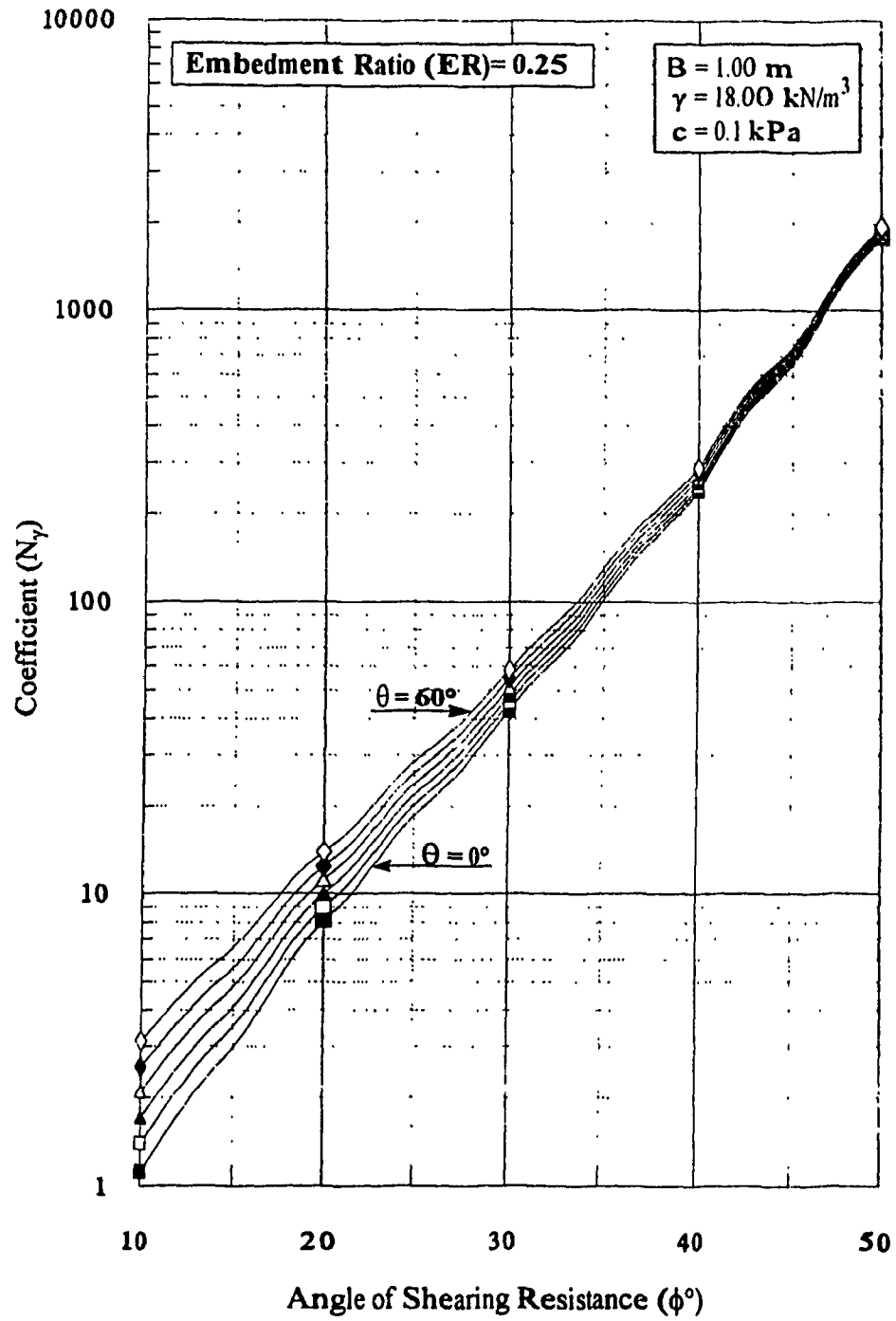


Figure 5.17 Design Chart for Bearing Capacity Coefficient ( $N_\gamma$ ) for ER = 0.25

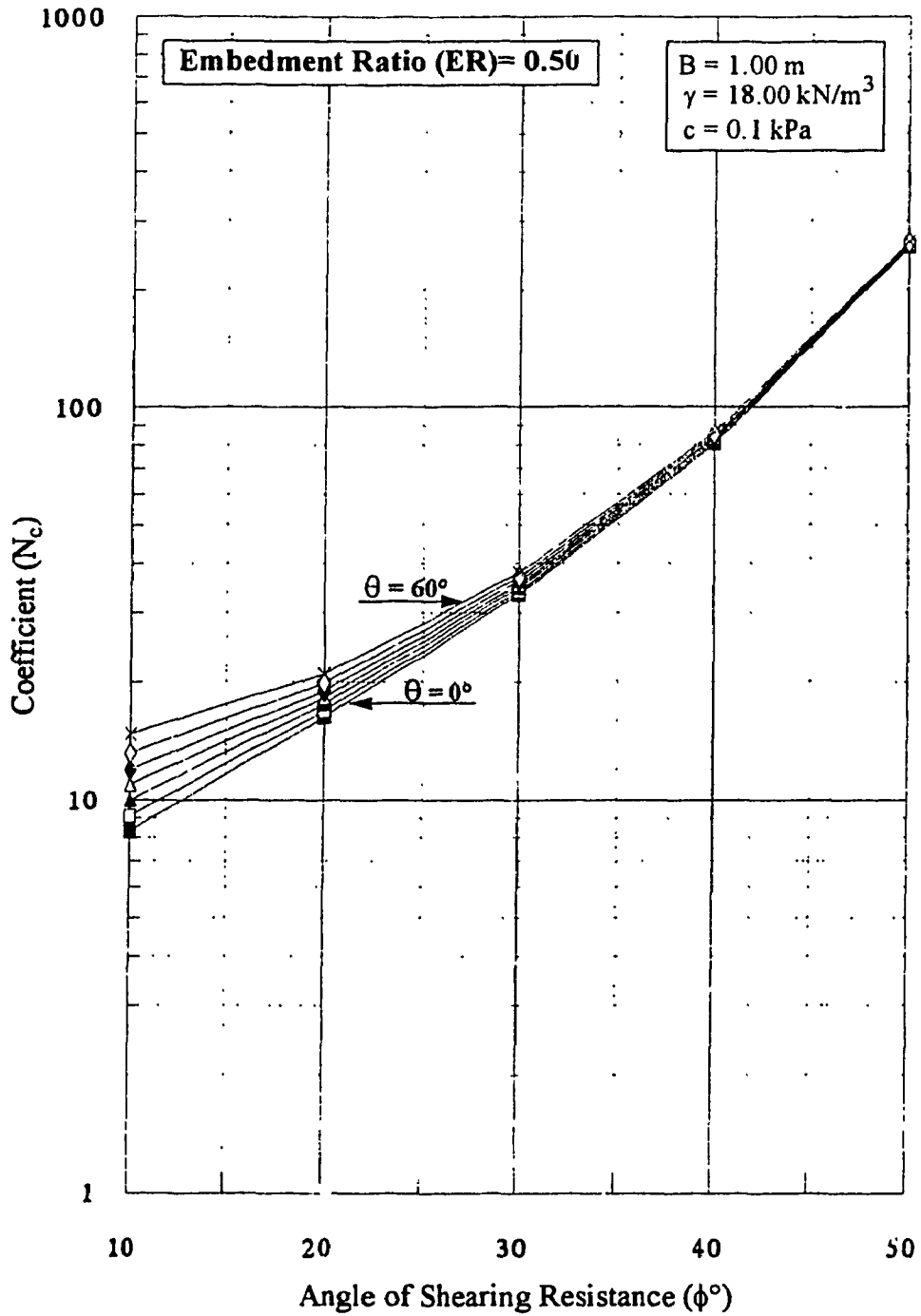


Figure 5.18 Design Chart for Bearing Capacity Coefficient ( $N_c$ ) for ER = 0.50



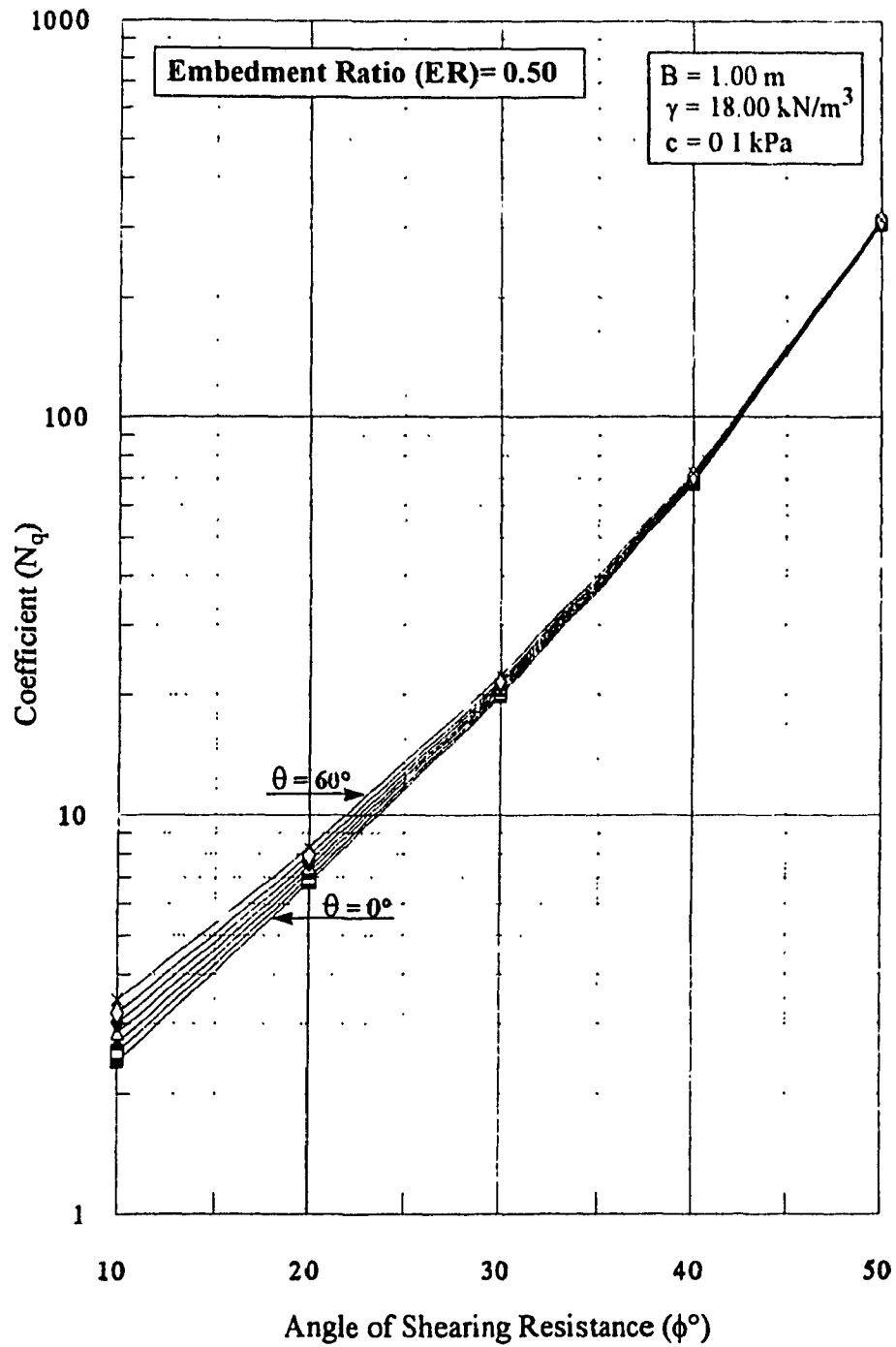


Figure 5.19 Design Chart for Bearing Capacity Coefficient ( $N_q$ ) for ER = 0.50

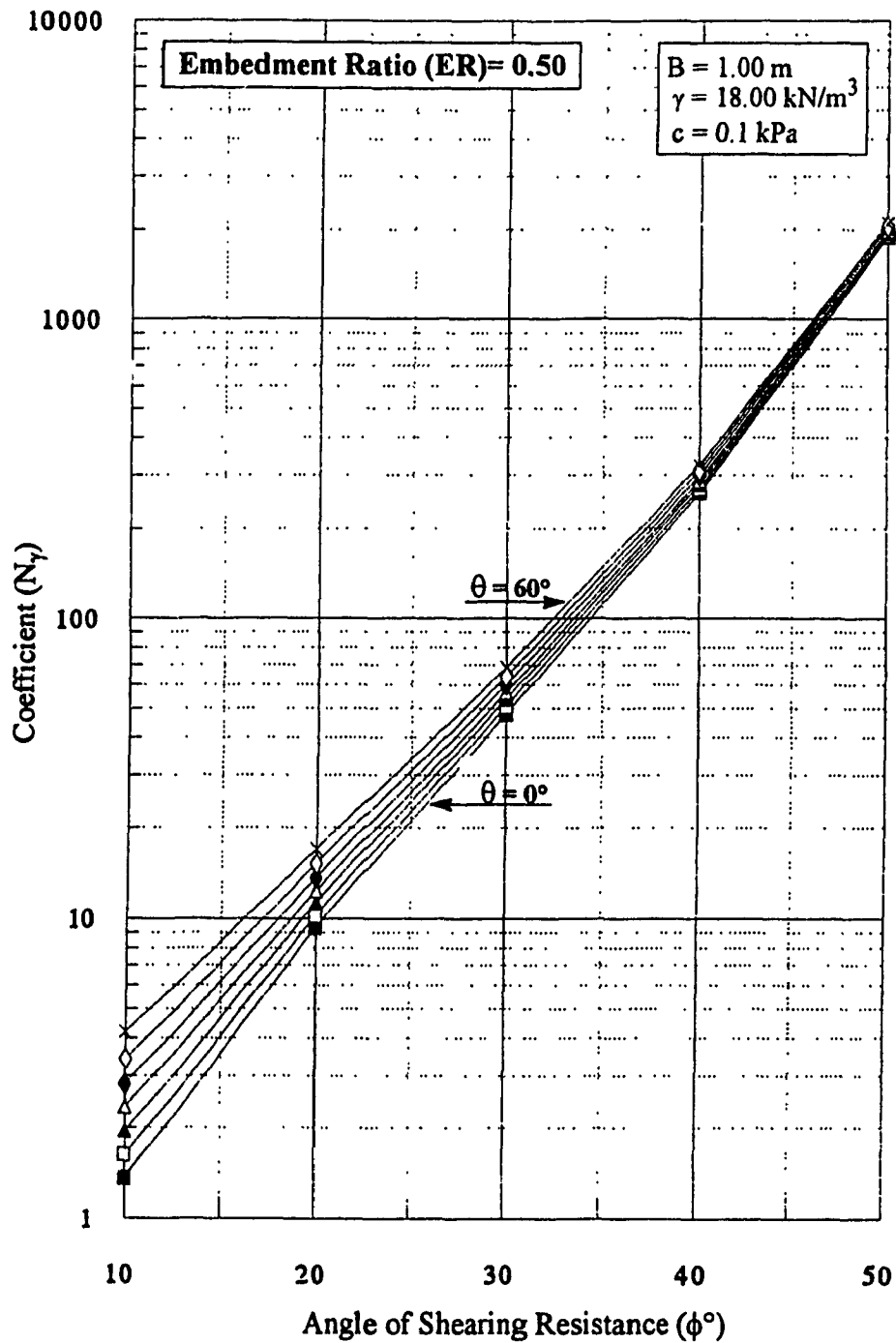


Figure 5.20 Design Chart for Bearing Capacity Coefficient ( $N_\gamma$ ) for ER = 0.50

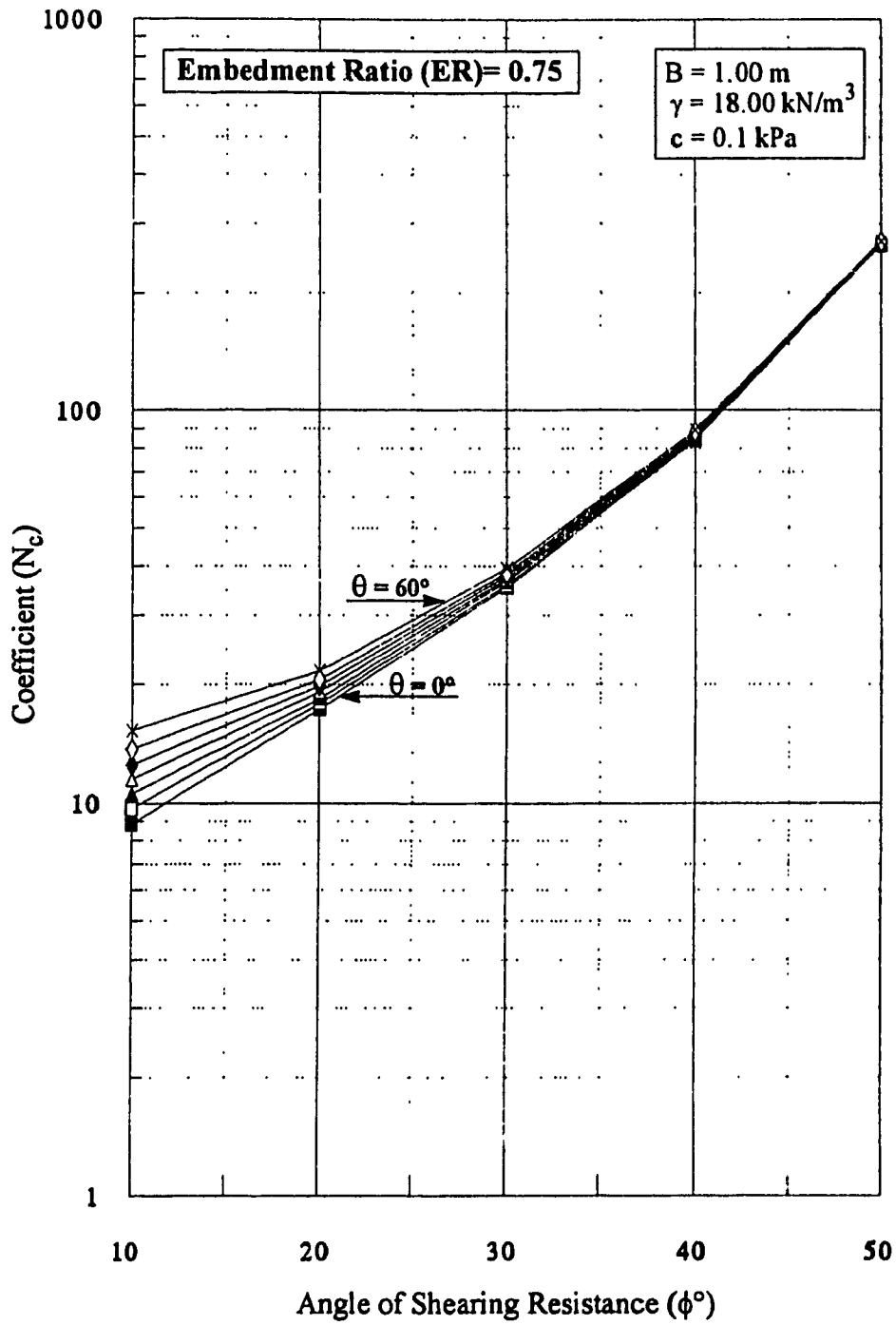


Figure 5.21 Design Chart for Bearing Capacity Coefficient ( $N_c$ ) for ER = 0.75

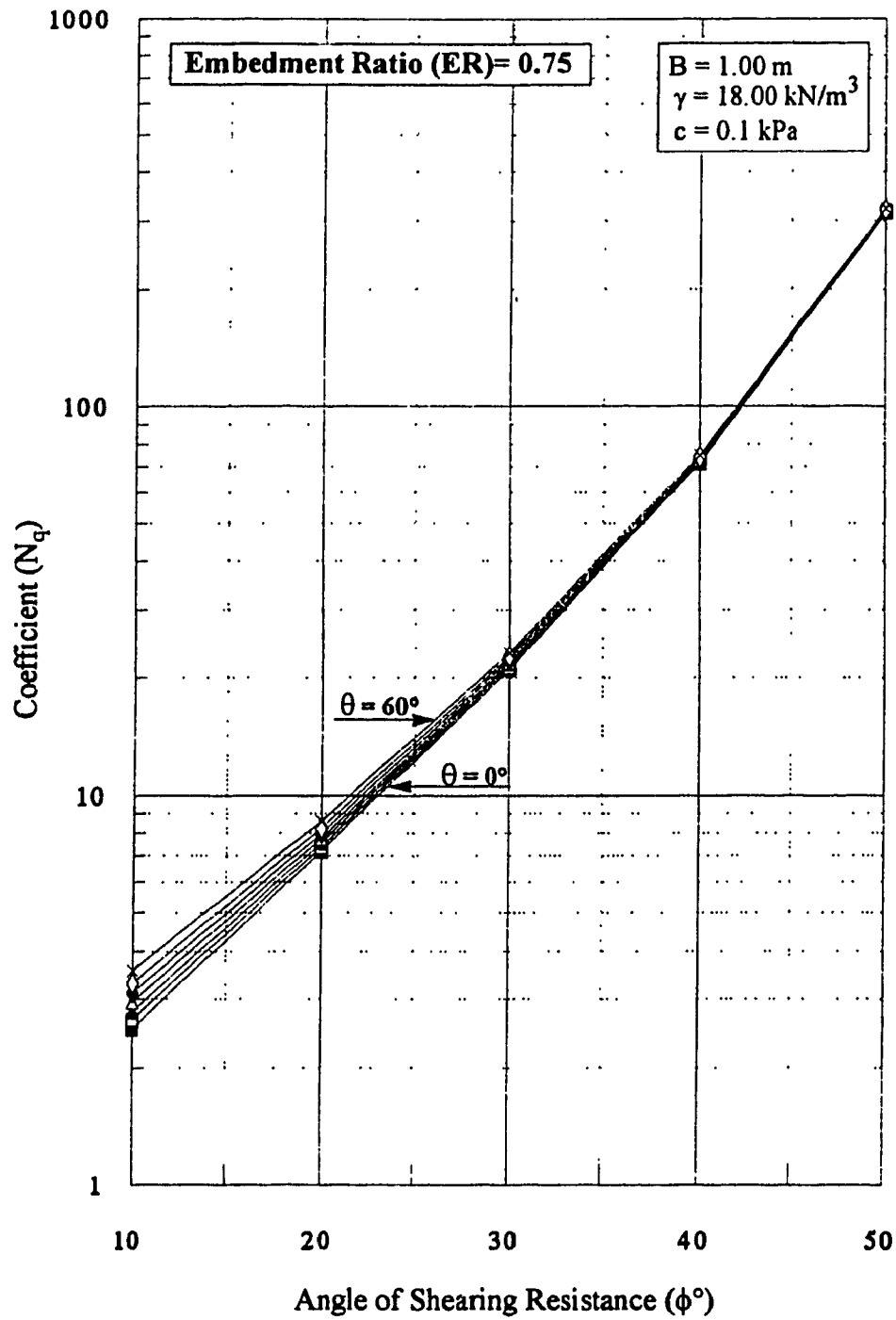


Figure 5.22 Design Chart for Bearing Capacity Coefficient ( $N_q$ ) for ER = 0.75

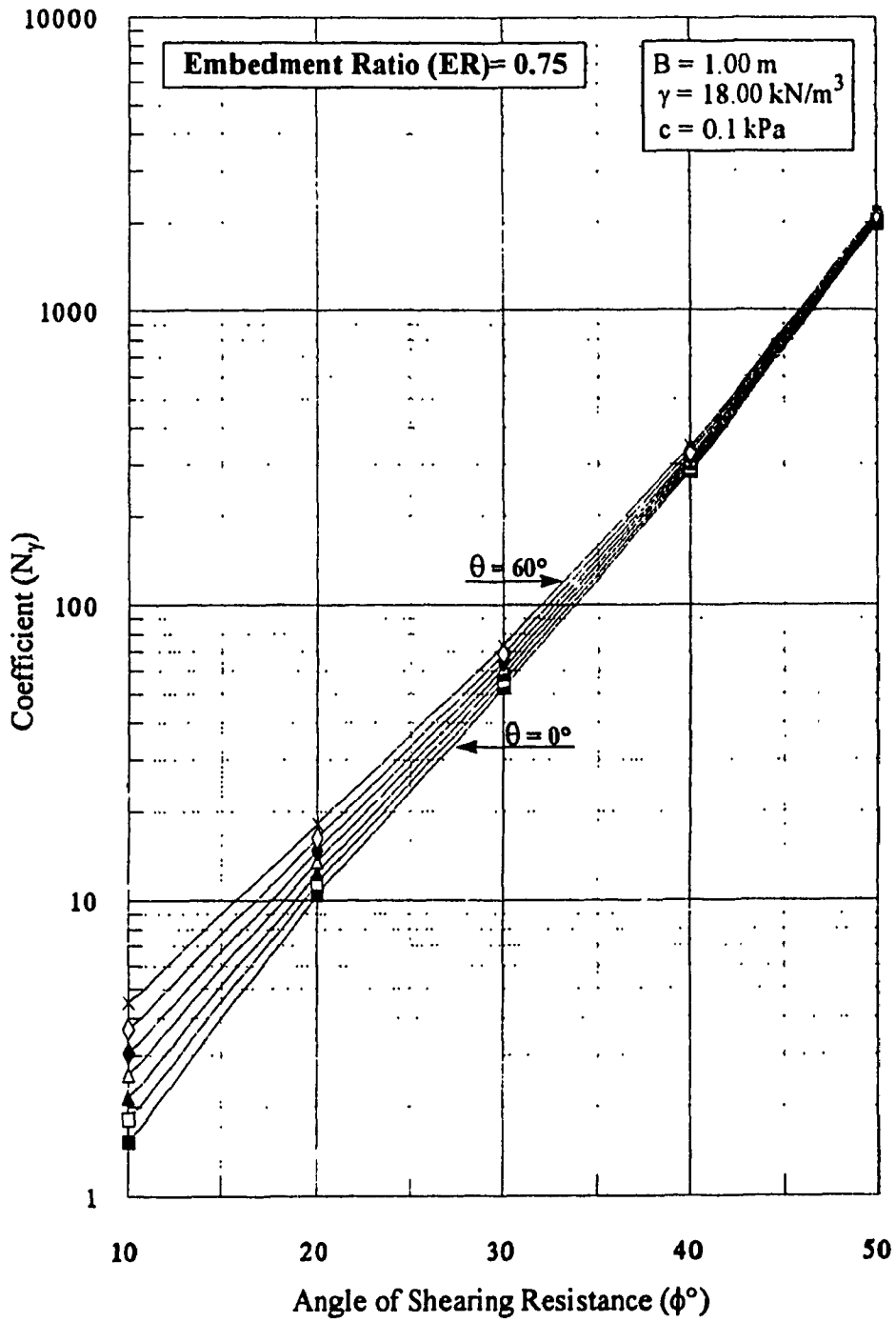


Figure 5.23 Design Chart for Bearing Capacity Coefficient ( $N_\gamma$ ) for ER = 0.75

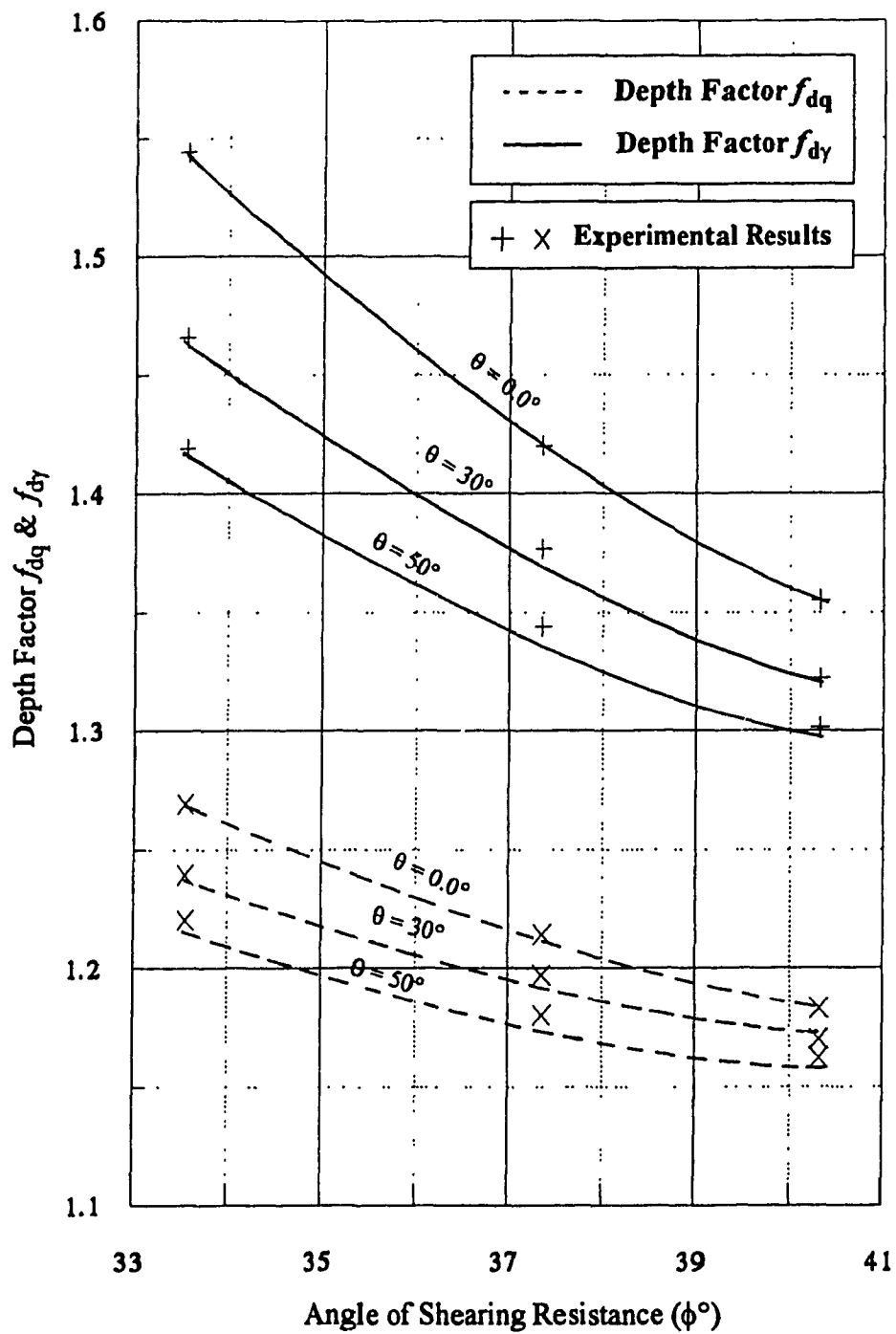


Figure 5.24 Depth Factors  $f_{dq}$  &  $f_{dy}$  from The Experimental Results

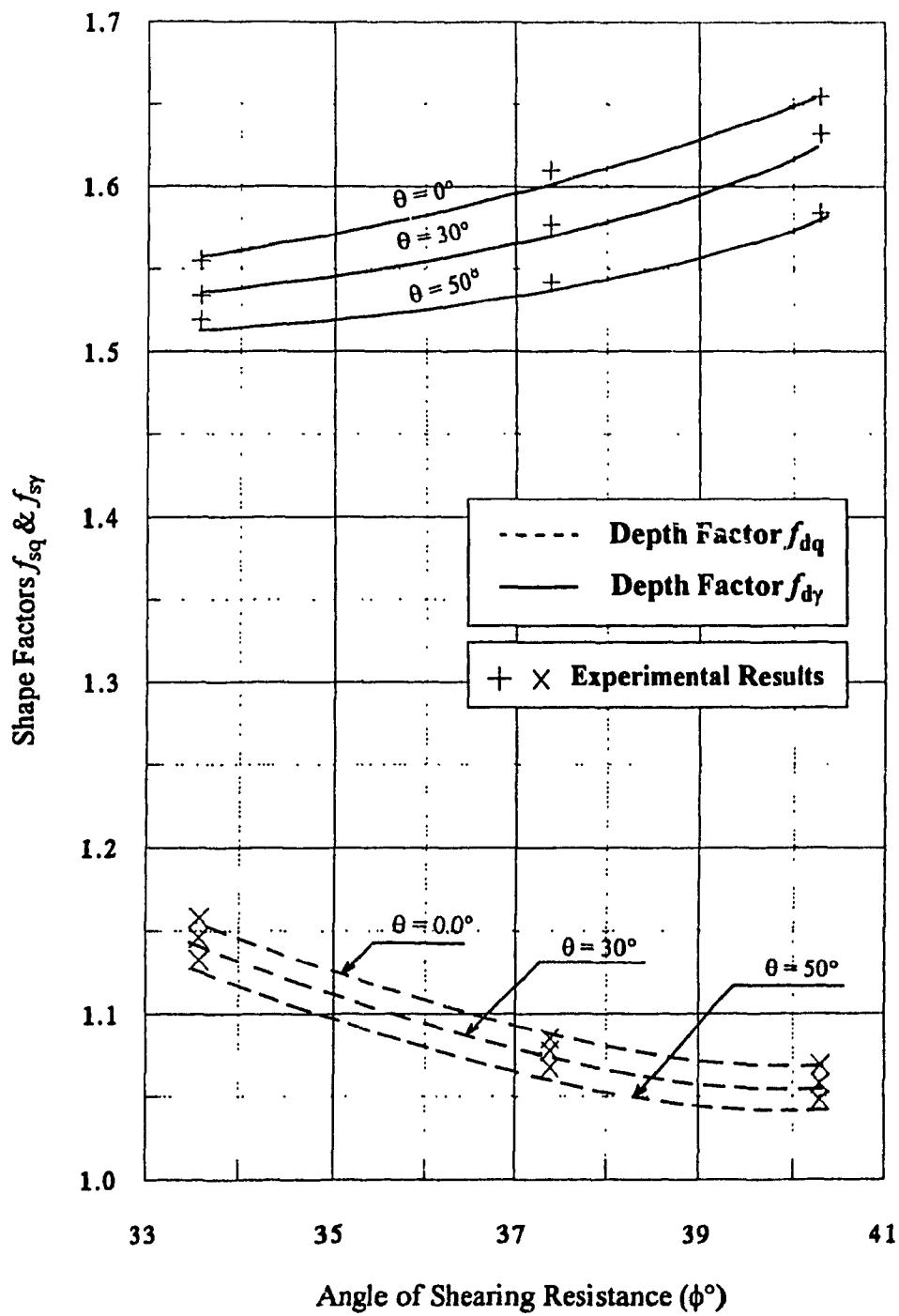


Figure 5.25 Shape Factors  $f_{sq}$  &  $f_{sy}$  for The Axisymmetrical Condition

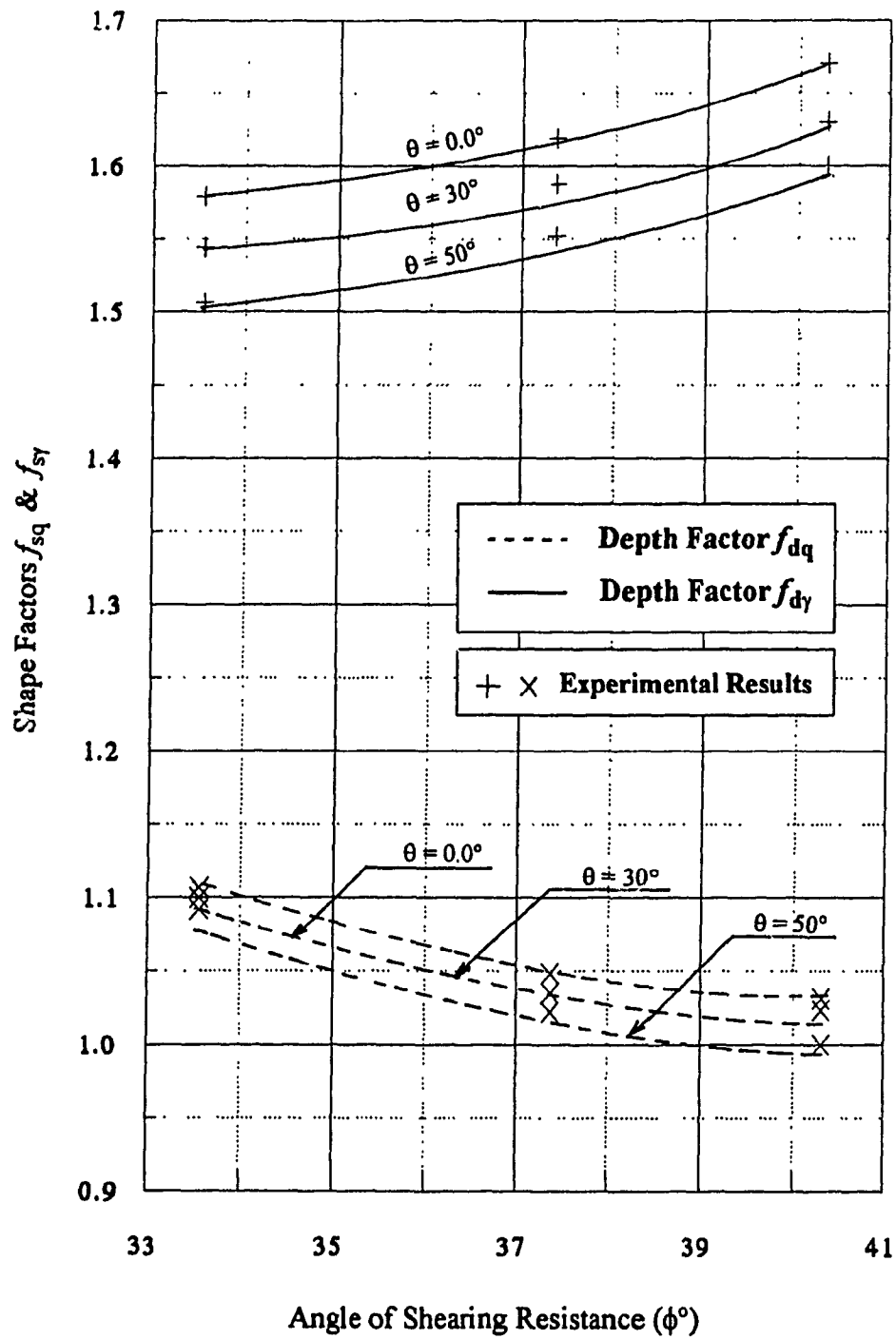


Figure 5.26 Shape Factors  $f_{sq}$  &  $f_{sy}$  for The Three Dimensional Condition



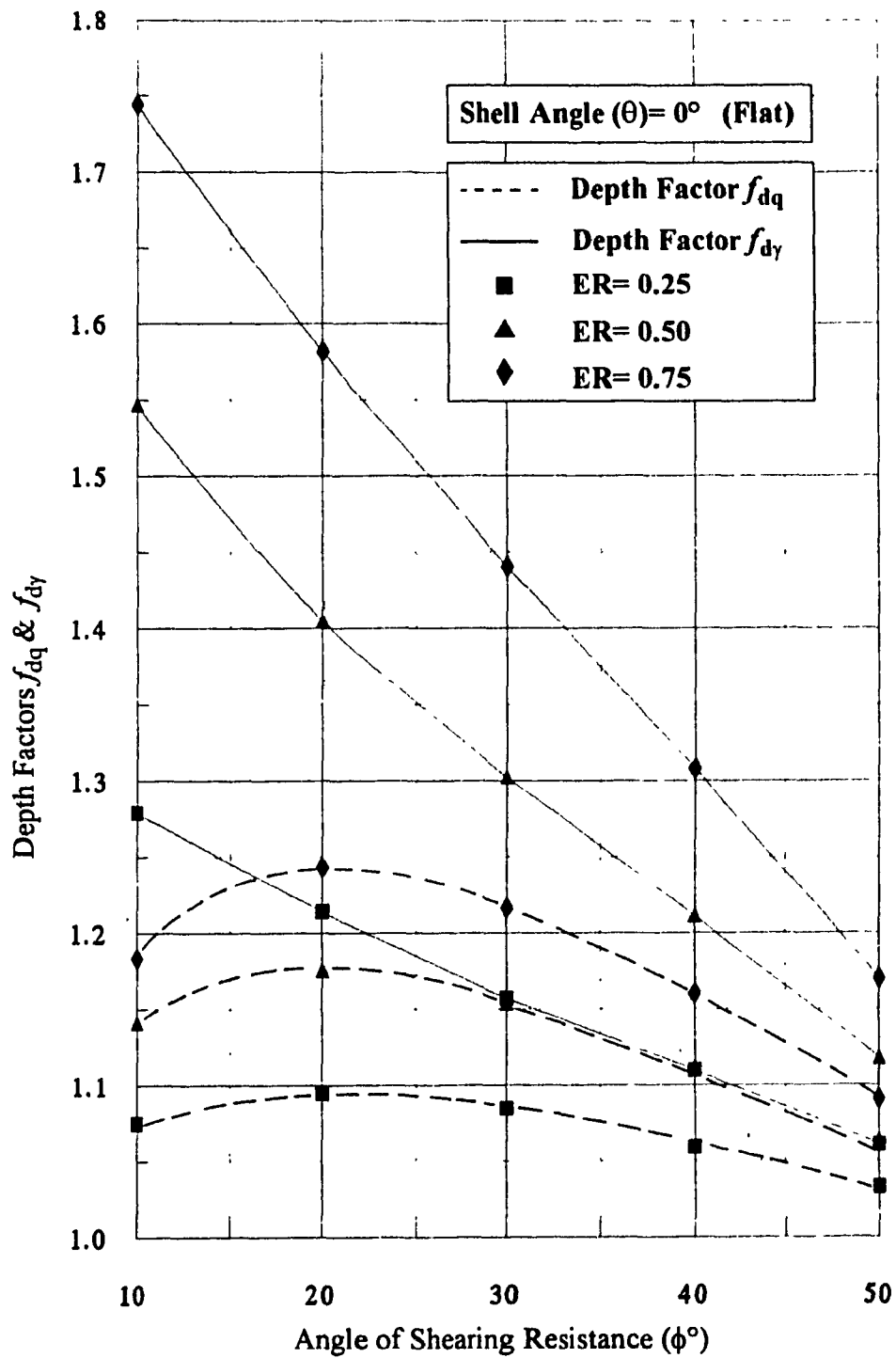


Figure 5.27 Design Chart for Depth Factors  $f_{dq}$  &  $f_{dy}$  for Flat Footing Angle ( $\theta = 0^\circ$ )

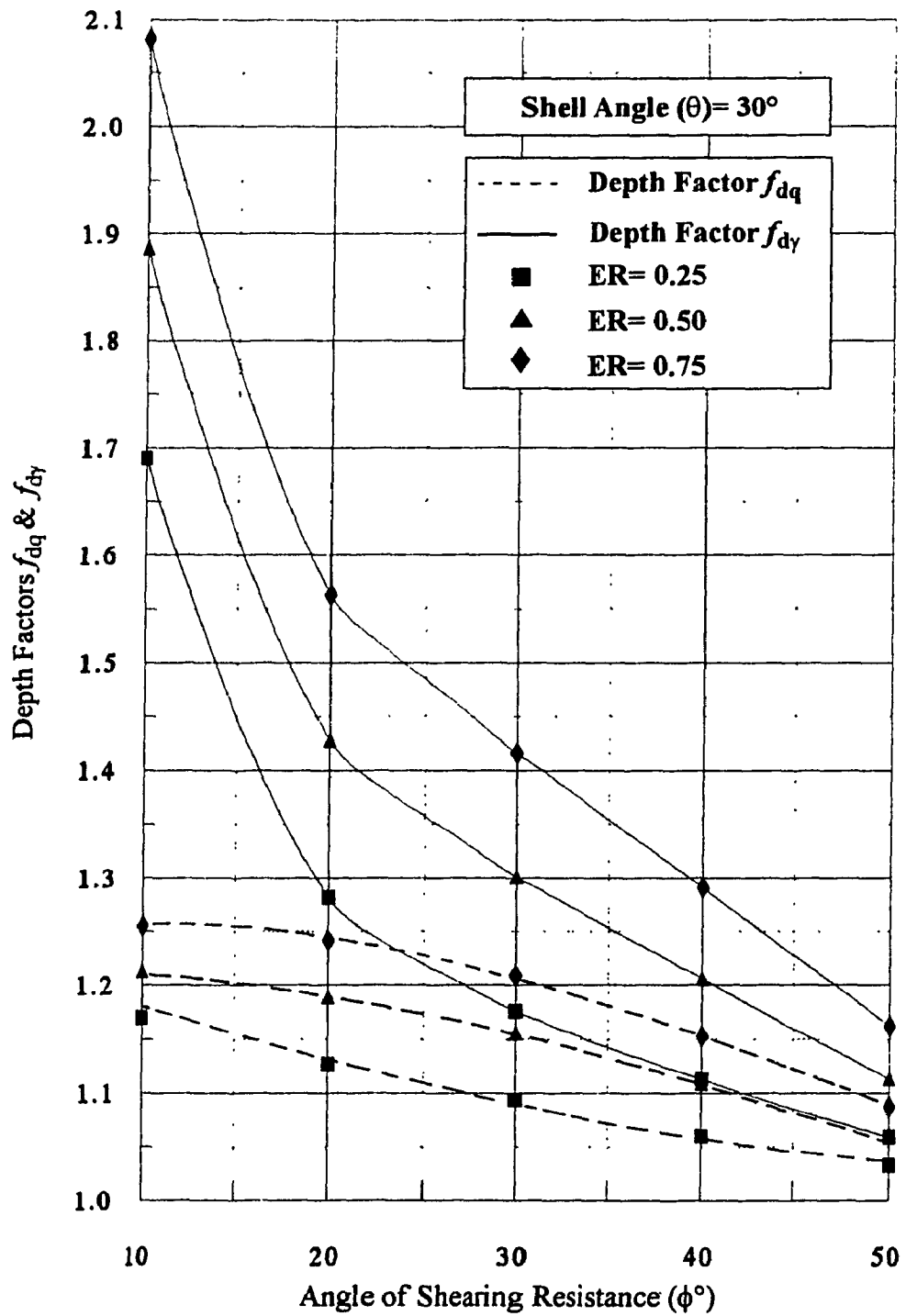


Figure 5.28 Design Chart for Depth Factors  $f_{dq}$  &  $f_{dy}$  for Shell Angle ( $\theta = 30^\circ$ )

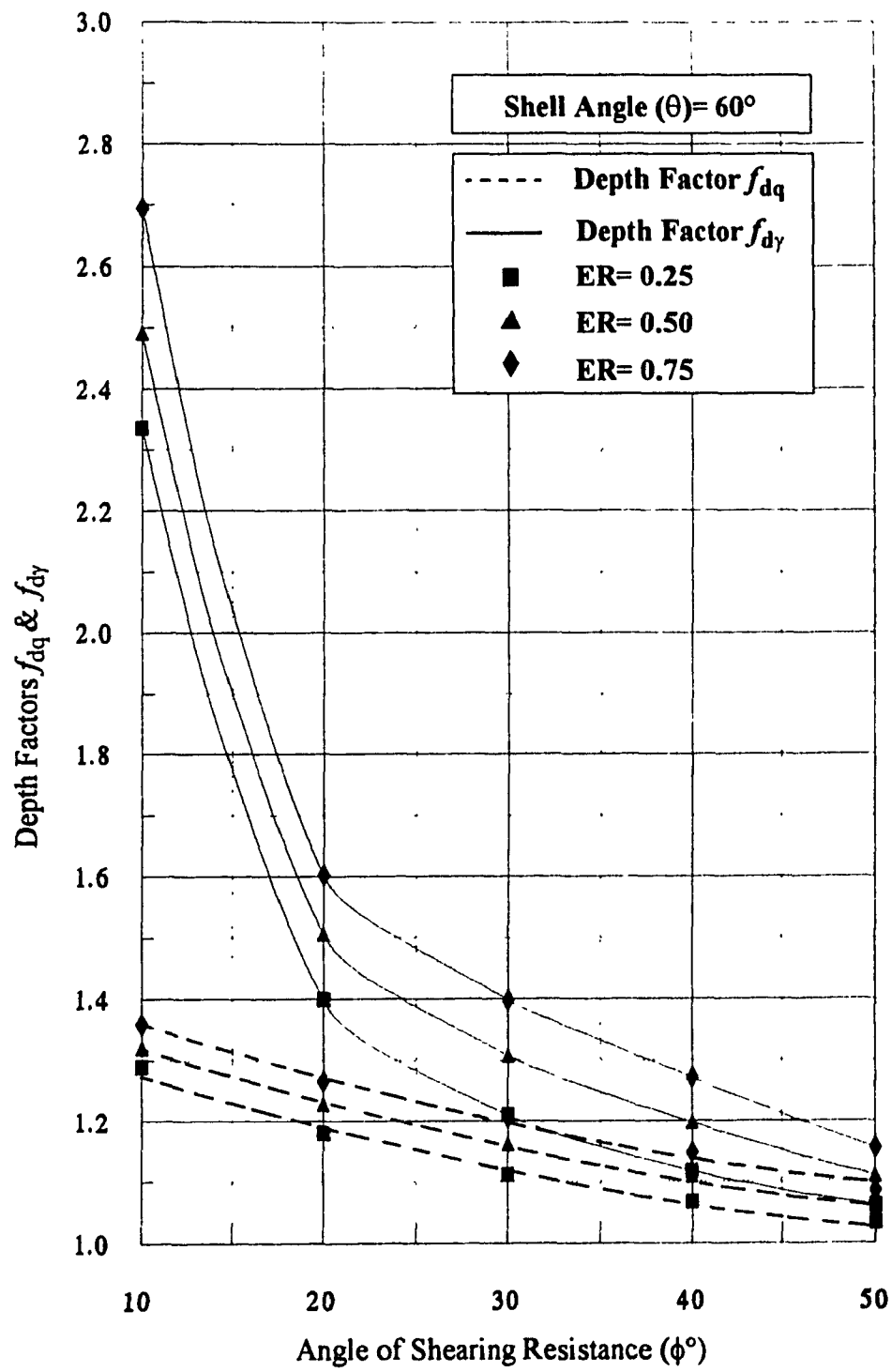


Figure 5.29 Design Chart for Depth Factors  $f_{dq}$  &  $f_{dy}$  for Shell Angle ( $\theta = 60^\circ$ )

## CHAPTER 6

### CONCLUSIONS & RECOMMENDATIONS

#### 6.1 General

A literature review demonstrated that shell foundations have been employed effectively in different parts of the world because of their admirable performance and cost effectiveness. However in most cases, enthusiasm for using shell foundations, generated by the large saving in construction materials and better geotechnical performance, is restrained by the high cost of labor needed for their construction. The reliability and development of precast concrete technology and the use of robotics in excavation and soil molding can contribute to the optimization of the use of shell foundations.

#### 6.2 Conclusions

In the present research work, the geotechnical behavior of shell foundation was investigated and compared with the conventional flat counterparts. Experimental, numerical, and theoretical investigations were carried out on nine foundation models, which represent plane strain, axisymmetrical, and three dimensional loading conditions. Based on the results of the present investigation, the following conclusions can be drawn:

1. The ultimate bearing capacity of shell foundations are remarkably higher than that of the conventional flat counterparts with the same plan dimensions.
2. For a given shell foundation, the ultimate bearing capacity increases due to an increase of the shell angle ( $\theta$ ). An increase of  $19^\circ$  of the shell angle ( $\theta$ ) led to an increase in the ultimate bearing capacity of 8 to 15% depending on the sand state.

3. A shell efficiency factor ( $\eta$ ) was introduced to represent the increase in the ultimate load of shell foundations as compared to the flat counterparts.

The shell efficiency factor ( $\eta$ ) decreases for higher angle of shearing resistance ( $\phi$ ), i.e., the effect of shell configuration reduces as a result of the increase in soil strength.

The shell efficiency factor ( $\eta$ ) decreases remarkably for the embedded shell footings as compared to surface ones. This trend held true for all sand states used in the present investigation and the reduction in ( $\eta$ ) varied from 37 to 45%. This shows that the depth of embedment seems to undermine the positive contribution of shell configuration on the ultimate bearing capacity.

The shell efficiency factor ( $\eta$ ) for the conical and pyramidal shell footings were slightly higher (about 3%) than that for the triangular strip footings for all tests. This indicates that the confinement of the sand underneath the shell surface has a relatively positive effect on the ultimate bearing capacity.

The shell efficiency factor ( $\eta$ ) for the conical shell footings was marginally higher than that for the pyramidal shell footings with the exception of the tests conducted on surface footings on loose sand.

The shell efficiency factor ( $\eta$ ) in the present investigation varied from 6%, for the embedded triangular (1) shell footing on dense sand, up to 38% for the surface pyramidal (2) shell footing on loose sand.

4. A non dimensional settlement factor ( $F_{\delta}$ ) was introduced to examine the settlement characteristics of shell foundations against the conventional flat counterparts. The results of the calculated settlement factor ( $F_{\delta}$ ) deduced from the present experimental investigation demonstrate that shell foundations have better settlement behavior than the conventional flat ones.

5. The contact pressure distribution showed that the contact pressure increases due to the increase of the applied load in nearly a linear fashion throughout the loading stages. However, some curvature existed at the ultimate stage.

The contact pressure envelopes for the triangular shell footings were relatively more confined than that for the strip flat one, which demonstrates less variation in the contact pressures over the base of the shell footings.

The trend of the contact pressure distribution for the axisymmetrical and three dimensional footings was not consistent with the above finding, where in some tests the contact pressure envelopes for the circular and square flat footings were more confined than that for the conical and pyramidal shell footings, respectively.

In general, the maximum contact pressure occurs at/or near the edge of the flat strip and triangular shell footings and at the center for the square flat and pyramidal shell footings.

The comparison between the circular flat and conical shell footings shows that while the maximum contact pressure occurs at/or near the center of the circular footing, it occurs at/or near the edge of the conical shell models.

6. The special loading tests conducted using colored sand layers in a plexiglas tank to monitor the movement of the sand particles during loading has proven to be an effective tool to predict the shape of the rupture surface.

The results deduced from these tests demonstrate that the rupture surfaces for the triangular shell footings are deeper than those for the flat one, which leads to the increase in the ultimate load for the shell footings.

7. In the numerical modelling, the elastic perfectly plastic soil model using Mohr-Coulomb's yield criterion proved able to provide a realistic representation of the behavior

of cohesionless soil as predicted from the present experimental investigation.

The comparison between the rupture surface determined from the results of the numerical modelling and the one deduced from the experimental results showed good agreement. This mechanism was used in the theoretical model to develop a theory for the ultimate bearing capacity of shell foundations.

8. The rupture surface employed in the theoretical analysis was composed of circular and plane surfaces; it provides a kinematically and statically admissible solution. Kötter's differential equation was employed successfully to simulate the shear stress distribution along the circular as well as the plane parts of the rupture surface.

The Shell Ratio (SR) was proposed and incorporated in the analysis to take into account the effect of shell configuration on the failure mechanism and accordingly the ultimate bearing capacity.

The developed ultimate bearing capacity coefficient ( $N_c$ ,  $N_q$ ,  $N_\gamma$ ) are not only functions of angle of shearing resistance ( $\phi$ ) but also of the foundation width (B), Shell Ratio (SR), Embedment Ratio (ER), unit weight of soil ( $\gamma$ ), and cohesion of soil (c)

The above finding might be the reason for the discrepancies in the results of the existing theories for the ultimate bearing capacity of flat foundations, in which the bearing capacity coefficients depend only on the angle of shearing resistance ( $\phi$ ).

9. A computer program "*BC-Shell*" was developed to predict the ultimate bearing capacity of shell foundations. The program was designed for easy application through an interactive mode.
10. A comparison between the experimental and theoretical results for the plane strain condition were presented and showed good agreement.

11. The results of the parametric study conducted to examine the sensitivity of the governing parameters on the factor ( $\rho$ ), and consequently on the bearing capacity coefficients ( $N_c$ ,  $N_q$ ,  $N_\gamma$ ) showed that the angle of shearing resistance ( $\phi$ ) has the most significant effect on the factor ( $\rho$ ).

The foundation width ( $B$ ) has a relatively significant effect on the factor ( $\rho$ ) for small size footings, however, this effect becomes negligible for larger footings. The effect of foundation width ( $B$ ) diminishes at higher angles of shearing resistance ( $\phi$ ).

The factor ( $\rho$ ) increases due to an increase in the Shell Ratio (SR), and consequently the ultimate bearing capacity increases. However, this contribution decreases for soil with higher angles of shearing resistance ( $\phi$ ).

The effect of the embedment ratio (ER) was consistent for the entire range of the angle of shearing resistance ( $\phi$ ). The factor ( $\rho$ ) increases due to an increase of the embedment ratio (ER).

The factor ( $\rho$ ) increases due to an increase of the cohesion of the soil ( $c$ ), however, at higher angles of shearing resistance ( $\phi$ ), the effect is relatively insignificant.

The unit weight of soil ( $\gamma$ ) had no effect on the factor ( $\rho$ ) and consequently on the bearing capacity coefficients for all sand states.

12. In order to facilitate the use of the developed theory for practicing engineers during the preliminary design phase of shell foundations, design charts and design tables for bearing capacity coefficients ( $N_c$ ,  $N_q$ ,  $N_\gamma$ ) and depth factors ( $f_{sq}$ ,  $f_{s\gamma}$ ) were also presented within the range of practical use. In addition, the developed theory was utilized to predict the ultimate bearing capacity of shell foundations in axisymmetrical and three dimensional conditions by introducing shape factors ( $f_{sq}$ ,  $f_{s\gamma}$ ).



13. The results of the present investigation support the contention that shell foundations should come into wider use in the geotechnical field in the future as a serious alternative to shallow and deep foundation, whenever the scope exists to employ them effectively.

### **6.3 Recommendations for Future Research**

Although the results of laboratory tests are always questioned due to the scale effects and boundary conditions, they can provide an economical alternative to field tests and can be a good source of information. However, in order to enhance the knowledge of the geotechnical performance of shell foundations and encourage their applications in practice, future research should be directed to the following:

1. Conduct field tests to examine further the theoretical model developed in the present investigation.
2. Study other shapes of shell foundations which might provide more uniform contact pressure distribution.
3. Develop theoretical models or empirical formulas to determine the settlement, contact pressure, and stress distributions within the soil mass for shell foundations.
4. Further investigations should be directed to study the effect of the parameters affecting the bearing capacity coefficients deduced from the present investigation to minimize the discrepancies in the results of the existing bearing capacity theories for flat foundations. The overconsolidation represented by the overconsolidation ratio (OCR) should also be investigated.
5. Examine the performance of shell foundations in resisting lateral forces to simulate wind or earthquakes loading conditions as the passive earth pressure developed on the side of the shell surface will have positive contribution.

6. Investigate the use of strip shell foundations in retaining walls to resist sliding forces and overturning moment due to earth pressure.
7. Investigate the use of transverse multiple units of strip shell foundations as concrete pavement elements in roads and highways especially on weak soils, which might contribute in savings in their construction cost.
8. Develop new construction techniques in order to economize on the construction cost of shell foundations.

## LIST OF REFERENCES

- Abdel-Rahman, M. M., and Hanna, A. M. (1994). "Vertical Displacement induced in Soil by Conical Shell Foundations.", *Proc. Vertical and Horizontal Deformations of Foundations and Embankments, Settlement '94*, ASCE, University of Texas at A & M, Geotechnical Special Publication No. 40, 2, 937-948
- Abdel-Rahman, M. M. (1987). "Ultimate bearing capacity of triangular shell strip footings on sand." *M. Eng. thesis*, Dept. of Civil Engrg., Concordia University, Montreal, Quebec, Canada.
- Agarwal, K. B., and Gupta, R. N. (1983). "Soil structure interaction in shell foundations." *Proc. Int. Workshop Soil Structure Interaction*, University of Roorkee, India, 1, 110-112.
- Anderson, A. R. (1960). "Precast, prestressed stadium floats on hyperbolic- paraboloids." *Engrg. News Record*, 164 (7), 62-63.
- Anon (1965). "R.C. shells in roof & foundations of factory buildings." *Bull. Int. Ass. Shell and Spatial Structures*, (22), 55-58.
- Arai, K., Ohnishi, Y., and Yasukawa, I. (1987). "Measurement and interpretation of loading tests of concrete top blocks on soft ground." *Proc. 2nd Int. Symp. on Field Measurements in Geomechanics*, Kobe, Japan, A. A. Balkema, 2, 1177-1184.
- Arai, K., Ohnishi, Y., Horita, M., Yasukawa, I., and Nakaya, S. (1988) "Interpretation of concrete top base foundation behaviour on soft ground by coupled stress flow finite element analysis" *Proc. 6th Int. Conf. Numerical Methods in Geomechanics*, Innsbruck, Austria, A. A. Balkema, 1, 625-630.

- Atkinson, J. H., and Bransby, P. L. (1978) *The mechanics of soils: an introduction to critical state soil mechanics*. McGraw-Hill Book Company (UK) Ltd.
- Atkinson, J. H. (1981). *Foundations and slopes*. McGraw-Hill Book Company (UK) Ltd.
- Atkinson, J. H. (1993). *An introduction to the mechanics of soils and foundations*. McGraw-Hill Book Company (UK) Ltd.
- Bhattacharya, B., and Ramaswamy, G. S. (1977). "A finite element analysis of funicular shells on a two parameter foundation model." *Bull. Int. Ass. Shell and Spatial Structures*, 18 (65), 45-54.
- Bolton, M. D. (1991). *A guide to soil mechanics*. M D & K Bolton.
- Britto, A. M., and Gunn, M. J. (1987). *Critical state soil mechanics via finite elements*. Ellis Horwood, Ltd., Chichester, England.
- Britto, A. M., and Gunn, M. J. (1992). *CRISP user's and programmer's guide*. Dept. of Engrg., Cambridge University, England.
- Candela, F. (1955). "Structural applications of hyperbolic paraboloidal shells." *J. ACI*, 26 (5), 397-415.
- Chen, W. F. (1975). *Limit analysis and soil plasticity*. Elsevier Scientific Publishing Company.
- Chen, W. F., and Liu, X. L. (1990). *Limit analysis in soil mechanics*. Elsevier Scientific Publishing Company.
- Chen, W. F., and Mizuno, E. (1990). *Nonlinear analysis in soil mechanics: theory and*

*implementation*. Elsevier Scientific Publishing Company

- Ciesielski, R. (1966). "Shell foundations for tower-shaped structures." *Proc. Symp. Tower Shaped Steel Reinforced Concrete Structures*, Bratislava, Czechoslovakia, 337-346.
- Das, Y. C., and Kedia, K. K. (1977). "Shells on elastic foundations." *Transactions 4th Int. Conf. Structural Mech. in Reactor Technology*, San Francisco, USA, M(3/6), 1-11.
- Dierks, K., and Kurian, N. P. (1981). "Zum Verhalten von Kegelschalenfundamenten unter zentrischer und exzentrischer Belastung." *Bauingenieur*, 56 (2), 61-65 (in German).
- Dierks, K., and Kurian, N. P. (1988). "Zum Verhalten von Kugel und Doppelkegelschalenfundamenten unter zentrischer und exzentrischer Belastung." *Bauingenieur*, 63 (7), 325-333 (in German).
- Enriquez, R. R., and Fierro, A. (1963). "A new project for Mexico City." *Civil Engrg.*, 33 (6), 36-38.
- Fareed, A., and Dawoud, R.H. (1979). "Cylindrical shells on elastic foundation." *World Congress on Shell and Spatial Structures*, Madrid, Spain, 3, 5.33- 5.46.
- Griffiths, D.V. (1982). "Computation of bearing capacity factors using finite elements." *Geotechnique*, 32 (3),195-202.
- Hanna, A. M., and Hadid, W. (1987). "New models of shallow foundations." *Int. J. Math. Modeling*, 9 (11), 799-811.
- Hanna, A. M. (1988). "Shell foundations: the future alternative." *Int. J. Housing Science*

*and Its Applications*, 12 (4), 289-295

Hanna, A. M., and Abdel-Rahman, M. M. (1990). "Ultimate bearing capacity of triangular shell strip footings on sand." *J. Geotech. Engrg.*, ASCE, 116 (12), 1851-1863.

Harr, M. E. (1966). *Foundations of theoretical soil mechanics*. McGraw-Hill, New York.

He Chongzhang (1984) "Hollow conic shell foundation and calculation." *Proc. 5th Engrg. Mech. Div.*, Specialty Conf. in Engrg. Mech. in Civil Engrg., ASCE, University of Wyoming, Laramie, Wyoming, USA, 1, 535-538.

He Chongzhang (1984). "Rational calculation of conic shells." *Proc. 5th Engrg. Mech. Div.*, Specialty Conf. in Engrg. Mech. in Civil Engrg., ASCE, University of Wyoming, Laramie, Wyoming, USA, 1, 547-550.

He Chongzhang (1985). *Hollow conic shell foundation*. The Scientific Publisher, Beijing, China (in Chinese).

Huang-Yih (1984). "The theory of conical shell and its applications." *Proc. 5th Engrg. Mech. Div.*, Specialty Conf. in Engrg. Mech. in Civil Engrg., ASCE, University of Wyoming, Laramie, Wyoming, USA, 1, 539-542.

Iyer, T. S., and Rao, N. R. (1970). "Model studies on funicular shells as rafts on sands." *Proc. Symp. Shallow Foundations*, Bombay, India, 1, 149-156.

Jain, V. K., Nayak, G. C., and Jain, O. P. (1977). "General behaviour of conical shell foundation.", *Proc. 3rd Int. Symp. Soil Structure Interaction*, University of Roorkee, India, 2, 53-61.

Jumikis, A. R. (1987). *Foundation engineering*. Robert E. Krieger Publishing Company,

Malabar, Florida, USA.

- Kaimal, S. S. (1967). "Hypar footings for a housing project in India." *Bull. Int. Ass. Shell and Spatial Structures*, (32), 7-12.
- Kotoda, K., and Numakami, K. (1987). "Stabilizing effect of shell foundation." *Memoirs School of Science & Engineering, Waseda University, Waseda, Japan*, (51), 77-87.
- Kurian, N. P., and Varghese, P. C. (1969). Discussion of "Design and testing of cone and hypar footings," by D. L. Nicholls, and M. V. Izadi. *J. Soil Mechanics and Foundations Div., ASCE*, 95 (SM1), 415-416.
- Kurian, N. P., and Varghese, P. C. (1971). "Model studies on the elastic behaviour of hypar footings in sand." *Bull. Int. Ass. Shell and Spatial Structures*, (45), 35-40.
- Kurian, N. P. (1971). "Investigations on the structural performance of hyperbolic paraboloid shell footings on sand." *Indian Geotech. J.*, 1 (2), 202-206.
- Kurian, N. P., and Jeyachandran, S. R. (1972). "Model studies on the behaviour of sand under two and three dimensional shell foundations." *Indian Geotech. J.*, 2 (1), 79-90.
- Kurian, N. P., and Varghese, P. C. (1972). "The ultimate strength of reinforced concrete hyperbolic paraboloidal footings." *Indian Concrete J.*, 46 (12), 513-519.
- Kurian, N. P., and Varghese, P. C. (1973). "A simplified approach to the bending of umbrella shell, and single hypar and plate on elastic foundation." *Indian Concrete J.*, 47 (1), 30-33.
- Kurian, N. P. (1973). "Ultimate strength design of hyperbolic paraboloidal shell footings."

*Bull. Int. Ass. Shell and Spatial Structures*, (51), 71-77.

Kurian, N. P., and Shah, S. H. (1974). "A novel technique for the installation of precast hypar footings." *Bull. Int. Ass. Shell and Spatial Structures*, (56), 61-66.

Kurian, N. P., and Mohan, C. S. (1980). "Ultimate strength and behaviour of hypar shell foundations under vertical loads and moments." *Indian Geotech. J.*, 10 (4), 380-385.

Kurian, N. P., and Mohan, C. S. (1981). "Contact pressures under shell foundations." *Proc. 10th Int. Conf. Soil Mechanics and Foundation Engrg.*, Stockholm, Sweden, 2, 165-168.

Kurian, N. P. (1982). *Modern foundations: introduction to advanced techniques*. Tata McGraw-Hill Co., New Delhi, India.

Kurian, N. P. (1983). "Ultimate strength analysis of shell foundations." *Proc. Int. Workshop Soil Structure Interaction*, University of Roorkee, India, 1, 99-109.

Kurian, N. P., and Shah, S. H. (1984). "Economy of conical and inverted dome shell foundations." *J. Institution of Engineers*, (64), 281-286.

Kurian, N. P. (1994). "Behaviour of shell foundations under subsidence of core soil." *Proc. 13th Int. Conf. Soil Mechanics and Foundation Engrg.*, New Delhi, India, 2, 591-594.

Lambe, T. W., and Whitman, R. V. (1979). *Soil mechanics*. John Wiley & Sons.

Melerski, E. (1988). "Thin shell foundation resting on stochastic soil." *J. Structural Engrg.*, ASCE, 114 (12), 2692-2709.



- Minami, J. K. (1949) "Research on shell foundations. experiments, theory, design, construction, and applications." *Transactions of the Architectural Institute of Japan*, (39), 1-17.
- Nath, Y., and Jain, R. K. (1985). "Orthotropic annular Shells on elastic foundations." *J. Engrg. Mechanics*, ASCE, 111 (10), 1242-1256.
- Nicholls, R. L , and Izadi, M V. (1968). "Design and testing of cone and hypar footings" *J. Soil Mechanics and Foundations Div.*, ASCE, 94 (SM1), 47-72.
- Nikitin, N. V., and Travush, V. I. (1970). "Designing and investigations of foundation settlement of the Ostankino television tower." *Proc. Int. Ass. Shell and Spatial Structures, 3<sup>rd</sup> Meeting on Shell and Spatial Foundations of Tower and High Buildings*, Sopron, Hungary, 77-100.
- Paliwal, D. N., Sinha, S. N., and Choudhary, B. K. (1986). "Shallow spherical shells on Pasternak foundation." *J. Engrg. Mechanics*, ASCE, 112 (2), 175-182.
- Paliwal, D. N., and Sinha, S. N. (1986). "Static and dynamic behaviour of shallow spherical shells on Winkler foundation." *J. Thin-Walled Structures*, 4 (6), 411-422.
- Paliwal, D. N., and Rai, R. N. (1986). "Shallow spherical shell on Pasternak foundation subjected to elevated temperature." *J. Thin-Walled Structures*, 5 (5), 343-349.
- Pandian, N. S., and Ranganatham, B. V. (1970). "Hyperbolic paraboloidal shell foundations." *Proc. Symp. Shallow Foundations*, Bombay, India, 1, 142-148.
- Tam, H. K., and Woods, R. I. (1989). "A parametric study of Cam-Clay." *3<sup>rd</sup> Int. Symp. Numerical Models in Geomechanics (NUMOG III)*, Niagra Falls, Canada, 264-271.

Sharma, A. K. (1973) "Investigation of spherical shell foundation." *J. Soil Mechanics and Foundations Div.*, ASCE, 99 (SM6), 489-493.

Sharama, A. k. (1984). "Economy in shell foundations in soft soils." *West Indian J. of Engrg.*, 9 (2), 20-26.

Wang Chunxiao (1985). "Design and construction of M type shell structure foundation for spheroidal tank." *Proc. Int. Ass. Shell and Spatial Structures Int. Congress, Application of Shells in Engrg. Structures*, Moscow, USSR, 3, 390-403.

Yasuda, S., Hakuno, M., Nagase, H., Kobayashi, S., and Yoshida, T. (1994). "Effectiveness of top-shaped concrete blocks in preventing settlement of foundations in liquefied ground." *J. Japanese Society of Soil Mechanics and Foundation Engineering*, 34 (1), 65-76.

Zadroga, B. (1994). "Bearing capacity of shallow foundations on noncohesive soils." *J. Geotech. Engrg.*, ASCE, 120 (11), 1991-2008.

"Parisians lay an egg underground." (1964). *Engrg. News Record*, 24.

## APPENDIX I

Computer Program "*BC-Shell*"

```

CLS
LOCATE 1, 14: PRINT "*****"
LOCATE 2, 14: PRINT " * ULTIMATE BEARING CAPACITY OF SHELL FOUNDATION * "
LOCATE 3, 14: PRINT " * PROGRAM BC-Shell * "
LOCATE 4, 14: PRINT " * © Mohamed Abdel-Rahman 1995 * "
LOCATE 5, 14: PRINT "*****"
LOCATE 6, 14: INPUT " * Enter Total Width of Strip Footing (2b in meters) : ", w
LOCATE 7, 14: INPUT " * Enter Min Horizontal Shell Angle ( $\theta_1^\circ$ ; 0.0 if Flat) : ", theta1
LOCATE 8, 14: INPUT " * Enter Max Horizontal Shell Angle ( $\theta_2^\circ$ ) : ", theta2
LOCATE 9, 14: INPUT " * Enter Interval for Horizontal Shell Angle : ", acct
LOCATE 10, 14: INPUT " * Enter Depth of The Foundation Level ( $D_f$  in meters) : ", D
LOCATE 11, 14: INPUT " * Enter Min Unit Weight of Soil ( $\gamma_1$  in kN/m3) : ", gama1
LOCATE 12, 14: INPUT " * Enter Max Unit Weight of Soil ( $\gamma_2$  in kN/m3) : ", gama2
LOCATE 13, 14: INPUT " * Enter Interval for Unit Weight of Soil : ", accg
LOCATE 14, 14: INPUT " * Enter Min Soil Cohesion ( $c_1$  in kPa) : ", coh1
LOCATE 15, 14: INPUT " * Enter Max Soil Cohesion ( $c_2$  in kPa) : ", coh2
LOCATE 16, 14: INPUT " * Enter Interval for Soil Cohesion : ", accc
LOCATE 17, 14: INPUT " * Enter Min Angle of Soil Shearing Resistance ( $\phi_1^\circ$ ) : ", fi1
LOCATE 18, 14: INPUT " * Enter Max Angle of Soil Shearing Resistance ( $\phi_2^\circ$ ) : ", fi2
LOCATE 19, 14: INPUT " * Enter Interval for Angle of Soil Shearing Resistance : ", accf
LOCATE 20, 14: PRINT "*****"
OPEN "CIR out" FOR OUTPUT AS #3
CONST PI = 3.141593
IF D > 0! THEN EMB = 1 ELSE EMB = 0
b = w / 2
'w is the total width of the foundation
PRINT #3, "-----"
PRINT #3, " Fai Theta SR alfa xc zc Ro R L Nc Nq Ng qu Qut "
PRINT #3, "-----"
FOR i = fi1 TO fi2 STEP accf
fai = (i / 180) * PI
cst = (PI / 4) - (fai / 2)
cit = (PI / 4) + (fai / 2)
FOR j = theta1 TO theta2 STEP acct
th = (j / 180) * PI
'th is the horizontal shell angle; i.e. the vertical shell angle = PI - 2*th
'th for flat footing = 0 and the vertical angle = 180
*****
'Data for the geometry of footing
gamac = 20
a = .02
t = .04
Dt = .16
dbs = D - t - (b - a) * TAN(th)
dc = Dt - t - b * TAN(th)
*****
SR = (PI + 2 * th) / PI
alfa = fai + (SR - 1) * ((PI/4) - (2*fai/3))
alfi = alfa * 180 / PI
'SR is Shell Ratio and it lies between 1 and 2
'1 for flat footing and 2 for pile foundation
'alfa is the horizontal angle of the failure surface from the edge of the footing
'it varies from (fai) to (cit), i.e PI/4 + fai/2
*****

```

```

'Get the value of Ro which satisfies equilibrium: (Ro = Rof)
FOR gama = gama1 TO gama2 STEP accg
q = gama * na * D
FOR c = coh1 TO coh2 STEP accc
cbg = c / (b * gama)
R1 = 1
R2 = 9
accr = .01
FOR Ro = R1 TO R2 STEP accr
R = Ro * b
*****
D2b = D / w
db = D / b
Dbf = db + TAN(alfa)
Dbt = D + b * TAN(alfa)
H = Dbt + (R * (SIN(cit) - COS(cit)))
*****
xc = R * SIN(cit)
zc = -R * COS(cit) + b * TAN(alfa)
'R is the radius of the sliding circular failure surface
'xc and zc are the coordinates of the center of the circle
*****
'Constants to solve the shear stress equation:
C1 = (1 + SIN(fai))
C2 = SIN(cit) - COS(cit)
C3 = SIN(fai) * TAN(cit)
C4 = 1 + (4 * TAN(fai) ^ 2)
C5 = EXP(2 * cst * TAN(fai))
C6 = SIN(fai) * ((2 * TAN(fai) * SIN(cit)) - COS(cit))
C7 = (C2 * C3) + (C6 / C4)
C8 = (EXP(-2 * cst * TAN(fai))) * COS(cit)
C9 = (EXP(PI * TAN(fai)) * (TAN(cit) ^ 2)) + TAN(cit) - (2 * TAN(fai))
C10 = (PI / 4) + (COS(fai) / 2) - (SIN(fai) * TAN(fai))
C11 = -(SQR(2) * COS(fai / 2)) / SIN(fai)
C12 = (C3 * C5 * C8 * C9) / (C4 * SIN(fai))
C13 = ((C5 * C7 * C8 * C9) / (C4 * SIN(fai))) + (C10 / C4)
C14 = ((C1 * C5 * C8 * C9) / (C4 * SIN(fai))) + C11
C15 = (PI / 2) - 2 * SIN(cit) * COS(cit)
C16 = C13 - C2 * COS(cit) - (C15 / 2)
C17 = C12 - SIN(cit) - COS(cit)
C18 = C2 + C14
C19 = -2 * TAN(fai)
C20 = (1 / C19) * (EXP(cst * C19) - EXP(-cit * C19))
C21 = (-SIN(fai) / C4) * (SQR(2) * ((2 * TAN(fai) * SIN(fai / 2)) - COS(fai / 2)))
C22 = (C5 * C7 * C20) + C21
C23 = C3 * C5 * C20
C24 = C1 * C5 * C20
*****
'Weights of soil blocks and lever arms to calculate "MW":
W1 = (gama / 2) * (H ^ 2) * TAN(cit)
W2 = (gama / 2) * (b ^ 2) * TAN(alfa)
W3 = gama * Dbt * (R * SIN(cit) - b)
W4 = H * R * gama * COS(cit)
W5 = (gama / 2) * (R ^ 2) * (cit - SIN(cit) * COS(cit))

```

```

W6 = (gama / 2) * (R ^ 2) * (cst - SIN(cst) * COS(cst))
Wt = W1 + W2 + W3 + W4 + W5 + W6
'*****

x1 = ((H * TAN(cit)) / 3) + (R * COS(cit))
x2 = (R * SIN(cit)) - (2 * b / 3)
x3 = ((R * SIN(cit)) - b) / 2
x4 = (R * COS(cit)) / 2
x5a = 1 - ((3 / 2) * COS(cit)) + ((1 / 2) * (COS(cit) ^ 3))
x5b = cit - (SIN(cit) * COS(cit))
x5 = (2 / 3) * R * (x5a / x5b)
x6a = 1 - ((3 / 2) * COS(cst)) + ((1 / 2) * (COS(cst) ^ 3))
x6b = cst - (SIN(cst) * COS(cst))
x6 = (2 / 3) * R * (x6a / x6b)
'*****

Mwf1 = -gamac * a * dc * (R * SIN(cit) - (a / 2))
Mwf2 = -(gamac / 2) * a ^ 2 * TAN(th) * (R * SIN(cit) - (2 * a / 3))
Mwf3 = -gamac * t * b * (R * SIN(cit) - (b / 2))
Mws1 = -gama * (b - a) * dbs * (R * SIN(cit) - (a / 2) - (b / 2)) * EMB
Mws2 = -(gama / 2) * ((b - a) ^ 2) * TAN(th) * (R * SIN(cit) - (a / 3) - (2 * b / 3)) * EMB
Mwfs = Mwf1 + Mwf2 + Mwf3 + Mws1 + Mws2
'*****

MW = ((W4 * x4) + (W6 * x6)) - ((W2 * x2) + (W3 * x3) + (W5 * x5)) + Mwfs
'*****

'Horizontal Earth Pressure Eh and lever arms to calculate "ME"
Ec = 2 * c * H * TAN(cit)
Eg = ((gama / 2) * (H ^ 2) * (TAN(cit) ^ 2))
Eh = Ec + Eg
zec = R * SIN(cit) - (H / 2)
zeg = R * SIN(cit) - (H / 3)
ME = Ec * zec + Eg * zeg
'*****

'Shear stress Tao and Moment "MT" :
Tao1 = c * C1
Tao2 = C5 * (R * gama * C7 + gama * Dbt * C3 + c * C1)
'*****

'Shear Stress at plane part Taop:
Taop = gama * SIN(fai) * TAN(cit) * H + Tao1
'*****

'Shear Stress at circular part Taoc:
Taoc = Tao2 * EXP(-2 * cst * TAN(fai)) - (R * gama * C6 / C4)
MT = (R ^ 2) * Tao2 * C20 + (R ^ 3) * gama * C21
'*****

Cv = c * Dbt
Tpv = (gama / 2) * TAN(cit) * (H ^ 2) + c * H
Tcv = (gama * R * Dbt * C12) + (gama * (R ^ 2) * C13) + c * R * C14
'*****

'Different Values of "P":
Pv = (Tpv + Tcv - Wt - Cv)
Pvfg = gama * b ^ 2 * ((Ro ^ 2) * C16 + Ro * TAN(alfa) * C17 + (TAN(alfa) / 2))
Pvfq = gama * D * b * (Ro * C17 + 1)
Pvfc = c * b * Ro * C18
Pvf = Pvfg + Pvfq + Pvfc
'*****

qvg = gama * b * ((Ro ^ 2) * C16 + Ro * TAN(alfa) * C17 - (TAN(th) / 2))

```

```

quq = gama * D * (Ro * C17 + 1)
quc = c * (Ro * C18 + TAN(alfa))
qu = qug + quq + quc
Pvq = qu * b + (gama / 2) * b ^ 2 * (TAN(alfa) + TAN(th)) - c * b * TAN(alfa)
'PRINT Pv; Pvf, Pvq . . for check
'*****
'Note that the final Pv does not depends at all on theta
'*****
Ph = Pv * TAN(alfa - fai)
'Ph is the horizontal component
'*****
Mp1 = -qu * b * (R * SIN(cit) - (b / 2))?
Mp2 = -(gama / 2) * (b ^ 2) * (TAN(alfa) + TAN(th)) * ((R * SIN(cit)) - (b / 3))
Mp3 = c * b * ((TAN(alfa) * R * SIN(cit)) - R * COS(cit))
MP = Mp1 + Mp2 + Mp3
'*****
Mtot = MW + MT + ME + MP
'*****
'The factors required to calculate Ro
FRow3a = -(gama / (6 * SQR(2))) * (b ^ 3) * (4 - COS(fai)) * SIN(fai / 2)
FRow3b = (SQR(2) / 2) * gama * (b ^ 3) * SIN(fai / 2) * (SIN(cst) ^ 2)
FRow3 = FRow3a + FRow3b
'*****
FRot3 = gama * (b ^ 3) * C22
'*****
FRoe3a = Mf * (gama / 2) * (TAN(cit) ^ 2) * SIN(cit) * (b ^ 3) * (C2 ^ 2)
FRoe3b = -Mf * (gama / 6) * (TAN(cit) ^ 2) * (b ^ 3) * (C2 ^ 3)
FRoe3 = FRoe3a + FRoe3b
'*****
FRop3 = -(gama) * (b ^ 3) * SIN(cit) * C16
'*****
FRo3 = FRow3 + FRot3 + FRoe3 + FRop3
'*****
FRow2a = -(gama / 2) * (b ^ 2) * D * (SIN(cit) ^ 2) - (gama / 2) * (b ^ 3) * TAN(alfa) * (SIN(cit) ^ 2)
FRow2b = (gama / 2) * (b ^ 2) * D * (SIN(cst) ^ 2) + (gama / 2) * (b ^ 3) * TAN(alfa) * (SIN(cst) ^ 2)
FRow2 = FRow2a + FRow2b
'*****
FRot2a = gama * (b ^ 2) * Dbt * C23
'*****
FRot2b = c * (b ^ 2) * C24
FRot2 = FRot2a + FRot2b
'*****
FRoe2a = Mf * gama * (TAN(cit) ^ 2) * SIN(cit) * Dbt * (b ^ 2) * C2
FRoe2b = -Mf * (gama / 2) * (TAN(cit) ^ 2) * Dbt * (b ^ 2) * (C2 ^ 2)
FRoe2c = 2 * Mf * c * TAN(cit) * SIN(cit) * (b ^ 2) * C2
FRoe2d = -Mf * c * TAN(cit) * (b ^ 2) * (C2 ^ 2)
FRoe2 = FRoe2a + FRoe2b + FRoe2c + FRoe2d
'*****
FRop2a = -(gama) * (b ^ 3) * SIN(cit) * TAN(alfa) * C17
FRop2b = -(gama) * (b ^ 2) * D * SIN(cit) * C17
FRop2c = -c * (b ^ 2) * SIN(cit) * C18
FRop2d = (gama / 2) * (b ^ 3) * C16?
FRop2 = FRop2a + FRop2b + FRop2c + FRop2d
'*****

```

```

FRo2 = FRow2 + FRot2 + FRoe2 + FRop2
'*****
FRow1a = gama * (b ^ 2) * D * SIN(cit) + (gama / 2) * (b ^ 3) * TAN(alfa) * SIN(cit)
FRow1f = -gamac * b * SIN(cit) * (a * dc + (a ^ 2 / 2) * TAN(th) + b * t)
FRow1s = -gama * b * SIN(cit) * (b - a) * (dbs + ((b - a) * TAN(th) / 2)) * EMB
FRow1 = FRow1a + FRow1f + FRow1s
'*****
FRot1 = 0
'*****
FRoel1a = Mf * (gama / 2) * (TAN(cit) ^ 2) * SIN(cit) * b * (Dbt ^ 2)
FRoel1b = -Mf * (gama / 2) * (TAN(cit) ^ 2) * (Dbt ^ 2) * b * C2
FRoel1c = 2 * Mf * c * TAN(cit) * SIN(cit) * Dbt * b
FRoel1d = -2 * Mf * c * TAN(cit) * Dbt * b * C2
FRoel1 = FRoel1a + FRoel1b + FRoel1c + FRoel1d
'*****
FRop1a = gama * (b ^ 3) * SIN(cit) * TAN(th) / 2
FRop1b = -(gama) * (b ^ 2) * D * SIN(cit)
FRop1c = -c * (b ^ 2) * SIN(cit) * TAN(alfa)
FRop1d = (gama / 2) * (b ^ 3) * TAN(alfa) * C17
FRop1e = (gama / 2) * (b ^ 2) * D * C17
FRop1f = (c / 2) * (b ^ 2) * C18
FRop1g = -(gama / 2) * (b ^ 3) * SIN(cit) * TAN(alfa)
FRop1h = -(gama / 2) * (b ^ 3) * SIN(cit) * TAN(th)
FRop1i = c * (b ^ 2) * SIN(cit) * TAN(alfa)
FRop1j = -c * (b ^ 2) * COS(cit)
FRop1 = FRop1a + FRop1b + FRop1c + FRop1d + FRop1e + FRop1f + FRop1g + FRop1h +
FRop1i + FRop1j
'*****
FRo1 = FRow1 + FRot1 + FRoe1 + FRop1
'*****
FRow0a = -(gama / 6) * (b ^ 3) * TAN(alfa) - (gama / 2) * (b ^ 2) * D
FRow0f = gamac * ((a ^ 2 * dc / 2) + (a ^ 3 * TAN(th) / 3) + (b ^ 2 * t / 2))
FRow0s = gama * (b - a) * ((dbs * (a + b) / 2) + (TAN(th) * (b - a) * ((a / 2) + b) / 3)) * EMB
FRow0 = FRow0a + FRow0f + FRow0s
'*****
FRot0 = 0
'*****
FRoe0a = -Mf * (gama / 6) * (TAN(cit) ^ 2) * (Dbt ^ 3)
FRoe0b = -Mf * c * TAN(cit) * (Dbt ^ 2)
FRoe0 = FRoe0a + FRoe0b
'*****
FRop0a = -(gama / 4) * (b ^ 3) * TAN(th)
FRop0b = (gama / 2) * (b ^ 2) * D
FRop0c = (c / 2) * (b ^ 2) * TAN(alfa)
FRop0d = (gama / 6) * (b ^ 3) * TAN(alfa)
FRop0e = (gama / 6) * (b ^ 3) * TAN(th)
FRop0 = FRop0a + FRop0b + FRop0c + FRop0d + FRop0e
'*****
FRo0 = FRow0 + FRot0 + FRoe0 + FRop0
'*****
FRo = ((Ro ^ 3) * FRo3) + ((Ro ^ 2) * FRo2) + (Ro * FRo1) + FRo0
'PRINT , Ro, FRo, Mtot .. for check
'*****
FRod1 = 3 * (Ro ^ 2) * FRo3 + 2 * Ro * FRo2 + FRo1

```



```

DRo = -FRo / FRod1
Rof = Ro
IF ABS(DRo) < accr THEN GOTO Root
'*****
qufg = gama * b * ((Rof ^ 2) * C16 + Rof * TAN(alfa) * C17 - (TAN(th) / 2))
qufq = gama * D * (Rof * C17 + 1)
qufc = c * (Rof * C18 + TAN(alfa))
quf = qufg + qufq + qufc
Pvq = quf * b + (gama / 2) * b ^ 2 * (TAN(alfa) + TAN(th)) - c * b * TAN(alfa)
L = b * (Rof + Dbf * SIN(cit)) / COS(cit)
'*****
Ng = (Rof ^ 2) * C16 + Rof * TAN(alfa) * C17 - (TAN(th) / 2)
Nq = 1 + Rof * C17
Nc = Rof * C18 + TAN(alfa)
'*****
qux = c * Nc + D * gama * Nq + b * gama * Ng
Qut = qux * (w ^ 2)
'*****
NEXT Ro
'*****
GOTO jump
Root:
Rof = Ro
Rf = R
FRof = FRo
Mtotf = Mtot
GOTO Finish
'PRINT FRof, Mtotf .... for check
jump:
'*****
PRINT #3, "-----"
PRINT #3, "***NO SOLUTION** For : Fai =", i, " "; "Gama =", gama, " "; "cb/g =", cbg, " "; "Ro =",
R1; "To"; R2; "( acc = "; accr, ")"
PRINT #3, "-----"
'*****
GOTO Cont
Finish:
'*****
qufg = gama * b * ((Rof ^ 2) * C16 + Rof * TAN(alfa) * C17 - (TAN(th) / 2))
qufq = gama * D * (Rof * C17 + 1)
qufc = c * (Rof * C18 + TAN(alfa))
quf = qufg + qufq + qufc
'Fht = quf * b * TAN(th) - c * b
'PRINT Fht; Ph... for check
Pvq = quf * b + (gama / 2) * b ^ 2 * (TAN(alfa) + TAN(th)) - c * b * TAN(alfa)
L = b * (Rof + Dbf * SIN(cit)) / COS(cit)
'*****
Ng = (Rof ^ 2) * C16 + Rof * TAN(alfa) * C17 - (TAN(th) / 2)
Nq = 1 + Rof * C17
Nc = Rof * C18 + TAN(alfa)
'*****
qux = c * Nc + D * gama * Nq + b * gama * Ng
Qut = qux * (w ^ 2)
'*****

```

```

PRINT #3, USING "##### ##", i, j, SR; alfi; xc; zc; Rof; Rf; L; Nc; Nq; Ng; qux; Qut
'*****
Cont:
NEXT c
NEXT gama
NEXT j
NEXT i
Mxw = (Rof ^ 3) * FRow3 + (Rof ^ 2) * FRow2 + Rof * FRow1 + FRow0
Mxt = (Rof ^ 3) * FRot3 + (Rof ^ 2) * FRot2 + Rof * FRot1 + FRot0
Mxe = (Rof ^ 3) * FRoe3 + (Rof ^ 2) * FRoe2 + Rof * FRoe1 + FRoe0
Mxp = (Rof ^ 3) * FRop3 + (Rof ^ 2) * FRop2 + Rof * FRop1 + FRop0
Mtxt = Mxw + Mxt + Mxe + Mxp
'*****
'For check only
PRINT ; MW; Mxw
PRINT ; MT; Mxt
PRINT ; ME; Mxe
PRINT ; MP; Mxp
PRINT ; Mtotf; Mtxt; FRof
'*****
PRINT #3, "-----"
CLOSE #3
END
'*****

```

## APPENDIX II

### Design Tables for $N_c$ , $N_q$ & $N_\gamma$

$\phi^\circ$	$0^\circ$	$N_c$	$N_q$	$N_\gamma$	$N_c$	$N_q$	$N_\gamma$
		Embedment Ratio = 0.0			Embedment Ratio = 0.25		
10	0	6.56	2.13	0.88	7.47	2.29	1.12
	10	7.02	2.19	0.99	8.42	2.44	1.40
	20	7.54	2.27	1.12	9.36	2.59	1.72
	30	8.10	2.35	1.27	10.36	2.75	2.11
	40	8.67	2.44	1.44	11.41	2.92	2.56
	50	9.25	2.52	1.59	12.66	3.13	3.14
	60	9.89	2.62	1.70	14.21	3.38	3.90
11	0	7.12	2.35	1.14	8.06	2.53	1.43
	10	7.59	2.42	1.28	8.93	2.68	1.74
	20	8.07	2.50	1.43	9.85	2.85	2.11
	30	8.60	2.59	1.62	10.77	3.01	2.54
	40	9.13	2.67	1.81	11.80	3.19	3.05
	50	9.73	2.77	2.02	12.99	3.40	3.69
	60	10.38	2.88	2.20	14.48	3.67	4.54
12	0	7.66	2.58	1.42	8.62	2.79	1.77
	10	8.14	2.67	1.60	9.52	2.96	2.15
	20	8.63	2.76	1.80	10.36	3.12	2.56
	30	9.12	2.84	2.02	11.26	3.30	3.04
	40	9.67	2.94	2.27	12.27	3.49	3.63
	50	10.27	3.05	2.53	13.38	3.71	4.32
	60	10.89	3.16	2.76	14.82	3.99	5.25
13	0	8.22	2.84	1.76	9.27	3.09	2.20
	10	8.72	2.94	1.99	10.08	3.26	2.61
	20	9.16	3.03	2.21	10.95	3.44	3.10
	30	9.72	3.14	2.51	11.82	3.62	3.64
	40	10.23	3.23	2.79	12.75	3.82	4.27
	50	10.80	3.34	3.09	13.85	4.05	5.04
	60	11.43	3.46	3.39	15.22	4.34	6.05
14	0	8.82	3.14	2.16	9.96	3.42	2.70
	10	9.33	3.24	2.44	10.74	3.60	3.16
	20	9.78	3.34	2.72	11.57	3.79	3.71
	30	10.30	3.45	3.04	12.42	3.97	4.32
	40	10.82	3.56	3.38	13.32	4.18	5.01
	50	11.41	3.68	3.76	14.39	4.42	5.88
	60	12.00	3.80	4.10	15.69	4.72	6.96
15	0	9.50	3.47	2.66	10.62	3.77	3.26
	10	9.97	3.58	2.97	11.43	3.97	3.81
	20	10.44	3.68	3.30	12.23	4.16	4.42
	30	10.97	3.80	3.69	13.04	4.36	5.09
	40	11.45	3.91	4.06	13.91	4.57	5.85
	50	12.05	4.04	4.52	14.96	4.82	6.81
	60	12.66	4.18	4.95	16.24	5.14	8.00

$\phi^\circ$	$\theta^\circ$	$N_c$	$N_q$	$N_\gamma$	$N_c$	$N_q$	$N_\gamma$
16	0	10.17	3.83	3.22	11.39	4.18	3.94
	10	10.65	3.95	3.58	12.15	4.38	4.55
	20	11.13	4.07	3.97	12.92	4.58	5.22
	30	11.62	4.18	4.40	13.70	4.78	5.95
	40	12.17	4.32	4.88	14.60	5.01	6.83
	50	12.73	4.45	5.38	15.62	5.28	7.88
	60	13.35	4.60	5.91	16.82	5.59	9.15
17	0	10.94	4.25	3.90	12.19	4.63	4.75
	10	11.37	4.36	4.29	12.92	4.84	5.41
	20	11.87	4.49	4.75	13.72	5.05	6.19
	30	12.37	4.62	5.25	14.46	5.26	6.98
	40	12.93	4.76	5.82	15.32	5.49	7.94
	50	13.44	4.89	6.36	16.31	5.77	9.08
	60	14.09	5.05	6.99	17.55	6.11	10.54
18	0	11.69	4.69	4.66	13.05	5.13	5.68
	10	12.20	4.83	5.16	13.80	5.36	6.45
	20	12.64	4.95	5.65	14.50	5.56	7.24
	30	13.16	5.09	6.23	15.32	5.80	8.20
	40	13.67	5.23	6.84	16.15	6.04	9.24
	50	14.26	5.40	7.53	17.10	6.32	10.49
	60	14.86	5.56	8.22	18.26	6.66	12.00
19	0	12.55	5.20	5.58	13.96	5.69	6.76
	10	13.01	5.34	6.12	14.67	5.91	7.59
	20	13.53	5.49	6.74	15.45	6.15	8.56
	30	14.06	5.64	7.41	16.17	6.37	9.53
	40	14.59	5.80	8.13	17.02	6.63	10.72
	50	15.13	5.95	8.87	17.95	6.92	12.06
	60	15.75	6.13	9.68	19.14	7.29	13.79
20	0	13.47	5.77	6.66	14.99	6.32	8.07
	10	13.94	5.91	7.28	15.66	6.54	8.97
	20	14.47	6.08	8.00	16.39	6.78	10.00
	30	14.95	6.23	8.71	17.13	7.02	11.11
	40	15.50	6.40	9.53	17.95	7.29	12.39
	50	16.06	6.56	10.39	18.90	7.60	13.91
	60	16.69	6.76	11.33	20.06	7.98	15.79
21	0	14.51	6.42	7.97	16.09	7.03	9.60
	10	14.99	6.58	8.69	16.77	7.26	10.63
	20	15.48	6.74	9.45	17.47	7.50	11.73
	30	15.97	6.90	10.27	18.23	7.76	13.00
	40	16.53	7.08	11.21	19.00	8.03	14.36
	50	17.11	7.26	12.20	19.92	8.34	16.00
	60	17.69	7.45	13.21	21.05	8.74	18.02
22	0	15.55	7.12	9.43	17.18	7.78	11.28
	10	16.05	7.29	10.25	17.89	8.04	12.46

$\phi^\circ$	$\theta^\circ$	$N_c$	$N_q$	$N_\gamma$	$N_c$	$N_q$	$N_\gamma$
	20	16.55	7.46	11.13	18.61	8.30	13.71
	30	17.05	7.64	12.06	19.33	8.56	15.06
	40	17.64	7.84	13.14	20.12	8.84	16.60
	50	18.23	8.04	14.28	21.07	9.19	18.46
	60	18.83	8.24	15.44	22.17	9.59	20.64
23	0	16.73	7.92	11.20	18.50	8.67	13.41
	10	17.24	8.11	12.14	19.16	8.92	14.66
	20	17.76	8.30	13.15	19.83	9.18	15.99
	30	18.28	8.49	14.22	20.57	9.46	17.51
	40	18.81	8.67	15.35	21.39	9.77	19.26
	50	19.42	8.89	16.65	22.30	10.11	21.24
	60	20.04	9.11	17.99	23.43	10.55	23.71
24	0	18.00	8.81	13.26	19.84	9.63	15.78
	10	18.53	9.02	14.33	20.52	9.91	17.19
	20	19.06	9.22	15.48	21.21	10.18	18.70
	30	19.60	9.43	16.70	21.97	10.49	20.44
	40	20.14	9.63	17.99	22.75	10.79	22.29
	50	20.77	9.87	19.48	23.68	11.17	24.53
	60	21.41	10.11	21.02	24.78	11.61	27.18
25	0	19.43	9.84	15.75	21.35	10.74	18.63
	10	19.90	10.03	16.87	22.05	11.03	20.25
	20	20.45	10.25	18.17	22.76	11.33	21.97
	30	21.01	10.48	19.56	23.48	11.63	23.79
	40	21.57	10.70	21.03	24.28	11.96	25.89
	50	22.22	10.96	22.73	25.17	12.33	28.27
	60	22.88	11.22	24.49	26.30	12.82	31.26
26	0	20.97	10.99	18.66	22.96	11.96	21.94
	10	21.45	11.19	19.93	23.69	12.29	23.78
	20	22.02	11.44	21.42	24.35	12.57	25.57
	30	22.52	11.64	22.85	25.09	12.89	27.64
	40	23.18	11.92	24.68	25.92	13.26	30.01
	50	23.77	12.16	26.45	26.84	13.66	32.70
	60	24.45	12.45	28.46	27.93	14.15	35.90
27	0	22.63	12.27	22.04	24.79	13.37	25.94
	10	23.13	12.49	23.49	25.46	13.68	27.86
	20	23.72	12.75	25.18	26.14	13.99	29.89
	30	24.23	12.97	26.81	26.90	14.34	32.23
	40	24.83	13.24	28.71	27.68	14.69	34.72
	50	25.52	13.55	30.90	28.63	15.13	37.75
	60	26.23	13.85	33.19	29.68	15.61	41.16
28	0	24.50	13.74	26.14	26.75	14.94	30.58
	10	25.02	13.98	27.78	27.45	15.28	32.76
	20	25.54	14.22	29.53	28.15	15.61	35.07
	30	26.16	14.51	31.57	28.86	15.95	37.52

$\phi^\circ$	$\theta^\circ$	$N_c$	$N_q$	$N_\gamma$	$N_c$	$N_q$	$N_\gamma$
	40	26.78	14.80	33.73	29.66	16.33	40.33
	50	27.41	15.08	36.02	30.56	16.76	43.53
	60	28.14	15.42	38.63	31.74	17.34	47.61
29	0	26.52	15.39	30.91	28.96	16.75	36.18
	10	27.06	15.65	32.79	29.60	17.06	38.45
	20	27.69	15.97	34.98	30.33	17.43	41.06
	30	28.24	16.23	37.09	31.06	17.79	43.83
	40	28.89	16.54	39.54	31.90	18.21	47.01
	50	29.54	16.85	42.14	32.83	18.68	50.63
	60	30.30	17.22	45.11	33.87	19.20	54.72
30	0	28.80	17.30	36.70	31.36	18.77	42.72
	10	29.36	17.58	38.83	32.02	19.11	45.29
	20	29.92	17.86	41.09	32.68	19.45	48.00
	30	30.49	18.15	43.48	33.44	19.85	51.13
	40	31.16	18.49	46.27	34.31	20.30	54.72
	50	31.84	18.83	49.22	35.19	20.76	58.53
	60	32.63	19.23	52.59	36.37	21.38	63.43
31	0	31.28	19.43	43.46	33.95	21.04	50.33
	10	31.86	19.74	45.89	34.64	21.41	53.24
	20	32.44	20.05	48.46	35.33	21.78	56.32
	30	33.14	20.42	51.46	36.12	22.22	59.87
	40	33.73	20.73	54.34	36.92	22.65	63.62
	50	34.44	21.10	57.69	37.94	23.21	68.24
	60	35.26	21.54	61.53	39.07	23.82	73.46
32	0	34.07	21.90	51.66	36.88	23.65	59.51
	10	34.68	22.24	54.44	37.59	24.06	62.82
	20	35.29	22.58	57.36	38.31	24.46	66.31
	30	35.90	22.91	60.45	39.14	24.94	70.34
	40	36.63	23.32	64.05	39.98	25.41	74.60
	50	37.37	23.72	67.86	40.93	25.95	79.47
	60	38.11	24.13	71.88	42.00	26.55	84.99
33	0	37.23	24.76	61.62	40.18	26.67	70.60
	10	37.75	25.05	64.45	40.81	27.04	74.01
	20	38.39	25.42	67.77	41.56	27.48	77.97
	30	39.03	25.79	71.29	42.43	27.99	82.54
	40	39.79	26.23	75.38	43.19	28.44	86.96
	50	40.56	26.67	79.71	44.18	29.02	92.47
	60	41.33	27.11	84.27	45.41	29.76	99.14
34	0	40.69	27.99	73.34	43.78	30.08	83.62
	10	41.23	28.31	76.57	44.56	30.56	87.91
	20	41.89	28.71	80.36	45.23	30.96	92.00
	30	42.56	29.11	84.36	46.02	31.44	96.75
	40	43.36	29.59	89.02	46.93	32.00	102.21
	50	44.04	30.00	93.51	47.85	32.57	108.00

$\phi^\circ$	$\theta^\circ$	$N_c$	$N_q$	$N_\gamma$	$N_c$	$N_q$	$N_\gamma$
	60	44.85	30.48	98.70	49.14	33.37	115.55
35	0	44.59	31.73	87.59	47.85	34.02	99.37
	10	45.16	32.08	91.27	48.54	34.46	103.79
	20	45.85	32.52	95.61	49.37	34.98	108.92
	30	46.55	32.96	100.18	50.19	35.51	114.33
	40	47.26	33.40	105.00	51.02	36.04	120.03
	50	48.10	33.93	110.60	51.99	36.65	126.59
	60	48.95	34.46	116.52	53.21	37.44	134.60
36	0	48.88	35.99	104.42	52.32	38.49	117.93
	10	49.48	36.37	108.63	53.18	39.06	123.51
	20	50.21	36.85	113.58	53.91	39.54	128.81
	30	50.94	37.33	118.79	54.78	40.12	134.96
	40	51.68	37.81	124.29	55.65	40.70	141.45
	50	52.56	38.39	130.67	56.66	41.37	148.90
	60	53.45	38.97	137.41	57.81	42.14	157.39
37	0	53.75	40.93	124.91	57.52	43.78	141.05
	10	54.51	41.46	130.32	58.29	44.31	146.81
	20	55.14	41.88	135.39	59.05	44.83	152.86
	30	55.91	42.41	141.34	59.96	45.46	159.87
	40	56.69	42.94	147.63	60.88	46.10	167.26
	50	57.47	43.46	154.26	61.81	46.73	175.06
	60	58.40	44.09	161.94	63.02	47.57	184.70
38	0	59.27	46.70	149.90	63.27	49.82	168.49
	10	60.08	47.28	156.10	64.08	50.40	175.09
	20	60.74	47.74	161.91	64.88	50.98	182.00
	30	61.55	48.32	168.74	65.70	51.56	189.26
	40	62.37	48.90	175.93	66.66	52.25	197.68
	50	63.19	49.48	183.52	67.64	52.95	206.56
	60	64.17	50.17	192.30	68.91	53.87	217.54
39	0	65.56	53.43	180.45	69.80	56.87	201.91
	10	66.25	53.94	186.79	70.49	57.38	208.65
	20	67.10	54.58	194.25	71.35	58.01	216.56
	30	67.80	55.09	201.26	72.20	58.65	224.86
	40	68.67	55.72	209.49	73.22	59.41	234.47
	50	69.54	56.36	218.17	74.25	60.18	244.60
	60	70.57	57.12	228.21	75.60	61.20	257.14
40	0	72.72	61.32	217.88	77.07	64.96	241.78
	10	73.45	61.88	225.19	77.97	65.66	250.47
	20	74.19	62.44	232.85	78.70	66.23	258.57
	30	75.09	63.14	241.84	79.61	66.93	268.08
	40	75.84	63.70	250.33	80.69	67.77	279.09
	50	76.76	64.40	260.28	81.77	68.61	290.68
	60	77.85	65.24	271.78	83.03	69.59	303.95



$\phi^\circ$	$\theta^\circ$	$N_c$	$N_q$	$N_\gamma$	$N_c$	$N_q$	$N_\gamma$
41	0	80.72	70.42	262.82	85.54	74.60	291.60
	10	81.50	71.04	271.24	86.31	75.22	300.50
	20	82.28	71.66	280.06	87.27	75.99	310.94
	30	83.24	72.43	290.41	88.05	76.61	320.73
	40	84.21	73.21	301.28	89.20	77.54	333.37
	50	85.00	73.83	311.59	90.35	78.47	346.65
	60	86.16	74.75	324.80	91.51	79.40	360.64
42	0	90.08	81.30	319.29	95.03	85.76	351.51
	10	90.90	81.98	329.04	95.86	86.44	361.77
	20	91.73	82.67	339.24	96.88	87.30	373.81
	30	92.56	83.36	349.93	97.71	87.99	385.07
	40	93.59	84.21	362.46	98.74	88.85	398.25
	50	94.44	84.90	374.32	99.96	89.88	413.50
	60	95.67	85.93	389.52	101.38	91.08	430.94
43	0	100.62	93.96	387.64	105.93	98.91	425.18
	10	101.50	94.72	398.94	106.81	99.67	437.04
	20	102.38	95.48	410.74	107.69	100.44	449.43
	30	103.27	96.25	423.09	108.78	101.39	463.94
	40	104.16	97.01	436.07	109.88	102.34	479.14
	50	105.26	97.96	451.25	110.98	103.29	495.11
	60	106.37	98.91	467.23	112.29	104.44	513.54
44	0	112.98	109.17	473.87	118.47	114.48	516.09
	10	113.70	109.81	485.34	119.41	115.32	529.84
	20	114.65	110.66	499.03	120.36	116.17	544.18
	30	115.59	111.51	513.35	121.30	117.02	559.18
	40	116.54	112.36	528.37	122.48	118.08	576.73
	50	117.72	113.42	545.94	123.65	119.14	595.14
	60	118.91	114.48	564.41	125.06	120.42	616.38
45	0	127.04	127.04	579.17	132.96	132.96	628.69
	10	127.81	127.75	592.52	133.97	133.91	644.67
	20	128.82	128.70	608.45	134.98	134.86	661.33
	30	129.84	129.65	625.09	136.00	135.81	678.72
	40	130.86	130.59	642.52	137.02	136.75	696.94
	50	132.12	131.78	662.91	138.28	137.94	718.23
	60	133.15	132.73	682.20	139.79	139.36	742.78
46	0	143.35	148.37	710.43	149.76	155.01	768.69
	10	144.44	149.44	728.31	150.85	156.07	787.33
	20	145.27	150.23	744.59	151.68	156.87	804.30
	30	146.36	151.29	763.99	152.77	157.93	824.51
	40	147.46	152.36	784.29	153.87	158.99	845.64
	50	148.56	153.42	805.57	155.23	160.32	870.34
	60	149.93	154.75	830.41	156.85	161.92	898.80
47	0	162.64	174.26	877.41	169.33	181.43	943.51
	10	163.54	175.16	895.67	170.22	182.33	962.49

$\phi^\circ$	$\theta^\circ$	$N_c$	$N_q$	$N_\gamma$	$N_c$	$N_q$	$N_\gamma$
	20	164.43	176.05	914.70	171.40	183.52	985.14
	30	165.62	177.25	937.39	172.30	184.42	1005.83
	40	166.80	178.44	961.09	173.76	185.91	1033.37
	50	167.99	179.64	985.90	174.96	187.11	1059.17
	60	169.19	180.83	1011.93	176.43	188.60	1089.25
48	0	184.93	205.15	1084.45	192.22	213.25	1162.85
	10	185.90	206.16	1105.90	193.19	214.26	1185.10
	20	186.87	207.17	1128.23	194.16	215.27	1208.27
	30	188.15	208.52	1154.85	195.44	216.62	1235.86
	40	189.13	209.53	1179.25	196.42	217.63	1261.17
	50	190.42	210.88	1208.24	198.02	219.32	1294.73
	60	191.72	212.23	1238.60	199.31	220.67	1326.24
49	0	211.15	242.57	1346.02	218.80	251.38	1435.44
	10	212.20	243.72	1371.31	219.86	252.53	1461.60
	20	213.26	244.87	1397.60	220.92	253.68	1488.79
	30	214.66	246.40	1428.94	222.31	255.21	1521.19
	40	215.72	247.55	1457.59	223.38	256.36	1550.81
	50	217.13	249.08	1491.61	224.78	257.89	1585.98
	60	218.54	250.61	1527.19	226.53	259.80	1626.97
50	0	242.53	288.62	1682.84	250.59	298.22	1785.25
	10	243.69	289.93	1712.80	251.75	299.53	1816.16
	20	244.85	291.24	1743.91	252.90	300.84	1848.25
	30	246.01	292.55	1776.28	254.07	302.15	1881.63
	40	247.18	293.86	1810.03	255.23	303.46	1916.44
	50	248.35	295.17	1845.30	256.77	305.21	1957.76
	60	249.89	296.91	1887.09	258.31	306.95	2000.88
		Embedment Ratio = 0.50			Embedment Ratio = 0.75		
10	0	8.29	2.43	1.36	8.82	2.52	1.53
	10	9.09	2.56	1.62	9.67	2.66	1.82
	20	9.99	2.70	1.95	10.51	2.79	2.16
	30	10.94	2.85	2.35	11.46	2.95	2.58
	40	11.94	3.02	2.81	12.47	3.11	3.06
	50	13.14	3.21	3.39	13.67	3.30	3.67
	60	14.69	3.46	4.18	15.22	3.56	4.50
11	0	8.85	2.68	1.69	9.49	2.81	1.93
	10	9.67	2.83	2.02	10.26	2.94	2.26
	20	10.49	2.97	2.39	11.09	3.09	2.65
	30	11.42	3.13	2.84	11.96	3.24	3.11
	40	12.40	3.31	3.37	12.89	3.40	3.64
	50	13.53	3.51	4.01	14.03	3.61	4.31
	60	14.93	3.76	4.83	15.47	3.87	5.19
12	0	9.49	2.97	2.11	10.15	3.11	2.39
	10	10.28	3.12	2.49	10.89	3.25	2.77

$\phi^\circ$	$\theta^\circ$	$N_c$	$N_q$	$N_\gamma$	$N_c$	$N_q$	$N_\gamma$
	20	11.07	3.28	2.91	11.69	3.41	3.22
	30	11.92	3.44	3.40	12.48	3.56	3.71
	40	12.88	3.62	3.99	13.39	3.73	4.30
	50	13.95	3.83	4.69	14.45	3.94	5.03
	60	15.33	4.10	5.61	15.84	4.21	5.99
13	0	10.17	3.29	2.60	10.90	3.46	2.96
	10	10.93	3.45	3.03	11.61	3.61	3.39
	20	11.69	3.61	3.50	12.32	3.76	3.86
	30	12.51	3.78	4.05	13.09	3.91	4.41
	40	13.38	3.96	4.68	13.96	4.09	5.07
	50	14.43	4.18	5.46	14.95	4.30	5.85
	60	15.74	4.46	6.47	16.27	4.58	6.89
14	0	10.88	3.65	3.17	11.64	3.84	3.59
	10	11.60	3.81	3.65	12.31	3.99	4.07
	20	12.33	3.97	4.18	13.04	4.15	4.64
	30	13.12	4.15	4.79	13.77	4.31	5.24
	40	14.02	4.35	5.53	14.57	4.49	5.93
	50	14.99	4.57	6.35	15.53	4.70	6.79
	60	16.23	4.85	7.43	16.77	4.99	7.92
15	0	11.63	4.04	3.84	12.47	4.27	4.37
	10	12.32	4.21	4.37	13.11	4.42	4.90
	20	13.07	4.39	4.99	13.74	4.57	5.48
	30	13.83	4.57	5.67	14.50	4.75	6.19
	40	14.64	4.76	6.43	15.26	4.93	6.94
	50	15.63	5.00	7.39	16.19	5.15	7.89
	60	16.80	5.29	8.54	17.36	5.44	9.08
16	0	12.43	4.48	4.63	13.29	4.73	5.23
	10	13.14	4.66	5.25	13.95	4.90	5.86
	20	13.79	4.83	5.88	14.60	5.06	6.53
	30	14.57	5.03	6.66	15.26	5.23	7.26
	40	15.35	5.23	7.50	16.04	5.43	8.13
	50	16.31	5.48	8.54	16.89	5.64	9.11
	60	17.46	5.77	9.81	18.03	5.94	10.42
17	0	13.27	4.96	5.53	14.17	5.24	6.24
	10	13.94	5.15	6.21	14.84	5.42	6.96
	20	14.61	5.33	6.94	15.45	5.58	7.69
	30	15.35	5.53	7.79	16.13	5.77	8.52
	40	16.16	5.75	8.75	16.87	5.97	9.47
	50	17.09	6.00	9.89	17.68	6.19	10.53
	60	18.21	6.31	11.28	18.80	6.50	11.97
18	0	14.22	5.52	6.64	15.15	5.82	7.45
	10	14.85	5.70	7.37	15.78	6.00	8.23
	20	15.55	5.90	8.22	16.35	6.16	9.00
	30	16.24	6.10	9.13	17.05	6.36	9.96

$\phi^\circ$	$\theta^\circ$	$N_c$	$N_q$	$N_\gamma$	$N_c$	$N_q$	$N_\gamma$
	40	17.01	6.32	10.16	17.75	6.56	10.98
	50	17.91	6.58	11.40	18.59	6.80	12.20
	60	19.00	6.90	12.91	19.68	7.12	13.77
19	0	15.17	6.11	7.86	16.19	6.46	8.85
	10	15.82	6.30	8.70	16.78	6.63	9.68
	20	16.47	6.50	9.61	17.36	6.81	10.58
	30	17.19	6.72	10.65	18.02	7.01	11.60
	40	17.92	6.94	11.76	18.75	7.23	12.76
	50	18.84	7.23	13.17	19.54	7.47	14.07
	60	19.90	7.56	14.81	20.61	7.80	15.78
20	0	16.25	6.78	9.34	17.31	7.17	10.47
	10	16.85	6.97	10.23	17.91	7.36	11.43
	20	17.52	7.19	11.27	18.44	7.53	12.37
	30	18.19	7.41	12.38	19.12	7.74	13.54
	40	18.94	7.65	13.64	19.80	7.96	14.78
	50	19.83	7.94	15.16	20.62	8.23	16.27
	60	20.92	8.30	17.03	21.65	8.56	18.12
21	0	17.39	7.53	11.05	18.49	7.95	12.35
	10	18.01	7.74	12.08	19.11	8.16	13.44
	20	18.63	7.95	13.17	19.66	8.34	14.51
	30	19.33	8.19	14.44	20.29	8.55	15.75
	40	20.10	8.45	15.88	20.99	8.79	17.16
	50	20.95	8.74	17.50	21.77	9.05	18.75
	60	22.01	9.11	19.52	22.76	9.40	20.74
22	0	18.61	8.35	13.02	19.82	8.84	14.60
	10	19.25	8.58	14.20	20.38	9.04	15.75
	20	19.89	8.81	15.45	20.96	9.24	16.97
	30	20.54	9.04	16.78	21.53	9.45	18.27
	40	21.26	9.30	18.31	22.26	9.70	19.87
	50	22.14	9.62	20.15	22.99	9.96	21.55
	60	23.16	9.99	22.32	24.02	10.34	23.81
23	0	19.98	9.30	15.40	21.23	9.83	17.20
	10	20.57	9.52	16.64	21.75	10.02	18.40
	20	21.16	9.74	17.95	22.34	10.24	19.79
	30	21.82	9.99	19.46	22.93	10.46	21.26
	40	22.57	10.27	21.18	23.61	10.71	22.94
	50	23.40	10.58	23.14	24.36	10.99	24.85
	60	24.46	10.99	25.59	25.35	11.37	27.26
24	0	21.37	10.32	18.04	22.75	10.93	20.21
	10	21.98	10.56	19.44	23.28	11.14	21.57
	20	22.66	10.83	21.06	23.89	11.37	23.15
	30	23.28	11.07	22.64	24.43	11.58	24.67
	40	24.05	11.37	24.60	25.12	11.85	26.58
	50	24.91	11.72	26.81	25.91	12.16	28.74

$\phi^\circ$	$0^\circ$	$N_c$	$N_q$	$N_\gamma$	$N_c$	$N_q$	$N_\gamma$
	60	25.93	12.13	29.44	26.85	12.53	31.32
25	0	22.94	11.48	21.21	24.37	12.15	23.68
	10	23.57	11.74	22.81	24.92	12.37	25.22
	20	24.20	12.00	24.49	25.47	12.59	26.85
	30	24.91	12.30	26.43	26.11	12.85	28.74
	40	25.63	12.59	28.49	26.75	13.11	30.73
	50	26.44	12.93	30.84	27.56	13.45	33.17
	60	27.50	13.37	33.81	28.53	13.86	36.08
26	0	24.70	12.81	25.03	26.20	13.54	27.83
	10	25.35	13.09	26.84	26.76	13.78	29.59
	20	25.92	13.34	28.60	27.33	14.02	31.44
	30	26.58	13.62	30.62	27.91	14.27	33.39
	40	27.33	13.94	32.94	28.57	14.55	35.64
	50	28.17	14.31	35.59	29.33	14.87	38.21
	60	29.18	14.75	38.75	30.34	15.32	41.50
27	0	26.60	14.29	29.45	28.16	15.09	32.64
	10	27.19	14.56	31.33	28.74	15.35	34.63
	20	27.86	14.87	33.50	29.33	15.61	36.72
	30	28.55	15.17	35.79	29.93	15.88	38.93
	40	29.23	15.48	38.23	30.53	16.14	41.27
	50	30.10	15.88	41.21	31.31	16.50	44.17
	60	31.07	16.32	44.57	32.28	16.94	47.66
28	0	28.64	15.95	34.58	30.36	16.86	38.41
	10	29.25	16.23	36.71	30.87	17.10	40.44
	20	29.95	16.57	39.16	31.49	17.38	42.81
	30	30.57	16.86	41.54	32.10	17.67	45.31
	40	31.28	17.19	44.28	32.73	17.96	47.95
	50	32.19	17.62	47.65	33.54	18.34	51.22
	60	33.19	18.10	51.44	34.45	18.77	54.92
29	0	30.94	17.84	40.74	32.73	18.83	45.10
	10	31.57	18.16	43.15	33.27	19.09	47.40
	20	32.21	18.47	45.70	33.81	19.36	49.83
	30	32.85	18.78	48.39	34.45	19.67	52.65
	40	33.59	19.15	51.49	35.09	19.98	55.62
	50	34.43	19.56	55.03	35.94	20.40	59.32
	60	35.47	20.09	59.30	36.88	20.87	63.49
30	0	33.42	19.96	47.91	35.29	21.04	52.85
	10	34.08	20.30	50.64	35.85	21.33	55.46
	20	34.74	20.65	53.52	36.51	21.67	58.48
	30	35.41	20.99	56.56	37.08	21.95	61.38
	40	36.18	21.38	60.06	37.75	22.29	64.75
	50	36.96	21.78	63.77	38.53	22.69	68.61
	60	38.04	22.35	68.60	39.51	23.20	73.31

$\phi^\circ$	$\theta^\circ$	$N_c$	$N_q$	$N_\gamma$	$N_c$	$N_q$	$N_\gamma$
31	0	36.22	22.40	56.52	38.17	23.58	62.15
	10	36.90	22.77	59.62	38.76	23.89	65.10
	20	37.49	23.08	62.58	39.34	24.19	68.21
	30	38.18	23.45	66.02	40.03	24.57	71.81
	40	38.98	23.89	69.98	40.73	24.94	75.61
	50	39.79	24.32	74.17	41.44	25.31	79.63
	60	40.82	24.88	79.27	42.46	25.86	84.94
32	0	39.25	25.14	66.57	41.41	26.49	73.32
	10	39.97	25.54	70.08	42.02	26.82	76.67
	20	40.58	25.88	73.44	42.63	27.16	80.19
	30	41.30	26.28	77.33	43.24	27.50	83.90
	40	42.03	26.69	81.44	43.86	27.83	87.82
	50	42.98	27.23	86.55	44.71	28.31	92.74
	60	43.94	27.77	91.94	45.67	28.85	98.34
33	0	42.67	28.29	78.66	44.94	29.76	86.36
	10	43.30	28.66	82.27	45.57	30.13	90.16
	20	44.05	29.10	86.47	46.09	30.42	93.74
	30	44.69	29.47	90.48	46.73	30.79	97.93
	40	45.45	29.91	95.13	47.49	31.23	102.78
	50	46.33	30.42	100.48	48.26	31.67	107.91
	60	47.45	31.08	107.00	49.26	32.26	114.23
34	0	46.52	31.92	93.25	48.90	33.53	102.05
	10	47.18	32.33	97.36	49.44	33.85	105.91
	20	47.85	32.73	101.68	50.11	34.25	110.42
	30	48.52	33.13	106.23	50.78	34.66	115.17
	40	49.31	33.61	111.50	51.45	35.06	120.19
	50	50.23	34.17	117.56	52.26	35.54	125.99
	60	51.28	34.82	124.45	53.30	36.18	133.15
35	0	50.74	36.04	110.39	53.25	37.79	120.45
	10	51.43	36.48	115.07	53.81	38.14	124.82
	20	52.12	36.91	119.98	54.51	38.58	129.94
	30	52.83	37.35	125.14	55.08	38.93	134.79
	40	53.66	37.88	131.12	55.91	39.46	141.01
	50	54.50	38.41	137.45	56.75	39.99	147.59
	60	55.59	39.11	145.25	57.73	40.60	155.11
36	0	55.36	40.70	130.55	58.14	42.72	142.62
	10	56.09	41.18	135.86	58.74	43.10	147.59
	20	56.82	41.66	141.44	59.33	43.48	152.81
	30	57.56	42.14	147.30	60.07	43.97	158.92
	40	58.43	42.72	154.10	60.81	44.45	165.35
	50	59.31	43.29	161.27	61.69	45.02	172.80
	60	60.46	44.06	170.13	62.71	45.70	181.33
37	0	60.74	46.20	155.55	63.54	48.31	168.73
	10	61.36	46.62	160.96	64.16	48.73	174.38

$\phi^\circ$	$0^\circ$	$N_c$	$N_q$	$N_r$	$N_c$	$N_q$	$N_r$
	20	62.13	47.15	167.31	64.93	49.26	181.01
	30	62.90	47.68	173.99	65.56	49.68	187.25
	40	63.68	48.20	181.01	66.34	50.21	194.56
	50	64.74	48.94	189.87	67.26	50.84	203.02
	60	65.82	49.68	199.20	68.19	51.47	211.94
38	0	66.68	52.48	185.16	69.79	54.91	201.06
	10	67.33	52.95	191.34	70.44	55.38	207.52
	20	68.14	53.52	198.59	71.10	55.84	214.28
	30	68.95	54.10	206.20	71.77	56.30	221.39
	40	69.77	54.68	214.21	72.59	56.88	229.71
	50	70.75	55.38	223.47	73.41	57.46	238.48
	60	71.87	56.19	234.09	74.54	58.27	249.47
39	0	73.42	59.80	221.13	76.72	62.47	239.42
	10	74.11	60.30	228.20	77.25	62.85	245.90
	20	74.80	60.81	235.61	77.95	63.36	253.61
	30	75.66	61.45	244.28	78.80	64.00	262.63
	40	76.52	62.09	253.41	79.51	64.50	271.17
	50	77.55	62.85	263.97	80.38	65.14	281.15
	60	78.74	63.74	276.06	81.41	65.90	292.66
40	0	80.91	68.19	263.94	84.42	71.13	285.01
	10	81.64	68.75	272.04	85.15	71.70	293.44
	20	82.55	69.45	281.53	85.89	72.26	302.26
	30	83.29	70.01	290.43	86.63	72.82	311.52
	40	84.20	70.71	300.86	87.37	73.38	321.25
	50	85.28	71.56	312.92	88.29	74.08	332.63
	60	86.38	72.40	325.63	89.39	74.92	345.76
41	0	89.64	78.16	317.27	93.38	81.42	341.65
	10	90.41	78.78	326.58	93.98	81.88	350.13
	20	91.19	79.40	336.32	94.76	82.50	360.23
	30	91.97	80.02	346.52	95.54	83.12	370.82
	40	92.94	80.80	358.47	96.33	83.74	381.94
	50	93.92	81.57	371.04	97.30	84.52	394.95
	60	95.25	82.66	386.81	98.46	85.45	409.95
42	0	99.42	89.70	381.28	103.42	93.31	409.51
	10	100.24	90.39	392.00	104.05	93.82	419.25
	20	101.07	91.08	403.19	104.88	94.51	430.85
	30	101.90	91.76	414.91	105.71	95.20	442.99
	40	102.93	92.62	428.63	106.55	95.88	455.74
	50	103.96	93.48	443.05	107.39	96.57	469.17
	60	105.20	94.51	459.69	108.63	97.60	486.32
43	0	110.63	103.29	459.82	114.92	107.29	492.61
	10	111.51	104.06	472.18	115.59	107.87	503.82
	20	112.19	104.63	483.50	116.27	108.44	515.54
	30	113.28	105.58	498.58	117.16	109.20	529.49

$\phi^\circ$	$\theta^\circ$	$N_c$	$N_q$	$N_\gamma$	$N_c$	$N_q$	$N_\gamma$
	40	114.17	106.34	512.75	118.05	109.96	544.12
	50	115.27	107.29	529.30	119.15	110.91	561.20
	60	116.58	108.44	548.40	120.26	111.87	579.17
44	0	123.53	119.35	556.51	127.92	123.60	592.87
	10	124.25	119.99	569.00	128.64	124.23	605.79
	20	125.19	120.84	583.89	129.58	125.08	621.19
	30	126.14	121.69	599.46	130.31	125.72	635.35
	40	127.09	122.54	615.78	131.26	126.57	652.18
	50	128.27	123.60	634.84	132.22	127.41	669.86
	60	129.45	124.66	654.87	133.40	128.48	690.48
45	0	138.17	138.17	673.91	143.15	143.15	718.53
	10	139.18	139.12	690.49	143.92	143.86	733.49
	20	139.96	139.83	705.62	144.69	144.57	749.11
	30	140.97	140.78	723.62	145.47	145.28	765.46
	40	141.99	141.73	742.47	146.49	146.23	784.88
	50	143.26	142.91	764.48	147.52	147.18	805.26
	60	144.53	144.10	787.59	148.79	148.36	829.01
46	0	155.40	160.85	821.83	160.53	166.16	871.66
	10	156.23	161.65	838.65	161.36	166.96	889.02
	20	157.32	162.71	858.71	162.19	167.76	907.12
	30	158.16	163.51	877.09	163.03	168.55	926.04
	40	159.26	164.57	898.93	164.13	169.62	948.52
	50	160.36	165.63	921.82	165.23	170.68	972.08
	60	161.72	166.96	948.51	166.34	171.74	996.82
47	0	175.18	187.71	1003.30	180.75	193.68	1061.93
	10	176.07	188.60	1022.91	181.64	194.58	1082.14
	20	177.25	189.80	1046.29	182.54	195.47	1103.18
	30	178.15	190.69	1067.65	183.44	196.37	1125.16
	40	179.34	191.89	1093.05	184.35	197.26	1148.16
	50	180.53	193.08	1119.63	185.54	198.46	1175.45
	60	182.00	194.58	1150.61	186.74	199.65	1204.06
48	0	198.60	220.33	1233.66	204.37	226.74	1299.50
	10	199.57	221.35	1256.62	205.04	227.42	1319.57
	20	200.54	222.36	1280.52	206.01	228.43	1344.09
	30	201.52	223.37	1305.44	206.99	229.44	1369.66
	40	202.50	224.38	1331.50	207.97	230.46	1396.40
	50	203.79	225.73	1362.42	209.26	231.81	1428.11
	60	205.39	227.42	1398.46	210.55	233.16	1461.32
49	0	225.79	259.42	1519.56	231.78	266.31	1593.55
	10	226.85	260.57	1546.52	232.84	267.46	1621.19
	20	227.57	261.33	1570.40	233.90	268.61	1649.91
	30	228.63	262.48	1599.54	234.63	269.37	1675.55
	40	230.03	264.01	1634.19	235.69	270.52	1706.74
	50	231.11	265.16	1666.07	237.10	272.05	1743.74



$\phi^\circ$	$\theta^\circ$	$N_c$	$N_q$	$N_\gamma$	$N_c$	$N_q$	$N_\gamma$
	60	232.52	266.69	1703.82	238.17	273.20	1778.01
50	0	257.92	306.95	1880.94	264.51	314.81	1969.18
	10	258.70	307.83	1907.83	265.30	315.68	1996.73
	20	259.86	309.13	1940.77	266.46	316.99	2030.47
	30	261.02	310.44	1975.02	267.25	317.86	2060.47
	40	262.19	311.75	2010.74	268.42	319.17	2097.00
	50	263.36	313.06	2048.04	269.59	320.48	2135.15
	60	264.90	314.81	2092.22	271.13	322.23	2180.32